



Universidade do Porto

Faculdade de Engenharia

FEUP

New Design Tools for Activated Sludge Process

Ph.D. Dissertation
in
Environmental Engineering
by

Anna Maria Karpinska Portela

Supervisors

Ricardo Jorge Nogueira dos Santos

Madalena Maria Gomes de Queiroz Dias

Rui Alfredo da Rocha Boaventura



Laboratory of Separation and Reaction Engineering - LSRE
Laboratório Associado LSRE/LCM
Departamento de Engenharia Química
Faculdade de Engenharia
Universidade do Porto

December 2013

Acknowledgments

The completion of this PhD thesis marks the end of a long and eventful stage in my mountaineering route that required commitment, perseverance, resilience and passion for hiking. Now, with just a few more steps ahead to reach the target peak, it is the right time to look over the journey past and remember all the people who have helped and supported me along this long and fulfilling route up.

I would like to express the deepest admiration and heartfelt gratitude to my supervisors, whose contribution was of immense importance in the preparation and completion of this thesis. I could not have asked for better role models, each inspirational, supportive, and patient. My first debt of gratitude must go to my supervisor, Dr. Ricardo Santos, who took a chance on me back in 2007 and offered me a scientific fellowship within CFD research group, and two years later enabled this PhD project. I am grateful for his fundamental role in my doctoral work, not to mention his friendship and support, but also thoughtful guidance, time and effort during shaping the direction of this work and sharing his unsurpassed knowledge on good CFD modelling practice in wastewater engineering. I would like to thank Professor Madalena Dias, my thesis co-supervisor and Director of Associated Laboratory LSRE/LCM, for her availability and support, time and effort during review of my doctoral work, publications, presentations and providing encouraging and constructive feedback. I am also very grateful to Professor Rui Boaventura, my thesis co-supervisor, who had offered me a chance to pursue my scientific career at LSRE within his environmental research group back in 2006, and thanks to whose recommendation I joined Dr. Ricardo's environmental project. I wish to thank not only for his guidance, precious suggestions and effort during review of my scientific work, but also for friendship and support along the way.

I would like to acknowledge LSRE, Laboratory of Separation and Reaction Engineering-Associated Laboratory LSRE/LCM, one of the foremost research units of Portugal, where my doctoral work was carried out. It has been a great privilege to spend nearly seven years at LSRE, and its members, both staff and team, especially from Mixing Group, will always remain dear to me. I would like to thank Professor José Carlos Lopes for giving me an opportunity to be a part of Mixing Group and for numerous productive discussions on CFD and boundary layer. I wish to thank Professor Alírio Rodrigues, former director of Associated Laboratory LSRE/LCM, Professor Eugénia Macedo, Professor José Miguel Loureiro and Professor Mário Rui Costa for inspirational discussions. I am sincerely grateful to Susana Cruz, who provided me with administrative assistance in the complex bureaucratic

procedures on numerous occasions. I wish to thank her also for precious advices and friendship.

I gratefully acknowledge the funding received towards my PhD from the FCT- Fundação para a Ciência e a Tecnologia - SFRH/BD/47673/2008. I am also grateful for the financial support for this work provided by national research grant FCT PTDC/AMB/65983/2006.

I would like to thank my friends and former LSRE researchers, Elisabete Pereira and Joana Pereira, for their contribution in the pilot and full-scale studies carried on oxidation ditches. I appreciate also help of António Gouveia and Telmo Santos in providing data acquisition for my aeration system and variable frequency drive for my pilot ditch. Special thanks go to Ângela Novais, past Mixing Group member and a good friend of mine, for lunchtime fun and help with “workbenching” complicated geometries.

I would like to thank my remaining colleagues from Mixing Group, both past and present, for all the great times that we have shared (in chronological order): Ertugrul Erkoç, Ashar Sultan, Paulo Gomes, Cláudio Fonte and Carlos Fonte, Nuno Gomes, Marina Verencevic Torres, Kateryna Krupa Figueiredo, Enis Leblebici, Marcelo Costa, Rómulo Oliveira and Gabriela Ruphuy. Special thanks to Tatiana Pozdniakova, my fellow from Environmental Science and Engineering Research Group, for her friendship, numerous office-talks and useful tips concerning use of analytical equipment.

I take this opportunity to acknowledge my master’s supervisors, great mentors and passionate mountaineers, Dr. Marek Molczan and Dr. Andrzej Bilyk from the Institute of Environment Protection Engineering, Wroclaw University of Technology, for their encouraging and supportive role in pursuing my scientific career in Portugal.

Words cannot express my gratitude to my parents, Malgorzata and Krzysztof Karpinsky, for their unconditional love and support beyond measures, and for all sacrifices they made on my behalf. I am also sincerely grateful to my mother-in-law Ilda Duro, for her love, commitment and indescribable support in every matter during all these years since my first steps on Portuguese land. They, along with my grandparents, encouraged me to follow my dreams, respected my choices, helped me at every stage of my personal and academic life, and longed to see this achievement come true. I extend my heartfelt thanks to my Portuguese grandparents for providing a loving environment for me and for their unconditional support. Special thanks to my twin-brother Pawel and sister-in-law Olga, for their advices, relaxing talks and unlimited support along the way.

Last but not least, I would like to thank my loving, supportive, encouraging, and remarkably patient husband Luís, for being my best cheerleader, intellectual sounding board and emotional base, for giving me confidence and motivating me in so many ways, for staying awake countless nights during the last stages of writing this Ph.D. thesis, always ready to help and without whom I would have struggled to find the inspiration and motivation needed to complete this dissertation.

To my Family

“Here, in the pool of this river, under boughs of hazel from which dropped the Nuts of Knowledge on the stream, lived Fintan the Salmon of Knowledge, which whoso ate of him, would enjoy all wisdom of the ages.”

Thomas W. Rolleston
in Myths & Legends of the Celtic Race (1929)

Abstract

In this work Computational Fluid Dynamics (CFD) is used as a design tool in development of a new aeration method for oxidation ditches, consisting of an external unit, a pressurized aeration chamber (PAC), cooperating with slot jet agitators (hydrojets). Wide range of operating and hydraulic conditions in PAC and oxidation ditch is simulated with CFD codes aiming selection of the most energy efficient design comprising enhanced aeration with efficient mixing. The results are validated experimentally in reaeration tests conducted on lab-scale PAC.

CFD simulations are also enabled to assess residence time distribution (RTD), and thus macromixing within the oxidation ditch. These results are compared with data from pilot- to full-scale oxidation ditches.

It is shown that fluid velocity and mixing patterns within the ditch have strong impact on occurrence of oxygen-deficit zones, and when comparing oxygen and nutrients profiles along the ditch it is clear, that reactor hydrodynamics is a key parameter in nitrification, denitrification and biodegradation process control. According to that, simulated mid-depth slot jets configuration, having energy efficiency of 31% and yielding 3% higher power demand than the most energy efficient design, was selected as the one providing optimal mixing conditions for efficient oxygenation of the tank content. It is also shown that the RTD curves and the hydrodynamics characteristics can be obtained from the CFD simulations and then used to generate a suitable reactor model, where the biokinetic activated sludge models, ASM, can be implemented.

Aeration in PAC using pure oxygen results in distinctly higher oxygen transfer efficiencies than the respective process parameters of current best available technologies (BAT), yielding Standard Oxygen Transfer Efficiency (SOTE) of minimum 120% and Standard Aeration Efficiency (SAE) up to 8.0 kgO₂/kWh. By overcoming SOTE limitations of air diffusers, aeration in PAC allows reduction of energy expenditure on aeration by over 90%.

When comparing with current BAT devices commonly used in oxidation ditches, membrane diffusers supplied by air or pure oxygen and agitated with slow speed mixers, proposed aeration system consisting of PAC cooperating with hydrojets allows distinct energy savings through reduction of energy consumption by 67% up to 93%.

Resumo

Neste trabalho a Computação de Fluidos Dinâmicos (CFD) é usada como ferramenta de projeto no desenvolvimento dum novo processo de arejamento, a Câmara de Arejamento Pressurizada (PAC), para aplicação em valas de oxidação agitadas por hidrojetos. Uma gama abrangente de condições de operação e escoamento na PAC é simulada com CFD com o objetivo de selecionar a configuração que permite melhorar a eficiência energética e a mistura. Os resultados são validados experimentalmente em testes de rearejamento numa PAC piloto.

A Distribuição de Tempos de Residência (RTD), ou seja a macromistura, na vala de oxidação também é estudada por meio de simulações de CFD. Os resultados são comparados com testes numa unidade piloto e em testes à escala real.

É demonstrado o impacto que têm a velocidade de escoamento e a mistura na vala de oxidação na geração de zonas anóxicas. Através da comparação de perfis de concentração de oxigénio e nutrientes, verifica-se o papel fundamental que a hidrodinâmica na vala de oxidação desempenha nos processos de nitrificação, desnitrificação e oxidação da matéria. As valas com agitadores a meia altura, com eficiências energéticas de 31%, 3% inferior à configuração ótima, foram selecionadas por promoverem as melhores condições para uma oxigenação eficiente de toda a vala de oxidação. Também se demonstra a utilização de simulações de CFD para a caracterização da hidrodinâmica e da RTD nos processos de vala de oxidação, que podem ser utilizados na geração dum modelo de reatores para ser acoplado a modelos biocinéticos de lamas ativadas.

Demonstra-se que o processo de arejamento na PAC com oxigénio puro é bastante mais eficiente que as melhores tecnologias disponíveis (BAT), atingindo valores de eficiência de transferência de oxigénio (SOTE) superiores a 120% e de eficiência de arejamento até 8.0 kgO₂/kWh. Ao ultrapassar o limite de SOTE dos difusores de ar, a PAC permite reduções de consumo de energia no processo de arejamento de aproximadamente 90%.

A PAC instalada numa configuração com agitação da vala por hidrojetos permite poupanças de energia entre 67% a 93% relativamente às BAT para arejamento em valas de oxidação: difusores de fundo para ar ou oxigénio puro agitados por turbinas de baixa velocidade de rotação.

Streszczenie

W niniejszej pracy zastosowano numeryczną mechanikę płynów (ang. Computational Fluid Dynamics, CFD) jako narzędzie projektowe w opracowaniu nowej technologii napowietrzania rowów biologicznych utleniających, składającej się z ciśnieniowej komory aeracyjnej (ang. Pressurized Aeration Chamber, PAC), współpracującej z inżektorami szczelinowymi. Szeroki zakres warunków eksploatacyjnych i hydraulicznych w PAC i bioreaktorze symulowano za pomocą CFD celem wyboru najbardziej energooszczędnej konfiguracji zapewniającej intensywne napowietrzanie i wydajne mieszanie. Wyniki symulacji PAC zostały potwierdzone eksperymentalnie w testach reaeracyjnych przeprowadzonych w skali laboratoryjnej.

Symulacje CFD użyto także do wyznaczenia rozkładu czasu przebywania płynu (ang. Residence Time Distribution, RTD) - makromieszania w rowie utleniającym. Wyniki symulacji porównano z danymi uzyskanymi z badań przeprowadzonych w skali pilotażowej i rzeczywistej.

Wykazano, że prędkość przepływu i mieszanie płynu wewnątrz rowu mają wpływ na występowanie stref deficytu tlenowego. Na podstawie otrzymanych profili składników odżywczych i tlenu potwierdzono rolę hydrodynamiki reaktora jako kluczowego parametru w kontroli procesów nitrifikacji, denitrifikacji i biodegradacji. Symulowana konfiguracja rowu z inżektorami położonymi na połowie głębokości, o 31-procentowej wydajności energetycznej i zapotrzebowaniu na moc wyższym o 3% od optymalnego modelu została wybrana jako wariant zapewniający najlepsze warunki natlenienia objętości ścieków. Wykazano także, że krzywe RTD oraz dane hydrodynamiczne otrzymane z symulacji CFD mogą być użyte do generacji precyzyjnego modelu reaktora, z którym mogą zostać sprzężone modele biokinetyczne osadu czynnego z serii ASM.

Zasilanie komory PAC czystym tlenem spowodowało wyraźnie wyższą skuteczność napowietrzania w porównaniu z najlepszymi obecnie dostępnymi technologiami BAT, dając wartości SOTE $\geq 120\%$ i SAE ≤ 8.0 kgO₂/kWh. Pokonując ograniczenia SOTE dyfuzorów drobnopęcherzykowych, zastosowanie PAC umożliwia obniżenie wydatku energetycznego na napowietrzanie o ponad 90%.

System napowietrzania składający się z PAC i inżektorów szczelinowych umożliwia oszczędność energii w 67 do 93% w porównaniu z obecnymi urządzeniami BAT powszechnie stosowanymi w rowach utleniających- dyfuzorami membranowymi zasilanymi powietrzem lub czystym tlenem i współpracującymi z mieszadłami wolnoobrotowymi.

Table of Contents

	Page
1 Introduction.....	1
1.1 Wastewater Treatment - Health and Human Well-Being.....	1
1.2 Water Policy - Tailoring Wastewater Treatment Objectives	1
1.3 Emerging Challenges: Water and Energy Nexus.....	1
1.4 Relevance and Motivation	1
1.5 Thesis Objectives and Layout.....	1
2 Aeration Technologies.....	11
2.1 Introduction	11
2.2 Aeration in Activated Sludge Processes	12
2.2.1 Diffused Aeration Systems	13
2.2.1.1 Nonporous Diffusers.....	15
2.2.1.2 Porous Diffusers	16
2.2.1.3 Jet Aerators	17
2.2.1.4 U-tube Aerators.....	18
2.2.2 Mechanical Aeration Systems	19
2.2.2.1 Horizontal Rotors.....	20
2.2.2.2 Low-speed Surface Aerators.....	21
2.2.2.3 Draft Tube Aerators.....	22
2.2.2.4 Aspirating Aerators.....	22
2.2.2.5 High-speed Aerators	23
2.2.3 Oxygen Transfer in Clean Water	24
2.2.3.1 Oxygen Mass Transfer Theory	25
2.2.3.2 Clean Water Test	27
2.2.3.3 Oxygen Transfer Rate Parameters	31

Table of Contents

2.2.3.4	Process Parameters for Selected Aeration Devices	33
2.2.4	Recent Achievements in Aeration Field	36
2.3	Pressurized Aeration Chamber - CFD studies	42
2.3.1	Design Considerations	42
2.3.2	CFD Model	43
2.3.3	2D Geometry	44
2.3.4	Governing Equations	45
2.3.5	Boundary and Operating Conditions	49
2.3.6	Flow Solver	50
2.3.6.1	Solution Controls	50
2.3.7	Numerical Simulation Set-up	50
2.3.8	2D Studies - Results and Discussion	51
2.3.9	3D Geometry	55
2.3.10	Governing Equations	57
2.3.11	Boundary and Operating Conditions	57
2.3.12	Flow Solver	57
2.3.13	Numerical Simulation Set-up	57
2.3.14	3D CFD Studies - Results and Discussion	57
2.4	Pressurized Aeration Chamber - Experimental Studies	61
2.4.1	Aerator Design	61
2.4.2	Experimental Setup and Flow Loop	63
2.4.3	Clean Water Test	64
2.4.4	Experimental Flow and Pressure Ranges	66
2.4.5	Determination of the Process Parameters	68
2.4.6	Results and Discussion	72
2.4.6.1	Steady- State Experiments	72
2.4.6.2	Unsteady- State Experiments	76
2.4.6.3	Validation of 3D CFD Studies of PAC	80

Table of Contents

2.5	2D Bubble Column Reactor	84
2.5.1	Bubble Column Reactors in Activated Sludge Systems	84
2.5.2	2D Reactor	86
2.5.3	Experimental Set-up and Flow Loop	88
2.5.4	Experimental Air-Water Flow Ranges and Experiments.....	91
2.5.5	Imaging Experiments	92
2.5.5.1	Image Acquisition.....	92
2.5.5.2	Flow Regime Determination	93
2.5.5.3	Determination of Volumetric Fraction of Air via Image Processing	95
2.5.6	Clean Water Test.....	99
2.5.6.1	Determination of the Process Parameters.....	99
2.5.7	Results and Discussion.....	101
2.5.7.1	Flow Regime.....	101
2.5.7.2	Gas Hold-up	103
2.5.7.3	Clean Water Test Results	104
2.6	Conclusions	110
3	Hydrodynamics of the Oxidation Ditch	113
3.1	Introduction	113
3.2	Literature Review.....	114
3.3	Pilot Scale Studies	119
3.3.1	Piston Flow Reactor Set-up.....	119
3.3.2	PFRR Start-up and Operation.....	124
3.3.3	Materials and Methods	125
3.3.3.1	Sampling	125
3.3.3.2	Measurement of the Axial Velocity	126
3.3.3.3	Measurement of Dissolved Oxygen.....	127
3.3.3.4	Determination of <i>COD</i>	127
3.3.3.5	Determination of <i>NH₄ – N</i>	128

Table of Contents

3.3.3.6	Determination of <i>NO₃ – N</i>	128
3.3.3.7	Determination of <i>PO₄ – P</i>	128
3.3.3.8	Determination of <i>TSS</i>	128
3.3.4	RTD Determination.....	129
3.3.4.1	Pulse Tracer Experiment.....	129
3.3.4.2	Step Tracer Experiment.....	130
3.3.5	Results and Discussions.....	131
3.3.5.1	Wastewater Characteristics.....	131
3.3.5.2	Reactor Start-up and Treatment Efficiency.....	131
3.3.5.3	Velocity Profiles along the PFRR Ditch.....	135
3.3.5.4	Dissolved Oxygen Profiles along the PFRR Ditch.....	137
3.3.5.5	Nutrients Profiles along the PFRR Ditch.....	137
3.3.5.6	RTD of the PFRR Ditch.....	141
3.4	Real Scale Experiments.....	145
3.4.1	Areosa WWTP - Viana do Castelo.....	145
3.4.2	Oxidation Ditch System.....	146
3.4.3	Materials and Methods.....	147
3.4.3.1	Sampling.....	147
3.4.3.2	Measurement of the Surface Velocity.....	148
3.4.3.3	Measurement of Dissolved Oxygen.....	148
3.4.3.4	Determination of Nutrients and <i>TSS</i> Content.....	149
3.4.4	Results and Discussions.....	149
3.4.4.1	Velocity Profiles along the Oxidation Ditch.....	149
3.4.4.2	Dissolved Oxygen Profiles along the Oxidation Ditch.....	150
3.4.4.3	Nutrients Profiles along the Oxidation Ditch.....	156
3.5	Conclusions.....	161
4	CFD Simulations of the Oxidation Ditch.....	165
4.1	Introduction.....	165

Table of Contents

4.2	Literature Review.....	166
4.3	CFD Model.....	169
4.3.1	Design Consideration	170
4.3.2	3D Geometry	171
4.3.3	Hydrodynamics Modelling.....	175
4.3.3.1	Reynolds Averaged Navier-Stokes Simulations.....	175
4.3.3.2	Large Eddy Simulation	183
4.3.4	Channel Flow	184
4.3.5	Residence Time Distribution Computing	188
4.4	Boundary and Operating Conditions	189
4.5	Flow Solver	190
4.5.1	Solution Controls.....	191
4.5.2	Numerical Simulation Set-up.....	191
4.6	Results and Discussion	192
4.6.1	Hydrodynamics of the Oxidation Ditch	192
4.6.2	Energy Expenditure for Mixing	198
4.6.3	Modelling of the Boundary Layer	200
4.6.3.1	Grid Configuration in Near-wall Region Treatment.....	201
4.6.3.2	Turbulence Model in Near-wall Region Treatment.....	213
4.6.3.3	Surface Roughness.....	216
4.6.4	Energy Expenditure for Different Mesh Properties and Turbulence Models ..	224
4.6.5	Macromixing	227
4.7	Conclusions	230
5	New Designs and Energy Efficiency Evaluation.....	233
5.1	Introduction	233
5.2	Oxygen Demand for Wastewater Aeration.....	234
5.2.1	Actual Air and Oxygen Demand	236
5.2.2	Actual Air/Oxygen Demand for Diffused Aeration	237

Table of Contents

5.3	Energy Expenditure in Aeration Systems.....	238
5.3.1	Surface Aerators.....	238
5.3.2	Diffused Aeration Systems	240
5.3.2.1	Air Piping	240
5.3.2.2	Power Demand by Blower - Air System	240
5.3.2.3	Power Demand by Blower - Pure Oxygen System.....	242
5.3.2.4	Power Demand for Oxygen Generation	243
5.3.3	Evaluation of Energy Expenditure of Aeration Systems	244
5.4	Aeration of the Oxidation Ditch with Hydrojets - Energy Analysis.....	245
5.4.1	Oxidation Ditch System	245
5.4.2	Power Demand on Aeration.....	246
5.4.2.1	Air Piping	246
5.4.2.2	Power Demand by Blower - Air System	249
5.4.2.3	Power Demand by Blower - Oxygen System	249
5.4.2.4	Power Demand for Oxygen Generation	250
5.4.3	Power Demand on Mixed Liquor Recirculation and Reinjection	250
5.4.3.1	Head Loss in Piping System	251
5.4.3.2	Head Loss in Hydrojets	257
5.4.3.3	Pump Head	262
5.4.3.4	Power Demand for Wastewater Pumping through PAC	263
5.4.4	Energy Analysis	266
5.5	Conclusions	267
6	Final Remarks.....	269
6.1	Introduction	269
6.2	General Conclusions.....	269
6.3	Future Work	276
7	References	277

Table of Figures

	Page
Figure 2.1 Conformal quadrilateral mesh used in 2D geometries of PAC.....	44
Figure 2.2 Maps of the velocity magnitude obtained for various 2D geometries of the PAC: a) squared; b) rectangular; c) with central topwall baffle; d) with topwall baffles; e) with central bottom baffle; f) with bottom baffles; g) with alternating baffles.	53
Figure 2.3 Maps of the DO concentration obtained for various 2D geometries of the PAC: a) squared; b) rectangular; c) with central topwall baffle; d) with topwall baffles; e) with central bottom baffle; f) with bottom baffles; g) with alternating baffles....	54
Figure 2.4 3D configurations of the PAC: a) without baffles; b) with bottom baffles; c) with alternating set of baffles.	56
Figure 2.5 Example of surface mesh generated for the geometry with bottom baffles. ...	56
Figure 2.6 Maps of the velocity magnitude obtained for various 3D geometries of the PAC: a) without baffles; b) with bottom baffles; c) with alternating baffles.....	59
Figure 2.7 Maps of the DO concentration obtained for various 3D geometries of the PAC: a) without baffles; b) with bottom baffles; c) with alternating baffles.	60
Figure 2.8 Pressurized Aeration Chamber (PAC) scheme.....	61
Figure 2.9 Pressurized Aeration Chamber (PAC): a) without, and b) with outer steel casing.	62
Figure 2.10 Experimental set-up and the flow loop: 1- reservoir; 2- stirrer; 3- multi meter; 4- probe; 5-pump; 6- PAC; 7- flowmeter; 8- pressure regulator; 9- pressure transducer; 10, 11- tubing; 12- DO controller; 13, 14- flow cell adapter; 15- valve; 16- acquisition board; 17- PC.	64
Figure 2.11 Flow conditions within PAC.....	67
Figure 2.12 Example of the determination of oxygen mass transfer coefficient (KLa) using data obtained in steady-state clean water test.....	69
Figure 2.13 Steady-state DO concentration obtained in steady- state clean water test for various oxygen pressures.	74
Figure 2.14 Oxygen mass transfer coefficient (KLa) obtained in steady- state clean water test for various oxygen pressures.....	74
Figure 2.15 Oxygen transfer rate (OTR) obtained in steady- state clean water test for various oxygen pressures.....	75

Table of Contents

Figure 2.16 Oxygen transfer efficiency (<i>OTE</i>) obtained in steady- state clean water test for various oxygen pressures.	75
Figure 2.17 Aeration efficiency (<i>AE</i>) obtained in steady- state clean water test for various oxygen pressures.....	76
Figure 2.18 Oxygen mass transfer coefficient (<i>KLa</i>) obtained in unsteady- state clean water test for various oxygen pressures.....	78
Figure 2.19 Oxygen transfer rate (<i>OTR</i>) obtained in unsteady- state clean water test for various oxygen pressures.....	78
Figure 2.20 Oxygen transfer efficiency (<i>OTE</i>) obtained in unsteady- state clean water test for various oxygen pressures.....	79
Figure 2.21 Aeration efficiency (<i>AE</i>) obtained in unsteady- state clean water test for various oxygen pressures.....	79
Figure 2.22 Schematic discharge to and from the PAC through the: a) inlet, and b) outlet orifice.....	81
Figure 2.23 Bubble Column Reactor layout.	87
Figure 2.24 Image of structure packing.	88
Figure 2.25 A photograph of experimental installation.	90
Figure 2.26 Experimental set-up and flow loop: 1- reservoir; 2- stirrer; 3- multi meter; 4- probe; 5-pump; 6- BCR; 7- flowmeter; 8- pressure regulator; 9- air flowmeter; 10- pressure transducer; 11- influent tube; 12- outflow from the separator; 13- DO controller display; 14, 15- flow cell adapter; 16- acquisition board; 17- PC; 18-CCD camera; 19- halogen lamp; 20- light diffuser; 21- PC.	91
Figure 2.27 Image acquisition system.	93
Figure 2.28 Example of the raw image captured by CCD camera.....	96
Figure 2.29 Image processing algorithm.	97
Figure 2.30 Flow regime contour maps obtained for the BCR.	102
Figure 2.31 Different flow patterns observed in BCR: a) bubbly; b) slug; c) churn; and d) annular flow.....	103
Figure 2.32 Contour map of gas hold-up obtained for different gas-fluid velocities.	104
Figure 2.33 Standard volumetric mass coefficient <i>KLa20</i> obtained in clean water test for different water and air velocities.....	105
Figure 2.34 Standard Oxygen Transfer Rate <i>SOTR</i> obtained in clean water test for different water and air velocities.	106

Table of Contents

Figure 2.35 Standard Oxygen Transfer Rate <i>SOTE</i> obtained for different water and air velocities	107
Figure 2.36 Standard Aeration Efficiency <i>SAE</i> obtained for different water and air velocities.	109
Figure 2.37 Standard Aeration Efficiency <i>SAE</i> obtained for different water and air velocities for blower discharge pressure of 2.0 bar.	110
Figure 3.1 Pilot installation of the tubular closed-loop PFRR with feed tank and the secondary settler.....	120
Figure 3.2 Pilot scale closed-loop PFRR reactor.	121
Figure 3.3 Schematic layout of the PFRR reactor.	122
Figure 3.4 Distribution of the sampling points along the PFRR ditch.	122
Figure 3.5 Horizontal paddlewheel impeller.	123
Figure 3.6 Bottom diffused air system.	123
Figure 3.7 Distribution of the sampling points for velocity measurement.	127
Figure 3.8 Scheme of the RTDs experiments.	130
Figure 3.9 Quality parameters of the synthetic wastewater during system start-up.....	132
Figure 3.10 <i>COD</i> concentration in the influent and within the PFRR reactor during start-up.	133
Figure 3.11 <i>NH₄ – N</i> concentration in the influent and within the PFRR reactor during start-up.	133
Figure 3.12 <i>NO₃ – N</i> concentration in the influent and within the PFRR reactor during start-up.	134
Figure 3.13 <i>PO₄ – P</i> concentration in the influent and within the PFRR reactor during start-up.	134
Figure 3.14 <i>TSS</i> concentration in the influent and within the PFRR reactor during start-up.	135
Figure 3.15 Velocity profiles along the PFRR ditch obtained for the paddlewheel rotation obtained with frequency of a) 24 RPMs and b) 38 RPMs.	136
Figure 3.16 <i>DO</i> profile along the pilot PFRR ditch.	137
Figure 3.17 <i>COD</i> profile along the pilot PFRR ditch.	138
Figure 3.18 <i>NH₄ – N</i> profile along the pilot PFRR ditch.	139

Table of Contents

Figure 3.19 NO₃ – N profile along the pilot PFRR ditch.	139
Figure 3.20 PO₄ – P profile along the pilot PFRR ditch.....	140
Figure 3.21 TSS profile along the pilot PFRR ditch.	140
Figure 3.22 The plots of the response curves of the fluid in the pilot reactor obtained from the pulse tracer experiment presented as the a) conductivity curve b) normalized concentration curve.	142
Figure 3.23 Plot of the conductivity of the fluid in the pilot reactor obtained from the pulse tracer experiment.	143
Figure 3.24 The plots of the response curves of the fluid in the pilot reactor obtained from the step tracer experiment presented as the a) Cstep curve b) normalized concentration curve.	144
Figure 3.25 Areosa WWTP - Viana do Castelo (www.adnoroste.pt).	145
Figure 3.26 Scheme of the oxidation ditch in the Areosa WWTP.	146
Figure 3.27 Scheme of the oxidation ditch of Areosa WWTP - top view.	147
Figure 3.28 Distribution of the sampling points along the oxidation ditch.	148
Figure 3.29 Velocity profiles along the oxidation ditch.	150
Figure 3.30 DO concentration profile obtained for the wastewater temperature of 30 °C.	152
Figure 3.31 DO concentration profile under non-aeration period obtained for the wastewater temperature of 30 °C.	153
Figure 3.32 DO concentration profile obtained for the wastewater temperature of 27 °C.	153
Figure 3.33 DO concentration profile under non-aeration period obtained for the wastewater temperature of 27 °C.	154
Figure 3.34 DO concentration profile obtained for the wastewater temperature of 23.5 °C.	154
Figure 3.35 DO concentration profile under non-aeration period obtained for the wastewater temperature of 23.5 °C.	155
Figure 3.36 DO concentration profile obtained for the wastewater temperature of 20 °C.	155
Figure 3.37 DO concentration profile under non-aeration period obtained for the wastewater temperature of 20 °C.	156

Figure 3.38 COD profile along the real scale oxidation ditch.	158
Figure 3.39 NH4 – N profile along the real scale oxidation ditch.....	158
Figure 3.40 NO3 – N profile along the real scale oxidation ditch.	159
Figure 3.41 PO4 – P profile along the real scale oxidation ditch.	159
Figure 3.42 Nutrient concentration in function of DO content in real scale oxidation ditch.....	160
Figure 3.43 TSS profile along the real scale oxidation ditch.	160
Figure 4.1 Oxidation ditch system scheme: 1- oxidation ditch; 2- hydrojets; 3- inlet; 4- outlet; 5- PAC; 6- recirculation pump; 7- recirculated mixed liquor from the ditch; 8- air/oxygen manifold; 9- oxygen rich mixed liquor.	171
Figure 4.2 Schematic design of the hydrojet device.....	172
Figure 4.3 Geometry of the oxidation ditch with hydrojets placed in the middle depth of the tank.....	172
Figure 4.4 Sketch of a channel flow (Pope, 2000).....	185
Figure 4.5 Velocity vector maps in the oxidation ditch using RANS, URANS and LES.....	194
Figure 4.6 Velocity maps in the oxidation ditch obtained from RANS, URANS and LES for different hydrojets' placement.....	195
Figure 4.7 Velocity distribution maps on the surface obtained from the simulations with URANS and LES.....	196
Figure 4.8 Maps of pressure field obtained from the simulations of the oxidation ditch with different models.	196
Figure 4.9 Location of the control section in the oxidation ditch.	197
Figure 4.10 Velocity maps obtained with different models for the cross section located in the centre of the ditch.....	197
Figure 4.11 Velocity maps obtained with different models for the cross-section through the bend, located at 4.8 m from the centre of the ditch.	198
Figure 4.12 Velocity maps in the control cross-sections considered in the near-wall region modelling.	201
Figure 4.13 Cross-section through the ditch channel geometry having different mesh. ...	202
Figure 4.14 Determination wall points and lines within the control cross-sections in the oxidation ditch.	203

Table of Contents

Figure 4.15 Velocity maps in the section planes for $z= 0.0$ m obtained for different meshes.	206
Figure 4.16 Velocity maps in the section planes for $z= 4.8$ m obtained for different meshes.	207
Figure 4.17 Streamwise mean velocity near-wall profiles in the central cross-section through the oxidation ditch.	208
Figure 4.18 Streamwise mean velocity near-wall profiles in the cross-section through the entrance to the bend.	210
Figure 4.19 Streamwise mean velocity near-wall profiles in the cross-section through the exit from the bend.	212
Figure 4.20 Velocity maps obtained from RANS with different turbulence models for the ditch cross-section at $z= 0$ m.	217
Figure 4.21 Velocity maps obtained from RANS with different turbulence models for the ditch cross-section at $z= 4.8$ m.	218
Figure 4.22 Streamwise mean velocity near-wall profiles in the central cross-section through the oxidation ditch obtained with different turbulence models.	219
Figure 4.23 Streamwise mean velocity near-wall profiles in the cross-section through the entrance to the bend obtained with different turbulence models.	221
Figure 4.24 Streamwise mean velocity near-wall profiles in the cross-section through the exit from the bend obtained with different turbulence models.	223
Figure 4.25 Power demand for mixing obtained from RANS, URANS and LES simulations with different turbulence models and for different mesh configurations.	227
Figure 4.26 RTD curves obtained from oxidation ditch simulations with RANS, URANS and LES.	229
Figure 5.1 Oxidation ditch system layout: 1- oxidation ditch; 2- hydrojets; 3- inlet; 4- outlet; 5- PAC; 6- recirculation pump; 7- recirculated mixed liquor from the ditch; 8- air/oxygen manifold; 9- oxygen rich mixed liquor.	246
Figure 5.2 Schematic layout of the wastewater piping system in the oxidation ditch.	253
Figure 5.3 Schematic design of the hydrojet device with multiple slot injectors.	261
Figure 5.4 Schematic design of the hydrojet device with single slot injector.	262

Table of Tables

	Page
Table 2.1 Summary of Standard Aeration Efficiency (SAE) and Standard Oxygen Transfer Efficiency (SOTE) for selected nonporous diffused air systems.....	33
Table 2.2 Summary of Standard Aeration Efficiency (SAE) and Standard Oxygen Transfer Efficiency (SOTE) for selected porous diffused air systems.	34
Table 2.3 Summary of Standard Aeration Efficiency (SAE) and Standard Oxygen Transfer Efficiency (SOTE) for selected fine bubble aerators.	35
Table 2.4 Summary of Standard Aeration Efficiency (SAE) for selected mechanical aeration systems.	36
Table 2.5 Geometric models used in 2D simulations of PAC.....	45
Table 2.6 Concentration of the dissolved oxygen at the outlet of the chamber obtained for various 2D PAC layouts.....	55
Table 2.7 Concentration of the dissolved oxygen at the outlet of the chamber obtained for various 3D PAC layouts.....	58
Table 2.8 Oxygen concentration in equilibrium for various values of operating pressure.	67
Table 2.9 Summary of typical operating parameters of the commercial VPSA systems....	70
Table 2.10 Average aeration process parameters obtained from steady- state clean water tests.	73
Table 2.12 Aeration efficiency obtained from the 3D CFD simulations of various PAC configurations.	84
Table 2.13 Water and air flow rates used in the experiments.	92
Table 3.1 Composition of the synthetic wastewater.....	125
Table 3.2 Spatial distribution of sampling points with assigned to them measurements. .	126
Table 3.3 The environment and wastewater temperature during sampling campaign.	151
Table 4.1 Characteristics of the meshes used in the simulations of the oxidation ditch. .	174
Table 4.2 Wall regions and layers and their properties.	188
Table 4.3 Average velocity of the fluid obtained with different turbulence models.....	195
Table 4.4 Power demand and energy efficiency obtained with different turbulence models.	200
Table 4.5 Element sizes of the meshes used in the CFD simulations of the boundary layer.....	203

Table of Contents

Table 4.6 Viscous flow parameters in the near-wall region in the central cross-section through the oxidation ditch.	209
Table 4.7 Viscous flow parameters in the near-wall region in the cross-section through the entrance to the bend.	211
Table 4.8 Viscous flow parameters in the near-wall region in the cross-section through the exit from the bend.	213
Table 4.9 Viscous flow parameters in the near-wall region in the central cross-section through the oxidation ditch obtained with different turbulence models.	220
Table 4.10 Viscous flow parameters in the near-wall region in the cross-section through the entrance to the bend obtained with different turbulence models.	222
Table 4.11 Viscous flow parameters in the near-wall region in the cross-section through the exit from the bend obtained with different turbulence models.	224
Table 4.12 Power demand and energy efficiency obtained from RANS simulations with different turbulence models and for different mesh configurations.	226
Table 5.1 Daily air/oxygen demand determined for mean cell residence time from 5 to 15 days.	237
Table 5.2 Actual air/oxygen demand for various aeration devices.	238
Table 5.3 Power and energy demand by blowers for different diffused aeration systems.	242
Table 5.4 Power and energy demand by blowers for different diffused aeration systems supplied by pure oxygen.	243
Table 5.5 Power and energy demand by oxygen generation in VPSA process for different diffused aeration systems.	244
Table 5.6 Power and energy demand by blowers for PAC supplied by air.	249
Table 5.7 Power and energy demand by blowers for PAC supplied by oxygen.	250
Table 5.8 Power and energy demand by oxygen generation in VPSA process for different diffused aeration systems.	250
Table 5.9 Local loss coefficients for the selected fittings.	257
Table 5.10 Head loss and pump head in proposed mixed liquor recirculation and reinjection system.	263
Table 5.11 Power and energy demand by recirculation pump for PAC supplied by air and pure oxygen.	266
Table 5.12 Energy expenditure in oxidation ditch system aerated with PAC.	267

Notation

a	specific area [m^{-1}]
A	area of the mass transfer [m^2]
A_b	total area of the air bubbles [m^2]
A_{CS}	area of the BCR cross-section [m^2]
A_n	area of nozzle [m^2]
A_1	outflow tube area [m^2]
A_2	manifold expansion cross-section area [m^2]
A_3	area of the surface flux [m^2]
AE	Aeration Efficiency [$\text{kgO}_2 \text{ kW}^{-1} \text{ h}^{-1}$]
b	width [m]
BOD	Biochemical Oxygen Demand [$\text{mgO}_2 \text{ L}^{-1}$]
BOD_{total}	per capital total Biochemical Oxygen Demand loading [$\text{gO}_2 (\text{capita} \cdot \text{day})^{-1}$]
BOD_5	per capital Biochemical Oxygen Demand after 5 days loading [$\text{gO}_2 (\text{capita} \cdot \text{day})^{-1}$]
C	flow coefficient [-]
C_d	discharge flow coefficient [-]
C_G	bulk gas phase oxygen concentration [mg L^{-1}]
C_i	concentration oxygen on the liquid side of the interface [mg L^{-1}]
C_{ij}	transport due to convection [W m^{-3}]
C_L	bulk liquid phase oxygen concentration [mg L^{-1}]
C_S	DO saturation concentration at the interface [mg L^{-1}]
C_{sal}	concentration of dissolved salts [mg L^{-1}]
C_{ST}^*	oxygen saturation concentration in the process temperature [mg L^{-1}]
C_{S20}^*	oxygen saturation concentration at standard temperature and pressure conditions [mg L^{-1}]
C_t	concentration of oxygen in bulk-liquid phase at the time t [mg L^{-1}]
$C_{w,alt}$	oxygen saturation at given temperature and altitude in clean water [mg L^{-1}]
C_0	initial oxygen concentration in bulk liquid phase [mg L^{-1}]
C_∞^*	oxygen saturation concentration at the time approaching infinity [mg L^{-1}]
$C_{\infty 20}^*$	oxygen saturation concentration under standard conditions and at the time approaching infinity [mg L^{-1}]
COD	Chemical Oxygen Demand [$\text{mgO}_2 \text{ L}^{-1}$]
d_h	hydraulic diameter [m]

Table of Contents

d_n	diameter of a nozzle [m]
d_{vc}	diameter of vena contracta cross-section [m]
D	inner diameter of the pipe [m]
$D_{L,ij}$	molecular diffusion [W m^{-3}]
$D_{i,m}$	mass diffusion coefficient of the i-th specie [$\text{m}^2 \text{s}^{-1}$]
D_m	molecular diffusion coefficient (diffusivity) [$\text{m}^2 \text{s}^{-1}$]
D_t	turbulent diffusivity [$\text{m}^2 \text{s}^{-1}$]
$D_{T,i}$	thermal diffusion coefficient of the i-th specie [$\text{m}^2 \text{s}^{-1}$]
$D_{T,ij}$	turbulent diffusion [W m^{-3}]
DP	delivered power [kW]
e	absolute roughness of the pipe [m]
e_B	blower efficiency [%]
e_M	motor efficiency [%]
E	specific energy of a fluid [J kg^{-1}]
E_{kWd}	daily energy demand [kWd]
E_{kWh}	hourly energy demand [kWh]
EC	electrical conductivity [$\mu\text{S cm}^{-1}$]
f	friction factor [-]
F_d	drag force [N]
F_{ij}	production by system rotation [W m^{-3}]
F_x	force in x-direction [N]
G_b	generation of turbulence kinetic energy due to buoyancy [W m^{-3}]
G_{ij}	buoyancy production [W m^{-3}]
G_k	generation of k due to mean velocity gradients [W m^{-3}]
G_ω	generation of ω due to mean velocity gradients [W kg^{-1}]
h	height [m]
h_f	friction headloss [m]
h_{fd}	discharge friction head [m]
$h_{f,d}$	discharge friction loss [m]
h_{fs}	suction friction head [m]
$h_{f,s}$	suction friction loss [m]
h_i	the specific enthalpy [J]
h_l	local headloss [m]
$h_{l,d}$	discharge local loss [m]
$h_{l,s}$	suction local loss [m]

Table of Contents

h_n	local loss on a nozzle [m]
h_{pd}	discharge surface pressure head [m]
h_{ps}	suction surface pressure head [m]
h_{sd}	discharge static head [m]
h_{ss}	suction static head [m]
h_{vel}	velocity head [m]
H_p	total pressure head [m]
H_S	system head [m]
J_i	diffusion flux of i species [$\text{kg m}^{-2} \text{s}^{-1}$]
k	turbulence kinetic energy, [$\text{m}^2 \text{s}^{-2}$]
k_d	endogenous decay coefficient [d^{-1}]
k_{eff}	effective conductivity [$\text{W m}^{-1} \text{K}^{-1}$]
k_G	gas film mass transfer coefficient [m s^{-1}]
k_l	local loss coefficient [-]
k_L	liquid film mass transfer coefficient [m s^{-1}]
k_s	surface roughness [m]
K_G	overall gas film coefficient [m s^{-1}]
K_L	overall liquid film coefficient [m s^{-1}]
$K_L a$	volumetric mass transfer coefficient [s^{-1}]
$K_L a_T$	clean water volumetric mass transfer coefficient at temperature T [s^{-1}]
$K_L a_{20}$	clean water volumetric mass transfer coefficient at 20°C [s^{-1}]
ℓ	turbulent length scale [m]
L	length [m]
L_e	equivalent length [m]
\dot{m}	oxygen mass flux [kg s^{-1}]
m_F	mass of filter [mg]
$m_{F,S}$	mass of filter with residues [mg]
M	momentum source [N m^{-3}]
M_t	turbulent Mach number [-]
np	number of passages [-]
$NH_4 - N$	ammonia concentration [mg L^{-1}]
$NO_3 - N$	nitrates concentration [mg L^{-1}]
$O_{2,out}$	oxygen mass flow rate in the outflow from the PAC [kg s^{-1}]
O_{TE}	Oxygen Transfer Efficiency [%]
O_{TR}	Oxygen Transfer Rate [$\text{kgO}_2 \text{h}^{-1}$]

Table of Contents

\bar{p}	averaged pressure field [Pa]
p_{O_2}	actual oxygen pressure [Pa]
$p_{O_2,N}$	normalized pressure of oxygen [Pa]
p_1	absolute pressures upstream blower [atm]
p_2	absolute pressures downstream blower [atm]
P	power [W]
P_G	partial pressure of the oxygen in the bulk gas phase [Pa]
P_i	partial pressure of the oxygen at the interface [Pa]
P_{ij}	stress production [$W\ m^{-3}$]
P_m	power demand of mechanical aeration unit in field conditions [kW]
P_{mix}	power demand for mixing [W]
P_{O_2}	power demand on oxygenation [W]
P_{ST}	power demand by aerator in standard pressure and temperature conditions and in clean water [kW]
P_u	power supplied to a fluid [W]
P_w	power demand for water pumping [W]
P_X	net waste activated sludge daily production [g VSS d ⁻¹]
$PO_4 - P$	phosphates concentration [$mg\ L^{-1}$]
q_p	wastewater flow rate per capita [$m^3\ d^{-1}$]
Q	volumetric flow rate [$m^3\ s^{-1}$]
Q_{Air}	air volumetric flow rate [$m^3\ s^{-1}$]
Q_{feed}	volumetric flow rate of the feed [$m^3\ s^{-1}$]
Q_{in}	volumetric flow rate at the inlet [$m^3\ s^{-1}$]
Q_{out}	volumetric flow rate at the outlet [$m^3\ s^{-1}$]
Q_{O_2}	oxygen flow rate [$m^3\ s^{-1}$]
Q_{rec}	recirculation volumetric flow rate [$m^3\ s^{-1}$]
Q_w	volumetric water flowrate [$m^3\ s^{-1}$]
r	rate of mass transfer rate per unit interfacial area per unit time [$kg\ m^{-2}\ s^{-1}$]
r_v	rate of mass transfer per unit volume and unit time [$kg\ m^{-3}\ s^{-1}$]
R_{Air}	air requirement [g d ⁻¹] or [$m^3\ d^{-1}$]
$R_{Air,act}$	actual air requirement [g d ⁻¹] or [$m^3\ d^{-1}$]
R_i	net rate of production of i species due to chemical reaction [$kg\ m^{-3}\ s^{-1}$]
R_{O_2}	oxygen requirement [g d ⁻¹] or [$m^3\ d^{-1}$]
$R_{O_2,act}$	actual oxygen requirement [g d ⁻¹] or [$m^3\ d^{-1}$]
$R_{O_2,th}$	theoretical oxygen requirement [g d ⁻¹]

Table of Contents

Re	Reynolds number [-]
Re_D	Reynolds number for bigger diameter [-]
Re_τ	friction Reynolds number [-]
S_e	effluent BOD [mg L^{-1}]
S_{ij}	mean rate-of-strain tensor [s^{-1}]
S_0	influent BOD [mg L^{-1}]
SAE	Standard Aeration Efficiency [$\text{kgO}_2 \text{ kW}^{-1} \text{ h}^{-1}$]
Sc_t	turbulent Schmidt number [-]
$SOTE$	Standard Oxygen Transfer Efficiency [%]
$SOTR$	Standard Oxygen Transfer Rate [$\text{kgO}_2 \text{ h}^{-1}$]
t	time [s]
t_p	particle relaxation time [s]
t_0	initial time [s]
T	temperature [$^{\circ}\text{C}$], [K]
T_{in}	blower inlet temperature [K], [$^{\circ}\text{C}$]
T_{O_2}	actual oxygen temperature [$^{\circ}\text{C}$], [K]
$T_{O_2,N}$	normalized oxygen temperature [$^{\circ}\text{C}$], [K]
TSS	Total Suspended Solids [mg L^{-1}]
u_{Air}	velocity of the air phase [m s^{-1}]
u_w	velocity of the water phase [m s^{-1}]
u_τ	friction velocity [m s^{-1}]
u^+	viscous velocity units [-]
\bar{U}	bulk velocity [m s^{-1}]
U_0	centreline velocity [m s^{-1}]
v	velocity [m s^{-1}]
v_i, v_j, v_l	velocity components [m s^{-1}]
\bar{v}_i	averaged velocity term [m s^{-1}]
v'_i	fluctuating velocity term [m s^{-1}]
v_1	velocity in the inflow to PAC [m s^{-1}]
v_2	velocity in the hydrojet manifold [m s^{-1}]
v_3	velocity of the jet [m s^{-1}]
ϑ	turbulent velocity scale [m s^{-1}]
V	volume [m^3]
V_{Air}	volume of the air phase [m^3]
V_{mix}	volume of the air-water mixture [m^3]

Table of Contents

V_{O_2}	actual volume of oxygen [m ³]
$V_{O_2,N}$	normalized volume of oxygen [m ³]
V_{sample}	sample volume [mL]
w	air mass flow rate [kg s ⁻¹]
w_{O_2}	mass flow rate of oxygen [kg h ⁻¹]
WP	wired power [kW]
x	distance [m]
\bar{x}	average finite element cell size [m]
x_i, x_j, x_l	spatial coordinates (displacement in the streamwise direction) [m]
x_{img}	image width [m]
y	distance from the wall [m]
y_B	distance from the bottom [m]
y_{img}	image height [m]
y_I	distance from the inside wall [m]
y_O	distance from the outside wall [m]
y^+	wall unit [-]
Y	synthesis yield coefficient [gVSS (gBOD ₅) ⁻¹]
Y_i	mass fraction of the i-th species [%]
Y_k	dissipation of k due to turbulence [W m ⁻³]
Y_M	contribution of the fluctuating dilatation in compressible turbulence to the overall dissipation rate [W m ⁻³]
Y_{obs}	observed biomass yield coefficient [gVSS (gBOD ₅) ⁻¹]
Y_ω	dissipation of ω due to turbulence [W m ⁻³]
z_0	level of the recirculation pump [m]
z_1	level of the oxidation ditch [m]

Greek letters

α	wastewater correction factor for oxygen transfer coefficient [-]
α^*	damping function coefficient [-]
β	thermal expansion coefficient [K^{-1}]
β_s	salinity - surface tension factor [-]
γ	solubility reduction factor [-]
Γ_k	effective diffusivity for k [$kg\ m^{-1}\ s^{-1}$]
Γ_ω	effective diffusivity for ω [$kg\ m^{-1}\ s^{-1}$]
δ_ν	viscous length scale [m]
ε	turbulent kinetic energy dissipation rate [$m^2\ s^{-3}$]
ε_{ij}	turbulent kinetic energy dissipation rate [$m^2\ s^{-3}$]
η	overall efficiency of the aeration equipment [%]
θ	temperature coefficient [-]
θ_T	potential temperature [K]
λ	friction coefficient [-]
μ	dynamic viscosity of the fluid [Pa s]
μ_t	turbulent viscosity [Pa s]
$\mu_{t,SGS}$	dynamic subgrid-scale viscosity [Pa s]
ν	kinematic viscosity [$m^2\ s^{-1}$]
ρ	fluid density [$kg\ m^{-3}$]
$\rho_{Air,N}$	air density in 0 °C [$kg\ m^{-3}$]
$\rho_{Air,20}$	air density in 20 °C [$kg\ m^{-3}$]
ρ_{O_2}	actual oxygen density [$kg\ m^{-3}$]
$\rho_{O_2,N}$	normalized oxygen density in 0 °C [$kg\ m^{-3}$]
$\rho_{O_2,20}$	oxygen density in 20 °C [$kg\ m^{-3}$]
ρ_p	particle density [$kg\ m^{-3}$]
ρ_0	is constant density of water [$kg\ m^{-3}$]
τ	mean hydraulic residence time [s]
τ_c	mean cell residence time [d]
τ_{ij}	subgrid scale stress tensor [Pa]
τ_{kk}	isotropic part of the subgrid-scale stresses [Pa]
τ_s	shear stress [Pa]
τ_T	temperature correction factor [-]
τ_w	wall shear stress [Pa]

Table of Contents

φ_{Air}	volumetric fraction of air [%]
ϕ_{ij}	transport due to pressure strain [$W\ m^{-3}$]
ω	specific turbulence dissipation (turbulence frequency) [s^{-1}]
Ω_{ij}	mean rate-of-rotation tensor [s^{-1}]

Indices

<i>act</i>	refers to actual air/oxygen requirement
<i>alt</i>	refers to altitude
<i>Air</i>	refers to air phase
<i>b</i>	refers to bubble phase or buoyancy
<i>B</i>	refers to bottom wall or blower
<i>c</i>	refers to cell
<i>CS</i>	refers to cross-section
<i>d</i>	refers to decay, drag force or discharge
<i>D</i>	refers to diameter
<i>e</i>	refers to equivalent length
<i>eff</i>	refers to effective conductivity
<i>f</i>	refers to friction
<i>feed</i>	refers to bioreactor's feed
<i>F</i>	refers to filter
<i>G</i>	refers to gaseous phase
<i>h</i>	refers to hydraulic diameter
<i>i</i>	index or counter
<i>I</i>	refers to inner wall
<i>img</i>	refers to image
<i>in</i>	refers to inlet
<i>j</i>	index or counter
<i>k</i>	refers to turbulence kinetic energy
<i>kWd</i>	refers to daily energy demand
<i>kWh</i>	refers to hourly energy demand
<i>l</i>	index or counter
<i>L</i>	refers to liquid phase
<i>m</i>	refers to molecular or mass diffusivity or mechanical aeration unit
<i>mix</i>	refers to mixture or mixing

Table of Contents

<i>M</i>	refers to motor efficiency or Mach number
<i>n</i>	refers to nozzle
<i>N</i>	refers to normalized conditions at 0 °C
<i>obs</i>	refers to observed process
<i>out</i>	refers to outlet
<i>O</i>	refers to outer wall
<i>O₂</i>	refers to oxygen
<i>p</i>	refers to particle or pressure
<i>rec</i>	refers to recirculation loop
<i>s</i>	refers to surface, shear stress, suction head or static head
<i>sal</i>	refers to salinity
<i>sample</i>	refers to sample
<i>S</i>	refers to oxygen saturation conditions, solids or system head
<i>SGS</i>	refers to subgrid-scale
<i>ST</i>	refers to standard temperature conditions
<i>t</i>	refers to turbulence
<i>th</i>	refers to theoretic requirement
<i>total</i>	refers to total quantity
<i>T</i>	refers to process temperature
<i>u</i>	refers to power of fluid
<i>v</i>	refers to unit volume
<i>vc</i>	refers to vena contracta
<i>vel</i>	refers to velocity head
<i>w</i>	refers to water phase or wall
<i>X</i>	refers to biomass
<i>ν</i>	refers to viscosity
<i>τ</i>	refers to shear stress
<i>ω</i>	refers to turbulence frequency
<i>+</i>	refers viscous wall units
<i>*</i>	refers to oxygen saturation concentration or damping functions
<i>∞</i>	refers to time approaching infinity
<i>0</i>	refers to initial state or position
<i>1</i>	index or counter
<i>2</i>	index or counter
<i>3</i>	index or counter

Table of Contents

5	index or counter
20	refers to the standard conditions at 20 °C

Abbreviations

AE	Aeration Efficiency
ALR	Airlift Reactor
AOP	Advanced Oxidation Processes
AS	Activated Sludge
ASCE	American Society of Civil Engineers
ASM	Activated Sludge Model
BAT	Best Available Technology Economically Achievable
BCR	Bubble Column Reactor
BOD	Biochemical Oxygen Demand
CARPT	Computer Automated Radioactive Particle Tracking
CBCT	Cone-Beam type X-ray Computed Tomography
CBOD	Carbonaceous Biochemical Oxygen Demand
CFD	Computational Fluid Dynamics
COD	Chemical Oxygen Demand
CPU	Central Processing Unit
CSTR	Continuous Stirred Tank Reactor
CT	Computed Tomography
CWA	Clean Water Act
DAQ	Data Acquisition
DO	Dissolved Oxygen
DPM	Discrete Phase Model
DWD	Drinking Water Directive
DWP	Dynamic Wet Pressure
EC	Electrical Conductivity
ECT	Electrical Capacitance Tomography
EPA	Environmental Protection Agency
EPDM	Ethylene- Propylene Diene Monomers
EU	European Union
EWT	Enhanced Wall Treatment
FAO	Food and Agriculture Organization of the United Nations
HDPP	High Density Polypropylene

Table of Contents

HPO-AS	High Purity Oxygen - Activated Sludge
HRT	Hydraulic Retention Time
IPPC	Integrated Pollution Prevention and Control
LDA	Laser Doppler Anemometry
LDV	Laser Doppler Velocimetry
LES	Large Eddy Simulation
LSRE	Laboratory of Separation and Reaction Engineering
MABR	Membrane-Aerated Biofilm Reactor
MBR	Membrane Bioreactor
MCRT	Mean Cell Residence Time
MF	Microfiltration
MLSS	Mixed Liquor Suspended Solids
NIH	National Institutes of Health
NPDES	National Pollutant Discharge Elimination System
OC	Oxygenation Capacity
OTE	Oxygen Transfer Efficiency
OTR	Oxygen Transfer Rate
PAC	Pressurized Aeration Chamber
PBR	Packed Bed Reactor
PDA	Particle Dynamic Analyzer
PFR	Plug Flow Reactor
PFRR	Plug Flow Reactor with Recirculation
PIV	Particle Image Velocimetry
RAM	Random Access Memory
RANS	Reynolds Averaged Navier-Stokes Simulations
RSM	Reynolds Stress Model
RTD	Residence Time Distribution
SAE	Standard Aeration Efficiency
SAN	Styrene- Acetylonitrile
SGS	Sub-grid Scale
SOTE	Standard Oxygen Transfer Efficiency
SOTR	Standard Oxygen Transfer Rate
SRT	Solid Retention Time
SWT	Standard Wall Function
TDS	Total Dissolved Solids

Table of Contents

TMDL	Total Maximum Daily Loads
TSS	Total Suspended Solids
UF	Ultrafiltration
URANS	Unsteady Reynolds Averaged Navier-Stokes Simulations
US	United States
UWWTD	Urban Waste Water Treatment Directive
VPSA	Vacuum Pressure Swing Adsorption
WEF	Water Environment Federation
WHO	World Health Organization
WFD	Water Framework Directive
WSS	Water Supply and Sanitation
WWT	Wastewater Treatment
WWTP	Wastewater Treatment Plant

1 Introduction

1.1 Wastewater Treatment - Health and Human Well-Being

Activity of every community is inextricably linked to generation of both, solid and liquid waste and air emissions. Wastewater is defined as any liquid runoff, consisted of water adversely affected in quality by anthropogenic influence. From the point of view of sources of generation, it comprises liquid or water-carried wastes discharged by residences, institutions, commercial and industrial establishments, agriculture together with surface water, groundwater and stormwater runoff (Tchobanoglous et al., 2003). Wastewater composition varies depending on the characteristics of the source. For example, a typical municipal wastewater encompasses: water- 95% or more, including industrial cooling and process water; organic biodegradable compounds; nutrients; toxic non-biodegradable compounds; inorganic particulate matter; solids and emulsions; broad variety of pathogens (bacteria, viruses, prions and parasitic worms); and non-pathogenic microorganisms. It is estimated, that over 90% of the wastewater generated globally is discharged into the environment untreated. Besides nuisance conditions due to malodour emissions, it carries serious health risks due to air and waterborne diseases epidemics affecting either human or animal hosts, not to mention disastrous environmental consequences, such as eutrophication of the waterways and polluting water resources with bio-accumulative mutagenic and carcinogenic substances, potentially harmful for aquatic eco-systems. According to the U.S. Environmental Protection Agency (EPA, 1972b), overflows of raw wastewater from aging municipal sewer systems and urban stormwater runoff are one of

major sources of pollution, contributing to the contamination of drinking water resources, beach and shellfish bed closures, and thus making water unsafe for drinking, fishing, swimming, and other activities.

On the other hand, in world regions affected by limited water resources, one well known and common wastewater use is in agriculture as an irrigation water source, where nutrient recycling and increase of available water supply are major benefits. Unfortunately, the majority cases of the agricultural wastewater applications in low-income and developing countries (e.g. Mexico, India or China) are not planned on the basis of nutrient recycling, but on economical aspect. In such situations the problem emerges due to public health constraints, when raw or partially treated wastewater containing pathogenic and industrial contaminants is not properly managed and discharged directly to reservoirs, rivers and canals supplying irrigation water. Therefore, efforts have been taken by the World Health Organization (WHO), the Food and Agriculture Organization (FAO) of the United Nations and the International Water Management Institute, resulting in development of guidelines considering safe use of effluent to irrigation and defining quantity and quality of effluent parameters minimizing potential health hazards (ETWWA, 2010; Hussain et al., 2002; Pescod, 1992; WHO, 2006).

Nowadays cholera, dysentery and other wastewater-related diseases manifested by severe diarrhoea are generally viewed as threats only in less developed countries in African and Southeast Asian regions. Epidemiologic reports revealed that gastrointestinal infections originated from water contamination due to lack of sanitation kill around 2.2 million people globally each year, mostly children under 5 years of age in developing countries, while there are approximately 4 billion cases of diarrhoea worldwide (WHO, 2000a, b). According to that, it seems surprising, that the number of households in small and rural communities in the U.S. still lack adequate facilities for the proper collection, treatment, and disposal of wastewater- all essential to protecting the environment and public health. However only in 90s, examples of large-scale outbreaks of the waterborne cryptosporidiosis in the United Kingdom, Canada, and states of Milwaukee and Wisconsin, help to illustrate the potential risk also to developed countries (Butler and Mayfield, 1996; Joseph et al., 1991). In the recent years also in Portugal, the problem of contamination of surface and ground water with nutrients and faecal coliforms emerged due lack of safe sanitation infrastructure in domestic and swine and cattle mini-industries in rural areas (Cabral and Marques, 2006; Vieira et al., 2013).

1.2 Water Policy - Tailoring Wastewater Treatment Objectives

Water pollution prevention and control measures are of critical importance to improve water quality and reduce the cost of wastewater and drinking water treatment. Due to the number of the water pollution sources, a variety of pollution prevention and control measures are needed, such as proposed by the United States Environmental Protection Agency, U.S. EPA (EPA, 1972a): green infrastructure and low impact development approaches and techniques for wet weather management; impaired waters and Total Maximum Daily Loads (TMDL) management; National Pollutant Discharge Elimination System (NPDES) permit program (regulating point source pollution); polluted runoff (regulating nonpoint source pollution); sediments management; source water protection; stormwater management; vessel sewage discharges limitations; wastewater programs; and watershed management.

Historically in the U.S., the real modern era in water pollution control began in 1972, when in response to public demand for safe, swimmable and fishable water, the Congress launched the amendments to Federal Water Pollution Control Act, commonly known as the Clean Water Act (CWA), which increased dramatically the role of government in water quality management and control of water pollution (Baker, 1997; EPA, 1972a). Pollution control strategy imposed by CWA in 1972 in section 402, established NPDES permit program (EPA, 1972b), an efficient legal tool linking ambient water quality standards with effluent limitation for discharges of industrial and municipal wastewater, i.e. by controlling point source pollution. Furthermore NPDES permitting program defined uniform, technological minimum standards for each discharger (Tchobanoglous et al., 2003). Such technology-based standard, referred as Best Available Technology Economically Achievable (BAT) means the most appropriate means available on a national basis for controlling the direct discharge of toxic and nonconventional pollutants to navigable waters. According to that, imposed BAT effluent limitations guidelines, represent the best existing performance of treatment technologies that are economically achievable within an industrial point source category or subcategory (EPA, 1972b). Further amendments to the CWA, were introduced in 1977 and later by launch of the Water Quality Act in 1987, which strengthened federal water quality regulations by providing changes in permitting, adding substantial penalties for permit violations by illegal discharges, amending control of solids and toxic pollutants present in wastewater. Further federal regulations complete CWA in terms of planning and design of wastewater treatment facilities (Tchobanoglous et al., 2003): 40 Code of Federal Regulations (CFR) Part 503 (1993) - Standards for the use or Disposal of Sewage Sludge, imposing limits for pathogens and metals concentrations; U.S. EPA National Combined

Sewer Overflow (CSO) Policy (1994) - coordinates planning, selection, design, and implementation of CSO Management Practices and Controls to comply with CWA requirement; Clean Air Act of 1970 with 1990 Amendments - related to standardized acceptable emissions levels for specific air pollutants for prevention of significant deterioration in air quality; 40 CFR Part 60 - establishes air emission limits for sludge incinerators of defined capacity; and TMDL (2000) Section 303(d) of the CWA - development of prioritized lists of impaired water bodies and to establish the maximum amount of pollutant that a water body can receive on daily basis and still meet water quality standards. The objectives of CWA remain valid today, however with the technological progress the required level of treatment has significantly increased due to more stringent water quality objectives established by the authorities.

Similar to the U.S., the main initiatives towards the introduction of the environmental policy in the European Union (EU) were initiated as a follow-up of the Declaration of The United Nations on the Human Environment proclaimed in Stockholm conference of 1972 (Baker, 1997). Due to the increasing demand by citizens and environmental organisations for cleaner surface water, groundwater and coastal beaches, furthermore limitation of the water resources resulted in establishment of European water policy, aiming protection of the water resources. The first wave of EU water policy was initiated in 1973 by a first of series of five-year Environmental Action Programmes. By the end of the 1970s several measures for the reduction and prevention of water pollution had been introduced in a number of Directives based primarily on a regulatory approach. These first wave Directives, considered subdivision of the aquatic ecosystems into individual protected commodities and defined quality targets, each of which had to be followed or achieved through pre-defined actions. In 1990, discharge of urban wastewater, due to its large volume, was identified as the major cause of water pollution resulting in increasing eutrophication of sea (Baltic, North and partially Mediterranean) and fish waters and deteriorating quality of European water resources. Consequently, two new legal rules, so called second wave Directives were adopted, setting strict rules on wastewater treatment and the use of nitrates in agriculture (Dworak et al., 2007). Thus, the Urban Waste Water Treatment Directive (UWWTD) 91/271/EEC concerned the collection, treatment and discharge of urban wastewater and treatment and discharge of wastewater from certain industrial sectors (UWWTD-REP, 2007). The Nitrate Directive 91/676/EEC aims to protect water quality by preventing nitrates from agricultural sources polluting ground and surface waters by limiting the amount of animal fertiliser used on fields and promoting good farming practices. Five years later, through implementation of the Integrated Pollution Prevention and Control (IPPC) Directive 96/61/EC (amended in 2008- IPPC Directive

2008/1/EC) a new rule for control emissions to the atmosphere, water and soil control was formulated, by imposing the obligations in which industrial and agricultural activities with a high pollution potential must comply, and similarly to U.S. legislation, and by imposing of the framework concept of BAT. Furthermore, the IPPC Directive establishes a procedure for authorising these activities and sets minimum requirements to obtain permits, particularly in terms of pollutants released. In addition to that, important aspects of water protection were included in a guideline Directive, controlling the dangers in the event of major accidents, known as the Seveso II Directive 96/82/EEC, replaced in 2012 by the Seveso III Directive (2012/18/EU). In 1996 the works of EC on a third wave Directives began (Dworak et al., 2007). In 1998, the Drinking Water Directive (DWD) 98/83/EC established the quality of water intended for human consumption. In 2000 a big step forward in integrated water management was achieved by the EU Water Framework Directive (WFD) 2000/60/EC acting as a framework for water policy legislation. The main objective of WFD is to achieve a good quality ecological and chemical status of all EU water bodies by 2015. Contrary to the first and second wave Directives, WFD covers areas as diverse as groundwater protection and urban waste water, drinking water quality, bathing water quality and protection of waters against pollution caused by nitrates from agricultural sources.

Today, the Water Supply and Sanitation (WSS) sector is managed by EU water policy confined to three Directives, on the basis of which each EU member state has introduced national legislation: UWWTD 91/271/EEC with amendments 98/15/EEC; DWD 98/83/EC; and WFD 2000/60/EC amended by 2008/32/CE. In addition to that, the institutional organisation of public WSS does not fall under the purview of the EU, but remains a prerogative of each member state. Water resources management in Portugal is responsibility of the Water Institute (*Instituto da Água*- INAg) created in 1993 and operating on the basis of the Water Law of 2005 (Law n.º 58/2005), which transposes the EU water framework directive into national law. While in 1997, the Water and Waste Services Regulation Authority (*Entidade Reguladora dos Serviços de Águas e Resíduos* - ERSAR) was created, as a national regulatory agency in charge of regulating public water supply services, urban wastewater management services and municipal waste management services.

Nowadays, facing global shortages of clean water resources and exponential increase of the global amount of wastewater generation, such as the effect of demographic growth and urbanization, WSS is under pressure from climate change, economic progress and social changes. For this reason, the ultimate objective of wastewater engineering branch is

protection of public health in a manner commensurate with environmental, economic, social, and political concerns, by taking up scientific and engineering measures leading to immediate removal of wastewater from its sources of generation by collection systems (sewers), followed by appropriate level of treatment, reuse and dispersal into the environment (Tchobanoglous et al., 2003).

1.3 Emerging Challenges: Water and Energy Nexus

To comply with global water policy aiming responsible management of the water resources and protection of the public health, wastewater collected from municipalities and communities must be treated to achieve levels imposed by discharge permits and maximal daily loads, allowing ultimately to be returned to receiving water bodies, or to the land or even to be reused. In the last century, application of scientific knowledge and engineering practice led to considerable development in wastewater sector, particularly in biological secondary treatment based on aerobic biological methods, namely activated sludge (AS) process (Arden and Lockett, 1914), which nowadays became a well documented standard for most wastewater treatment utilities. The objectives of secondary biological wastewater treatment in activated sludge process also expanded from an early emphasis on high levels of BOD and TSS removal to cover enhanced nutrients (nitrates and phosphates) removal, as the process itself has flexibility and numerous modifications can be tailored to meet specific requirements. One of the characteristics of the activated sludge process is the continuous operation of the aeration system and sludge recirculation pumps, and thus the process performance relies on a steady energy supply. When analysing the energy budget of a biological wastewater treatment train, aeration is the most energy-intensive key unit process and accounts for the largest fraction of the total wastewater treatment plant (WWTP) net electricity expenditure, ranging in average from 45 to 75% (Reardon, 1995) and in extreme cases of stringent discharge limits imposed, requiring e.g. enhanced nitrification, even up to 85%, thus having significant effect on the operation and maintenance budget of utilities (WEF, 2009). Furthermore, according to the data gathered by the Water Environment Federation (WEF) and the U.S. EPA (EPA, 2010, 2013), water and wastewater treatment plants are considered as the largest energy consumers in municipal governments, accounting for 30 to 40% of the total energy bill, and thus the search of sustainable solutions based on wind, solar, and hydroelectric power became more urgent in recent years. Furthermore, the U.S. EPA in “Energy Efficiency: On the Road to Net Zero Energy” report estimates, that drinking water and wastewater systems account for approximately 3-4% of energy use in the United States, adding over 45 million tons of greenhouse gases to the atmosphere annually (Paulson, 2012).

Due to the increased global emphasis on energy conservation, there is an urgent task in wastewater sector to reduce site energy usage. According to the reference guidelines (EPA, 2013; WEF, 2009) opportunities for improving energy efficiency can be obtained by: optimizing aeration processes or equipment upgrades, which focus on replacing items such as blowers with more efficient models; replacing the whole aeration system with less energy intensive systems (replacement of the surface aeration system by bottom diffusers); operational modifications, involving reduction of the energy requirements to perform specific functions by modification of the aeration control systems, which typically results in greater savings than equipment upgrades, and may not require capital investments; and modifications to facility buildings, such as installing energy-efficient lighting, windows, and heating and cooling equipment.

1.4 Relevance and Motivation

Major challenge in wastewater engineering sector is successful design and reliable and energy efficient operation, which ensures that the treatment efficiency will comply with the outflow quality restrictions, while keeping the investment and operating cost as low as possible (Brouckaert and Buckley, 1999; Do-Quang et al., 1999). Although the design of wastewater treatment plants is a key step to ensure these goals, it is usually based on the general guidelines and both, designers and operators experience, dominated by the rule of thumb (Bosma and Reitsma, 2007; Pereira et al., 2012; Stamou, 2008), therefore there is an urgent task in wastewater sector to introduce advanced engineering tools for development, diagnostics and energy-minded operation of site-specific wastewater treatment systems.

In this work the emerging challenges of wastewater treatment engineering are met by application of advanced modelling tools, namely Computational Fluid Dynamics (CFD) in design of activated sludge process. The oxidation ditch system was used in this work as a showcase mostly due to its universal applicability - the process is suitable in any situation where activated sludge treatment (conventional or extended aeration) is appropriate (EPA, 2000). Furthermore, as one of well known modifications of the AS process characterized by robust performance and high treatment efficiencies, oxidation ditch plants have been commonly adopted by many countries worldwide. Although being originally intended to serve small to medium-size municipalities, where the availability of the large land area is not a constraint, thus with the development of more efficient aeration systems, deep tank process configurations found numerous applications in large-scale wastewater treatment plants. Furthermore, as hydraulic and hydrodynamic properties of the oxidation ditches allow a wide range of aeration schemes to be implemented, therefore the emphasis in this

work was put on development of an innovative, energy-minded aeration scenario, allowing achievement of high process efficiencies (aeration and wastewater treatment) with maximal possible reduction of energy consumption during operation.

1.5 Thesis Objectives and Layout

The objective of this thesis was development of an innovative, energy-minded aeration system, based on the introduction of the external aeration unit - cooperating with modified jet aeration devices. The rationale behind the use of CFD codes in this work is to simulate a range of operating and hydraulic conditions: in the aeration unit - to evaluate overall aeration process performance and aeration efficiency and to compare results against conventional systems used in oxidation ditches; in the oxidation ditch - to assess the impact of the proposed aeration system configuration on overall mixing patterns within the oxidation ditch. Finally, for the proposed design of the wastewater treatment, the overall power requirements for mixing and aeration will be computed, selecting aeration schemes and device configurations allowing for maximal energy savings.

In **Chapter 2** fundamentals and importance of the aeration process in aerobic activated sludge process is given. Development of the aeration techniques, present technical status and the insight into ongoing research goals in the aeration sector are also comprehensively reviewed. Furthermore, the studies concerning applicability of two reactors, an innovative Pressurized Aeration Chamber (PAC) and a 2D bubble column reactor (BCR), as the aeration devices will be presented. Aeration in several configurations of PAC will be simulated with CFD aiming the selection of the most robust geometry in terms of enhanced oxygen mass transfer, leading to higher level of effluent saturation with oxygen. The most successful design will be later validated in lab-scale experiments carried on in accordance with standard clean water testing protocols for aeration devices. The same procedures will be used to determine the impact of the operating conditions on hydrodynamics and aeration efficiency of the BCR. The results obtained for PAC and BCR, thus oxygen transfer parameters and aeration efficiency will be later compared with the typical process parameters of the conventional aeration devices.

Although the oxidation ditch process is commonly used worldwide, its flow regime is scarcely studied. Therefore **Chapter 3** covers an experimental approach to determine hydrodynamics of the oxidation ditch, preceded by literature review on the process history, operating principles and the performance. Several works on experimental methods used in these systems to assess flow behaviour are also reviewed. Furthermore, the hydrodynamics and process performance of two oxidation ditches operating in different

aeration schemes (continuous and intermittent): a pilot-scale tubular piston flow reactor with recirculation (PFRR); and a full-scale oxidation ditch at Areosa WWTP (Viana do Castelo) will be experimentally determined. In these wastewater reactors, velocity, oxygen, nutrients and solids concentration profiles along the channel will be assessed, and PFRR ditch behaviour will be additionally evaluated in Residence Time Distribution experiments using pulse and step tracer techniques. Furthermore, from the results obtained for both ditches the impact of the hydrodynamics on the treatment efficiency will be assessed.

Chapter 4 comprises the hydrodynamic studies of the oxidation ditch using CFD simulation. A literature review gives an extensive insight into the typical trends in engineering design of the activated sludge systems. The rationale behind the use of CFD modelling to optimize wastewater treatment operation and process efficiencies is explained on the basis of several literature examples. CFD studies of the oxidation ditch will be carried on to evaluate the use of several configurations of slot jets compromising the functions of aerator and mixer. The impact of the aerator on the hydrodynamics of the oxidation ditch will be assessed by determination of the flow field and RTDs of the fluid. Furthermore, the influence of different turbulence models on the flow patterns evolution within the oxidation ditch and the energy expenditure for mixing will be assessed. For a chosen hydraulic configuration of the hydrojets and CFD model, further studies concerning the impact of mesh resolution and the near-wall treatment on the energy expenditure will be also made. Finally, the analysis of the effect of the turbulence models on the macromixing data obtained from the RTD simulations, which can be furthermore incorporated into the biokinetic Activated Sludge Models (ASM), will be also assessed.

Chapter 5 concerns assessment of the energy budget in the proposed activated sludge system. Daily energy expenditure per habitant will be assessed from the power demand by different groups of aeration devices used in oxidation ditch process, operated on the base of atmospheric air and pure oxygen. Furthermore, detailed analysis of energy expenditure in the proposed oxidation ditch system, aerated by external aeration unit - PAC cooperating with hydrojets will be performed. Computations of power demand on aeration will consider actual oxygen requirements by PAC unit, power demand by blower and by oxygen generation in Vacuum Pressure Swing Adsorption process. Energy expenditure on mixing will encompass determination of power demand for wastewater pumping, based on the total system head computed for all piping components, PAC, and two hydrojets types - multi-slot and single-slot injector and power demand on mixed liquor recirculation. The

data obtained for proposed aeration scheme will be compared with power demand by conventional systems to determine possible energy savings.

Finally, in **Chapter 6** final remarks based on the conclusions from present work are gathered and future paths are proposed.

2 Aeration Technologies

2.1 Introduction

This chapter is divided in two main sections: in the first section, a review on the aeration technologies used in the aerobic wastewater treatment systems is done; while the second refers to the modelling and experimental approach to assess aeration potential of two different reactors.

The review aims to present the fundamentals of the aeration process in the Activated Sludge (AS) systems. Short historical note concerning development of the aeration techniques and description of the conventionally used diffused air, mechanical and hybrid devices is also done. Furthermore, a theory behind the oxygen mass transfer and aeration efficiency is given. Alongside the standard method for aeration device testing, namely clean water test, typical ranges of the process parameters for selected aerators are also presented. At the end of this part, a short review on the recent research trends and achievements in the aeration sector with several literature examples is given.

Second part of the chapter concerns the application of two reactors, Pressurized Aeration Chamber (PAC) and 2D bubble column reactor (BCR), as the aeration devices, which can be used in AS process.

Computational Fluid Dynamics (CFD) was used to study the hydrodynamics and oxygen mass transfer in several geometries of PAC, aiming selection of the most efficient design, which was later applied in lab-scale studies. The experimental studies on PAC aim to determine oxygen transfer rate parameters in steady and unsteady clean water tests and validate

results obtained from the CFD studies. Aeration efficiencies obtained from clean water test were compared with the corresponding parameters, characteristic for the conventional aeration devices.

Experimental studies on BCR aimed determination of the hydrodynamics and the oxygen mass transfer. Flow regimes and gas hold-up in BCR were assessed for varying operating conditions using standard imaging technique. Aeration performance, therefore oxygen mass transfer parameters were determined from the results of steady state clean water test. Finally, the aeration efficiencies obtained for BCR were compared with the conventional aeration systems.

2.2 Aeration in Activated Sludge Processes

Aeration process is key unit process in the biological wastewater treatment train, which is of the crucial importance for the majority of the aerobic processes, based on the both, suspended and attached growth systems, such as activated sludge process and its variants, aerated lagoons, rotating biological contactors or trickling biofilters. In such biological systems, molecular oxygen is used by the aerobic heterotrophic microorganisms indigenous to the activated sludge, as an electron acceptor necessary to metabolize biodegradable organic matter present in the wastewater (Benfield and Randall, 1980) and in the effect, to promote biomass growth. Generally, in most of the aerobic wastewater systems, significantly larger quantities of oxygen must be transferred to meet the following requirements (Tchobanoglous et al., 2003): satisfy oxygen demand for microbiological degradation of organic substrate, endogenous respiration and nitrification; to maintain the minimum level of residual dissolved oxygen of 2.0 mg L^{-1} throughout the activated sludge tank. However, in natural conditions poor solubility of oxygen in liquid media contributes to the low oxygen transfer rates through the surface gas-wastewater interface and in conditions of the oxygen deficit, microbial metabolism is inhibited, what leads to treatment process failure manifested by the immediate deterioration of the effluent quality. From this reason, to overcome low gas transfer rates and to satisfy oxygen demand, additional oxygen-wastewater mass transfer interfaces have to be created through the introduction of the “artificial” aeration system into the activated sludge tank. Aeration systems transfer oxygen into the wastewater by (Stenstrom and Rosso, 2008; Tchobanoglous et al., 2003; von Sperling, 2007): releasing air or oxygen through macroscopic orifices or porous materials, which constitute part of submerged aeration devices, such as diffusers; dynamic shearing the fluid surface by rotating blades of the surface or mechanical aerators, causing exposure of the liquid droplets into the atmospheric air and allowing the entrance of the air into the liquid.

Even though the aeration is irreplaceable unit process in the wastewater treatment train, it is largely energy-intensive and accounts for the largest fraction of the total wastewater treatment plant energy expenditure, ranging in average from 45 to 75% (Reardon, 1995) and in extreme cases, even up to 85%. Nowadays, due to the increased global emphasis on energy conservation, there is an urgent task in wastewater sector reduce site energy usage through the application of advanced design and modelling tools for development, diagnostics and management of energy-minded aeration systems.

2.2.1 Diffused Aeration Systems

Diffused aeration technique is defined as the injection of air or oxygen enriched air below the liquid surface. Typical diffused aeration systems used in wastewater treatment include: submerged in the wastewater aeration device that introduces air or oxygen bubbles into the liquid; air header manifold and air piping system; blowers; and other supporting equipment through which the pumped air passes (Tchobanoglous et al., 2003; von Sperling, 2007). In the past, depending on the bubble size, diffused aeration devices have been divided in fine, medium and coarse bubble devices. However, such differentiation of the devices based on the measured bubble size is difficult and in some cases may be confusing (Mueller et al., 2002; Tchobanoglous et al., 2003). From this reason, the current division criteria are based on the physical characterization of the equipment used. Three categories are defined: porous or fine-pore diffusers; nonporous diffusers; other hybrid devices, i.e. jet aerators, aspirating aerators, sparge turbine aerators and U-tube aerators. Aeration performance by aspirating aerators and draft tube aerators is based on introducing of air bubbles in the liquid medium accompanied by simultaneous mixing, due to rotating action of the impeller. From this reason, these devices are often classified as mechanical aerators.

Historically, the first diffused aeration unit using perforated plate diffuser was patented in the UK in 1904. By the introduction of the activated sludge process in UK in 1914 (Arden and Lockett, 1914), coarse bubble units such as nozzles and perforated tubes were already used in practice of wastewater aeration since late 1880s. The effects of bubble size, air flow rate, tank geometry and diffuser placement on oxygenation efficiency were already known, and thus intense research focused on applications of various porous materials, such as firebrick, sandstone, mixture of sand and glass and pumice, aiming development of the media producing fine bubbles. Most of these materials were characterized by low permeability creating high head loss. The first porous plate diffuser produced from foundry slag and cement was introduced in 1915. By early 1930s, cement-slag and cement-sand based plate diffusers, exploited in activated sludge systems in UK and British colonies for

around two decades, were substituted by alundum plate diffusers. At the same time in Germany, patented Brandol plate diffusers, produced from quartz sand bonded by binding resin, were commercialized. Later modifications led to introduction of tube diffuser, produced from silica sand bonded by phenol formaldehyde resin (Mueller et al., 2002; Schmidt-Holthausen and Zievers, 1980).

In the U.S., patented in 1914 porous plates produced from bonded silica sand, were widely used in newly constructed activated sludge plants (Mueller et al., 2002). Parallel tests on aeration were conducted using porous tubes, porous wood, ceramic plates (Roe, 1945) and air jets (Mueller et al., 2002). Further research led to development of a wide range of porous media used in plate diffusers based on the alundum and silica sand bonded by various binding agents. Since the early years of exploitation, a serious operational problem was caused by diffusers clogging and thus their maintenance, especially in cases of more and more popular large capacity aeration tanks. From this reason, by the 1950s most of the wastewater treatment plants (WWTPs) in the U.S. turned to substitute fine pore diffused air units either with large orifice diffusers or mechanical aerators. Popularity of improved types of coarse bubble diffusers despite their lower oxygen transfer efficiency and higher power usage was mainly due to their resistance to fouling and easy maintenance. In the late 1950s fine bubble jet aeration became more popular in municipal systems due to its high oxygen transfer and mixing efficiencies, however industrial wastewater sector still remains as its biggest application field (Mueller et al., 2002).

Meanwhile in Europe, to overcome the problems caused by fouling and maintenance of the porous plates, ceramic dome diffuser units were developed in the UK (EPA, 1985), taking advantage of integral piping systems and raising the aeration units above the basin floor, preventing in this way settling the sludge into the porous media. The ceramic domes evolved into discs, which became the standard for fine pore aeration systems for over two decades.

Due to the energy crisis in 1970s in the U.S., the need of implementation of efficient but less energy-intensive aeration methods revived the interest in porous diffusers technology. Intense research in this field led to reintroduction on the global markets a wide range of new porous materials such as first generation of membranes, improved diffuser designs and configurations allowing for maximal efficiency with easier maintenance. New designs consider also energy efficient solutions for supporting equipments such as blowers. Further development of the membrane diffusers led to distinct improvement in the aeration performance and domination on the global markets. Nowadays coarse-bubble plants are being retrofitted by fine-pore diffusers.

In the last three decades, substitution of dissolved air systems by pure oxygen systems become competitive due to development of the new technologies allowing for more efficient dissolution of oxygen in the wastewater. The quantity of oxygen that can be injected into wastewater under specific process conditions yields four times the amount of oxygen delivered by air systems (Shammas and Wang, 2009). Due to that, significant savings can be achieved by reduction of operating costs for power demand by blowers. In design of new WWTPs, investment costs can be lowered due to reduced volume of aeration tank. Additional advantage is enhanced biokinetics of activated sludge, what makes the system suitable for operation in high rate mode and for efficient treatment of high-strength effluents.

2.2.1.1 Nonporous Diffusers

Coarse bubble systems use macroscopic orifices, holes or slots of the average diameter ranging from 6 to 12 mm to release large bubbles of the diameter bigger than 6 mm. The most common types of coarse bubble devices are (EPA, 1989; Mueller et al., 2002): fixed orifice diffusers, i.e. perforated piping, spargers and slotted tube; valved orifice diffusers, equipped with check valve preventing backflow when the air is shut; and static tube diffuser, consisting of a vertical tube with drilled orifices, fixed above the air header. In the past, coarse bubble aeration dominated the municipal field, and was particularly popular in plug flow tanks, also in some oxidation ditches.

The diffusers were arranged in a single, two or more rows, located on the sides of the tank in so called single- or dual-roll spiral, cross-roll, ridge or furrow configurations, with narrow or wideband diffusers placement (Henze et al., 2008; Mueller et al., 2002; Tchobanoglous et al., 2003). In the recent years, to optimize efficiency, these systems were upgraded the full-floor coverage configurations.

The coarse bubble diffusers operate at high air flow rates, what makes them more resistant to the clogging and scaling. From this reason, the coarse bubble system requires little maintenance mainly due to the corrosion of the air mains or diffusers. Discharged from the orifices rising bubbles are characterized by high interfacial air-liquid velocity, and thus as the bubble retention time is short, the area for oxygen transfer is also limited. Discharge of the bubbles through the nonporous media is characterized by low diffuser surface pressure drop, referred as the dynamic wet pressure, DWP, accounting for around 0.01 bar. On the other hand, to maintain high oxygen transfer rate in nonporous aeration system, large volumes of air must be delivered, and thus, high capacity compressors demanding more power must be used.

Nowadays, due to low aeration efficiency, existing coarse bubble installations are being successively replaced with porous diffusers. However despite of higher energy usage, coarse bubble units are sometimes the best choice, especially in aeration of the viscous fluid systems, such as found in aerobic digesters or membrane bioreactors operating at high Mixed Liquor Suspended Solids (MLSS), exceeding 8000 mg L^{-1} (Stenstrom and Rosso, 2008).

2.2.1.2 Porous Diffusers

Due to the higher aeration efficiency and around half the power required by nonporous and mechanical aeration units, fine pore diffusers dominated the worldwide wastewater treatment market. The performance of the porous diffusers is based on the release of small spherical bubbles of the average diameter ranging from 2 to 5 mm from the micro-orifices or pores in porous material. Porous media commonly used in diffusers are: ceramics, mainly alumina, silica and aluminium silicate; rigid porous plastics, made from several thermoplastic polymers, from which high density polypropylene (HDPP) and styrene-acetylonitrile (SAN) are the most popular (EPA, 1989); and perforated membranes, made from elastomers, such as rubber- ethylene-propylene diene monomers (EPDMs), flexible polyurethane, or silicone, having slits of the typical size of 1 mm (Mueller et al., 2002).

There are many shapes of diffusers from which the most popular are: domes, discs and plates, made of ceramic or porous plastic media; panels, made of flexible polyurethane membranes; and tubes, made of ceramic, porous plastic and perforated membrane media (EPA, 1985, 1999; Mueller et al., 2002; Tchobanoglous et al., 2003). Domes, discs and tubes can be mounted on the air mains, running by the sides of the tank, close to the bottom. New installations are usually mounted in grid pattern in full floor configurations, providing uniform and efficient aeration throughout the tank (Henze et al., 2008). Similarly, panel diffusers are mounted close or directly on the aeration tank bottom and fastened with the anchor bolts (Mueller et al., 2002; Tchobanoglous et al., 2003).

High aeration efficiency of the fine pore diffusers made them suitable for almost all suspended growth and attached growth activated sludge systems, including MBRs with moderated MLSS loading, horizontal flow systems, such as oxidation ditch equipped with flow generators (vertical agitators or banana blade mixers) and recently - aerated lagoons. The main disadvantage of the fine-pore system is that the diffusers are prone to clogging, due to build-up of biological (fouling) and inorganic (scaling) precipitates on their surface or within their porous structure, depending on the device type. Porous devices have higher DWP than for nonporous diffusers, that for ceramic devices is of around 0.015 - 0.030 bar,

and for membranes - up to 0.045 bar. Due to the clogging, these values increase up to 200% of the new device DWP. At the same time, with the increase of the head loss, overall aeration process efficiency decreases. Serious undesirable problems, such as tearing away the membranes or failures of blowers and overloaded motors are likely to occur due to diffusers clogging. From this reason, regular cleaning to remove foulants is always required to restore process efficiency and reduce power cost.

2.2.1.3 Jet Aerators

Jet aeration is a combination of liquid pumping with air diffusion which produces fine bubbles due to the hydraulic shear (Mueller et al., 2002; Tchobanoglous et al., 2003), through which both, oxygenation of wastewater and mixing of the tank content takes place. In such system, power demand accounts for energy used for wastewater pumping and air delivery. Jet aeration system includes: constant rate wastewater recirculation pump, such as end suction centrifugal pumps, vertical submersible pumps or vertical propeller pumps; jet aeration device; low pressure blower, e.g. rotary positive displacement blower, multi-stage centrifugal blowers, or turbine type compressor; and the air and wastewater piping. Typical jet device consists of: primary inner nozzle; mixing chamber, venturi or outer mixing nozzle; air inlet; and the secondary jet nozzle, having circular opening (conventional jet) or slot-shaped opening (slot injector) cross-section. Both, piping system and jet assembly are made of polypropylene, fiberglass reinforced plastics or stainless steel. Several types of jet aeration devices and the aeration systems configuration, has been developed (KLa Systems, Inc., Bayer AG) which are successfully commercialized.

Jet aerators can be arranged as directional devices or as clustered or radial devices. Radial devices, distributing jets in uniform way around the circumference of a central pressurized chamber, are used in smaller scale biological utilities having circular tanks. Jet manifold configuration is used in larger scale aeration basins. Manifold type jet aerators consist of jets placed on either one or both sides of a liquid distribution pipe. The jet nozzles are attached to an air header manifold by individual air ducts, having functions of an air source for the jets and support for the air header pipe. The aerator configuration, number of jet nozzles and nozzle spacing is designed for individual wastewater systems to maximize oxygen transfer and effective mixing.

The liquid phase, recirculated wastewater is discharged from the inner nozzle into the outer mixing chamber, where it converts into high velocity, low- pressure stream. At the same time, low pressure air pumped through a header is introduced perpendicularly to the wastewater stream into the mixing chamber. In conditions of high shear and intense mixing

of both fluids, air breaks into minute bubbles. The mixture is discharged into the tank through the secondary nozzle, forming high-velocity horizontal jet plume, carrying the cloud of fine bubbles. Air head loss through the jet is negligible, due to the ejecting action of the wastewater stream. The plume entrains the surrounding mixed liquor and disperses rising upwards to the surface bubbles, resulting in high oxygen mass transfer rate. Horizontal momentum from the discharged jet imparts velocity to the surrounding liquid, thus, besides efficient aeration, mixing process takes place.

Slot injectors, introduced by Bayer in early 1980s operate at different air-liquid flow ratios than conventional jets. Diverging change in shape of the nozzle opening allowed larger shear surface for mass transfer, than a circular jet of identical area. Due to that, the plume retains more of its kinetic energy as it exits the device, resulting in more effective gas dissolution into the bulk liquid.

Usually, depending on the air-wastewater flow rate ratios, in the continuous flow systems such as oxidation ditches, the energy of the jets is sufficient for keeping the mixed liquor in suspension and forcing the fluid circulation. Due to its high aeration- mixing efficiencies and its flow directional feature, jet aeration process is suited for a wide range of the activated sludge process: complete mix and plug flow activated sludge systems, sequencing batch reactors, oxidation ditches, high-purity oxygen activated sludge process (HPO-AS) systems and deep tank (>8 m) systems (Mueller et al., 2002; Shammass and Wang, 2009; Tchobanoglous et al., 2003).

2.2.1.4 U-tube Aerators

U-tube aeration system consists of a deep shaft (U-tube), usually 9-150 m deep (Mueller et al., 2002), divided into inner and outer zone. The wastewater flow is forced downwards to the bottom of the shaft and returns upwards towards the surface for further treatment. Pressurized air is introduced into the wastewater stream into downcomer zone. As the pressurized mixture travels downwards, the more oxygen is transfer in the bottom zone of the shaft, due to the increase of the oxygen partial pressure in lower the temperature (Mueller et al., 2002; Shammass and Wang, 2009; Tchobanoglous et al., 2003). The deeper the shaft, the higher the oxygen saturation, however the atmospheric air-based process may be troublesome due to the risk of the simultaneous nitrogen super-saturation. From this reason, pure oxygen aeration combined with low velocity fluid pumping is often used, yielding higher DO concentrations (Taricska et al., 2009a).

The power expenditure of the system depends upon the air demand on the biochemical processes and on the forcing the fluid circulation in the shaft. Usually, for the municipal

wastewater of the average quality, the quantity of air delivered for fluid circulation is sufficient for maintenance of the biological activity. For the concentrated wastewater, the air demand is governed by the biological oxygen demand, thus economics of the process increases with wastewater strength (Mueller et al., 2002).

2.2.2 Mechanical Aeration Systems

Mechanical aeration is defined as the transfer of oxygen to wastewater by mechanical devices, based on the liquid surface agitation and mixing, promoting the entrainment of atmospheric air and its dispersion in the bulk liquid (Mueller et al., 2002).

Introduction of mechanical aeration in activated sludge process to overcome existing problems with diffusers clogging is dated to the late 1910s in Europe, mostly in the UK. During next twenty years only in the UK the number of WWTPs with mechanical aeration units doubled the number of diffused aeration plants. In early 1920s the majority of the first generation mechanical devices used in the shallow activated sludge tanks constituted horizontal shaft rotors with different configurations of paddle wheels or inclined shaft propellers. At the same time, first deep tank aeration unit- vertical draft tube aerator was introduced in the UK. The technique spread worldwide and by the 1950s, draft tube aerators became the most popular mechanical device implemented in the U.S. (Mueller et al., 2002).

In late 1920s in Holland, Kessner developed so called brush aerator, which employed submerged in the wastewater street cleaning brushes mounted on the horizontal rotor, substituted later by paddles and blades. In 1954 the device was successfully implemented in the Pasveer oxidation ditch and by the 1960s, horizontal rotors with various configurations of blades and disks, patterned after the original Kessner brushes became popular device to aerate oxidation ditches. In case of small installations, horizontal cage rotors have been preferred. Nowadays, horizontal axis aerators are almost entirely associated with the oxidation ditches.

In the late 1950s and 1960s in the U.S. intense engineering works were focused on development of the low-speed vertical shaft turbines, which established their position in the aerators market by the mid 1970s. Soon, with the increasing popularity of the high capacity activated sludge tanks, low-speed radial flow devices became popular also in multichannel oxidation ditch systems, up to 5.0 m depth. Nowadays, low-speed aerators are very popular in HPO-AS systems, deep tanks up to 8.0 m, in Carrousel™ oxidation ditch process, aerated lagoons and other activated sludge based processes.

In the 1970s, aspirating devices, involving floating inclined hollow shaft unit equipped with marine propeller and submersible pump units equipped with draft tube became popular solution to aerate large basins, lagoons and oxidation ditch systems.

Parallel, floated configurations of the motor driven high-speed aerators, based on the nonsagging marine propeller were developed for lagoon and small aeration tanks applications. First generation of the motor-speed aerators encountered numerous mechanical problems during operation, mainly due to the motor failures. From this reason, intense works were made to improve device performance and reliability, and nowadays new versions of the high-speed aerators fitted with high efficient motor drives are commonly used.

2.2.2.1 Horizontal Rotors

The ditch system was originally fitted with Kessner brush aerator- a surface mechanical aerator extended across the ditch channel, consisted of horizontally placed cylinder rotor equipped with numerous bristles and submerged in the wastewater at approximately the one-half diameter (Mueller et al., 2002; Tchobanoglous et al., 2003; Thakre et al., 2008). Nowadays, the original Kessner bristled brushes are substituted by the rotors equipped with numerous configurations of angle steel, flat or curvilinear steel blades, or plastic bars, blades or discs (Mueller et al., 2002). The cylindrical shaft is driven by electric motor drive fitted with gear reducer providing rotor speed ranging from 40 to 80 rpm. Depending on the motor drive, aerator power requirements vary from about 2 to 90 kW.

With the rotation of the shaft, fluid surface is being splashed by blades or discs, causing turbulent spraying of the droplets into the atmospheric air where the oxygen is transferred at the air-liquid interfaces. Simultaneously, rotating blades capture and re-enter falling droplets into the wastewater. Due to the propelling action of the rotor, both, imparting of the horizontal velocity to the bulk liquid and mixing of the ditch content takes place. Depending on the rotor size and speed, the velocity imparted to the fluid ranges from 0.3 to 1.0 m s⁻¹ (Mueller et al., 2002).

The main disadvantage of the system is high energy expenditure on the fluid circulation, and additionally, the application of the horizontal rotors is limited by the wastewater depth in the ditch up to 4.0 m. Operation of horizontal shaft aerators is accompanied by liquid splash resulting in mists formation, carrying the risk of odour spread and air-borne diseases transmissions. In the cold climates, additional problems are caused by evaporation of the misty spray and cooling of wastewater, and as the result, to ice build-up during winter and slowing down the metabolic activity of the activated sludge. From this reason,

common practice to prevent excessive liquid splashing is installation of splash plates on the sides of the rotor protecting drive mechanism and also to reduce mist dispersal and heat loss by using rotor covers and heated hoods.

2.2.2.2 Low-speed Surface Aerators

Low-speed surface aerators are commonly used in: oxidation ditches, especially in Carrousel™ configurations up to 8 m depth (Mueller et al., 2002); in deep tanks with HPO-AS process; conventional and high-rate complete-mix AS systems. Such aeration system employs mechanical aerator, consisted of vertical shaft impeller positioned above the fluid surface, motor and gearbox reducing impeller speed to the range 40 to 100 rpm. Power demand ranges from 4 to 150 kW (Mueller et al., 2002). Low speed aerators are usually bridge or platform mounted, due to their size and weight, however currently, lighter floating units are being commercialised. Impeller design provides liquid pumping in a radial way, thus low-speed aerators are classified as the radial flow devices. There are number of impeller configurations, such as: flat disks with rectangular or slightly curved vanes attached to the periphery of the disk lower surface; curved blade disks; reverse curvature disks; pitched blade turbines; or inverted conical bodies with vertical blades.

Rotating impeller pulls the liquid upward in vertical direction. Accelerated by the impeller vanes fluid is discharged in horizontal direction at the impeller rim. High velocity plume contacts with low velocity bulk liquid in the tank, yielding hydraulic jump, accompanied with generation of a large interfacial area of efficient oxygen transfer. During operation, large volumes of liquid are pumped to maintain high oxygen transfer rate and to force the fluid circulation throughout the ditch.

Low-speed aerators are successfully used in deeper tanks, up to 10 m. These devices are usually equipped with draft tube system, providing sufficient oxygenation and mixing of the fluid. Other solution of deep tank aeration considers increase of the pumping and mixing capacity of the unit by introduction of the auxiliary submerged propeller mounted on the extension of the shaft. The main disadvantage of the low speed mechanical aerators is that the device performance depends rigorously on the impeller submergence. Slight changes in liquid level over the impeller may cause an increase of head and thus, increase of power demand on pumping ranging from 10 up to 50%, as well as affect the oxygen transfer. In the cold climates, generation of the surface spray “umbrella” during aeration may cause operational problems, especially during winter season due to possible freezing and also due to emission of odour and air-borne diseases. From this reason, common practice include montage of the mist shrouds above the impeller, allowing to lower the trajectories of the spray and reducing accumulation of the ice underneath the platform.

The other option considers installation of the space heaters in the motor frame, preventing condensation and freezing.

2.2.2.3 Draft Tube Aerators

Draft tube turbines found application in aeration of deeper tanks up to 10 m, thus they are used in aeration of deeper ditches, such as barrier ditch (Boyle et al., 1989; Mueller et al., 2002). The device combines aeration and mixing functions and consists of a submerged down-pumping axial impeller, placed within a draft tube and equipped with an air sparger fixed below the impeller. The impeller shaft is driven by motor fitted with gear reducer. Typical rotational speed of impeller ranges from 50 to 100 rpm, and the motor size up to 112 kW (Mueller et al., 2002). The air is supplied to the draft tube by blower. Even for the deep tanks, typical sparger submergence at the mid-depth of the ditch allows for efficient aeration with the conventional depth air pressures generated by blowers. Typical impellers used in draft tube aerators, flat blade or airfoil, are mounted on the vertical shaft driven by a gear motor.

Aeration performance is based on the generation of the high-energy turbulent field by the rotating impeller just above the bubble column released by the sparger, promoting bubbles break up and their distribution within the bulk wastewater. Aeration performance and efficiency depends on the turbine and basin geometry, operating air flow rates and the turbine speed.

2.2.2.4 Aspirating Aerators

Another group of equipment, commonly used to aerate and mix the content in the oxidation ditch systems and lagoons constitutes aspirating aerators, classified also as air-diffusion devices (Tchobanoglous et al., 2003). Depending on the configuration of the air supply, self aspiration aerators and blower assisted aerators are considered. Power demand ranges from around 1 to 75 kW (Mueller et al., 2002). Self aspirating aerator consists of motor and air intake port located above the wastewater surface and hollow shaft equipped with propeller, submerged in wastewater at an adjustable angle. Depending on the activated sludge basin geometry, direction of the flow, mixing intensity and aeration requirements, the devices are mounted on booms, pontoons or float and at various angles.

Due to rotating action of the propeller, liquid is draw down through the hollow tube generating local low-pressure zone at the propeller hub. Created pressure gradient causes aspiration of the atmospheric air through the intake port to the hub, where it contacts

with the wastewater in the conditions of the turbulent mixing, breaking up the air bubbles. Aerated stream is discharged into the ditch with the energy sufficient to provide efficient oxygen dispersion and mixing of the tank content.

Other type of self aspirating aerators combines submerged aerator, mixer, and pump within one unit. The device uses submersible pump to draw the liquid and the vertical air intake standpipe open to the atmosphere (Mueller et al., 2002). The principals of the aerator performance are the same as the propeller based configuration, therefore the pressure gradient at the propeller hub accompanied by aspiration of the air occurs due to the pumping action, successively followed by intense mixing and discharge of the aerated plume through a nozzle. Submerged aspirators are usually mounted on the tank floor and fixed to the ditch side walls with the movable guide rails.

Blower assisted aspirators provide passage of larger volumes of air through the aerator at higher operating gas pressures and velocities, thus they are recommended in cases when higher oxygen transfer rates are required. Each unit uses separate regenerative blower, mounted on the device float system or integrated with the motor and connected to the air intake port. Aeration performance is based on the same principals as the propeller based systems. For this group of devices mixing becomes independent from aeration and allows for direct control of oxygen levels by either turning on and off entire units or turning on and off only the unit blowers without sacrificing energy on mixing of the basin volume.

2.2.2.5 High-speed Aerators

High speed aerators are commonly used in lagoons, aerobic digesters and in lesser extent in small activated sludge facilities. The typical device consists of a motor driven propeller placed in the rim, and the casing directing the fluid flow. The aerator operates with the speed of 900-1800 rpm. Available motor sizes range from about 1 to 112 kW (Mueller et al., 2002). The first generation of the devices were equipped with marine nonsagging type propellers, but nowadays, among many new improved designs providing higher water pumpage rates than the original one, Archimedes screw-type impeller (screwpropeller) and scooped impeller, are commonly used (Mueller et al., 2002).

The operation of the typical aerator is based on the drawing the liquid upward by the rotating screwpropeller through the vertical intake cone. The direction of flow changes from an axial to radial, and the liquid jets of high kinetic energy are discharged from the unit in the direction determined by the casing design. Liquid jets projected outwards the aerator break into the fine droplet spray, creating extended interfacial area for oxygen transfer. Falling droplets entrain and disperse atmospheric air into bubbles into the bulk liquid in

the tank. At greater depths, device is usually fitted with draft tube system attached to the intake cone providing enhanced oxygen transfer and mixing. The high-speed aerator units use smaller impellers with short shafts and operate with lower pumping rates than low-speed devices. As they are lighter than the low-speed aerators, the typical configurations consider single float mounted units. The flow patterns generated by the aerator are similar but there is practically no liquid circulation within the tank.

Aerator performance is accompanied by mist formation. To prevent excessive expansion of the spray umbrella, the device operation is based on generation of low trajectory jets by using casing designed to direct the flow downwards and away the unit. Other options consider installation of the spray containment domes, controlling and redirecting discharge, and also retaining heat.

2.2.3 Oxygen Transfer in Clean Water

Back in 1976, under the sponsorship of United States Environmental Protection Agency (US EPA), American Society of Civil Engineers (ASCE) set up an international committee on Oxygen Transfer Standard, which main task was to gather up to date state of the art in oxygen transfer measurements and finally, to standardize testing procedures for aerators in both, clean and process waters. Consequently, one of the main efforts was to establish consistent and repeatable test condition to estimate clean water parameters: mass transfer coefficient, $K_L a$, and equilibrium saturation concentration of oxygen, C_{∞}^* from reaeration data, and successively, translating clean water rates to process conditions.

A long-term partnership of the committee members, manufacturers and practitioners in the field of aeration resulted in publication of the first ASCE Standard in 1984, which was subsequently updated and republished in 1991 and 2006 (Mueller et al., 2002). Worldwide application of Standard for the Measurement of Oxygen Transfer in Clean Water (ASCE, 1991, 2007) and Standard Guidelines for In-Process Oxygen Transfer Testing (ASCE, 1997) allowed characterizing unambiguously aeration device/system performance through determination of oxygen transfer in clean or process water, per quantity of energy delivered during aeration. Global spread of these standards, reduced variability not only in device testing procedures, affecting reliability of the data contained in the specifications of the unit, but also in the guidelines regarding design and dimensioning of the aeration systems.

2.2.3.1 Oxygen Mass Transfer Theory

Modelling of oxygen transfer in water is based on two film theory (two resistance theory) postulated by Lewis and Whitman (1924). The theory (Lewis and Whitman, 1924; Stenstrom et al., 2006; Tchobanoglous et al., 2003) considers interface between films of two phases: gas and liquid. The interface between the films is in the equilibrium state, thus the resistance to the mass transfer across the interface can be neglected. The passage of the gaseous phase through the interface occurs due to the relatively slow rate of molecular diffusion. In case of the gases of low solubility, such as oxygen, the resistance of the gas film can be neglected and consequently, entire resistance to the passage of the gas into the liquid is due to the liquid film. It is assumed that beyond the films, the concentration and partial pressure in both, bulk liquid and bulk gas phase are considered uniform (completely mixed).

Mathematical description of the gas mass transfer by molecular diffusion through the interface being in equilibrium is given by Fick's first law of diffusion:

$$r = -D_m \frac{\partial C}{\partial x} \quad (2.1)$$

where r denotes mass transfer rate per unit interfacial area per unit time, $\text{kg m}^{-2} \text{s}^{-1}$; D_m represents the molecular diffusion coefficient (diffusivity) in x direction, $\text{m}^2 \text{s}^{-1}$; $\partial C / \partial x$ is the concentration gradient; and x is a distance, m.

Considering aeration process, to describe the passage of the oxygen into the water, Equation (2.1) can be written using film coefficients and concentration gradients expressed in each phase from the bulk values to the interface values. Hence, for the oxygen layer we have:

$$r = k_G(P_G - P_i) \quad (2.2)$$

and for the water layer:

$$r = k_L(C_i - C_L) \quad (2.3)$$

where k_G denotes gas film mass transfer coefficient, m s^{-1} , P_G - is the partial pressure of the oxygen in the bulk gas phase, P_i - is the partial pressure of the oxygen at the interface, being in equilibrium with concentration C_i of oxygen in water, mg L^{-1} , k_L designates liquid film mass transfer coefficient, in m s^{-1} and C_L is the concentration of the oxygen in the bulk liquid phase, mg L^{-1} .

The gradients $(P_G - P_i)$ and $(C_i - C_L)$ represent driving forces causing mass transfer in the either phase, in sequence. Substituting the values k_G and k_L by the overall gas and liquid film coefficients, K_G and K_L , and considering existence of the resistance, but only in the liquid film, mass transfer rate can be expressed as follows:

$$r = K_L(C_S - C_L) = k_G(P_G - P_i) = k_L(C_i - C_L) \quad (2.4)$$

where C_S - is the concentration of the oxygen at the interface in equilibrium with the partial pressure of the oxygen in bulk gas phase, mg L^{-1} , and C_L denotes the concentration of the oxygen in water phase, mg L^{-1} .

The relationship at the interface is expressed by Henry's law of the following form:

$$P_G = HC_S \quad (2.5)$$

and

$$P_i = HC_i \quad (2.6)$$

where H denotes Henry's constant. Combining Equations (2.4), (2.5) and (2.6), the balance of driving forces equals:

$$(C_S - C_L) = (C_S - C_i) + (C_i - C_L) \quad (2.7)$$

Combining Equations (2.2), (2.3) and (2.5), (2.6) yields the following:

$$\frac{1}{K_L} = \frac{1}{k_L} + \frac{1}{Hk_G} \quad (2.8)$$

where the left side of the equation expressed as $1/K_L$ denotes the total resistance to gas component transfer, calculated as a sum of the resistances to oxygen transfer in liquid ($1/k_L$) and in gas phase ($1/Hk_G$).

Henry's law given in Equation (2.5) is employed to assess the oxygen saturation concentration, C_∞^* , defined as the concentration value in equilibrium with the concentration in the bulk gas phase, reached at the time approaching infinity. Since the resistance in the gas side is negligible, therefore the oxygen concentration at the interface equals bulk concentration in gas phase. Thus we have:

$$C_\infty^* = \frac{C_G}{H} \quad (2.9)$$

where C_{∞}^* denotes oxygen saturation concentration, mg L^{-1} , and C_G is the concentration in bulk gas phase, mg L^{-1} .

To assess the flux of oxygen from the gas phase to the liquid phase, water, Equation (2.4) is modified by replacing C_L for C_t :

$$r = K_L(C_{\infty}^* - C_t) \quad (2.10)$$

where C_t is concentration in bulk-liquid phase at the time t .

To express the change of oxygen concentration in time, Equation (2.10) will be multiplied by interfacial area per unit volume:

$$r_v = K_L \frac{A}{V} (C_{\infty}^* - C_t) = K_L a (C_{\infty}^* - C_t) \quad (2.11)$$

where r_v denotes rate of mass transfer per unit volume and unit time, $\text{kg m}^{-3} \text{s}^{-1}$, $K_L a$ is volumetric mass transfer coefficient, s^{-1} , A is the area through which the mass is transferred, m^2 , V denotes the volume in m^3 , in which the concentration of the oxygen is increasing and A/V denotes specific area, a .

The Equation (2.11) expressed often as

$$\frac{\partial C}{\partial t} = K_L a (C_{\infty}^* - C_t) \quad (2.12)$$

is the fundamental equation used to describe oxygen transfer in actual aeration systems.

2.2.3.2 Clean Water Test

To determine process water transfer rates the procedure based on aerator testing in clean water is commonly used, due to its reproducibility and validity for aeration devices operating in both, laboratory- and full-scale water volumes and for a wide range of mixing conditions. A method developed within the Standard (ASCE, 1984, 1991, 2007) covers the determination of the process parameters, related to the mass of oxygen transferred in a volume of water by an aeration device or system, operating under specified gas flow rate, power and process conditions.

Depending on the flow characteristics within the considered aerated system, clean water test can be carried on using non-steady (unsteady) and steady methods (von Sperling, 2007). Both methods require test water tank, previously washed with clean water and filled to the desired volume. Dissolved oxygen (DO) is removed from the water by oxidizing

with sodium sulphite in the presence of cobalt catalyst. During deoxygenation aeration device is switched off. Deoxygenation stage is followed by reoxygenation to near-the saturation level.

Most aeration tests are performed using the unsteady- state type of experiment. Unsteady-state method, called also reaeration method, is based on the monitoring of water volume DO inventory during reoxygenation stage, through measurements of DO concentration in the characteristic points, selected to represent the tank content. From the DO-versus-time data set, aeration capacity is calculated on the base of the rate of increase of the DO content during reaeration. Data obtained from each determination point during unsteady-state test are introduced into the simplified mass transfer model, defined by Equation (2.12), to estimate the values of apparent mass transfer coefficient, $K_L a$, and the oxygen saturation concentration, C_∞^* .

Log deficit form for oxygen transfer parameter estimation (Mueller et al., 2002; Stenstrom et al., 2006) uses the integrated form of the equation (2.12):

$$\ln \frac{C_\infty^* - C_0}{C_\infty^* - C_t} = K_L a (t - t_0) \quad (2.13)$$

where C_0 denotes initial DO concentration at time $t = t_0$, and the terms $C_\infty^* - C_0$ and $C_\infty^* - C_t$ represent the degrees of the undersaturation: initial at the time t_0 , and after any time t , respectively.

Log deficit method requires *a priori* methods of the C_∞^* parameter estimation, based on the knowledge about the aeration system. These methods account for the effect of the hydrostatic pressure of the column water on gas bubble, therefore the value of C_∞^* becomes the function of tank depth, and the mass transfer efficiency. Thus, depending on the aerator submergence, the value of the oxygen saturation concentration varies considerably from the handbook values. Additionally, *a priori* methods revealed to have other pitfalls, such as unintended transformation of the actual DO measurement errors in the logarithms or bias due to the incorrectly determined value of C_∞^* , that may affect the final overall transfer rate value. The extreme limits of bias of around ± 15 to 20% in $K_L a$ estimation occurred when the C_∞^* value applied into the log deficit form was too high. Nonetheless, performing log deficit for the data set using values up to 80% of saturation generates residuals of the range 2 to 4%. The alternative way to estimate aeration parameters from data obtained in reaeration test was introduced in the ASCE Standard. Nonlinear Regression Model, known also as the best fit method, based on nonlinear regression of equation (2.13) in the exponential form:

$$C_t = C_\infty^* - (C_\infty^* - C_0) \cdot \exp[K_L a(t - t_0)] \quad (2.14)$$

The method is based on the selection of the best estimates of $K_L a$, C_∞^* and C_0 , as the minimized residual sum of squares between the data predicted in equation and obtained experiment, is reached. Fitting the experimental data to equations may generate inversely correlated errors in parameters estimates, increasing or decreasing slightly C_∞^* and $K_L a$ values. Although, contrary to *a priori* models, the ASCE Method eliminates bias, the computational procedure requires a computer or programmable calculator to estimate the parameters; therefore popularity of the method was delayed until wide-spread use of personal computers (PC). In case of rapid on-site estimates and for the data up to 80% of saturation, log deficit method should provide rapid estimates of $K_L a$ values, differing for less than 5% from the values obtained using nonlinear regression technique.

The principles of the steady-state method of clean water testing are the same as those for non-steady. Steady-state test in clean water is performed on continuous flow system, in which all conditions are considered constant, such as the influent DO concentration, flow rate or mixing patterns within the tank (Abusam et al., 2001; ASCE, 1997; von Sperling, 2007). Therefore, after addition of deoxygenation agents, aerator remains switched off while the DO concentration in the tank drops to zero. After starting up the aerator, DO concentration is monitored in several points of the tank, until the steady- state concentration is reached.

Since the diffusivity of oxygen at the exposure time is constant, therefore overall liquid film coefficient, K_L , the specific area a , may also be considered constant. The test is performed on clean water and there is no oxygen consumption in the liquid medium during aeration, therefore the oxygen concentration increases to the steady-state value, that in this case is the saturation concentration: $C_\infty^* = C_S$.

The rate of change of the oxygen concentration, r , in a steady-state system equals:

$$r = \frac{\partial C}{\partial t} = K_L a(C_S - C_t) \quad (2.15)$$

After rearrangement, the oxygen transfer coefficient is:

$$K_L a = \frac{r}{C_S - C_t} \quad (2.16)$$

The mass of oxygen per unit volume and time is expressed through a rearrangement of the Equation (2.15) (von Sperling, 2007):

$$\frac{\dot{m}}{V} = K_L a (C_S - C_t) \quad (2.17)$$

where \dot{m} denotes mass flux of oxygen, kg s^{-1} .

After integration and rearrangement of the Equation (2.15), the concentration of the oxygen at any time can be computed from the following (ASCE, 1991):

$$C_t = C_S - (C_S - C_0) \cdot \exp[-K_L a (t - t_0)] \quad (2.18)$$

where C_0 denotes initial DO concentration at time $t = t_0$, and the term $C_S - C_0$ represent the initial oxygen deficit initial at the time t_0 .

For the same aeration device tested in different tanks the key parameters determined from the clean water test may vary due to the impact of such physical conditions, as barometric pressure, water temperature, or salt content. To allow uniform characterization of the aerator and avoid bias, assessed transfer rate values are successively adjusted to the standard conditions, namely: clean water; zero DO concentration; water temperature of 20 °C; barometric pressure of 1.0 atm; and altitude of 1.0 m (sea level).

Depending on the water temperature, the oxygen saturation concentration will vary, therefore the adjustment to the standard conditions requires introduction of the correction factor, τ_T :

$$\tau_T = \frac{C_{ST}^*}{C_{S20}^*} \quad (2.19)$$

where C_{ST}^* is the oxygen saturation concentration in the process temperature, mg L^{-1} , and C_{S20}^* is the saturation concentration at temperature of 20 °C , 1.0 atm total pressure and zero salinity.

The influence of the temperature on the $K_L a$ values can be expressed using following relationship:

$$K_L a_T = K_L a_{20} \theta^{T-20} \quad (2.20)$$

where $K_L a_T$ denotes $K_L a$ coefficient at any temperature T , s^{-1} , $K_L a_{20}$ is the $K_L a$ coefficient at the standard temperature of 20 °C, and θ is the temperature coefficient. The recommended value of θ is 1.024.

Presence of Total Dissolved Solids (TDS) in water affects solubility of the oxygen. Carrying multiple clean water experiments on the same water is a common practice, however due to the addition of deoxygenating chemicals salt content within the tank will constantly increase. Therefore, the upper limit of TDS concentration is 2000 mg L⁻¹. The effect of the salinity on the dissolved oxygen can be described with the following formula (Pöpel, 1979):

$$\gamma = 1 - 10^{-6} \cdot C_{sal} \quad (2.21)$$

where γ denotes solubility reduction factor (for clean water γ equals 1), and C_{sal} is concentration of dissolved salts, in mgCl⁻ L⁻¹.

Presence of the dissolved organics, soaps and surfactants and other contaminants in the wastewater may have a significant impact on the $K_L a$ values. From this reason, an experimentally measured for each aeration device parameter - α factor, accounting for the reduction in oxygen transfer rate caused by impurities in the wastewater, was introduced.

$$\alpha = \frac{K_L a_{wastewater}}{K_L a_{tap\ water}} \quad (2.22)$$

The α factor is the most uncertain of the various oxygen transfer parameters. Typically, the values of α vary from 0.6 to 1.2 for mechanical aeration systems, and from 0.4 to 0.8 for diffused oxygen systems (Tchobanoglous et al., 2003).

2.2.3.3 Oxygen Transfer Rate Parameters

Oxygen Transfer Rate, referred also as the oxygenation capacity, OC , is defined as the mass of oxygen transferred per unit time into a given volume of water V at the temperature T :

$$OTR = K_L a_T C_{\infty}^* V \quad (2.23)$$

where OTR denotes Oxygen Transfer Rate in clean water and under operating conditions, kgO₂ h⁻¹.

Employing standard conditions, Standard Oxygen Transfer Rate, is defined as:

$$SOTR = K_L a_{T20} C_{\infty 20}^* V \quad (2.24)$$

where $SOTR$ denotes Standard Oxygen Transfer Rate in clean water and under standard conditions, $\text{kgO}_2 \text{h}^{-1}$.

Aeration Efficiency is referred as the oxygen transfer rate in clean water in $\text{kgO}_2 \text{h}^{-1}$ per unit power consumed (kW), and is expressed as:

$$AE = \frac{OTR}{P} \quad (2.25)$$

where AE denotes the Aeration Efficiency in clean water and under operating conditions, $\text{kgO}_2 \text{kW}^{-1} \text{h}^{-1}$, and P denotes power input, kW.

Thus, Standard Aeration Efficiency is:

$$SAE = \frac{SOTR}{P} \quad (2.26)$$

where SAE is the Standard Aeration Efficiency in clean water and under standard conditions, $\text{kgO}_2 \text{kW}^{-1} \text{h}^{-1}$.

The power input may be assessed from either on delivered DP or on wired power WP (Mueller et al., 2002):

$$P = DP = \frac{WP}{\eta} \quad (2.27)$$

where η denotes overall efficiency of the aeration equipment and is the product of the individual efficiencies of the mechanical equipment, such as blowers, motors, coupling or gearboxes.

For diffused aeration systems, delivered power of blowers is computed from the adiabatic compression equation, expressed as:

$$P = \frac{wRT}{29.7 \cdot n \cdot e_B \cdot e_M} \left[\left(\frac{p_2}{p_1} \right)^{0.283} - 1 \right] \quad (2.28)$$

where P is the power requirement for each blower in kW, w is air mass flow rate in kg s^{-1} , R is universal gas constant for air and $R= 8.314 \text{ kJ kmol}^{-1} \text{K}^{-1}$, and T is the inlet temperature in K, n is the constant and equals 0.283 for air, p_1 and p_2 are absolute pressures upstream and downstream (inlet, outlet) of compressor in atm, e_B is blower efficiency, usually in the range 70-90%, and e_M is motor efficiency, usually in the range of 90-94%.

The Oxygen Transfer Efficiency is one of the essential parameters characterizing diffused aeration systems, which is calculated from the following formula:

$$OTE = \frac{OTR}{w_{O_2}} \cdot 100 \quad (2.29)$$

where OTE denotes Oxygen Transfer Efficiency in % and w_{O_2} is oxygen supply mass flow rate, $kgO_2 h^{-1}$. Considering standard conditions, the Standard Oxygen Transfer Rate is:

$$SOTE = \frac{SOTR}{w_{O_2}} \cdot 100 \quad (2.30)$$

where $SOTE$ denotes Standard Oxygen Transfer Efficiency in %.

2.2.3.4 Process Parameters for Selected Aeration Devices

The typical values of the process parameters, Standard Aeration Efficiency, SAE and Standard Oxygen Transfer Efficiency, $SOTE$, for selected nonporous and porous diffusers and other hybrid fine bubble devices are listed in Table 2.1, Table 2.2 and Table 2.3.

The values of SAE for mechanical aeration devices are presented in Table 2.4.

Table 2.1 Summary of Standard Aeration Efficiency (SAE) and Standard Oxygen Transfer Efficiency ($SOTE$) for selected nonporous diffused air systems.

Aeration device	SAE ($kgO_2 kW^{-1} h^{-1}$)	Reference	$SOTE$ (%)	Reference
Nonporous diffusers	0.6-1.5	(Stenstrom and Rosso, 2008)	9-13	(Tchobanoglous et al., 2003)
	0.6-1.2	(Quasim, 1999)	4-8	(Quasim, 1999)
	0.6-1.2	(Taricska et al., 2009b)	-	-
Fixed orifice perforated tube	2.0-2.2	(Yunt and Hancuff, 1988)	17-20	(Yunt and Hancuff, 1988)
Sparger	1.8-1.9	(Yunt and Hancuff, 1988)	15-17	(Yunt and Hancuff, 1988)
Static tube	1.7-1.9	-	13-20	(Semblex, 1987)
	1.2-1.6	(Quasim, 1999)		(Quasim, 1999)

2 Aeration Technologies

Table 2.2 Summary of Standard Aeration Efficiency (SAE) and Standard Oxygen Transfer Efficiency (SOTE) for selected porous diffused air systems.

Aeration device	SAE (kgO ₂ kW ⁻¹ h ⁻¹)	Reference	SOTE (%)	Reference
Porous diffusers	3.6-4.8	(Stenstrom and Rosso, 2008)	10-30	(Quasim, 1999)
	1.2-2.0	(Quasim, 1999)		
	1.2-2.1	(Taricska et al., 2009b)		
Ceramic dome	3.4-6.0	(Mueller et al., 2002)	27-37	(Tchobanoglous et al., 2003)
			25-44	(EPA, 1989)
Ceramic disc	3.6-6.1	(Mueller et al., 2002)	25-35	(Tchobanoglous et al., 2003)
			25-40	(EPA, 1989)
Ceramic plate	-	-	26-33	(EPA, 1989; Tchobanoglous et al., 2003)
Rigid porous plastic tubes	4.5-5.2	(Mueller et al., 2002)	28-32	(EPA, 1989)
Rigid porous plastic disc	-	-	22-32	(EPA, 1989)
Rigid porous plastic plate	-	-	30-40	(Mueller et al., 2002)
Nonrigid porous plastic tubes	-	-	26-36	(Tchobanoglous et al., 2003)
Perforated membrane disc	2.4-7.9	(Mueller et al., 2002)		
Perforated EPDM membrane tube	3.4-5.8	(Mueller et al., 2002)	21	(EPA, 1989)
			22-29	(Tchobanoglous et al., 2003)
Perforated membrane panels	3.1-6.9	(Mueller et al., 2002)	38-43	(Tchobanoglous et al., 2003)

2 Aeration Technologies

Table 2.3 Summary of Standard Aeration Efficiency (*SAE*) and Standard Oxygen Transfer Efficiency (*SOTE*) for selected fine bubble aerators.

Aeration device	<i>SAE</i> (kgO ₂ kW ⁻¹ h ⁻¹)	Reference	<i>SOTE</i> (%)	Reference
Jet aerator	1.2-1.8	(Stenstrom and Rosso, 2008)		
	1.2-2.4	(Quasim, 1999)	10-25	(Quasim, 1999)
Directional configuration	1.7-2.0	(Yunt and Hancuff, 1988) and	15-24	(Tchobanoglous et al., 2003; Yunt and Hancuff, 1988)
Cluster configuration	1.6-2.2	(Yunt and Hancuff, 1988) and	21-33	(Yunt and Hancuff, 1988)
U-tube aerator	1.3-2.4	(Quasim, 1999)	15-20	(Quasim, 1999)

2 Aeration Technologies

Table 2.4 Summary of Standard Aeration Efficiency (SAE) for selected mechanical aeration systems.

Aeration device	SAE (kgO ₂ kW ⁻¹ h ⁻¹)	Reference
Horizontal rotor	1.5 -2.1	(Mueller et al., 2002; Tchobanoglous et al., 2003)
	1.2-2-0	(von Sperling, 2007)
	1.5-2-1	(Stenstrom and Rosso, 2008)
	1.0-2.0	(Quasim, 1999)
Low-speed aerators	1.9-2.2	(Mueller et al., 2002)
	1.4-2.0	(von Sperling, 2007)
	1.5-2.1	(Tchobanoglous et al., 2003)
Low-speed with draft tube	1.2-2-8	(Tchobanoglous et al., 2003)
	1.2-2.7	(Quasim, 1999)
Submerged turbines	1.1-2.1	(Tchobanoglous et al., 2003)
	1.2-2-0	(Quasim, 1999)
Axial flow	1.0-1.6	(Mueller et al., 2002)
Radial flow	1.1-1.5	(Mueller et al., 2002)
Submerged turbine with draft tube/sparger	1.6-2.4	(Mueller et al., 2002)
	1.2-2.0	(Tchobanoglous et al., 2003)
Submerged turbine with draft tube - barrier ditch	0.8-1.2	(Mueller et al., 2002)
Aspirating aerators	0.4-0.9	(Mueller et al., 2002)
	0.6-1.2	(von Sperling, 2007)
	1.5-2.5	(Quasim, 1999)
High-speed aerators	1.1-1.4	(Mueller et al., 2002; Tchobanoglous et al., 2003)
	0.9-1.3	(Stenstrom and Rosso, 2008)
	1.0-1.4	(von Sperling, 2007)
	1.2-2.7	(Quasim, 1999)

2.2.4 Recent Achievements in Aeration Field

Nowadays and not exclusively in wastewater sector, water-energy issues are of growing importance in the context of water shortages, higher energy and material costs and

a climate change. High energy use patterns of the aeration process impose implementation of the energy conservation measures and energy management programs, which are directly related to such cost-effective energy conservation practices, as introduction of new technologies or upgrades of aeration devices and their operation strategies. From this reason, wide range of multidisciplinary approaches with a diverse methodology constitute an important input into current research on aeration of the AS systems: some of the studies concern aerator design and performance, others evaluate methods of oxygen transfer measurement, or focus on application of the advanced computational tools to predict and correct failures of the existing aeration systems.

Accurate estimation of the *OTR* in AS basin is fundamental for verification of the aerator design specification and improved process design and operation. Standardized methods practiced extensively for *OTR* determination include: clean water test and process water tests; off-gas method based on the DO mass balance of the water column under a hood floating onto the aerated wastewater surface; and radioactive and non-radioactive tracer techniques (Abusam et al., 2001; Leu et al., 2010; Rosso et al., 2011; Rosso and Stenstrom, 2005). Literature offers a handful of examples of research studies focused on the analysis and the interpretation of the in situ measurements of *OTR* performed for different aeration systems and conducted on either full scale WWTPs (Brannock et al., 2010; Chiemchaisri and Yamamoto, 2005; Cornel and Krause, 2006; Cornel et al., 2003; Diamantis et al., 2010; Duchène et al., 2001; Fayolle et al., 2010; Gillot and Héduit, 2000; Le-Clech et al., 2003; Potier et al., 2005; Rosso et al., 2011; Rosso et al., 2008b; Vermande et al., 2007) or laboratory scale systems (Fonade et al., 2001; Gillot et al., 2005; Jin and Lant, 2004; Jin et al., 2006; Jing et al., 2009; Le Moullec et al., 2008a; Mineta et al., 2011; Nicoletta et al., 1998; Zerari et al., 2013). Data obtained from the oxygen transfer measurements, i.e. DO profiles within the aerated tanks and oxygen transfer parameters (*OTR*, *OTE* and *AE*) allow to evaluate the impact on the process efficiency and economy of the particular conditions, such as: operating air or oxygen rates; aerator type, placement, submergence, configuration and density, corresponding to percentage of the tank floor coverage with diffusers or the number of units in mechanical aeration systems (Bhuyar et al., 2009; Capela et al., 2001; DeMoyer et al., 2003; Fayolle et al., 2010; Fonade et al., 2001; Gillot and Héduit, 2000; Kossay and Al-Ahmady, 2006; Rao and Kumar, 2007; Rao et al., 2009; Thakre et al., 2008). Nonetheless, data obtained from the onsite clean water tests performed for different aeration devices before the start-up of the WWTP may be insufficient to predict a series of factors affecting oxygen transfer, such as hydraulic and operating conditions, especially in case of deep tank aeration systems (Fayolle et al., 2010; Gillot et al., 2005).

As the physics of the AS systems is complex, not only due to the presence of the multiphase flow, consisted of mixed liquor and air/oxygen, but also due the scale gap between tank dimensions, flocs and bubbles released by diffusers, and different velocities of the phases imparted by mixers and aerators (Pereira et al., 2012), therefore improved forecast of the oxygen transfer, based on the detailed insight into hydrodynamics of the aeration tank may be crucial for the process design and optimization. Moreover, since overall biochemical conversion reaction in AS are of orders greater than zero, thus wastewater treatment efficiency will also depend on the biological reactor hydrodynamics (Le Moullec et al., 2008b). Nowadays, increasing availability of computational resources have enabled the use of the Computational Fluid Dynamics (CFD) as a tool for the analysis of the multiphase flow behaviour, interfacial mass transfer and chemical reaction in gas-liquid reactors, and it has been exploited by the academic and industrial community for the design and optimization of AS process equipment (Brouckaert and Buckley, 1999; Cockx et al., 2001; Fayolle et al., 2007; Gresch et al., 2011; Kochevsky, 2004; Le Moullec et al., 2010a, b; Le Moullec et al., 2008b; Rigopoulos and Jones, 2003; Versteeg and Malalasekera, 1995). The flow patterns within the aeration tank are obtained from the solution of nonlinear partial differential equations, expressing balances of mass, momentum and energy coupled to the transport equations of the inert or reactive species in a local scale (Do-Quang et al., 1999). Linearization of these equations requires modelling of the fluctuating small flow structures and interaction forces between the phases by introduction of additional turbulence closures, such as two equation $k - \varepsilon$ model (Pope, 2000; Tabib et al., 2008; Zhang et al., 2006). The complete simulation of the aeration tank is difficult to handle, due to the complex hydrodynamics, resulting in high number of CPU required with long computational times involved. A common modelling practice is to simulate separately with CFD codes individual parts of the aeration tanks and afterwards couple the results (Karpinska et al., 2012a; Karpinska et al., 2012b; Pereira et al., 2012). Thus, some works focus mainly on the study and optimization of the aerator performance (Bhuyar et al., 2009; Cockx et al., 2001; Dahikar et al., 2007; Dhotre and Joshi, 2007; Do-Quang et al., 1999; Morchain et al., 2000), others model oxygen transfer and overall mixing phenomena in aeration tanks (Brannock et al., 2010; Dhanasekharan et al., 2005; Fan et al., 2010; Gillot et al., 2005; Le Moullec et al., 2010a, b; Le Moullec et al., 2008b; Moraveji et al., 2012; Tabib et al., 2008; Talvy et al., 2007; Wu and Chen, 2011; Xu et al., 2010). Examples of biokinetic models incorporated in the CFD simulations of the aeration tanks can be also found in the literature (Fayolle et al., 2007; Gresch et al., 2011; Zima et al., 2009).

Determined in the CFD studies spatial distribution of such hydrodynamic features of the AS system as gas hold-up, DO profiles and axial velocity of the mixed liquor within the tank, provide precise information about the global and local physical phenomena occurring in the aeration basins, useful to optimize their operation and plan energy-minded upgrades. Nevertheless experimental calibration of the simulation input data and validation of a CFD results, especially in complex flow situations, is still desired. From this reason one of the scientific areas evolving dynamically next to the development of the aeration technologies and computational designing tools, are qualitative and quantitative methods associated with the dynamic measurements performed in such multiphase systems and based on the determination of liquid circulation velocity, gas hold-up and velocity, bubble distribution, and diffusion coefficients (Luo and Al-Dahhan, 2008).

Typically, time-averaged velocity field in liquid volume is obtained from the measurements using such nonintrusive methods, as Laser Doppler Velocimetry, LDV (Le Moullec et al., 2008b), Particle Image Velocimetry, PIV (Fan et al., 2005; Janzen et al., 2010), Acoustic Doppler Velocimetry (Gresch et al., 2011) or using Particle Dynamic Analyzer (PDA) (Fan et al., 2010). Several techniques have been developed to assess mass transfer and diffusion coefficients in water (Pinelli et al., 2010) using data obtained from clean water tests and dynamic tests such as dynamic peroxide method (Marcelino et al., 2009). Usually, dissolved oxygen measurements include use of zirconia ceramic, electro-chemical (galvanic) and luminescent digital probes and laser based methods (Suresh et al., 2009). Thus, several works focus on application of nonintrusive optical methods, such as Planar Laser Induced Fluorescence (PLIF), based on a local measurement of fluorescent dye concentration in air-water reactor systems (Dani et al., 2007; Janzen et al., 2010; Jimenez et al., 2013). PLIF method found wide application in lab-scale aeration vessels and allows obtaining maps representing DO concentration fields, however its application in large scale tanks is limited by the costs of large quantities of expensive oxygen selective fluorescent dyes, such as pyrene butyric acid or ruthenium complexes (Dani et al., 2007; Jimenez et al., 2013).

Instantaneous gas hold-up in aeration tanks is measured using flow intrusive probe-based methods, based on the local temperature, pressure and conductivity fluctuations (Shaikh and Al-Dahhan, 2007). Advanced techniques for gas hold-up and flow regime measurements include imaging and laser based methods, such as PIV, Laser Doppler Anemometry (LDA), Electrical Capacitance Tomography (ECT), Computer Automated Radioactive Particle Tracking (CARPT), gamma or X-rays Computed Tomography (CT) or Cone-Beam type X-ray Computed Tomography (CBCT), which allow to measure two- or three- dimensional distribution of the phases within the stirred vessels (Boden et al., 2008; Luo and Al-Dahhan, 2008). Typical method used to determine bubble size distribution within aeration

tank involves Sauter mean bubble diameter computation, obtained from processing of sequence of images taken by high speed CCD camera (Díaz et al., 2008a).

Overcoming relatively low *SOTE* values of around 40% obtained for current most efficient commercially available aeration devices, i.e. membrane diffusers, has been a driving force to develop innovating technologies, such as bubbleless aeration in membrane modules, referred in the literature as parallel flow aerators (Ahmed et al., 2000, 2004; Li et al., 2010) based on the same principals as the membrane-aerated biofilm reactor MABR (Syron and Casey, 2008), MF and UF membrane processes in water treatment, or aeration by supercavitation (Schmid, 2009), similar to modified jet aeration. The other trend in research concerns improvement of the aeration performance by modification and upgrade of the aeration unit, e.g. in case of vertical shaft aerators it was found, that even slight changes in the shape of blades or blade tip angle, introduction of multi-impeller configurations or system upgrade by fixing draft tubes below the aerators can have positive effects on the mixing patterns within the aeration tank, oxygenation capacity and power withdrawal by whole aeration system (Bhuyar et al., 2009; Fugasová et al., 2007; Janssen et al., 2002; Thakre et al., 2008). Similarly to vertical shaft aerators, positive effects were obtained by simple modification in the draft tube cross section in the jet loop bioreactor (Farizoglu and Keskinler, 2007).

For the last three decades, porous diffusers, proven to be more efficient and energy-minded have been extensively implemented in both, new WWTPs and existing plants, to retrofit less efficient aeration systems, such as coarse bubble diffusers or mechanical aerators. Large input in the studies on improvement of diffused air systems performance was made by Californian group of scientists under supervision of M.K. Stenstrom, by publishing over 30 scientific papers and even more reports on estimation of oxygen transfer in activated sludge plants, including HPO-AS systems. A number of papers concerned changes in performance of the diffusers made of different polymeric membranes over time in operation. The ageing of the diffusers, manifested with progressive membrane degradation due to scaling and fouling, is inseparably linked to the increase of the operating costs due to increase of the DWP and the headloss, with decrease of the operating efficiency of the system, and worsening of effluent quality. Due to that, understanding the character of changes in the porous material and selection of the mechanical properties parameters is of the great importance to ascertain diffuser fouling rates and develop cleaning techniques (Kaliman et al., 2008; Rosso et al., 2008a).

The assessment of the impact of process conditions, related to the α factor (Stenstrom and Gilbert, 1981), on decrease of *SOTE* for the fine bubble diffusers was also intensively studied. Although α relates to the presence of many contaminants in wastewater, surfactants have the strongest impact on its value (Rosso et al., 2006; Rosso et al., 2005; Rosso and Stenstrom, 2006). For AS systems operating with low Mean Cell Residence Times (MCRTs) and with the higher biodegradable organic fraction content, small alphas will yield lower oxygen transfer efficiency. Contrary to that, the plants operating at high solid retention times (SRTs) yield higher α and slight decrease in the *SOTE*, due to faster and more efficient uptake of soluble contaminants into the biomass, what can be easily observed in plug flow aeration tanks (Cornel et al., 2003; Rosso et al., 2006; Rosso et al., 2005; Rosso et al., 2011; Rosso and Stenstrom, 2005; Rosso and Stenstrom, 2006; Rosso et al., 2008b). In these systems, fouling rates are lower, what makes operation and maintenance of the aeration system less costly. It can be said, that by now, although the great deal of research was done to assess the mechanisms and theory of transfer rate reduction due to presence of surfactants, α factor still remains the most uncertain of the oxygen transfer parameters.

Assessment of the impact of process conditions related to the wastewater temperature on the equilibrium DO saturation concentration, and thus, oxygen transfer efficiency have been also made (Gillot and Vanrolleghem, 2003; Lippi et al., 2009). Although correction of the mixed liquor temperature is beyond the rational operation of the AS tanks, nonetheless the results of the modeling studies point out the manners of direct control of the factors impacting heat patterns in AS basins in the design stage. Thus, choice or upgrade of the aeration system, application of tank covers, surface to volume ratio, and aeration basin geometry can reduce the temperature amplitudes and improve the overall aeration performance.

The conclusions withdrawn from the evaluation of the impact of process water (e.g. variable alpha values, and diffusers fouling) on the values of oxygen transfer parameters and the knowledge about the system hydrodynamics are useful for management and the optimization of the aeration through the process control. When investigating energy expenditure on aeration in the biological WWTPs, two essential factors need to be accounted: effluent properties should comply with the quality requirements defined by the authorities, e.g. expressed as maximum levels of total nitrogen or ammonia in the discharge from the aeration tank, commonly defined as effluent nitrogen criterion; and operational costs of the most energy intensive processes, i.e. aeration, recycled sludge pumping and wasted sludge disposal, need to be as low as possible. From these reasons it

is clear, that DO concentration is a key process variable, which controls both, nutrient removal and thus effluent quality, and the operating cost of the WWTP (Åmand and Carlsson, 2012; Fernández et al., 2011; Fikar et al., 2005). While the estimative of the best operating DO profiles and nitrogen patterns in the AS system are obtained from the biokinetics modeling with ASM1 (Activated Sludge Model No. 1), the proper modeling of the optimization strategies requires implementation of the complex computational algorithms and off-line optimization techniques, which allow for coupling of the biological process with pre-defined control variables such as minimal DO concentration in the aeration tank or effluent nitrogen criterion (Åmand and Carlsson, 2012; Chachuat et al., 2005; Cristea et al., 2011; Fernández et al., 2011; Fikar et al., 2005; Holenda et al., 2007; Holenda et al., 2008; Kusiak and Wei, 2013). Examples of dynamic process control at WWTPs leading to energy efficient nutrient removal due to generation of alternating aerobic and anoxic conditions by switching on and off aeration can be found in the literature (Chachuat et al., 2001, 2005; Fernández et al., 2011; Lessard et al., 2007; Mueller et al., 2002). Many research was done on the different methods and structures for the aeration automation control (Åmand and Carlsson, 2012; De Araújo et al., 2011; Ekman et al., 2006; Fernández et al., 2011; Machado et al., 2009; O'Brien et al., 2011); aeration control strategies, which include design of air distribution systems from the collector to the diffuser selection and constraints; overview of control loops, DO and pressure control in blowers, DO and ammonia controllers, and controller tuning (Olsson, 2011); and finally, blower control, modelling and sizing (Brischke et al., 2008).

2.3 Pressurized Aeration Chamber - CFD studies

In this section, design assumptions of a novel aeration device, Pressurized Aeration Chamber (PAC) and the rationale behind the implementation of the CFD tool to model aeration process are given. 2D and 3D geometries of the PAC, studied in the simulations are described. Furthermore, detailed description of the CFD approach in flow field and oxygen transfer modelling for various configuration of PAC geometry is presented, including specifications of the models involved, boundary and operating conditions, features of the solver and simulations set-up parameters. Finally, the results obtained in both, 2D and 3D simulations of the flow field and the oxygen mass transfer in PAC are presented.

2.3.1 Design Considerations

Efficiency of conventional aeration devices depends on the maximization of contact area and contact time between gaseous air (oxygen) and mixed liquor. Relatively low oxygen

transfer efficiencies (*SOTE*) up to 40% for best state of the art aeration technologies, porous diffusers, are mainly due to the convection of the bubbles escaping to the atmosphere, and thus short contact times between both phases, air (oxygen) and water for efficient, “longer lasting” saturation.

In this work, Computational Fluid Dynamics (CFD) was enabled as a design tool in development of a new aeration device - Pressurized Aeration Chamber (PAC), aiming increase of the oxygen transfer efficiencies through an accurate prediction of the oxygen mass transfer. PAC is independent aeration unit, designed as a continuous flow component, included in the mixed liquor recirculation loop. The performance of PAC is based on the same principals as jet aeration. The device consists of a closed tank, filled with wastewater recirculated from the aeration tank, and supplied with air or oxygen delivered under pressure of up to 2.0 bars. High pressure conditions promote effective passage of the total delivered gaseous oxygen into dissolved in the wastewater form. Therefore, due to lack of bubbly form of the gas phase, the process in PAC can be compared with bubbleless aeration in membrane modules. Oxygen rich pressurized stream is later injected into the aeration tank. As the stream carries only dissolved oxygen, better oxygenation of the tank content is reached by delayed escape of the releasing bubbles to the atmosphere. Moreover, dissolved form of the oxygen is easier and faster assimilated by the activated sludge organisms yielding better wastewater treatment performance. The device can be fitted to every continuous flow activated sludge scheme and its performance can be fully used in plug flow and closed loop tanks.

All simulations of the PAC used Finite Volume Method and were performed using ANSYS Fluent 6.3.26 commercial CFD code in a HP Workstation with Intel® Xeon® 2.33 GHz 8-Core PC with 16.0 GB RAM memory.

2.3.2 CFD Model

CFD simulations consider a specific volume of water flowing through the PAC, being saturated with DO. The operation of the PAC is based on the intense mixing of both species, water and DO, and the high degree of turbulence generated due to the local velocity scales, PAC hydraulic features and the created flow patterns. The Reynolds numbers computed for the different velocity ranges are of the order 10^6 and from this reason turbulent flow regime within the chamber was simulated using transient formulation.

Preliminary studies of PAC carried on the 2D models aimed to predict the patterns of oxygen transport within several chamber geometries. Selected layouts, which ensure most efficient level of saturation with oxygen, will be subsequently studied in 3D scheme.

2.3.3 2D Geometry

2D PAC layouts were designed using ANSYS Gambit 2.3.16 pre-processing software. Several geometries of various chamber layouts were studied: from nearly square or rectangular, to rectangular with different topwall-bottom baffles arrangements. Square geometry has the dimensions of 0.50×0.60 m, and the rectangular one is 0.10×0.76 m. PAC geometry consists of: single inlet and outlet, each of 0.05 m, placed on both sides of the layout; topwall, having the function of the liquid-gas interface; and the bottom and side walls. For all geometries, meshes were built from structured grid of quadrilateral elements, as seen in the Figure 2.1. Several scaling tests were run to test grid convergence for coarser meshes of around 12 thousand elements to refined meshes having up to 200 thousand elements. Here, the grid independence test was conducted for each of PAC geometries. The initial simulations were run on the coarse mesh to assure the convergence for the residual error value of 10^{-6} . For unsteady monitor points and the fluctuations higher than 1%, the mesh was globally refined and the simulation was start over again for the same convergence criteria. The results, i.e. value of outflow concentration obtained for the finer mesh were compared against the results obtained for the coarser one. The differences higher than assumed 5% tolerance indicated dependency of the solution on the mesh resolution. This required further refinement and comparison with the results obtained for the antecedent mesh, and the procedure was repeated until the grid independent solution. At that point coarser mesh from the two was selected allowing for reduction of the simulation run time. All 2D geometries with chamber dimensions and mesh specifications are listed in the Table 2.5.

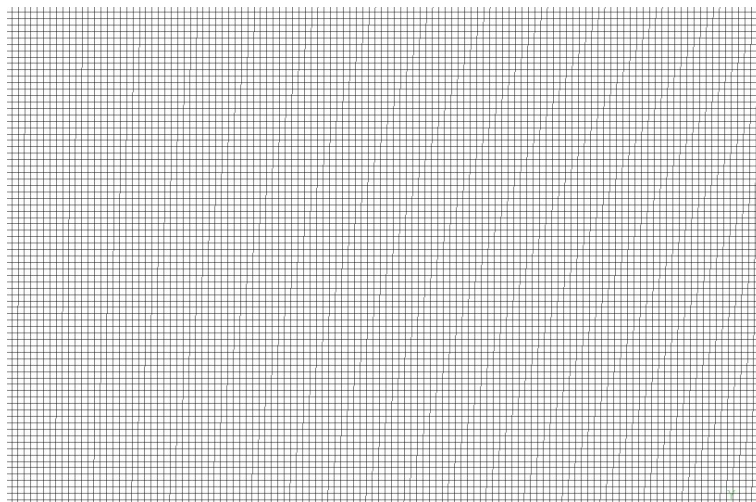

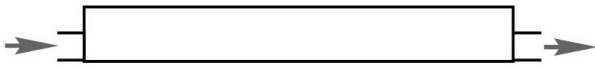
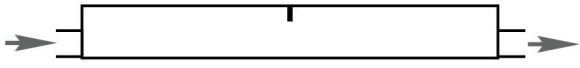
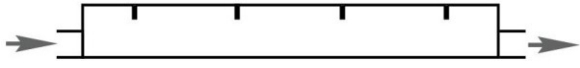
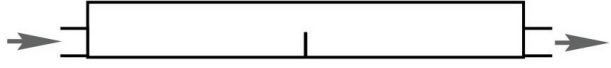
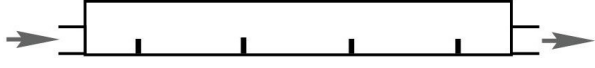
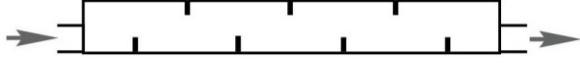


Figure 2.1 Conformal quadrilateral mesh used in 2D geometries of PAC.

Table 2.5 Geometric models used in 2D simulations of PAC.

PAC Layout	Dimensions (m)	N° of mesh elements
	0.50×0.60	33200
	0.10×0.76	134000
	0.10×0.76	133903
	0.10×0.76	133210
	0.10×0.76	133665
	0.10×0.76	133210
	0.10×0.76	130747

2.3.4 Governing Equations

For all considered PAC geometries, the flow field was simulated using unsteady Reynolds Averaged Navier-Stokes (URANS) equations. Flow is governed by the following mass conservation equation:

$$\frac{\partial \rho \bar{v}_i}{\partial x_i} = 0 \quad (2.31)$$

and momentum conservation equation:

$$\frac{\partial \bar{v}_i}{\partial t} + \frac{\partial}{\partial x_j} (\rho \bar{v}_i \bar{v}_j) = -\frac{\partial \bar{p}}{\partial x_i} + \frac{\partial}{\partial x_j} \left[\mu \left(\frac{\partial \bar{v}_i}{\partial x_j} + \frac{\partial \bar{v}_j}{\partial x_i} - \frac{2}{3} \delta_{ij} \frac{\partial \bar{v}_l}{\partial x_l} \right) \right] + \frac{\partial}{\partial x_j} (-\rho \overline{v'_i v'_j}) \quad (2.32)$$

where \bar{p} is the averaged pressure field, ρ and μ are the fluid density and viscosity, respectively, t is the time, x_i , x_j and x_l are the spatial coordinates, v_i , v_j and v_l are the velocity components and δ_{ij} is the Kronecker delta.

The velocity components are decomposed on a time averaged term, \bar{v}_i , and a fluctuating term, v'_i :

$$v_i = \bar{v}_i + v'_i \quad (2.33)$$

URANS equations are linearized and solved, however the fluctuating flow structures smaller than the numerical grid discretization, which are represented by the Reynolds Stresses and denoted as $-\overline{\rho v'_i v'_j}$ term, are unclosed, and thus they must be modelled. In this work, the turbulence model used for $-\overline{\rho v'_i v'_j}$ closure is the standard $k - \varepsilon$ model, where k is the kinetic energy of the velocity fluctuation (turbulence kinetic energy) and ε is its dissipation rate. Reynolds stresses modelling employs Boussinesq hypothesis relating these stresses to the mean velocity gradients, as follows:

$$-\overline{\rho v'_i v'_j} = \mu_t \left(\frac{\partial \bar{v}_i}{\partial x_j} + \frac{\partial \bar{v}_j}{\partial x_i} \right) - \frac{2}{3} \left(\rho k + \mu_t \frac{\partial v_k}{\partial x_k} \right) \delta_{ij} \quad (2.34)$$

where μ_t is the turbulent viscosity computed as a function of k and ε :

$$\mu_t = \rho C_\mu \frac{k^2}{\varepsilon} \quad (2.35)$$

where C_μ is a constant and amounts 0.09.

The transport equations for turbulence kinetic energy, k and its dissipation rate, ε are represented by the following equations:

$$\frac{\partial}{\partial t} (\rho k) + \frac{\partial}{\partial x_i} (\rho k \bar{v}_i) = \frac{\partial}{\partial x_j} \left[\left(\mu + \frac{\mu_t}{\sigma_k} \right) \frac{\partial k}{\partial x_j} \right] + G_k + G_b - \rho \varepsilon - Y_M \quad (2.36)$$

and

$$\frac{\partial}{\partial t} (\rho \varepsilon) + \frac{\partial}{\partial x_i} (\rho \varepsilon \bar{v}_i) = \frac{\partial}{\partial x_j} \left[\left(\mu + \frac{\mu_t}{\sigma_\varepsilon} \right) \frac{\partial \varepsilon}{\partial x_j} \right] + C_{1\varepsilon} \frac{\varepsilon}{k} (G_k + C_{3\varepsilon} G_b) - C_{2\varepsilon} \rho \frac{\varepsilon^2}{k} \quad (2.37)$$

In these equations, the term G_k represents the generation of turbulence kinetic energy due to the mean velocity gradients and G_b is the generation of turbulence kinetic energy due to buoyancy; Y_M is the contribution of the fluctuating dilatation in compressible turbulence to the overall dissipation rate; $C_{1\varepsilon}$, $C_{2\varepsilon}$ and $C_{3\varepsilon}$ are model constants - default values for $C_{1\varepsilon}$ and $C_{2\varepsilon}$ are 1.44 and 1.92, and $C_{3\varepsilon}$ is -0.33 ; σ_k and σ_ε are the turbulent Prandtl numbers for k and ε , and amount 1.0 and 1.3 respectively.

The production of turbulence kinetic energy, G_k , is approximated in a manner consistent with Boussinesq hypothesis by:

$$G_k = -\overline{\rho v'_i v'_j} \frac{\partial \bar{v}_j}{\partial x_i} = \mu_t S^2 \quad (2.38)$$

where S is the modulus of the mean rate-of-strain tensor, defined as follows:

$$S \equiv \sqrt{2S_{ij}S_{ij}} \quad (2.39)$$

and

$$S_{ij} = \frac{1}{2} \left(\frac{\partial \bar{v}_j}{\partial x_i} + \frac{\partial \bar{v}_i}{\partial x_j} \right) \quad (2.40)$$

Effect of buoyancy, G_b , is described by the following formula:

$$G_b = \beta g_i \frac{\mu_t}{Pr_t} \frac{\partial T}{\partial x_i} \quad (2.41)$$

where β is the coefficient of thermal expansion, g_i is the component of the gravitational vector in the i -th direction, Pr_t is the turbulent Prandtl number for energy and T is the temperature. For the standard $k - \varepsilon$ model the default value of Pr_t is 0.85.

The coefficient of thermal expansion, β , is defined as:

$$\beta = -\frac{1}{\rho} \left(\frac{\partial \rho}{\partial T} \right)_p \quad (2.42)$$

Contribution of the fluctuating dilatation in compressible turbulence, Y_M , is defined as follows:

$$Y_M = 2\rho\varepsilon M_t^2 \quad (2.43)$$

where M_t is the turbulent Mach number, defined as:

$$M_t = \sqrt{\frac{k}{v_s^2}} \quad (2.44)$$

where v_s is the speed of sound.

Oxygen transfer in the volume of water in PAC is obtained from multiphase flow simulations using mixture approach. Mixture consists of two liquid non-reacting species, water and DO. Transport and mixing, and thus prediction of local mass fraction of each species, is modelled by solving conservation equation describing convection and diffusion of the species:

$$\frac{\partial}{\partial t}(\rho \cdot Y_i) + \nabla(\rho \vec{v} Y_i) = -\nabla \cdot \vec{J}_i + R_i + S_i \quad (2.45)$$

where Y_i is the mass fraction of i -th specie; \vec{J}_i is the diffusion flux of i species; R_i is net rate of production of i species due to chemical reaction; S_i is the rate of creation by addition from the dispersed phase plus any user-defined sources. Here, for non-reactive species R_i is 0.

Equation (2.45) is solved for each of the fluid phase chemical species present in the considered system. Having only two species, water and DO, and knowing that the mass fraction of all species must sum to unity, second mass fraction is determined as one minus the solved mass fraction.

Since the flow regime within the chamber is turbulent, the mass diffusion flux is computed from the following formula:

$$\vec{J}_i = -\left(\rho D_{i,m} + \frac{\mu_t}{Sc_t}\right) \nabla Y_i - D_{T,i} \frac{\nabla T}{T} \quad (2.46)$$

where Sc_t is the turbulent Schmidt number; $D_{i,m}$ is mass diffusion coefficient; $D_{T,i}$ is the thermal diffusion coefficient. In this formula, turbulent Schmidt number is:

$$Sc_t = \frac{\mu_t}{\rho D_t} \quad (2.47)$$

where μ_t is the turbulent viscosity and D_t is the turbulent diffusivity. The default Sc_t is 0.7.

The energy equation is expressed as follows:

$$\frac{\partial}{\partial t}(\rho E) + \nabla \cdot [\vec{v}(\rho E + p)] = \nabla \left[k_{eff} \nabla T - \sum_{i=1}^n h_i \cdot \vec{J}_i + (\bar{\tau}_{eff} \cdot \vec{v}) \right] + S_h \quad (2.48)$$

where E is the specific energy of a fluid, k_{eff} is the effective conductivity, h_i is the specific enthalpy for i -th specie, $\bar{\tau}_{eff}$ denotes total stress tensor (accounting for viscous heating) and S_h is any source term which accounts for heat of chemical reaction, inter-phase heat exchange and any user defined volumetric heat sources.

Here, the effects of species diffusion on energy transport are expressed as the following term:

$$\nabla \cdot \left[\sum_{i=1}^n h_i \cdot \vec{J}_i \right] \quad (2.49)$$

where h_i denotes the specific enthalpy of i -th specie.

2.3.5 Boundary and Operating Conditions

In this study, mixture of two species, water and DO was set as the working fluid. The physical properties of water, density $\rho = 998.2 \text{ kg m}^{-3}$ and dynamic viscosity $\mu = 1.003 \times 10^{-3} \text{ Pa s}$ are constant. Physical properties of DO were set as identical to those of water. The simulations consider operating pressure of 101325 Pa (1 atm) and the acceleration due to gravity is 9.81 m s^{-2} .

As the changes in density of the flow are assumed to be negligible, Boussinesq model was used to relate density as a function of temperature:

$$(\rho - \rho_0)g \approx -\rho_0\beta(T - T_0)g \quad (2.50)$$

where ρ_0 is constant density of water, T_0 is operating temperature set at 288.16 K, β denotes thermal expansion coefficient, and the term $\rho = \rho_0(1 - \beta\Delta T)$ is known as Boussinesq approximation.

Velocity inlet boundary condition was imposed on the PAC inlet. The velocity of the water phase at the inlet, in the normal direction to the boundary was set as 1.0 m s^{-1} . The turbulence at the inlet was specified by setting values of turbulent kinetic energy k equal to $1.0 \text{ m}^2 \text{ s}^{-2}$ and its dissipation rate, ε equal to $1.0 \text{ m}^2 \text{ s}^{-3}$. As only water is discharged to PAC through the inlet, therefore mass fraction of the water species at the inlet was set to 1.

It was assumed, that there is no backflow during fluid discharge from the PAC and the diffusion fluxes in the direction normal to the exit plane are zero, therefore an outflow boundary condition was imposed at the outlet.

Topwall is simulated as the interface between two phases: water and gaseous oxygen, thus zero specific shear was set on the wall boundary. As the oxygen concentration at the wall was set as 20 mg L^{-1} , corresponding to the saturation concentration for 0.5 bar, and a mass fraction of water of 0.99998.

No slip condition was imposed on the chamber side and bottom walls, and thus the velocity component of the working fluid at fluid-solid boundary is equal to that of the solid boundary, i.e. zero.

2.3.6 Flow Solver

Flow and pressure fields are obtained using pressure-based coupled algorithm, which solves a coupled system of equations comprising the momentum equations and the pressure-based continuity equation. The remaining equations, thus energy, turbulence and species equations are solved in a decoupled fashion using the current values of the solution variables. Gradients necessary for constructing scalar values at the cell faces, computing secondary diffusion terms and velocity derivatives are computed using Green-Gauss Cell based method. Standard scheme was enabled for pressure interpolation. Momentum, turbulence, energy and species are interpolated using *Third-Order MUSCL* (Monotone Upstream-Centered Schemes for Conservation Laws) scheme.

2.3.6.1 Solution Controls

To stabilize the convergence, Courant Number value equal 50 was set. Due to nonlinearity of the momentum and continuity equations being solved, the changes in scalar values need to be controlled. From this reason, Explicit Relaxation Factors of 0.75 for the momentum and pressure were set, and all remaining Under-Relaxation Factors were accepted with the default value of 1.0, except from the k and ε , for whose the factor is 0.8. Convergence criteria for the solutions were accepted for the scaled residuals to decrease below 10^{-6} . All flow variables were initialized with a value equal to zero and considering volume of PAC filled with pure water.

2.3.7 Numerical Simulation Set-up

The CFD simulations of PAC were initially performed at steady- state, setting the transient term of Equation (2.32) equal to zero, such that:

$$\frac{\partial}{\partial x_j}(\rho \overline{v_i v_j}) = -\frac{\partial \bar{p}}{\partial x_i} + \frac{\partial}{\partial x_j} \left[\mu \left(\frac{\partial \bar{v}_i}{\partial x_j} + \frac{\partial \bar{v}_j}{\partial x_i} - \frac{2}{3} \delta_{ij} \frac{\partial \bar{v}_l}{\partial x_l} \right) \right] + \frac{\partial}{\partial x_j}(-\rho \overline{v_i' v_j'}) \quad (2.51)$$

Converged steady-state solution with the stabilized flow patterns within the PAC was set as the initial state for the transient URANS simulations. The Equation (2.32) was discretized with *First Order Implicit* formulation. Time step size, Δt between the iterations was computed from the following:

$$\Delta t = \frac{\bar{x}}{\bar{v}} \quad (2.52)$$

where \bar{x} denotes the average finite element cell size and \bar{v} represents local average velocity. For all geometries studied, Δt considered was 0.001 s. For each time step 20 iterations were done.

2.3.8 2D Studies - Results and Discussion

The contour plots of the velocity and DO concentration, obtained from the 2D CFD simulation of the PAC, are shown in the Figure 2.2 and Figure 2.3. The values of DO concentrations in the outflow from the PAC, obtained for the various device layouts are presented in Table 2.6.

When comparing the maps of the velocity magnitude within the simulated 2D geometries, shown in the Figure 2.2 it is clear, that the generated flow patterns will affect the degree of mixing of the tanks content, what will be decisive for the effective oxygen mass transfer. For squared geometry (Figure 2.2a), velocity distribution shows a markedly horizontal segregation of the flow, thus the mixing and the mass transfer between the fluid layers will be significantly hindered. The outflow DO concentration is also low and equals 0.5 mg L^{-1} . DO mass transport improvement is noticeable for rectangular geometry, yielding in $5.4 \text{ mgO}_2 \text{ per L}$ for simple configuration (Figure 2.2b and Figure 2.3b). As the oxygen rich zone is “fixed” at the topwall, the efficient aeration will depend upon the intense intermixing of the “pure” water fluid layers with the oxygen rich layers. However, by introduction of the baffles at the topwall, local dead zones (Figure 2.2c-d), characterized by high local dissolved oxygen concentration (Figure 2.3c-d) were created. Nonetheless, as more baffles are introduced, the fluid mixing at the topwall zone is being weakened, resulting in lower outflow DO concentrations, that are 6.4 mg L^{-1} for the central baffle configuration and 5.5 mg L^{-1} for the set of baffles. Introduction of the bottom baffles, deflecting the flow patterns towards the topwall (Figure 2.2 e-f) and contributing

to the creation of the wavy path, as observed in the developed zigzag flow (Figure 2.2g), is proven to be a good solution, when comparing the values of the DO concentrations in the outflow: 6.6 mg L⁻¹ for central baffle (Figure 2.3e); 7.8 mg L⁻¹ for the set of bottom baffles (Figure 2.3f); and 8.5 mg L⁻¹ for the multi-baffled configuration (Figure 2.3g).

Considering the conclusions withdrawn from the results of the CFD simulations in 2D scheme, rectangular, rectangular with bottom baffles and multi-baffled layouts were selected for further studies implemented within the 3D models.

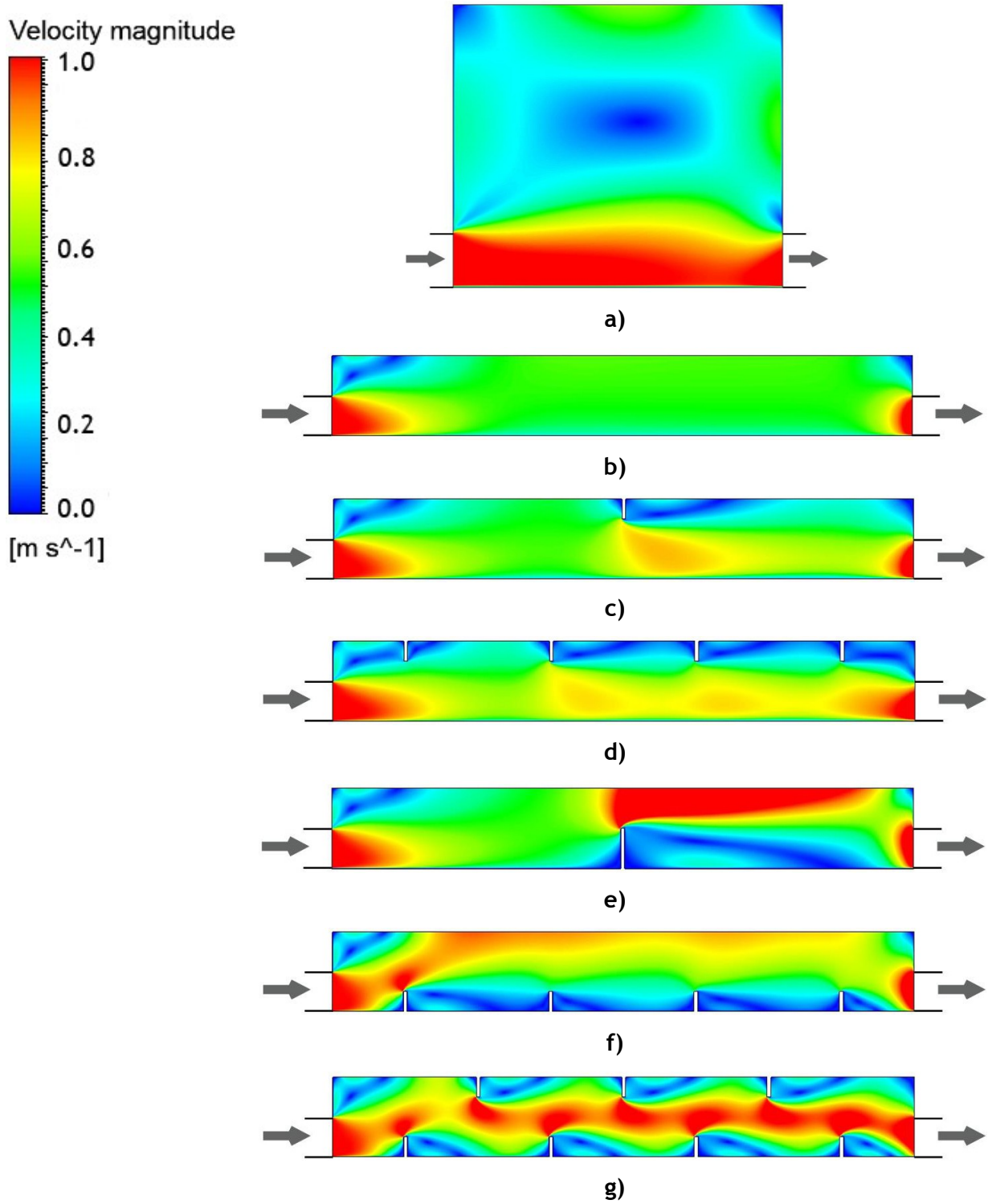


Figure 2.2 Maps of the velocity magnitude obtained for various 2D geometries of the PAC: a) squared; b) rectangular; c) with central topwall baffle; d) with topwall baffles; e) with central bottom baffle; f) with bottom baffles; g) with alternating baffles.

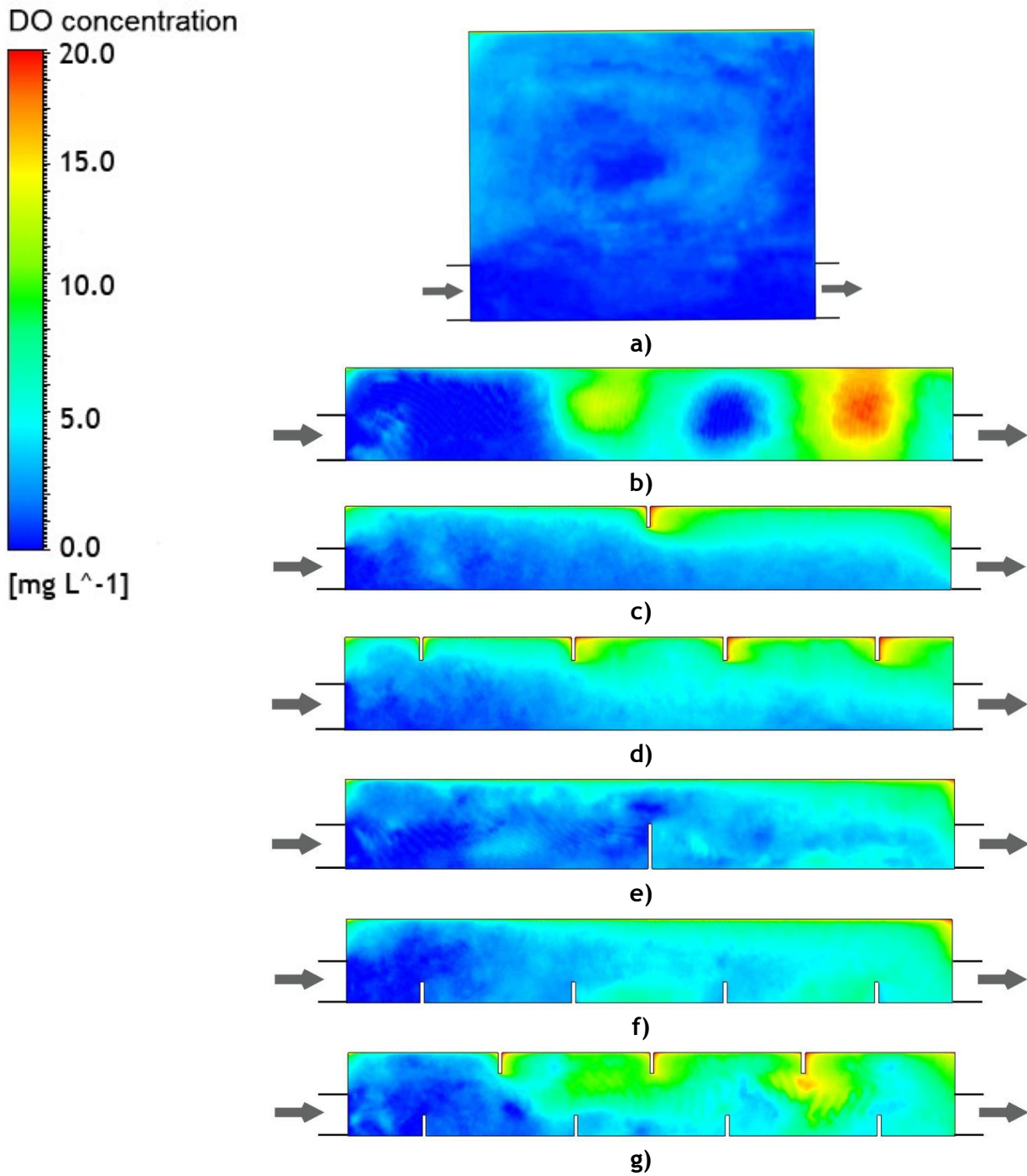


Figure 2.3 Maps of the DO concentration obtained for various 2D geometries of the PAC: a) squared; b) rectangular; c) with central topwall baffle; d) with topwall baffles; e) with central bottom baffle; f) with bottom baffles; g) with alternating baffles.

Table 2.6 Concentration of the dissolved oxygen at the outlet of the chamber obtained for various 2D PAC layouts.

PAC geometry	DO concentration (mg L ⁻¹)
Squared	0.50
Rectangular	5.36
Rectangular with central topwall baffle	6.40
Rectangular with topwall baffles	5.54
Rectangular with central bottom baffle	6.62
Rectangular with bottom baffles	7.75
Rectangular with alternating baffles	8.56

2.3.9 3D Geometry

3D PAC layouts were designed using ANSYS Gambit 2.3.16 pre-processing software. PAC was designed as rectangular chamber with the following dimensions: $0.16 \times 0.16 \times 0.70$ m. In the squared front and back wall are sets of four orifices, each with diameter 0.01 m, serving as inlets and outlets. However, in the CFD simulations we are considering only one single inlet and outlet, located near the bottom of the chamber.

Three geometry scenarios are considered: rectangular layout without baffles; rectangular layout with four bottom baffles; and rectangular layout with alternating system of baffles, three placed on the top and four on bottom. Each baffle was designed as a rectangular narrow plate and has the dimension of $0.08 \times 0.16 \times 0.002$ m. The layouts of all geometries studied are shown in Figure 2.4.

Designed PAC volumes were meshed with tetrahedral and hexahedral elements, as can be seen for the entire geometry with baffles fixed in the bottom, and in detail in Figure 2.5.

Depending on the layout, the number of generated mesh elements varies from 270 thousand for the rectangular; 320 thousand for the bottom baffled; and 500 thousand for the multi-baffled geometry. As for the 2D geometries, several preliminary scaling tests were run to test the grid adequacy for the CFD simulations.

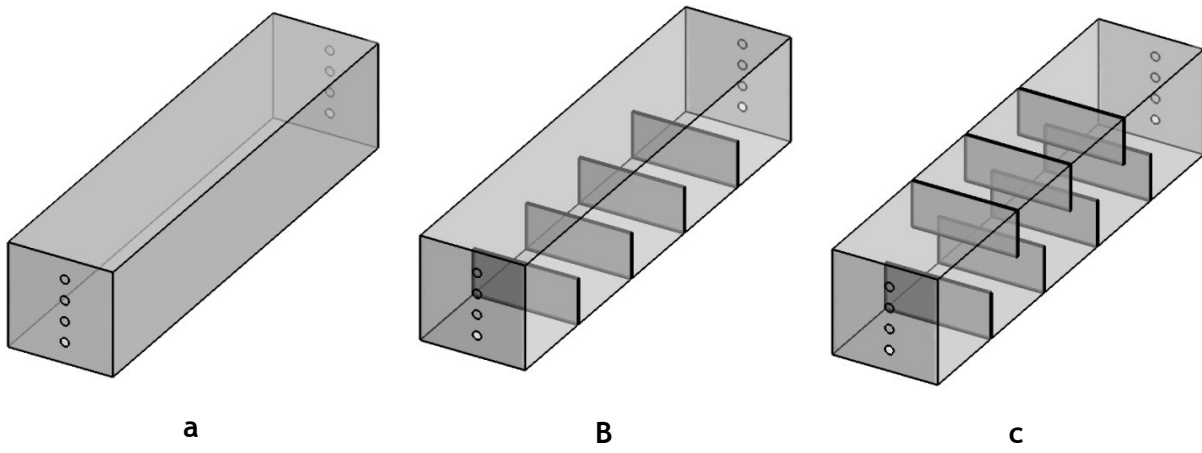


Figure 2.4 3D configurations of the PAC: a) without baffles; b) with bottom baffles; c) with alternating set of baffles.

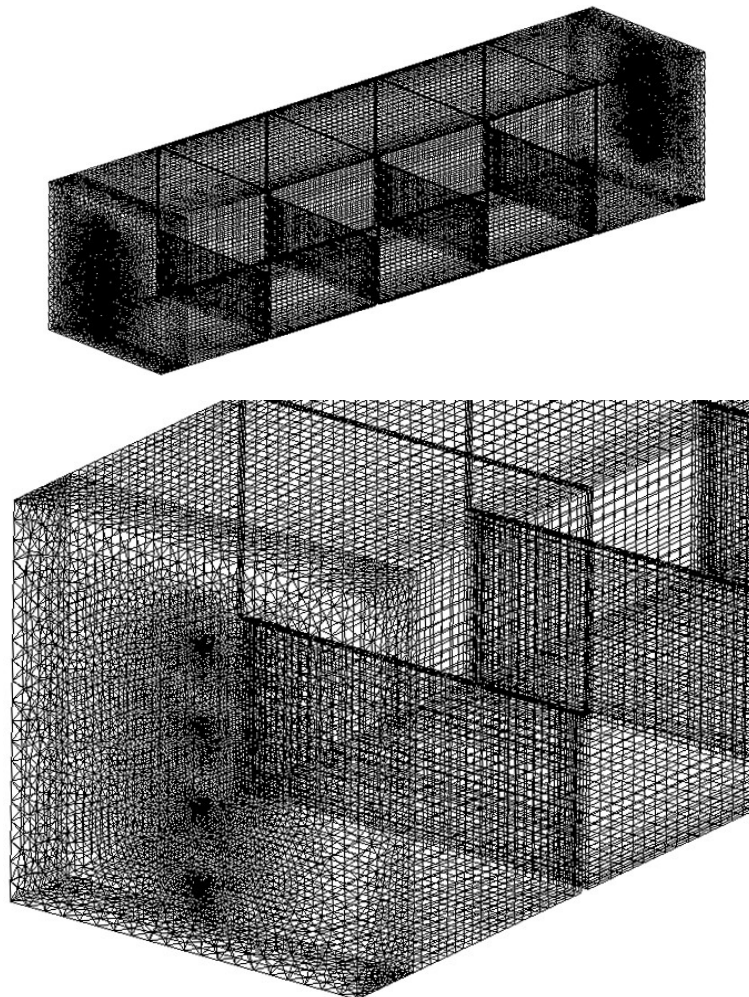


Figure 2.5 Example of surface mesh generated for the geometry with bottom baffles.

2.3.10 Governing Equations

For all considered PAC geometries, the flow field was simulated using URANS equations. Mass and continuity conservation equation, transport equations for turbulence kinetic energy, its dissipation rate and the species of water and DO were described in detail in the Section 2.3.4 of the following work.

2.3.11 Boundary and Operating Conditions

The properties of the working fluid, boundary conditions for the inlet, outlet, and the chamber walls, and operating conditions were described in detail in the Section 2.3.5 of the following work.

2.3.12 Flow Solver

Solver preferences and solution controls used in the CFD studies of PAC were described in detail in the Section 2.3.6 of the following work.

2.3.13 Numerical Simulation Set-up

The initialization of the URANS simulations was described in the Section 2.3.7 of the following work. For all simulated geometries, the Equation (2.32) was discretized with *Second Order Implicit* formulation. Time step size, Δt between the iterations, computed from the Equation (2.52) was 0.001 s.

2.3.14 3D CFD Studies - Results and Discussion

The contour plots of the velocity and DO concentration, obtained from the 3D CFD simulation of the PAC, are shown in the Figure 2.6 and Figure 2.7.

The values of the DO concentrations in the outflow from the PAC, obtained for the various device layouts are shown in Table 2.7. Similar to the results obtained from the CFD simulations performed in the 2D scheme, when comparing the contour maps of the velocity magnitude in the cross-sections through the simulated layouts (Figure 2.6), the effects of the geometry on the generated flow patterns and the degree of mixing of the PAC content is clearly seen.

For the regular rectangular layout (Figure 2.6a), velocity distribution characterizes formation of the high velocity horizontal plume from the inlet, deflected slightly towards the topwall. Poor mixing throughout the PAC volume results in oxygen-rich layer build-up just below the topwall boundary, as can be seen in the Figure 2.7a. Nonetheless, the outflow DO concentration is 12.6 mg L^{-1} , that is more than double value obtained from the

2D simulations. Introduction of the flow perturbation as baffles results in mixing improvement yielding higher DO outflow concentrations. From the velocity map obtained for the bottom baffled PAC configuration (Figure 2.6b) it is clear, that the large velocity gradients are generated due to the collision of the inflow plume with the first baffle. As a result, the flow patterns are directed to the topwall for enhanced saturation with DO, as can be seen in the Figure 2.7b, where the oxygen-rich zone spread in the last PAC compartments (separated with baffles), occupying almost 30% of the total volume. The improvement in the DO concentration in the discharge from PAC is also noticeable, as it reaches nearly 18 mg L^{-1} , also more than double of the concentration value obtained in the corresponding 2D CFD approach.

Presence of the velocity gradients in the first “compartment” of the PAC, and sinuous flow patterns generated on the alternating baffles (Figure 2.6c) promotes mixing, and thus dispersion of the oxygen-rich water. Expansion of the oxygen-enriched zone to around 70% of the PAC volume is also noticeable (Figure 2.7c). Further slight improvement was observed for multi-baffled geometry, yielding 18.2 mgO_2 per L in the discharged flow.

Table 2.7 Concentration of the dissolved oxygen at the outlet of the chamber obtained for various 3D PAC layouts.

PAC geometry	DO concentration (mg L^{-1})
Rectangular	12.56
Rectangular with bottom baffles	17.75
Rectangular with alternating baffles	18.21

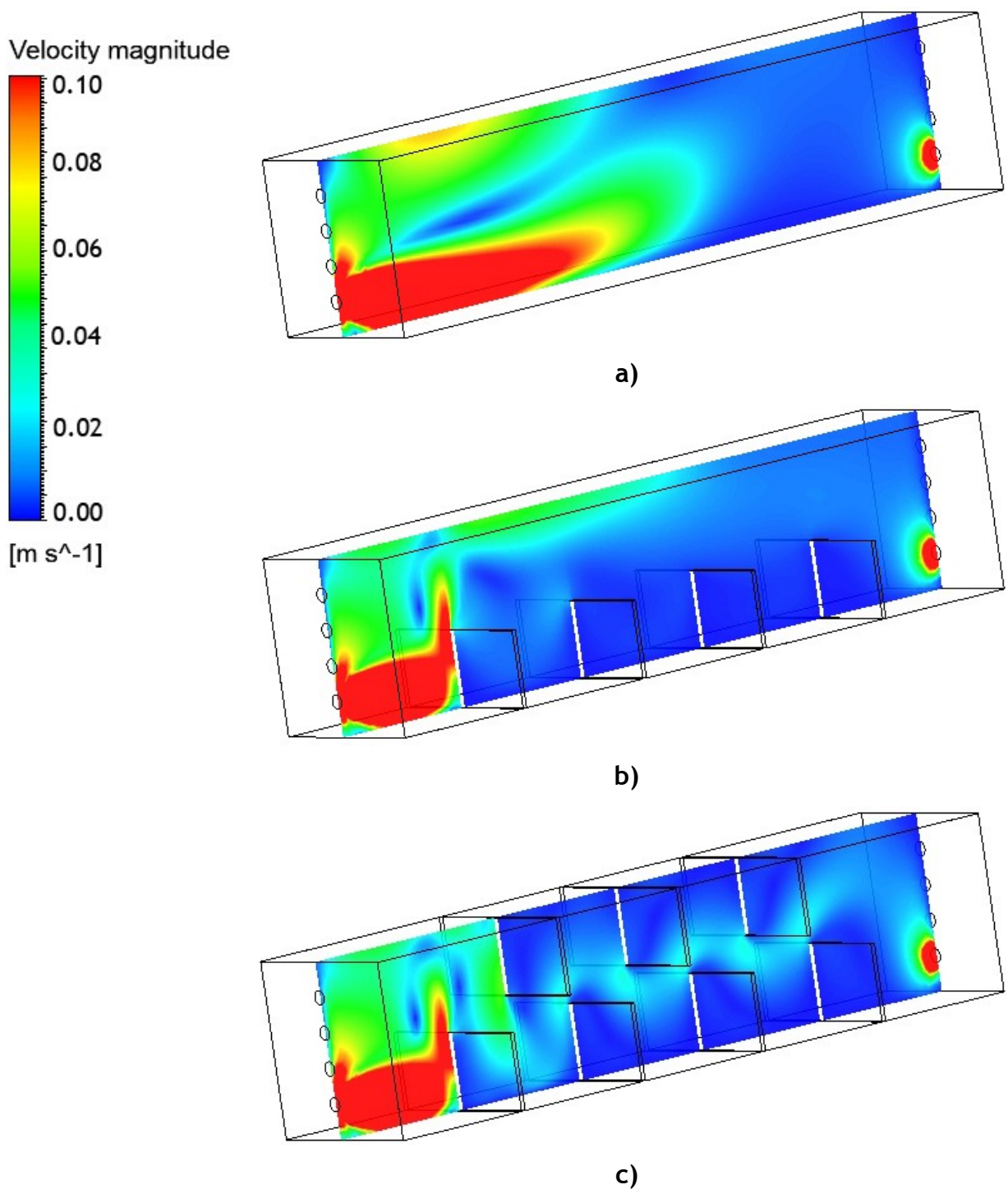
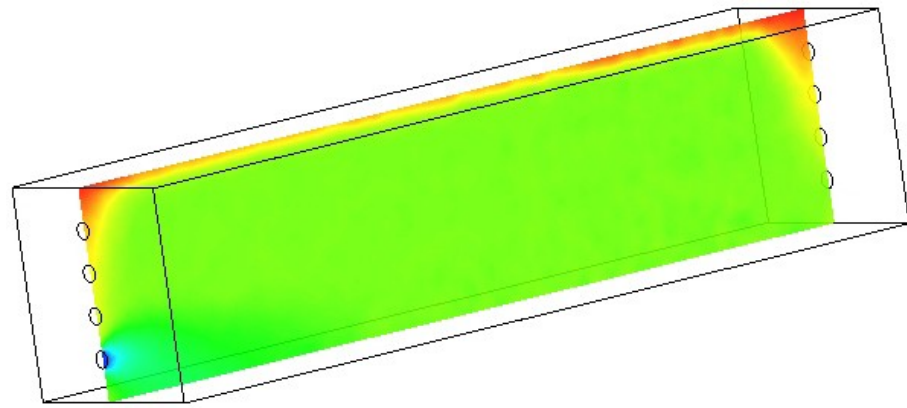
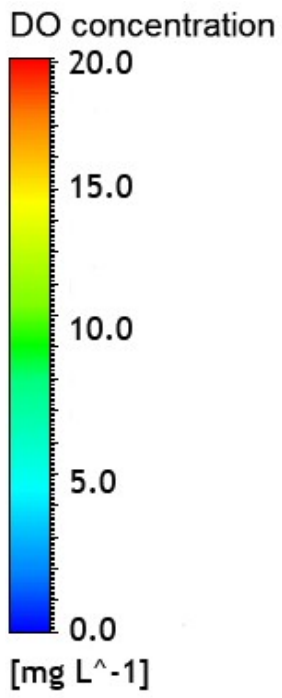
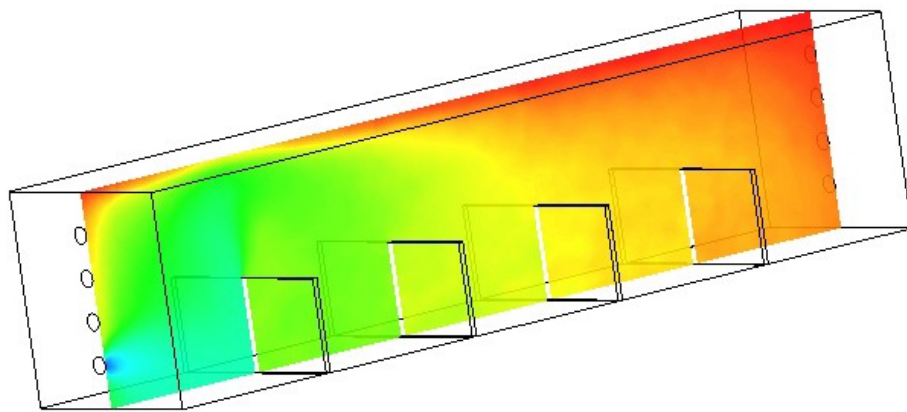


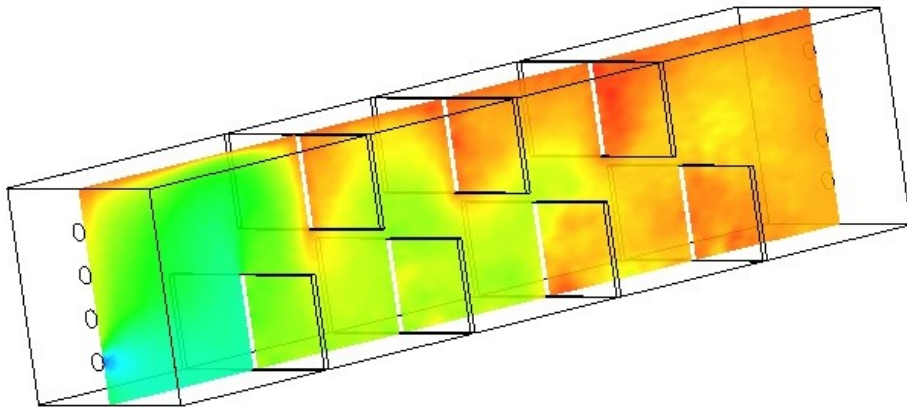
Figure 2.6 Maps of the velocity magnitude obtained for various 3D geometries of the PAC: a) without baffles; b) with bottom baffles; c) with alternating baffles.



a)



b)



c)

Figure 2.7 Maps of the DO concentration obtained for various 3D geometries of the PAC: a) without baffles; b) with bottom baffles; c) with alternating baffles.

2.4 Pressurized Aeration Chamber - Experimental Studies

In this section the pilot PAC unit and experimental setup are described. Experimental procedure of steady and unsteady clean water test for Oxygen Transfer Rate determination is given. Aeration performance of the device is evaluated on the base of the results obtained from the several experiments. Finally, process parameters, describing PAC performance expressed as oxygen mass transfer and energy efficiency are compared with the conventional aeration techniques and the results from the CFD simulations of PAC in 3D scheme.

2.4.1 Aerator Design

A PAC unit was built for experimental validation. The pilot PAC is continuous flow reactor, designed as a transparent horizontal, rectangular tank with dimensions $0.16 \times 0.16 \times 0.70$ m (Figure 2.8).

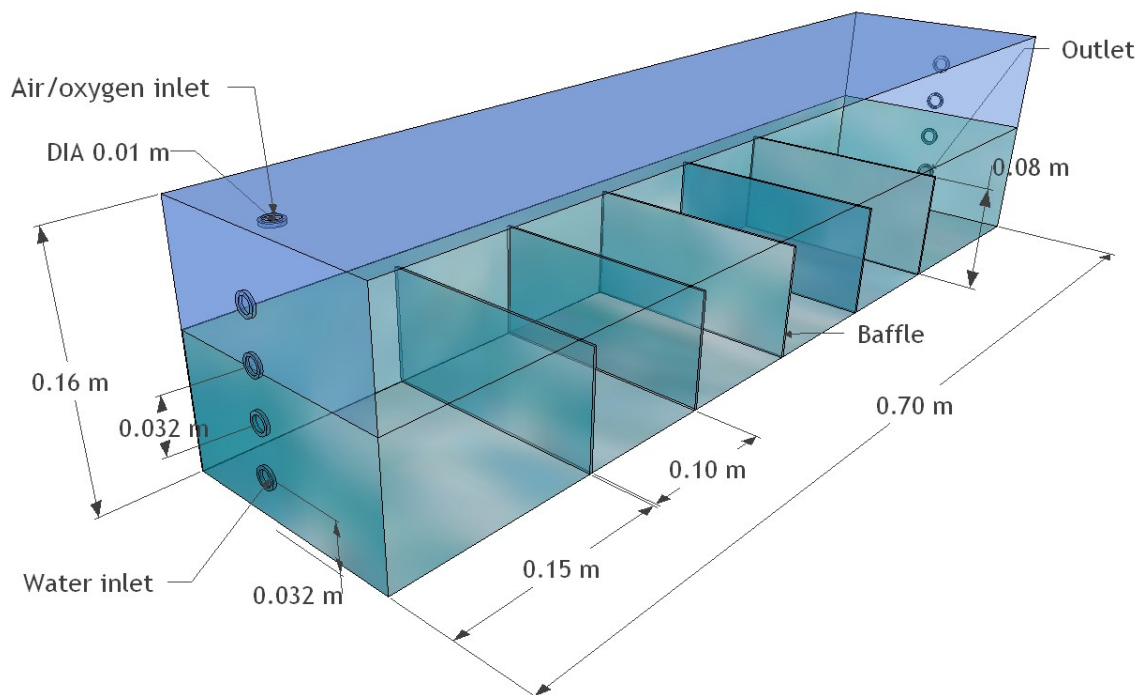
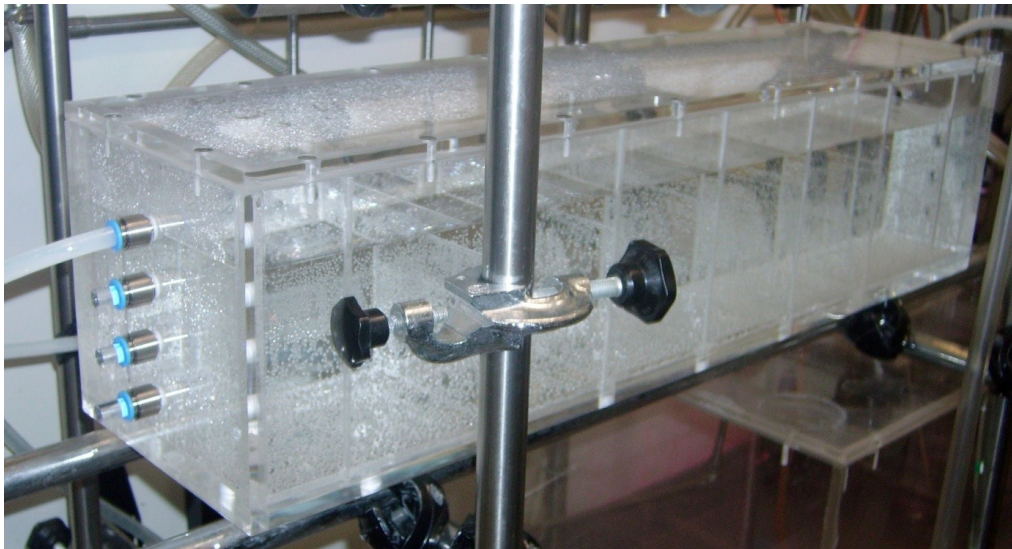


Figure 2.8 Pressurized Aeration Chamber (PAC) scheme.

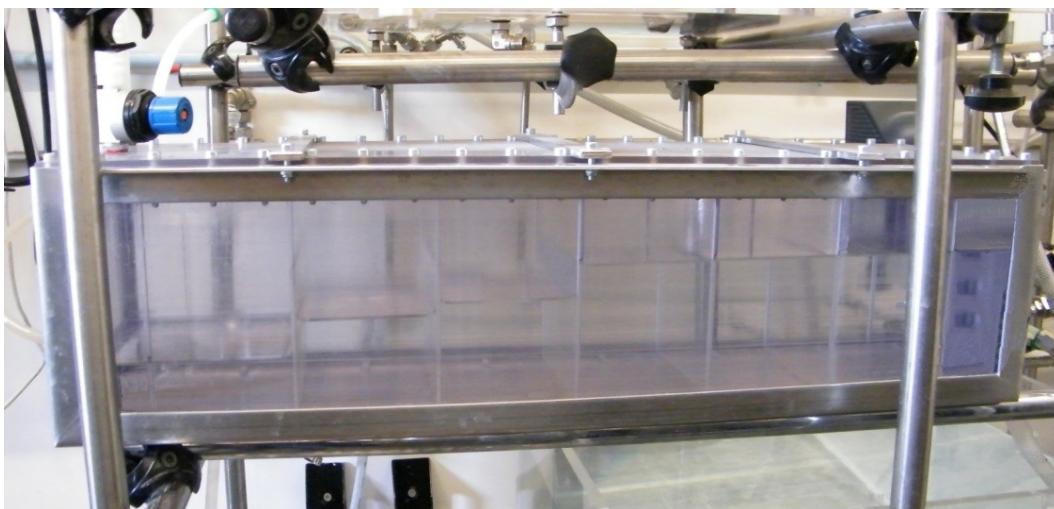
Due to the high pressure conditions in which the PAC will be operated, the tank was made of polycarbonate and equipped with pressure relief safety valve. The walls of the tank were glued and bolted to each other. The whole structure of the tank was additionally reinforced by fixing an outer steel casing (Figure 2.9). The tank is equipped with five acrylic removable baffles, placed at the bottom of the tank at intervals of 0.1 m from each other. Each baffle has the dimensions 0.16×0.08 m. The evenly spaced orifices in the front

2 Aeration Technologies

and the rear wall each of 3/8" and the single one of the same diameter in the top wall, were fitted with quick fitting connectors to be integrated with the tubing system as the water-air/oxygen ports. During the experiments, water is supplied through the inlet orifice located in the front wall of the tank. Air or oxygen is delivered through the inlet located on the top wall and the aerated water is discharged through the outlet port located in the rear wall. While the single pair of water and gas inlet and outlet ports are in operation, the remaining are tightly blocked with acrylic plugs.



a)



b)

Figure 2.9 Pressurized Aeration Chamber (PAC): a) without, and b) with outer steel casing.

2.4.2 Experimental Setup and Flow Loop

The standard procedure of oxygen transfer measurement considers aerator placed in the water tank, to resemble field conditions as close as possible. Application of PAC as the external aeration unit operating in the continuous flow mode was taken into account while designing the experimental setup. Scheme of the experimental setup and the flow loop are presented in Figure 2.10. Test water was stored in transparent, acrylic reservoir of capacity of 135 dm³ (1), equipped with mechanical overhead stirrer (Heidolph, model RZR 2021) and with vertical shaft crossed-blade impeller (2). Strictly defined standards of clean water quality in the reservoir during oxygen transfer experiments require constant monitoring, therefore DO concentration, electrical conductivity (EC) and temperature were continuously controlled with portable dual channel multi meter (3) (Hach Lange HQ40D) equipped with digital smart sensors (4): luminescent DO probe (IntelliCAL™ LDO10103) and conductivity probe (IntelliCAL™ CDC40103). The precision of the equipment is: 0.01 μS cm⁻¹ for conductivity probe; 0.01 mg L⁻¹ O₂ or 0.1% of DO saturation for oxygen probe; and 0.3 °C for temperature. Water from the reservoir is pumped to the PAC using positive displacement gear micropump (5) with magnetically coupled drive (Pacific Scientific, model 220/560C) with an external rpm speed controller. Test water is delivered to the PAC (6) through the inlet placed in the front wall of the PAC. The flow rate through the PAC is measured and controlled by variable area correlated flowmeter (7) (Gilmont Accucal, model GF 1660). The accuracy of the measurement can be estimated as ± 2% of reading or ± 1 of scale division. In-house compressed pure oxygen delivered from the external manifold is regulated by means of two pressure regulators (8) connected in series. The first pressure regulator, operates in the range 0.5 - 8 bar, and is integrated with the pure oxygen wall Point of Use (Air Liquide, PdG-8) with built-in diaphragm shut-off valve. Second reducer (Pneumax, model FIMET) equipped with air filter provides regulation of oxygen pressure from 0 to 4 bar. Oxygen is supplied to the PAC through the gas inlet, located in the top wall. The effluent stream of aerated water is discharged through the outlet in the back wall of the PAC to the pipeline. Pressure drop on the PAC is measured by means of differential pressure transducer (9) (Validyne, Type P0305D), inserted between inflow (10) and outflow tubes (11). DO concentration in the influent and effluent from the reactor are controlled continuously with a stand-alone measurement system, which consists of a standard controller display module (12) (Hach Lange sc100) and luminescent DO probes module (Hach Lange, LDO probe). The sensitivity of the probes is 0.01 mg L⁻¹ DO or 0.1% DO saturation. The probes are placed in a specially manufactured PVC flow cell adapters integrated with the PAC influent (13) and effluent tubing (14). Depending on the experiment type (steady or unsteady), the aeration test is conducted in an open or closed-

loop flow system. Easy switch between the flow schemes was made possible by mounting the 3/2 way directional valve (Whitey) on a pump feed pipeline (15). Water and oxygen pipeline system used in the experimental installation consist of 3/8" polyurethane and stainless steel tubing (Swagelok) and all necessary fittings: tube adapters, quick connect fittings, elbows, tees and regulation valves.

The measurements from the pressure transducer and LDO sensors are converted into digital data by Data Acquisition (DAQ) device (16) (National Instruments, NI SCC-68). Dell® Optiplex 755 PC (17) with a dual core Intel® Core™ 2 Duo CPU at 2.66 GHz and 2.33 GB of RAM controls the operation of the DAQ device and is used for processing and storing measurement data through an application made with LabVIEW (version 8.2).

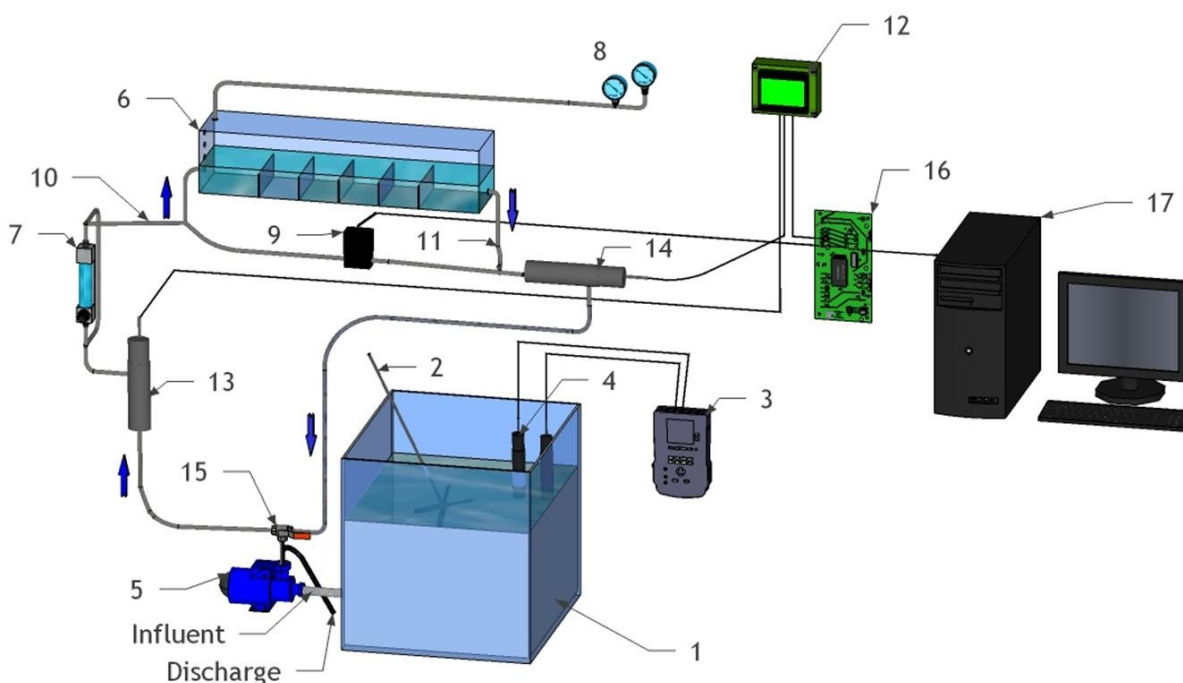


Figure 2.10 Experimental set-up and the flow loop: 1- reservoir; 2- stirrer; 3- multi meter; 4- probe; 5- pump; 6- PAC; 7- flowmeter; 8- pressure regulator; 9- pressure transducer; 10, 11- tubing; 12- DO controller; 13, 14- flow cell adapter; 15- valve; 16- acquisition board; 17- PC.

2.4.3 Clean Water Test

The test tank was filled with 125 L of clean tap water, where DO concentration, temperature and EC are constantly monitored. The temperature of the water was kept constant and as close to the standard conditions (20 °C) as possible, occasionally, by adding ice into the volume of water and additionally by controlling the room temperature with the air conditioner. For each experiment the salinity of the raw tap water and tap water after adding deoxygenation salts was determined through the EC measurement.

The average conductivity of clean tap water was of around $350\text{-}370\ \mu\text{S cm}^{-1}$, which corresponds to $224\text{-}237\ \text{mg L}^{-1}$ TDS, and after addition of deoxygenating salts increases to

460-500 $\mu\text{S cm}^{-1}$ equivalent to 294-320 mg L^{-1} TDS, therefore the effect of salinity on the oxygen solubility was not considered.

Deoxygenation chemicals used in the experiments are anhydrous sodium sulphite, Na_2SO_3 (Sigma Aldrich, ACS reagent grade, $\geq 98\%$ assay) and crystalline cobalt (II) chloride hexahydrate, $\text{CoCl}_2 \cdot 6\text{H}_2\text{O}$ (Sigma Aldrich, ACS reagent grade, $\geq 98\%$ assay). It was assumed, that the dose of sodium sulphite added to the clean water should be sufficient to depress uniformly DO concentration in the whole volume of the reservoir and to maintain DO level below 0.5 mg L^{-1} for at least half an hour. Na_2SO_3 dose was determined from theoretical demand for deoxygenation, which is 7.88 mg L^{-1} Na_2SO_3 per 1.0 mg L^{-1} DO increased by 25% of stoichiometric excess, as recommended in the Standard (ASCE, 1991, 2007). The solution was prepared in separate glass jar, by dissolving appropriate amount of sodium sulphite in tap water. The solution was homogenized by placing the jar on the magnetic stirrer (VWR, model VMS-C4) and mixing the content with intensity of 150 rpm approximately during 20 minutes. After this time, the solution was immediately added to the tank and uniformly distributed within water volume due to mixing action of the overhead stirrer.

At the same time the catalyst solution was prepared by pouring into the beaker a small amount of clean water and dissolving a proper amount of $\text{CoCl}_2 \cdot 6\text{H}_2\text{O}$. Theoretical $\text{CoCl}_2 \cdot 6\text{H}_2\text{O}$ dose was determined in accordance with the Standard guidelines, to ensure soluble cobalt concentration in the test water of 0.2 mg L^{-1} . The catalyst solution was added to the test water tank prior to the beginning of the test and was let to be homogenized with the tank volume for a long enough period.

When the oxygen in the water tank achieves steady close-to-zero DO concentration, the feed pump is turned on to fill the PAC and the tubing system with deoxygenated water during next couple of minutes. During this time, pressure transducer was cleansed to avoid errors in measurement, by unscrewing bleed ports to release trapped gas, clean the diaphragm and fill the pressure cavities with test water. Usually 5 to 10 minutes time is sufficient to obtain steady readings from both LDO probes, pressure transducer and to stabilize hydraulic conditions within the whole aeration system. Once the system is steady, the proper oxygen transfer test was initiated: the LabVIEW application for DO and pressure drop data recording with the time interval of 0.1 s was run and the oxygen supply shut-off valve was immediately opened.

Characterization of PAC as the aeration unit was performed using steady and unsteady-state experiments. Steady-state clean water test is performed in the open fluid flow system. During experiment, PAC is continuously supplied with deoxygenated water from the tank and the effluent from the outflow DO flow cell is directed to the drainage

collector. The reaeration test is considered completed, once the DO effluent concentration reached a steady-state value, maintained for at least 10 minutes.

Unsteady-state experiments were performed in closed-loop fluid flow system. Once the system reaches steady-state prior to switching on the oxygen supply, the directional valve position is manually changed and the effluent from the outflow DO flow cell is recirculated to the inlet of the PAC. The reaeration stage is considered completed, once DO concentration reaches a steady-state value, maintained for at least 10 minutes.

2.4.4 Experimental Flow and Pressure Ranges

The experiments were carried out with a water flow rate which ensures the constant level of water in the PAC, equivalent to approximately 49% of the chamber volume, with the remaining 51% to be filled with oxygen. The level of water was kept 5 mm above the baffles, with the spillway overflow after the last baffle. The thickness of the water behind the spillway is over 2 cm above the outlet port, as seen in the picture (Figure 2.11). Controlling the level of water in PAC, especially in the last compartment, minimised the risk of the exposure of the outlet to pure oxygen, what could overestimate significantly LDO sensor reading. Thus, for the supplied oxygen pressure of 0.5, 1.0 and 1.5 bar, the corresponding water flow rates, Q_w , were: $5.90 \cdot 10^{-5}$, $5.32 \cdot 10^{-5}$ and $4.73 \cdot 10^{-5} \text{ m}^3 \text{ s}^{-1}$.

To determine Oxygen Transfer Rate and aeration process parameters ($K_L a$, $SOTR$, $SOTE$ and SAE) clean water test was performed in steady and unsteady schemes for each pairs of water flow rate- oxygen pressure. For each test, the standard value of oxygen saturation concentration, C_s , was determined on the base of the actual measurement of electrical conductivity, (EC), and temperature, (T) (Tchobanoglous et al., 2003) of the test water in the reservoir. For the test conditions, the equilibrium concentration of oxygen C_{S,O_2} was calculated from the Henry's law described by Equation (2.5). For the oxygen in water, at the standard conditions of temperature (293-298 K), the Henry's constant is: $H = 1.3 \cdot 10^{-3} \text{ mol L}^{-1} \text{ atm}^{-1}$. The values of equilibrium concentrations of oxygen under operating gas pressures are presented in Table 2.8. Inlet (C_0), outlet (C_t) PAC DO concentration and pressure drop (Δp), were continuously monitored and recorded with a time interval of 0.1 s.

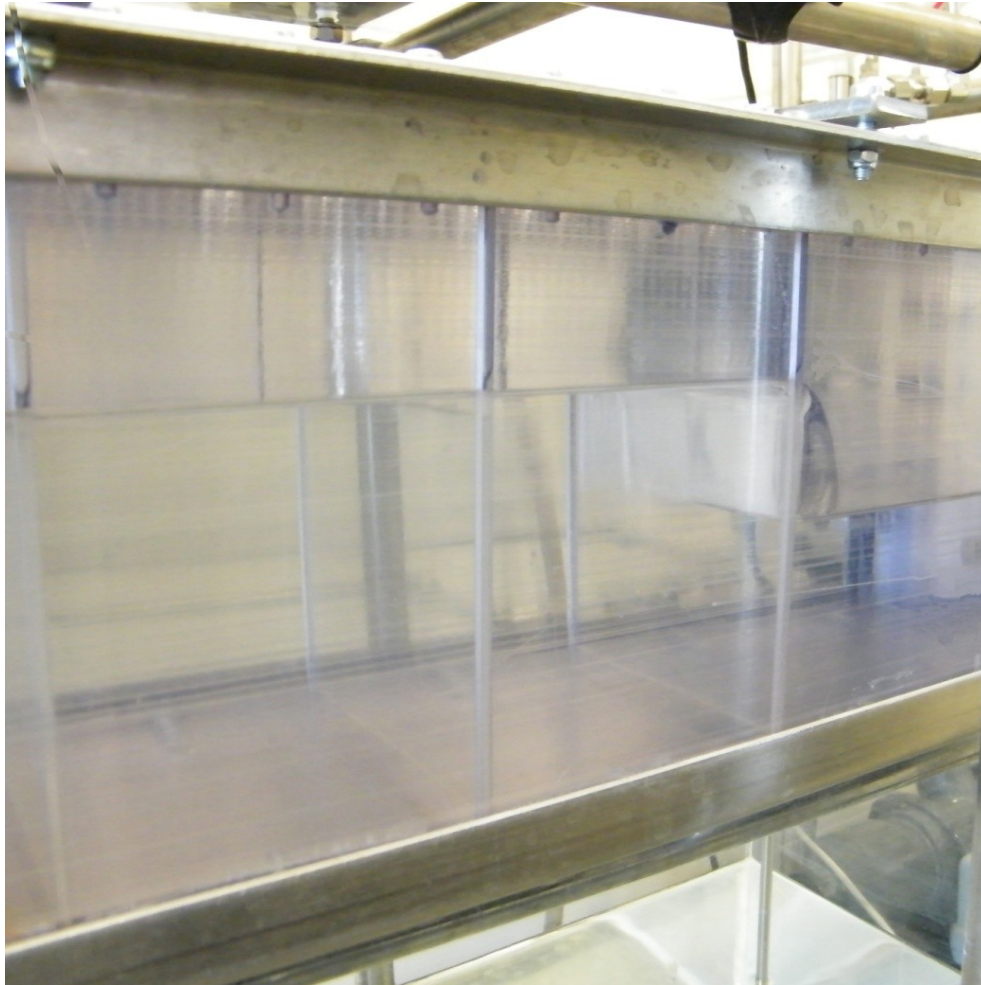


Figure 2.11 Flow conditions within PAC.

Table 2.8 Oxygen concentration in equilibrium for various values of operating pressure.

p_{O_2}		C_{s,O_2}
(bar)	(atm)	(mg L ⁻¹)
0.5	0.49	20.8
1.0	0.99	41.6
1.5	1.48	62.4

2.4.5 Determination of the Process Parameters

In steady-state approach, to determine the $K_L a$ values using Equation (2.17), the water volume and the oxygen flux must be computed. Considering the constant level of water in the chamber, the active volume of the PAC is $9.0 \cdot 10^{-3} \text{ m}^3$. The mass flux of oxygen is:

$$\dot{m} = (C_t - C_0) \cdot Q_w \quad (2.53)$$

where \dot{m} denotes mass flow rate of oxygen, kg s^{-1} .

Thus, the Equation (2.17) can be rewritten, as:

$$\frac{(C_t - C_0) \cdot Q_w}{V} = K_L a (C_S - C_t)$$

After rearrangement, we obtain:

$$K_L a = \frac{(C_t - C_0) \cdot Q_w}{(C_S - C_t) \cdot V} = \frac{1}{\tau} \cdot \frac{(C_t - C_0)}{(C_S - C_t)} \quad (2.54)$$

where τ is the residence time of the fluid in PAC.

In unsteady- state approach, $K_L a$ values were determined using log-deficit method. The DO measurements made by high-sensitivity digital LDO probes are recorded continuously in short time intervals of 0.1 s, moreover, tendency of logarithms of the measured values is almost linear, minimizing the possibility of occurrence of the transformation errors. Determined $K_L a$ values correspond to the slope of the best fit line, representing gradient of the DO concentration over time, as shown in Figure 2.12.

The remaining parameters were determined identically for both, steady and unsteady reaeration tests. The standardized mass transfer coefficient $K_L a_{20}$ was computed from the formula described by Equation (2.20), which after rearrangement has the form:

$$K_L a_{20} = \frac{K_L a_T}{\theta^{T-20}}$$

The Oxygen Transfer Rate in test and standard conditions was computed using Equations (2.23) and (2.24). To assess values of AE and SAE described by Equations (2.25) and (2.26), power withdrawal by whole aeration system, i.e. by water and oxygen system must be computed.

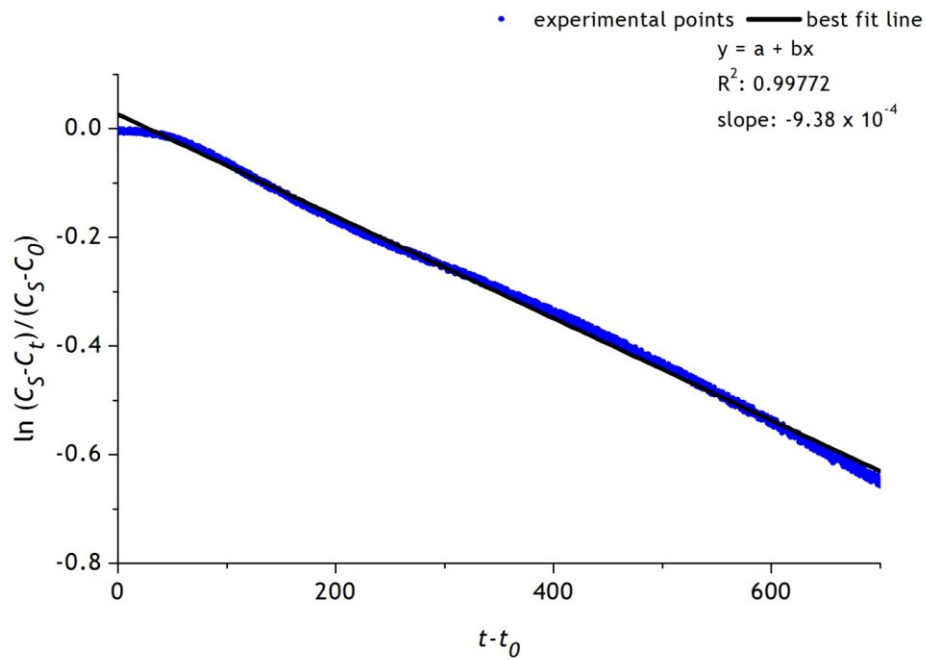


Figure 2.12 Example of the determination of oxygen mass transfer coefficient ($K_L a$) using data obtained in steady-state clean water test.

In incompressible fluid flow systems, power demand to pump water P_w is determined by the flow rate and the total head:

$$P_w = \rho g H_p Q_w \quad (2.55)$$

where P_w denotes power expenditure on pump action, in W, ρ is water density in kg m^{-3} , g is gravitational acceleration of 9.81 m s^{-2} and H_p is total pressure head in m and Q_w is water flow rate in $\text{m}^3 \text{ s}^{-1}$.

For PAC the Equation (2.55) can be written as:

$$P_w = \Delta p \cdot Q_w \quad (2.56)$$

where Δp is the pressure drop of the water, Pa.

The values of Δp measured during each experiment and recorded in the intervals of 0.1 s account for the local head loss at the entrance and discharge from the PAC. The final Δp value used in the computation is the average from the all measurement data registered during experiment.

For pure oxygen systems, power demand for oxygen generation in Vacuum Pressure Swing Adsorption (VPSA) process must be accounted. PAC is supplied with oxygen of standard purity: 93%. Considering technical data sheet of the commercial VPSA oxygen generators,

2 Aeration Technologies

typical power demand is 0.35 kWh per Nm³ of oxygen produced (Ratanayaka et al., 2009). Typical process outflow oxygen pressures and power requirements are listed in the Table 2.9. The typical outflow pressures for oxygen produced in the VPSA are low, thus when higher pressure is required, energy efficient oxygen compressor built-in the unit is considered.

Table 2.9 Summary of typical operating parameters of the commercial VPSA systems.

VPSA Manufacturer	Power demand (kWh/Nm ³)	Output oxygen pressure (bar)
Ally Hi-Tech Co	0.36-0.42	100 - 250
AIRMAX	0.36-0.42	0.2 - 0.4
Adsorptech EcoGen™	0.35	0.3 - 2.0
Adsorptech ModGen™	0.34	0 - 10
MVS Engineering	0.4	0 - 1.3
Pioneer	0.32-0.37	0 - 5
Radox Gases	0.35	1.3 - 50
Sam Gas	0.35-0.52	2.0 - 150
Sumitomo Seika Chemicals	0.34	0.5 - 1.0
Universal	0.35	0 - 5.0

To express power demand per volume of oxygen in standard pressure and temperature conditions of the clean water test, the Combined Gas Law must be applied:

$$V_{O_2,N} = \frac{p_{O_2} \cdot V_{O_2} \cdot T_{O_2,N}}{p_{O_2,N} \cdot T_{O_2}} \quad (2.57)$$

where $V_{O_2,N}$ is the normalized volume of 1 m³ of oxygen at the reference gas temperature $T_{O_2,N}$ of 273.16 K and the normalized pressure $p_{O_2,N}$ of 101325 Pa, V_{O_2} denotes the actual volume of oxygen in m³, T_{O_2} and p_{O_2} are the actual oxygen temperature and pressure, respectively.

For each test, actual oxygen density was determined using the Ideal Gas Law equation as follows:

$$\rho_{O_2} = \frac{p_{O_2} M}{RT_{O_2}} \quad (2.58)$$

where M is the molar mass of oxygen and amounts 32 g mol^{-1} , R is the universal gas constant equal to $8.314 \text{ J K}^{-1} \text{ mol}^{-1}$. The actual volume of oxygen is computed from the oxygen flow rate, Q_{O_2} ($\text{m}^3 \text{ h}$), which equals:

$$Q_{O_2} = \frac{Q_w(C_t - C_0)}{\rho_{O_2}} \quad (2.59)$$

Assuming, that the power demand for oxygen production in VPSA is 350 W per Nm^3 , and the pressure of generated oxygen is higher than 1.5 bar , power demand related to the whole oxygen system during clean water testing can be determined as follows:

$$P_{O_2} = 350 \cdot V_{O_2,N} \quad (2.60)$$

OTE and $SOTE$ for PAC are calculated from the Equations (2.29) and (2.30), where the oxygen supply mass flow rate, w_{O_2} , is computed from the following:

$$w_{O_2} = \rho_{O_2,N} \cdot Q_{O_2} \quad (2.61)$$

where $\rho_{O_2,N}$ denotes normalized density of gas (pure oxygen), which at the temperature of $0 \text{ }^\circ\text{C}$ is 1.429 kg m^{-3} .

Considering air purity of 93% , and the oxygen flow rate expressed by Equation (2.59) the formula can be written as:

$$w_{O_2} = 0.93 \cdot \rho_{O_2,N} \cdot \frac{Q_w(C_t - C_0)}{\rho_{O_2}} \quad (2.62)$$

Therefore the Equations (2.29) and (2.30) can be written, as follows:

$$OTE = \frac{OTR \cdot \rho_{O_2}}{0.93 \cdot \rho_{O_2,N} \cdot Q_w \cdot (C_t - C_0)} \quad (2.63)$$

and assuming that $C_t = C_{S20}$

$$SOTE = \frac{SOTR \cdot \rho_{O_2}}{0.93 \cdot \rho_{O_2,N} \cdot Q_w \cdot (C_{S20} - C_0)} \quad (2.64)$$

2.4.6 Results and Discussion

2.4.6.1 Steady- State Experiments

The average values of the process parameters obtained from the multiple steady- state experiments are shown in the Table 2.10. When the pressure of oxygen increases from 0.5 to 1.5 bar on the water surface in the PAC, an increase of 2.0 mg L⁻¹ in the steady- state DO concentration per every 0.5 bar was observed. This linear trend can be seen in Figure 2.13. At the same time, with the increase of the steady-state DO concentration, distinct decrease of $K_L a$ occurs, what may be explained when interpreting the Equation (2.54) applied for the $K_L a$ parameter estimation. Thus, for the increasing operating oxygen pressure, the difference between the oxygen saturation and the steady-state concentration, expressed by the term $C_S - C_t$ is much higher than the term $C_t - C_0$, what for almost identical τ yields lowering values of $K_L a$. With the accordance to the above statement it can be said, that under steady-state, the higher is the concentration of oxygen maintained in the tank, the lower is the transfer rate. The values of $K_L a$ obtained from the test nearly overlap with the values computed for the standard conditions, $K_L a_{20}$ (Equation (2.20)), as can be seen in the Figure 2.14.

As the oxygen transfer rate, OTR , is a function of the oxygen mass transfer coefficient, therefore identical decreasing tendency in values was observed. For the oxygen pressure of 0.5 bar the OTR is over 3.0 gO₂ h⁻¹ and decreases to around 1.0 gO₂ h⁻¹ for the oxygen supplied under pressure of 1.5 bar. The standardized values are distinctly higher than those computed for the test conditions, as they range from 6.0 to 4.0 gO₂ h⁻¹, as can be seen in the Figure 2.15.

Similar tendency is seen for the oxygen transfer efficiency OTE (Figure 2.16) calculated from the Equation (2.63), a parameter used in evaluations of the diffused air units in terms of the percentage of the oxygen absorbed, however the values obtained for different oxygen pressures vary within 16%. Thus, for the oxygen pressure of 0.5 bar, the average value of OTE is 66%, while for 1.0 and 1.5 bar decreases to around 50%. Contrary to that, at the standard temperature conditions, $SOTE$, computed from the Equation (2.64), increases due to the level of water saturation with oxygen, thus with increase of the pressure of oxygen delivered to PAC. The lowest value of $SOTE$ close to 120% was

determined for the oxygen pressure of 0.5 bar, which is higher than the corresponding values of currently most efficient aeration systems, i.e. membrane diffusers, having the efficiencies up to 44%. For the oxygen pressure of 1.0 bar *SOTE* is almost 150% and for 1.5 bar - 200%.

The aeration efficiency *AE* is the function of *OTR* and the power demand for water pumping and oxygenation, as can be deduced from the Equations (2.25) and (2.26). In PAC system, power expenditure for water pumping is low, due to the low operating flow rates and low average pressure drop on the chamber of the range 20 to 24 cm H₂O, corresponding to 2.0 to 2.4 kPa (Table 2.10). Therefore in PAC aeration, the most energy-intensive step is oxygen generation in VPSA process combined with increase of the operating pressure. This tendency can be seen in the Figure 2.17. Thus, more energy efficient solutions were obtained for the operating pressure of 0.5 bar, accounting in average for 4.5 kgO₂ kW⁻¹ h⁻¹ in test conditions, what gives nearly 8 kgO₂ kW⁻¹ h⁻¹ after conversion into standard conditions. These values are distinctly higher than for most conventional mechanical and diffused aeration systems, except from the group of perforated membrane disc diffusers, having also the efficiency of 7.9 kgO₂ kW⁻¹ h⁻¹ (Mueller et al., 2002). Average aeration efficiencies of 5.1 kgO₂ kW⁻¹ h⁻¹ obtained from the experiments conducted with the oxygen pressure of 1.0 bar are comparable with the efficiencies of perforated EPDM membrane tubes, panels and ceramic discs or domes (Mueller et al., 2002). The lowest average *SAE* of 4.7 kgO₂ kW⁻¹ h⁻¹, obtained for the oxygen pressure of 1.5 bar corresponds to the efficiencies reported for rigid porous plastic tubes (Mueller et al., 2002) and generalized group of porous diffusers (Stenstrom and Rosso, 2008).

Table 2.10 Average aeration process parameters obtained from steady- state clean water tests.

<i>p</i>	<i>Q_w</i>	Δp	<i>C_s</i>	<i>C_t</i>	<i>K_La</i>	<i>K_La₂₀</i>	<i>OTR</i>	<i>SOTR</i>	<i>OTE</i>	<i>SOTE</i>	<i>AE</i>	<i>SAE</i>
(bar)	($\times 10^{-5}$ m ³ s ⁻¹)	(Pa)	(mg L ⁻¹)		(h ⁻¹)		($\times 10^{-3}$ kgO ₂ h ⁻¹)		(%)		(kgO ₂ kW ⁻¹ h ⁻¹)	
0.5	5.90	2240	20.8	11.8	31.2	31.1	3.3	5.8	66	116	4.5	7.9
1.0	5.32	2010	41.6	13.7	10.4	10.2	1.3	3.8	49	145	1.7	5.1
1.5	4.73	2360	64.2	15.9	6.5	6.4	0.9	3.6	50	198	1.2	4.7

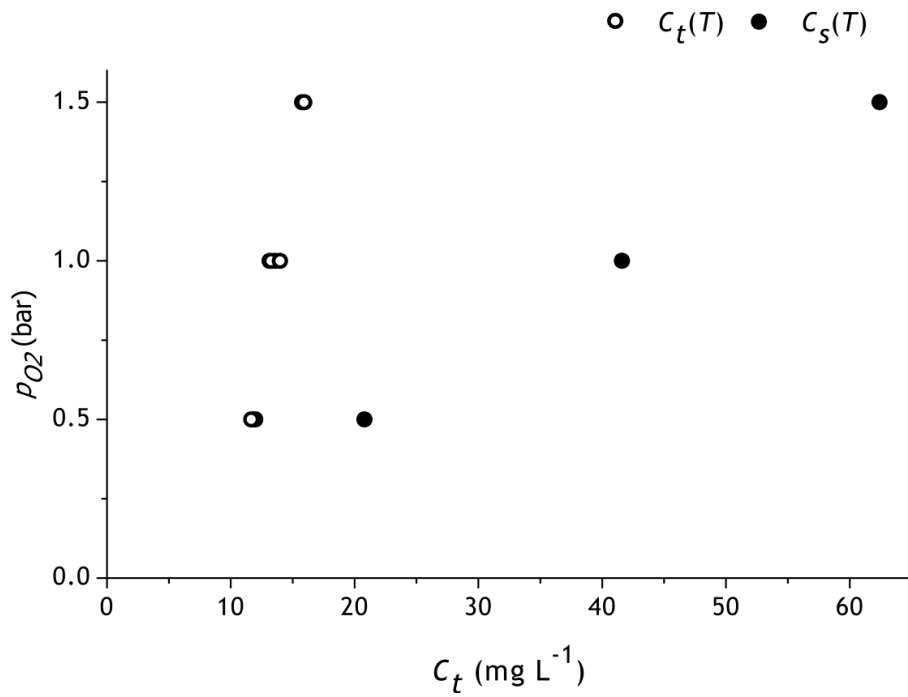


Figure 2.13 Steady-state DO concentration obtained in steady- state clean water test for various oxygen pressures.

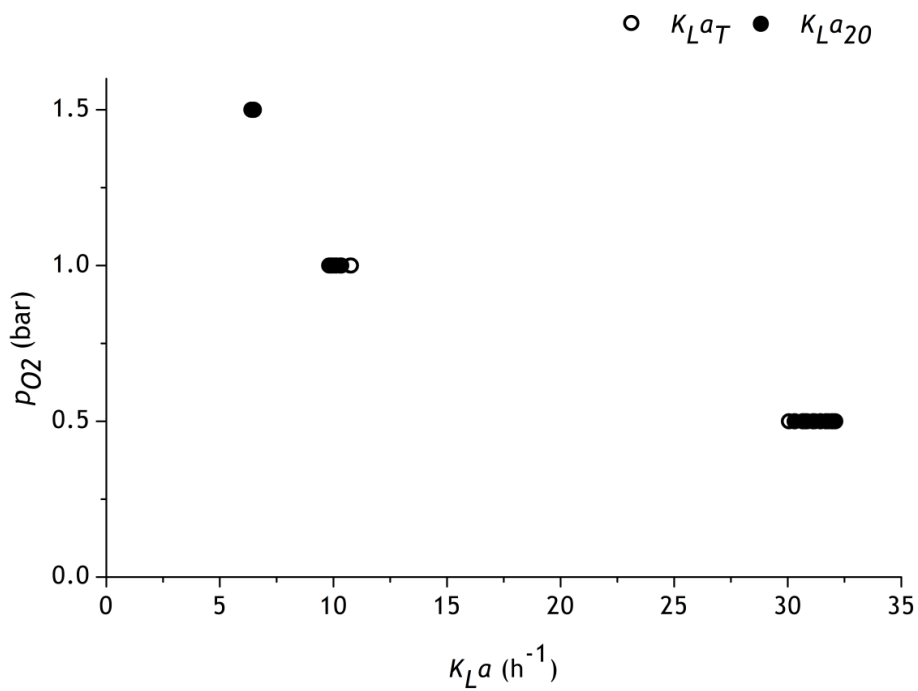


Figure 2.14 Oxygen mass transfer coefficient ($K_L a$) obtained in steady- state clean water test for various oxygen pressures.

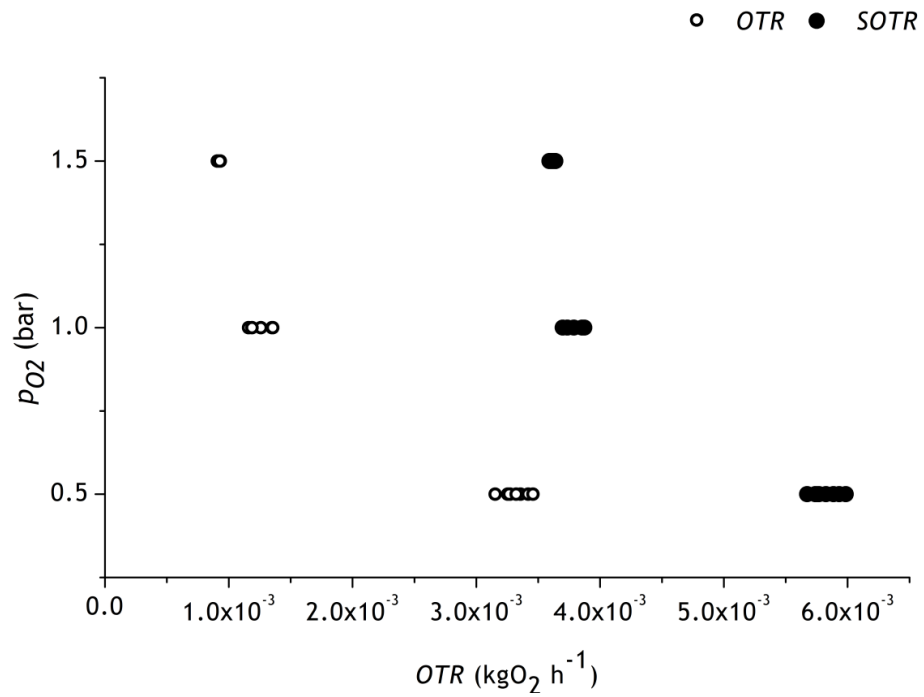


Figure 2.15 Oxygen transfer rate (OTR) obtained in steady- state clean water test for various oxygen pressures.

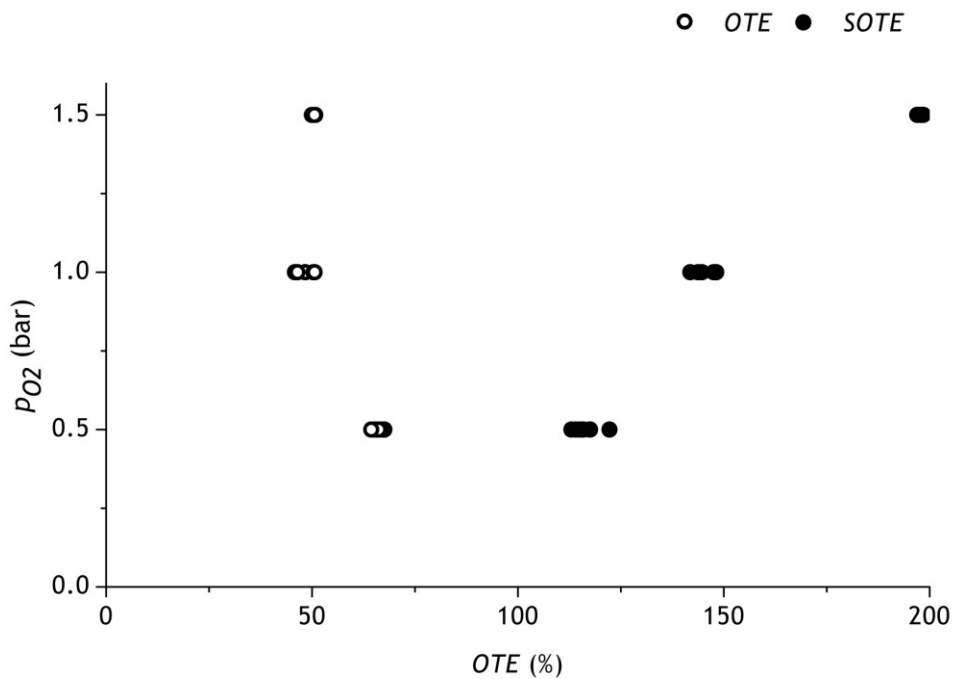


Figure 2.16 Oxygen transfer efficiency (OTE) obtained in steady- state clean water test for various oxygen pressures.

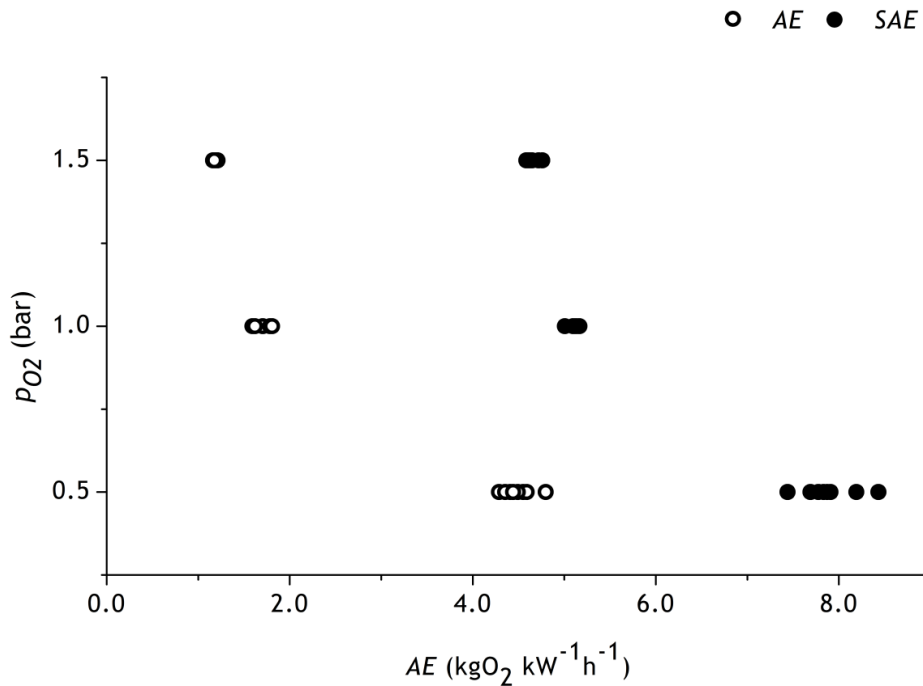


Figure 2.17 Aeration efficiency (*AE*) obtained in steady- state clean water test for various oxygen pressures.

2.4.6.2 Unsteady- State Experiments

The average values of the process parameters obtained from the unsteady-state experiments are shown in the Table 2.11. All experiments were run until DO saturation concentration in the PAC outflow, C_t , reached the stable value of 20.0 mg L⁻¹, which is the upper limit for measurement range by LDO sensor. The $K_L a$ values obtained in the unsteady- state approach and determined from log-deficit method are nearly four times lower than in case of steady- state tests, but with the same decreasing trend depending on the oxygen pressures. Here, similarly to the steady-state tests results, the average values of $K_L a$ for several tests overlap with $K_L a_{20}$, as can be seen in Figure 2.18.

Again, similarly to the previous experiments, *OTR* computed on the base of the $K_L a$, ranges from 0.3 to 1.4 g of oxygen per hour, for the oxygen input pressures from 1.5 to 0.5 bar, respectively. After converting into *SOTR*, these values vary from 1.0 to 1.5 gO₂ h⁻¹, depending on the pressures used, as seen in Figure 2.19.

On the other hand, with averaged values of *OTE* ranging from 16 to 10%, converted further into *SOTE* in the range of 17 to 31%, the quantity of oxygen absorbed during aeration of water in PAC is five to seven times less than in the steady-state approach. These ranges of *SOTE* correspond to the majority of the submerged aeration devices, including porous

diffusers, jet and U-tube aerators. The tendency in values is similar to the *OTE-SOTE* distribution obtained from the steady-state test, as can be seen in Figure 2.20.

Aeration efficiencies *AE* obtained from the unsteady-state experiments (Figure 2.21) are also lower than in steady approach, ranging for the test conditions from 0.2 to 1.2 kgO₂ kW⁻¹ h⁻¹ for the operating pressures from 1.5 to 0.5 bar. In standard conditions the increase in values is barely noticeable, and amounts 0.7-1.2 kgO₂ kW⁻¹ h⁻¹. These values are similar to the *SAE* typical for some nonporous diffusers (Quasim, 1999; Stenstrom and Rosso, 2008; Taricska et al., 2009b), jet aerators (Stenstrom and Rosso, 2008), and a wide range of the mechanical units such as: submerged turbines, including devices equipped with draft tubes (Mueller et al., 2002; Tchobanoglous et al., 2003); high-speed aerators (Stenstrom and Rosso, 2008; von Sperling, 2007); and aspirating aerators (von Sperling, 2007). These values may be to some extent a result of low *K_La*, affecting in the same way *OTR* values. On the other hand, considering average headloss on PAC of 25 cm, the largest contribution in the power expenditure would be due to intense oxygenation, as deduced from the *SOTE* values.

Table 2.11 Average aeration process parameters obtained from unsteady- state clean water tests.

<i>p</i>	<i>Q_w</i>	Δp	<i>C_S</i>	<i>K_La</i>	<i>K_La₂₀</i>	<i>OTR</i>	<i>SOTR</i>	<i>OTE</i>	<i>SOTE</i>	<i>AE</i>	<i>SAE</i>
(bar)	(×10 ⁻⁵ m ³ s ⁻¹)	(kPa)	(mg L ⁻¹)	(h ⁻¹)	(h ⁻¹)	(×10 ⁻³ kgO ₂ h ⁻¹)	(×10 ⁻³ kgO ₂ h ⁻¹)	(%)	(%)	(kgO ₂ kW ⁻¹ h ⁻¹)	(kgO ₂ kW ⁻¹ h ⁻¹)
0.5	5.90	2.3	20.8	7.9	7.9	1.4	1.5	16	17	1.2	1.2
1.0	5.32	2.7	41.6	2.7	2.7	0.5	1.0	11	23	0.4	0.8
1.5	4.73	2.5	64.2	1.6	1.6	0.3	0.9	10	31	0.2	0.7

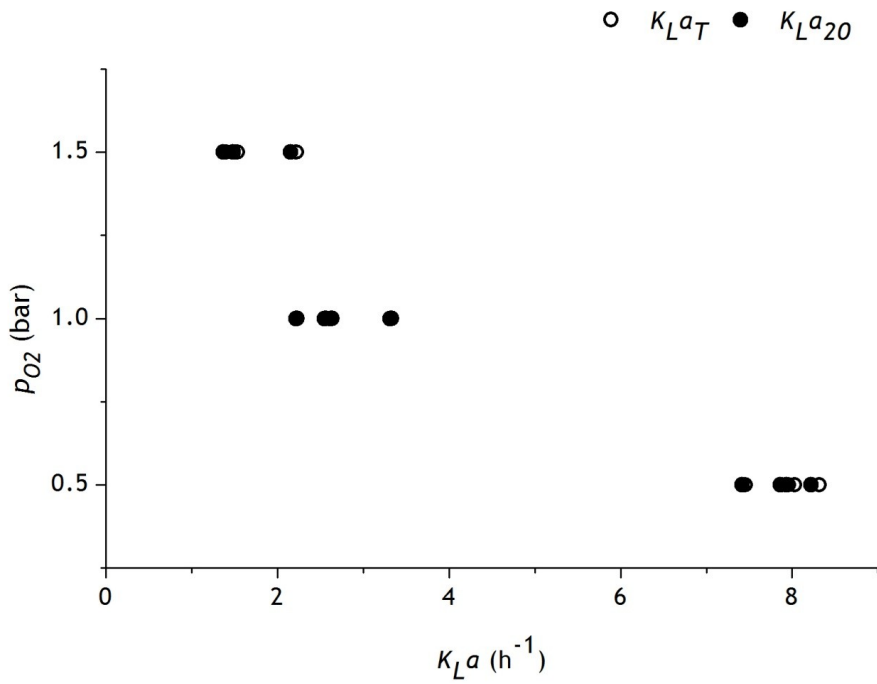


Figure 2.18 Oxygen mass transfer coefficient (K_La) obtained in unsteady- state clean water test for various oxygen pressures.

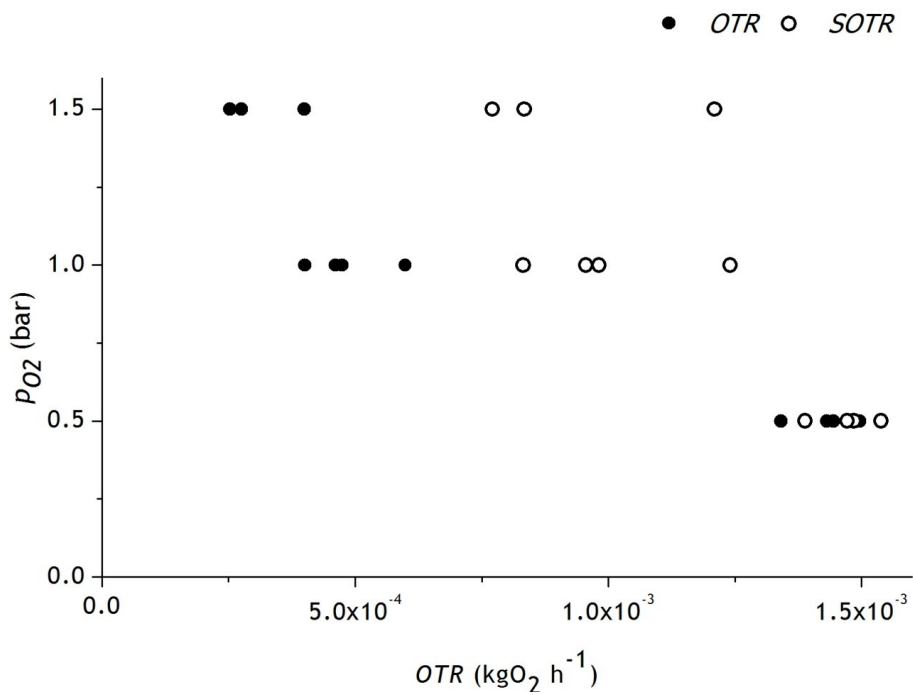


Figure 2.19 Oxygen transfer rate (OTR) obtained in unsteady- state clean water test for various oxygen pressures.

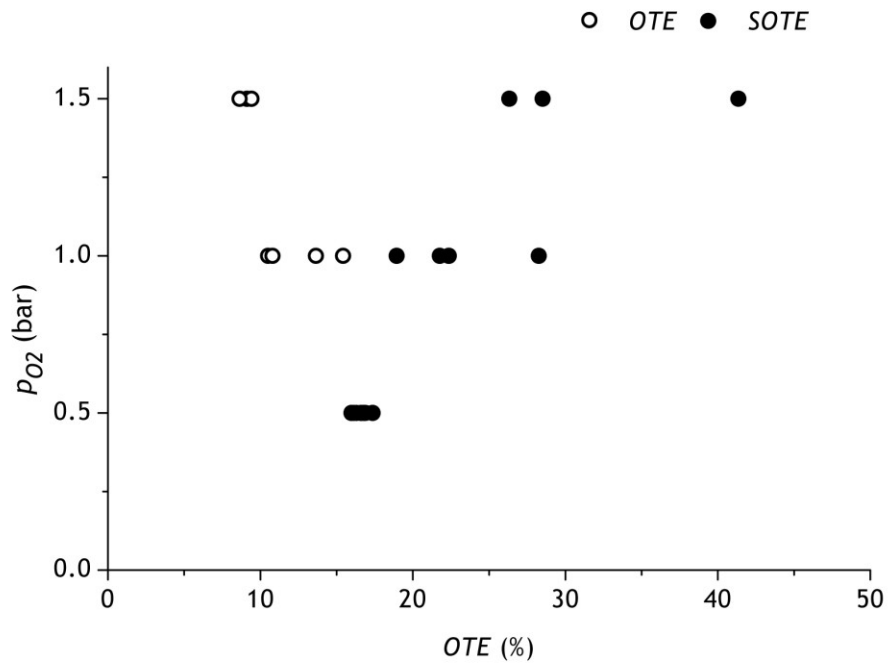


Figure 2.20 Oxygen transfer efficiency (*OTE*) obtained in unsteady- state clean water test for various oxygen pressures.

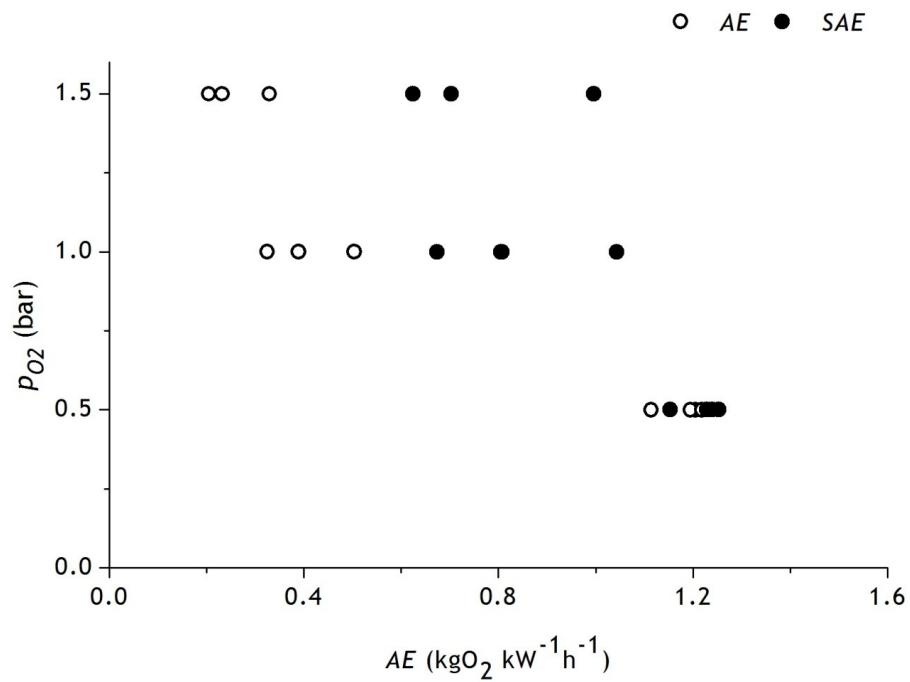


Figure 2.21 Aeration efficiency (*AE*) obtained in unsteady- state clean water test for various oxygen pressures.

2.4.6.3 Validation of 3D CFD Studies of PAC

To evaluate and compare the performance simulated with CFD in the 3D PAC with the results of the experiments carried on the lab-scale PAC, aeration efficiency of the device needs to be assessed. Aeration efficiency (AE) of PAC was computed from the following formula:

$$AE = \frac{O_{2,out}}{P} \quad (2.65)$$

where $O_{2,out}$ is the mass flux of oxygen in the outflow from the PAC, obtained from the CFD simulations.

Total power expenditure P accounts for the power demand on water pumping, P_w and on oxygenation, P_{O_2} . Power demand, P_w , is proportional to the pressure drop in the PAC and the water flow rate. P_w is computed from the formula described by Equation (2.56), for Q_w , volume flow rate of the chamber, obtained from CFD simulations and equal to $1.0 \cdot 10^{-4} \text{ m}^3\text{s}^{-1}$.

When comparing contour maps of the static pressure in the plane cut throughout the PAC volume, pressure drop in the outflow zone is negligible and of the order of 1.0 Pa. Hence, to assess pressure drop on the PAC, computational outline must be extended to include short sections of the inflow and outflow pipes, having diameter equal to inlet/outlet orifices in PAC, thus of 0.01 m. Here, pressure drop on PAC can be determined from the local headloss, computed for the two exits: from an inflow pipe to PAC, and from the PAC to the effluent pipe. The first case considers water discharge from the pipe to the PAC, which is characterized by flow expansion due to the sudden enlargement of the flow area, as shown in Figure 2.22a. Second case considers flow discharge from the PAC to the pipe characterized by formation of vena contracta, followed by headloss due to sudden expansion of the flow area after contraction section, as seen in Figure 2.22b.

For both cases presented in Figure 2.22 local headloss is determined from the Darcy's formula in the following form:

$$h_l = k_l \frac{v^2}{2g} \quad (2.66)$$

where h_l is the local loss in m, k_l denotes local headloss co-efficient, dimensionless and expression $v^2/2g$ is the velocity head.

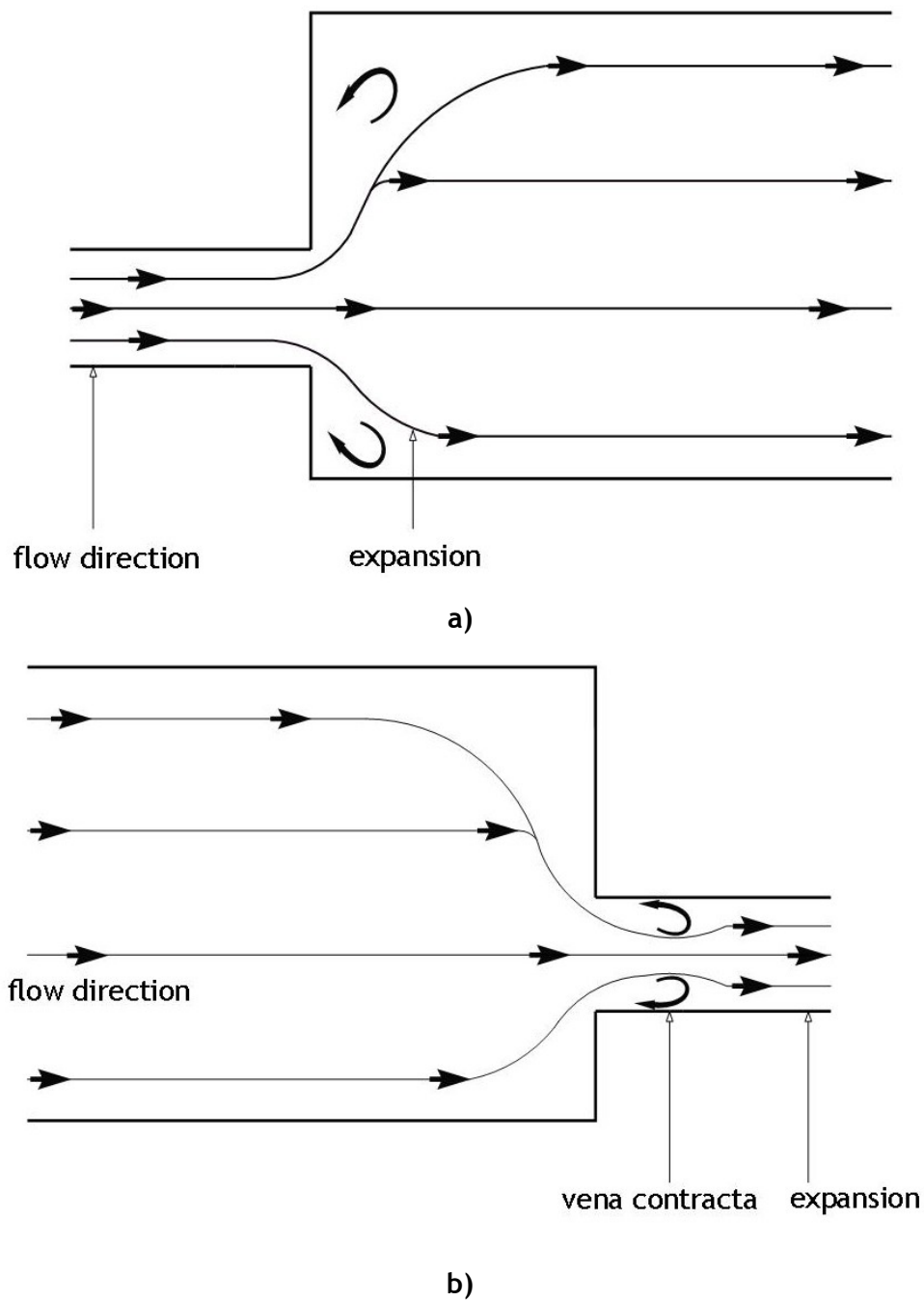


Figure 2.22 Schematic discharge to and from the PAC through the: a) inlet, and b) outlet orifice.

The example computation below aimed derivation of the formula for k_l for the case of sudden contraction. The momentum equation can be written as:

$$pA - p_1A_1 = \rho Q(v_1 - v) \quad (2.67)$$

where p , and v refer to the pressure and velocity in the contracted cross section area of the jet from PAC, A , and p_1 , v_1 correspond to converged flow conditions in the outflow tube of the area A_1 .

From the continuity equation we have:

$$Q = Av = A_1v_1 \quad (2.68)$$

and after rearrangement, Equation (2.67) is of the following form:

$$\frac{p_1 - p}{\rho g} = \frac{v_1}{2g}(v - v_1)$$

From the Bernoulli's energy conservation equation, for PAC and the outflow tube we have:

$$\frac{p}{\rho g} + \frac{v^2}{2g} = \frac{p_1}{\rho g} + \frac{v_1^2}{2g} + h_l \quad (2.69)$$

After combination and rearrangement of the Equations (2.67) and (2.69) we obtain:

$$h_l = \frac{(v - v_1)^2}{2g} \quad (2.70)$$

If the continuity equation of the form:

$$v = \frac{v_1 A_1}{A}$$

will be implemented into Equation (2.70), we obtain:

$$h_l = \left(\frac{A_1}{A} - 1\right)^2 \frac{v_1^2}{2g} \quad (2.71)$$

Comparing this equation with (2.66) yields

$$k_l = \left(\frac{A_1}{A} - 1\right)^2 \quad (2.72)$$

To determine k_l for vena contracta, it can be assumed, that the contraction is about 40% of the flow area in the pipe (Chadwick and Morfett, 1998). Therefore considering the region where head loss occurs, i.e. section with contraction-expansion, having the areas of $0.6A_1$ and A_1 respectively, k_l is 0.44.

For the assumed in the CFD simulations v equal to 1.0 m s^{-1} , the expansion headloss is $0.022 \text{ m H}_2\text{O}$, what corresponds to 216 Pa .

Analogically, for the case of sudden enlargement the procedure to determine k_l includes all the computational steps described from Equation (2.67) to (2.72), where the variables without subscript refer to the flow characteristics within the inlet pipe and the variables with subscript are the ones of the PAC. Here, the final formula for k_l will have the following form:

$$k_l = \left(1 - \frac{A}{A_1}\right)^2 \quad (2.73)$$

The value of A_1 in Equation (2.72) is much greater than A thus k_l is 1.

Hence for such sudden large expansion, the local headloss equals to the velocity head, which for v_1 of 1.0 m s^{-1} equals 0.051 m , corresponding to 500 Pa .

The total headloss on the PAC equals the sum of the local losses, which is 716 Pa , and thus the power demand for water pumping, computed from the Equation (2.56) is around 0.1 W . Power demand on oxygenation, P_{O_2} was computed as for the experimental PAC using Equations (2.57), (2.58), (2.59) and (2.60), for the values of pressure and temperature referred in Section 2.3.5.

The values of aeration efficiency obtained from the 3D CFD simulations of the PAC, which are presented in Table 2.12 are in good agreement with the results obtained from the steady-state experiments for the oxygen pressure of 0.5 bar , which account in average for $4.5 \text{ kg kW}^{-1} \text{ h}^{-1}$. Nonetheless, when considering the pressure drop on a chamber, the values computed for the CFD layouts are around 3 times lower than those obtained during experiments on lab-scale PAC.

Table 2.12 Aeration efficiency obtained from the 3D CFD simulations of various PAC configurations.

PAC geometry	DO (mg L^{-1})	Δp (Pa)	P_w (W)	P_{O_2} (W)	AE ($\text{kg kW}^{-1} \text{h}^{-1}$)
Rectangular	12.56	716	0.06	1.46	3.87
Rectangular with bottom baffles	17.75	716	0.06	2.06	3.92
Rectangular with alternating baffles	18.21	716	0.06	2.11	3.93

2.5 2D Bubble Column Reactor

In this section, description of 2D Bubble Column Reactor (BCR) and experimental setup are given. Standard imaging followed by image processing procedure used to determine hydrodynamics of the water flow through BCR aerated with atmospheric air and operated in concurrent gas-liquid upflow is studied. Besides flow regime and gas hold-up assessment, experimental procedure of steady-state clean water test for Oxygen Transfer Rate and aeration process parameters assessment is described. On the base of the hydrodynamics parameters and the clean water test results, aeration performance of the BCR for process conditions, i.e. air and water flow rates, is evaluated. Finally, oxygen mass transfer and energy efficiency obtained from the multiple experiments are compared with the aeration process parameters characteristic for conventional devices used in AS systems.

2.5.1 Bubble Column Reactors in Activated Sludge Systems

Aeration is a key unit process in biological wastewater treatment and its efficiency in such multiphase system as the activated sludge tank depends on the gas-liquid interfacial area and the gas hold-up. Many studies have been focused on the relationship between the gas hold-up and the physical properties of the liquid phase, reactor hydrodynamics and the bioreactor efficiency. Although aeration basins equipped with mechanical or diffused air units predominate in suspended growth AS systems, many multiphase reactors, such as packed bed reactors, bubble columns and airlift reactors associated until recent decades exclusively with chemical and bioengineering industry, found to be suitable alternative for aeration of both, suspended and attached growth AS systems. In the recent years, special attention is paid to the attached growth (fixed-film or biofilm) AS, having better resistance to high loading rates and thus higher capability to treat high-strength effluents than

conventional suspended growth AS systems. Multiphase reactors used in biofilm AS systems are, among the others, bubble column bioreactors and airlift bioreactors.

Bubble column reactors (BCR) or simply bubble columns, are inexpensive and easy and flexible in operation devices (Kantarci et al., 2005; Shaikh and Al-Dahhan, 2007; Wang and Zhong, 2007), consisted of vertical cylindrical vessel filled with the liquid and equipped with gas phase distributor, usually sparger or jet nozzle placed at the bottom. Performance of BCR is based on introduction of dispersing energy by gas injection into liquid or liquid-solid suspension. Flow patterns, and thus mixing within the vessel occurs by natural dynamics of the phases, and depends on gas-liquid velocities. Reactor performance yields in high mass and heat transfer efficiencies, however one of the serious drawbacks of bubble columns limiting their wide application in cell growth industry and also AS systems is large degree of backmixing in the liquid phase, decrease of the interfacial area due to bubble coalescence, and high pressure losses (Shaikh and Al-Dahhan, 2007; Wang and Zhong, 2007). To overcome these fails and improve mass transfer performance, modification in original design has been done by introduction of various kinds of packing and staging of the column height. In water and wastewater treatment technology BCRs are generally used in: advanced oxidation processes (AOPs) as ozone contactors, allowing for rapid and efficient dissolution of ozone in liquid media and air stripping in towers. They are also used, but still in lesser extent, in aeration of the AS process either in suspended growth or immobilized on packing biofilm systems.

For bubble columns, literature offers handful of papers published on experimental hydrodynamics studies, concerning flow regime and superficial gas velocity investigation with application of CFD studies and supported by advanced measurement techniques such as PIV, LDA or CARPT (Dani et al., 2007; Dhotre and Joshi, 2007; Díaz et al., 2008a; Díaz et al., 2008b; Klusener et al., 2007; Kulkarni et al., 2007; Nogueira et al., 2006; Shaikh and Al-Dahhan, 2007; Spicka et al., 2001; Spicka et al., 1999; Tabib et al., 2008). The influence of gas velocity on oxygen mass transfer and gas hold-up in a bubble columns have been also widely studied, with application of such nonintrusive techniques, as PLIF and PLIF with Inhibition (PLIFI) (Dani et al., 2007; Díaz et al., 2008b; Francois et al., 2011; Kantarci et al., 2005; Kulkarni et al., 2007; Shaikh and Al-Dahhan, 2007). The hydrodynamics and biokinetics of the AS in slurry columns are also objective of intense studies (Jin and Lant, 2004; Mineta et al., 2011; Terasaka et al., 2011).

Due to the relatively low power requirements for aeration and mixing, easy maintenance and potential for scaling up, airlift reactors (ALR) found wide applications in suspended growth systems, such as granular AS process conducted in SBR or biofilm systems,

operating as airlift activated sludge reactors. In the recent years, airlift bioreactors has been object of many studies using both, CFD and experimental approaches (Jin and Lant, 2004; Jin et al., 2006; Luo and Al-Dahhan, 2008; Moraveji et al., 2012; Nicoletta et al., 1998; Šimčík et al., 2011; Talvy et al., 2007; Xu and Yu, 2008). Airlift bioreactor has similar reactor design to bubble column, equipped additionally with a draft tube providing performance-improving internal circulation. Depending on the draft tube function, airlift reactors with either internal loop (inner tube) or external loop (external tube) are used. The principles of ALR aeration performance are the same as those of deep shaft (U-tube) aeration systems. As the aerated by sparger section has lower effective density than the air deficit section, the difference in hydrostatic pressure between the two promotes liquid flow upward and creates a draft, improving circulation and oxygen transfer and equalizing shear forces in the reactor. To enhance overall mixing and reduce backmixing, ALR can be fitted with mechanical agitation devices, placed in the bottom zone.

2.5.2 2D Reactor

Depending on the type of AS process BCR can be used in similar way to PAC, i.e. as a high rate flow component of the aeration tank recirculation loop in suspended growth systems. Considering attached growth systems, BCR can be used as an AS bioreactor itself. BCR system, shown in Figure 2.23 consists of three main built-in components: bottom tank; central section, with a vertically positioned rectangular, transparent, acrylic reactor; and the top wall tank. The reactor is operated in concurrent gas-liquid upflow through the packed bed. Fluid is delivered through the inlet orifice located in the bottom tank. Bottom tank has the dimensions of 0.32×0.12×0.17 m and is of rectangular cross-section which changes towards the top into trapezoidal prism. The narrowing tank cross section allows smooth passage of the fluid to the central section. Additionally, a flat, rectangular plate-flow deflector was fixed at a distance of approximately 1 cm above the inlet, allowing uniform and continuous fluid upflow. Gaseous phase is introduced into the bottom tank through a gas sparger extended along the tank width and precisely aligned with the horizontal axis of the central section. The sparger was made of an acrylic perforated tube with $2 \cdot 10^{-3}$ m diameter, with 40 equally spaced orifices, each having a diameter of $0.5 \cdot 10^{-3}$ m. Sparger design and position enable reasonably uniform distribution of the flow of the gas bubbles into the central section of the reactor. 2D reactor consists of two rectangular plates of dimensions 0.20×0.60 m. The plates are spaced from each other and connected along the sides with two internal acrylic strips reinforced with external stainless steel chasing, ensuring constant column gap thickness of $2 \cdot 10^{-3}$ m. The reactor bed packing consists of acrylic discs with diameter of $1 \cdot 10^{-2}$ m and thickness of $2 \cdot 10^{-3}$ m,

ordered in regular, diamond-shape matrix, as seen in the Figure 2.24. The horizontal distance between the centres of the adjacent disks is $2 \cdot 10^{-2}$ m and the vertical interval between two adjacent rows of packing is $1 \cdot 10^{-2}$ m, which results in bed porosity of 0.6. The upper tank has a function of gas-liquid separator, designed to maintain a stable level on the free liquid surface and therefore to minimize the risk of the undesirable changes in the hydrostatic pressure inside the reactor. The tank has two outlets: a gas outlet (vent) situated in the top wall; and the fluid outlet in the back wall of the phase-separator.

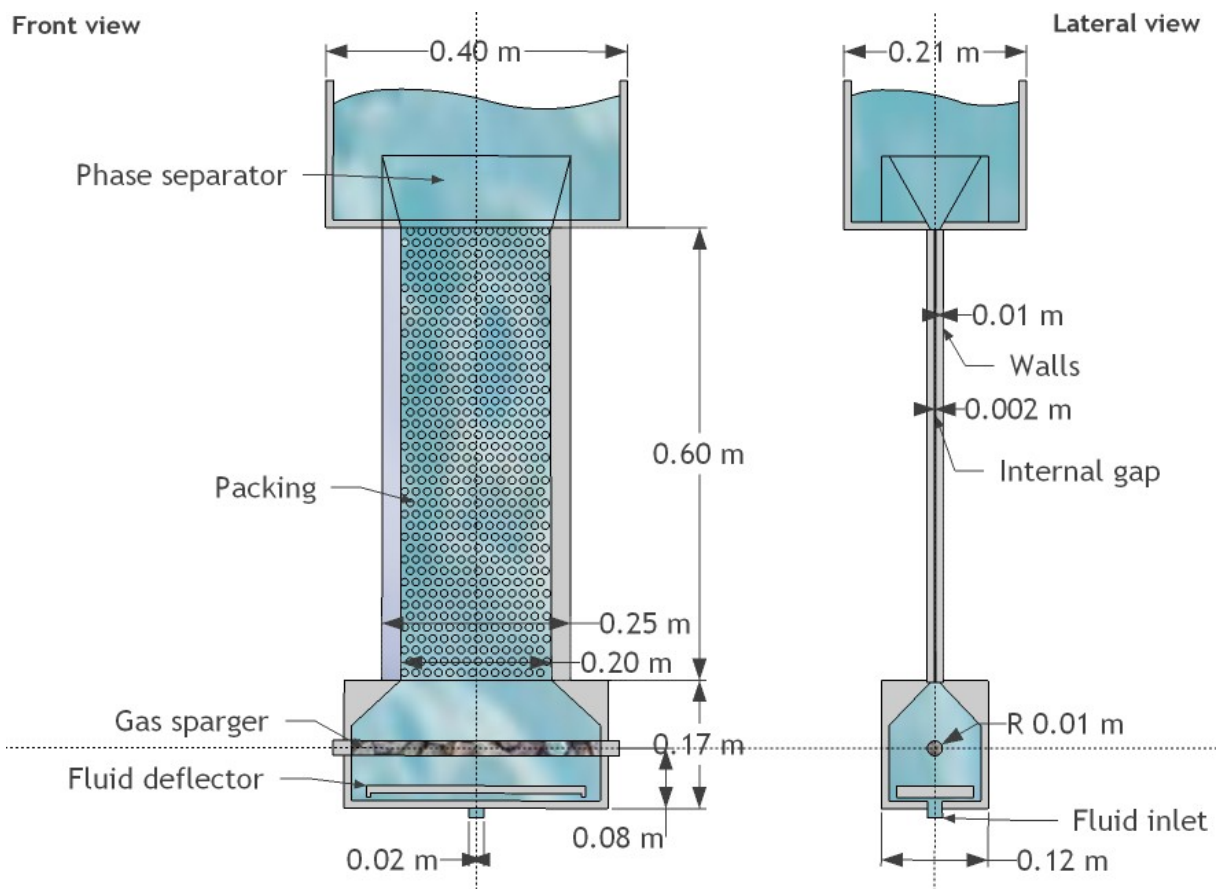


Figure 2.23 Bubble Column Reactor layout.

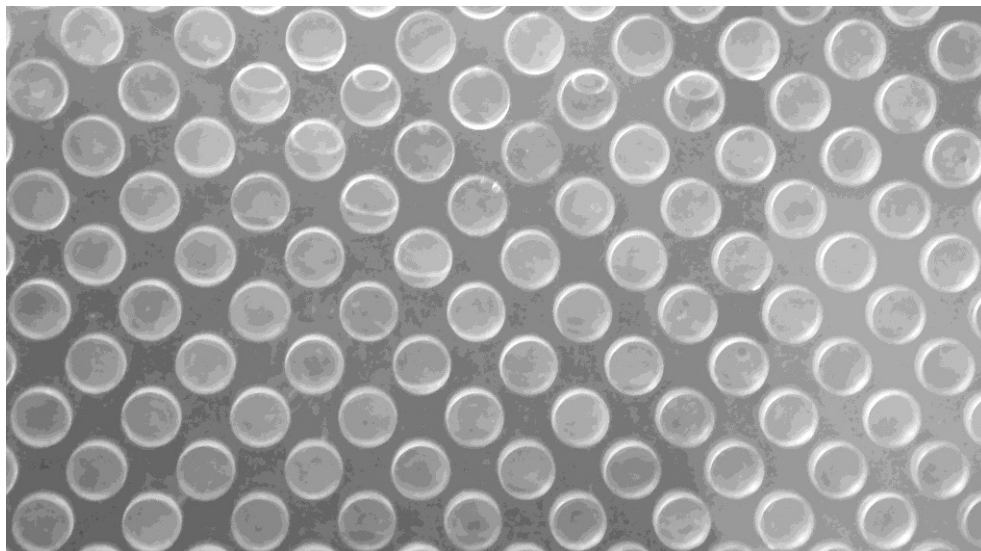


Figure 2.24 Image of structure packing.

2.5.3 Experimental Set-up and Flow Loop

Similarly to the oxygen transfer measurement experiments conducted on PAC, BCR is considered as an independent external aeration unit and a flow component included in the mixed liquor recirculation loop. Figure 2.25 shows the 2D reactor and the part of the experimental set-up. The entire installation and the flow loop are shown in Figure 2.26. Test water was stored in acrylic reservoir with capacity of 135 dm³ (1), equipped with mechanical stirrer (Heidolph, model RZR 2021) and with vertical shaft crossed-blade impeller (2). Strictly defined standards of water quality in the reservoir during oxygen transfer experiments require constant monitoring, therefore DO concentration, conductivity and temperature were continuously controlled with portable dual channel multi meter (3) (Hach Lange HQ40D) equipped with digital smart sensors (4): luminescent DO probe (IntelliCAL™ LDO10103) and conductivity probe (IntelliCAL™ CDC40103). The precision of the equipment is: 0.01 $\mu\text{S cm}^{-1}$ for conductivity probe; 0.01 mg L⁻¹ O₂ or 0.1% of DO saturation for oxygen probe; and 0.3 °C for temperature. Water fed from the reservoir is pumped using positive displacement gear micropump (5) with magnetically coupled drive (Pacific Scientific, model 220/560C) that has an external rpm speed controller. The aeration unit is operated in concurrent gas-liquid upflow mode, which means that the test water is delivered to the BCR (6) through the inlet port in the bottom tank. The water flow rate is additionally measured and controlled by variable area correlated flowmeter (7) (Gilmont Accucal, model GF 1660). The accuracy of the measurements can be estimated as $\pm 2\%$ of reading or ± 1 scale division. Atmospheric air is supplied through laboratory distribution manifold connected to an outdoor air compression

module mounted on the roof of the building. Pressurized air flow rate is regulated by means of two pressure regulators (8) connected in series. The first pressure regulator (Camozi MC202-R00), connected to the lab air manifold below shut-off valve, operates with pressure range 0-25 bar. Second regulator (Pneumax, model FIMET) equipped with air filter provides regulation of pressure from 0 to 4 bar. Air flow through the BCR is measured by variable area correlated flowmeter (9) (Cole Parmer, model 60648), with the reading accuracy of $\pm 2\%$ of full-scale. Air is supplied to the BCR with the tubing connected directly to the gas sparger, located in the bottom tank. Mixture of water and bubbles flow upwards BCR to the upper tank, where the excess air is released from the water surface and escapes through the vent to the atmosphere. The effluent aerated water is discharged through the outlet in the back wall of the separator to the pipeline and flows downwards to the drainage collector. Pressure drop on the BCR is measured by means of differential pressure transducer (10) (Validyne, Type P0305D), inserted between reactor feed pipe (11) and outflow pipe from the separator (12). DO concentration in the influent and effluent from the reactor are controlled continuously with another stand-alone measurement system, consisted of a standard controller display module (13) (Hach Lange sc100) and luminescent DO probe module (Hach Lange, LDO probe). The sensitivity of the probes is 0.01 mg L^{-1} DO or 0.1% DO saturation. The probes are placed in specially manufactured PVC flow cell adapters integrated with the BCR influent (14) and effluent tubing (15). Water and oxygen pipeline system used in the experimental installation consist of 3/8" polyurethane and stainless steel tubing (Swagelok) and all necessary fittings: tube adapters, quick connect fittings, elbows, tees and regulation valves.

The signals from the pressure transducer and LDO sensors are converted into digital data by the Data Acquisition (DAQ) device (16) (National Instruments, NI SCC-68). Dell® Optiplex 755 PC (17) with a dual core Intel® Core™ 2 Duo CPU at 2.66 GHz and 2.33 GB of RAM controls the operation of the DAQ device and is used for processing and storing measurement data through an application developed with LabVIEW (version 8.2).

During the experiment, the two-phase bubbly flow is imaged using high resolution imaging system. Image acquisition system consists of a 2 megapixel CCD camera (18) (TSI Powerview™ Plus, model 630157) connected to a frame grabber (TSI, model 600067), a source of light (19)- halogen lamp, light diffuser (20) and frame grabbing software- TSI Insight 3G™ (version 9.0) installed in the Dell® Precision 690 PC with a dual core Intel® Xeon® CPU at 2.33 GHz and 2 GB of RAM (21).

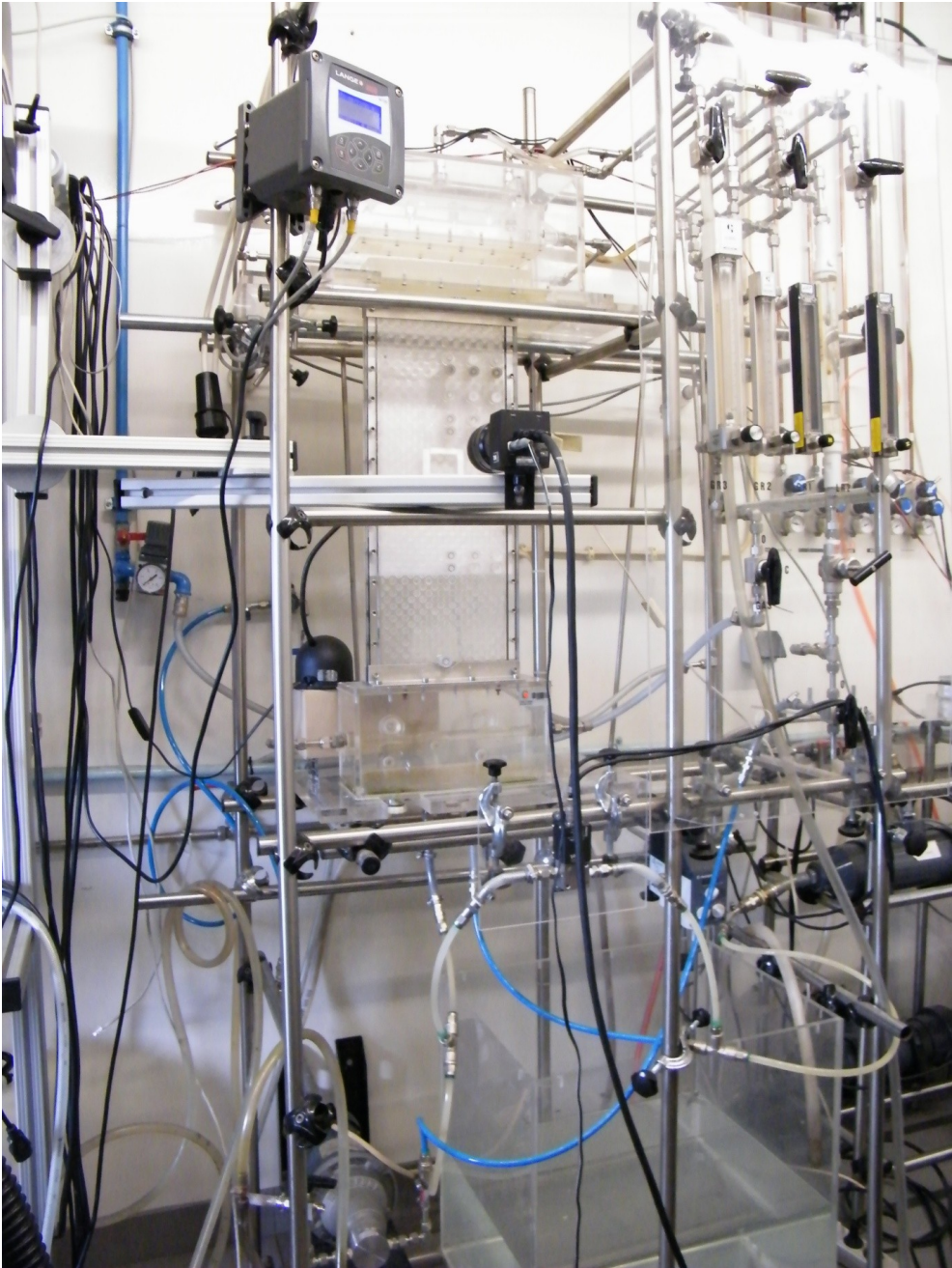


Figure 2.25 A photograph of experimental installation.

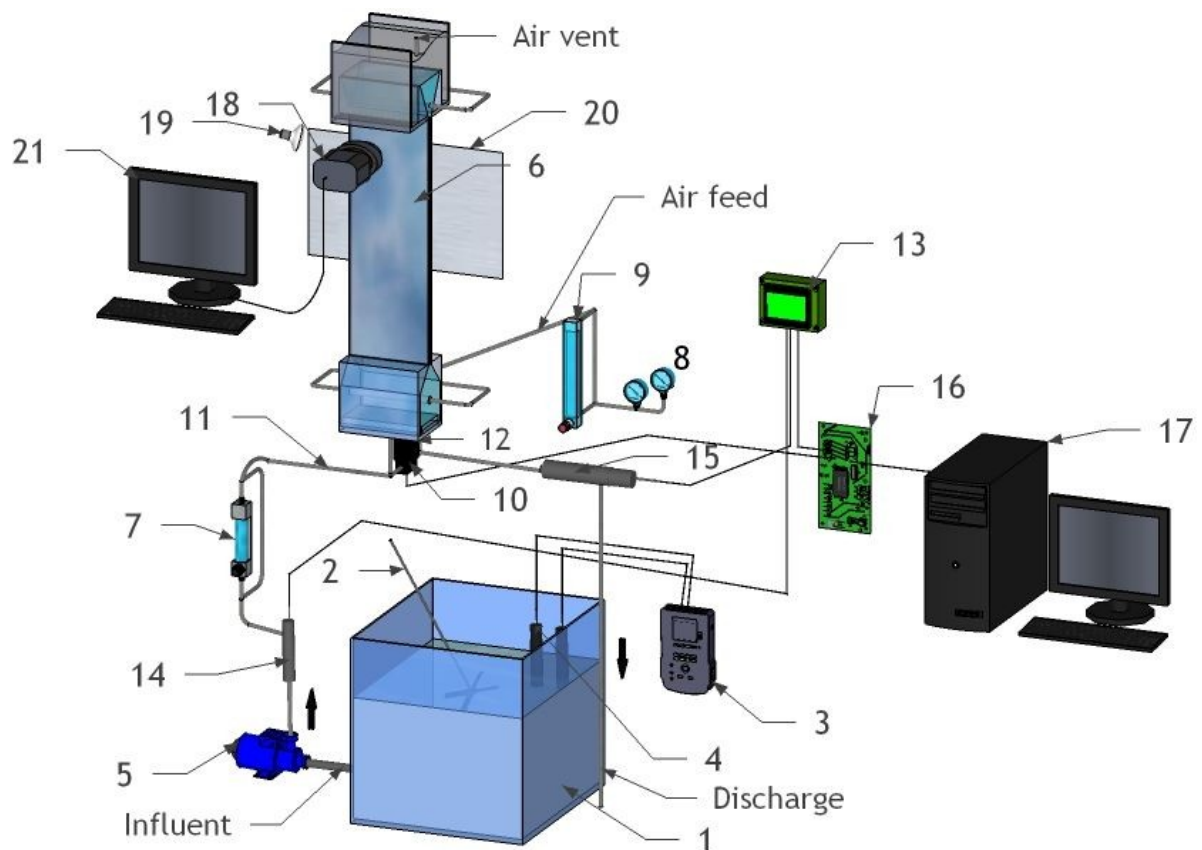


Figure 2.26 Experimental set-up and flow loop: 1- reservoir; 2- stirrer; 3- multi meter; 4- probe; 5-pump; 6- BCR; 7- flowmeter; 8- pressure regulator; 9- air flowmeter; 10- pressure transducer; 11- influent tube; 12- outflow from the separator; 13- DO controller display; 14, 15- flow cell adapter; 16- acquisition board; 17- PC; 18-CCD camera; 19- halogen lamp; 20- light diffuser; 21- PC.

2.5.4 Experimental Air-Water Flow Ranges and Experiments

The experimental studies of BCR were conducted for different pairs of water and air flow rates. The ranges of water, Q_w , and air, Q_{Air} , flow rates and the experiment objectives are listed in Table 2.13. Considering BCR bed porosity of 0.6, velocity of the liquid phase, u_w , is computed, as follows:

$$u_w = \frac{Q_w}{0.6 \cdot A_{CS}} \quad (2.74)$$

where u_w is surface velocity of water, $m \cdot s^{-1}$ and A_{CS} denotes BCR cross section, in m^2 .

Similarly, to assess the gas surface velocity, u_{Air} , following formula must be used:

$$u_{Air} = \frac{Q_{Air}}{0.6 \cdot A_{CS}} \quad (2.75)$$

where u_{Air} is surface air velocity, $m\ s^{-1}$.

Table 2.13 Water and air flow rates used in the experiments.

$Q_w (\times 10^{-5} m^3 s^{-1})$	$Q_{Air} (\times 10^{-5} m^3 s^{-1})$							
	1.60	3.71	5.76	7.89	9.96	1,19	13.80	15.80
0.57								
1.22								
1.92								
2.55								
3.38								
4.15								
4.95								
5.62								

2.5.5 Imaging Experiments

Characterization of the multiphase flow in BCR concerned qualitative and quantitative measurements to determine multiphase flow regime and volumetric fraction of gas or liquid as a function of water-air flow rates. Both approaches involved nonintrusive technique of standard imaging for data acquisition.

2.5.5.1 Image Acquisition

High resolution image acquisition system (Figure 2.26) used in the experiments consisted of the black and white high-speed CCD camera connected with the frame grabber, the halogen lamp, the light diffuser, and the frame grabbing software (TSI Insight 3G™ ver. 9.0) installed in the PC.

To obtain the most representative images of the flow field in the BCR, the image acquisition region of the most uniformed flow in terms of bubble distribution was selected and marked with the white frame, as seen in the Figure 2.27. The dimensions of the selected region of interest are 4.2×3.1 cm. The camera was positioned on an aluminum supporting arm (MayTec) at a distance of 0.2 m in front of the reactor and aligned parallel to the center of the acquisition frame. The light diffuser, a white paper sheet of high grammage, was placed adjacent to the rear wall of the reactor. The light from the halogen lamp, positioned behind the diffuser at the distance of 1 cm, enabled an uniform illumination of the frame background. For each experiment, an ensemble of one hundred

frames of 16-bit gray scale was captured by the camera at the shutter speed of $1 \cdot 10^{-5}$ s at frame rate of 14.5 frames per second. The size of each frame was 1600×1192 pixels with the resolution of 150 DPI (59.1 pixels per cm). The frames captured with the CCD camera were transferred to the computer through a frame grabber.

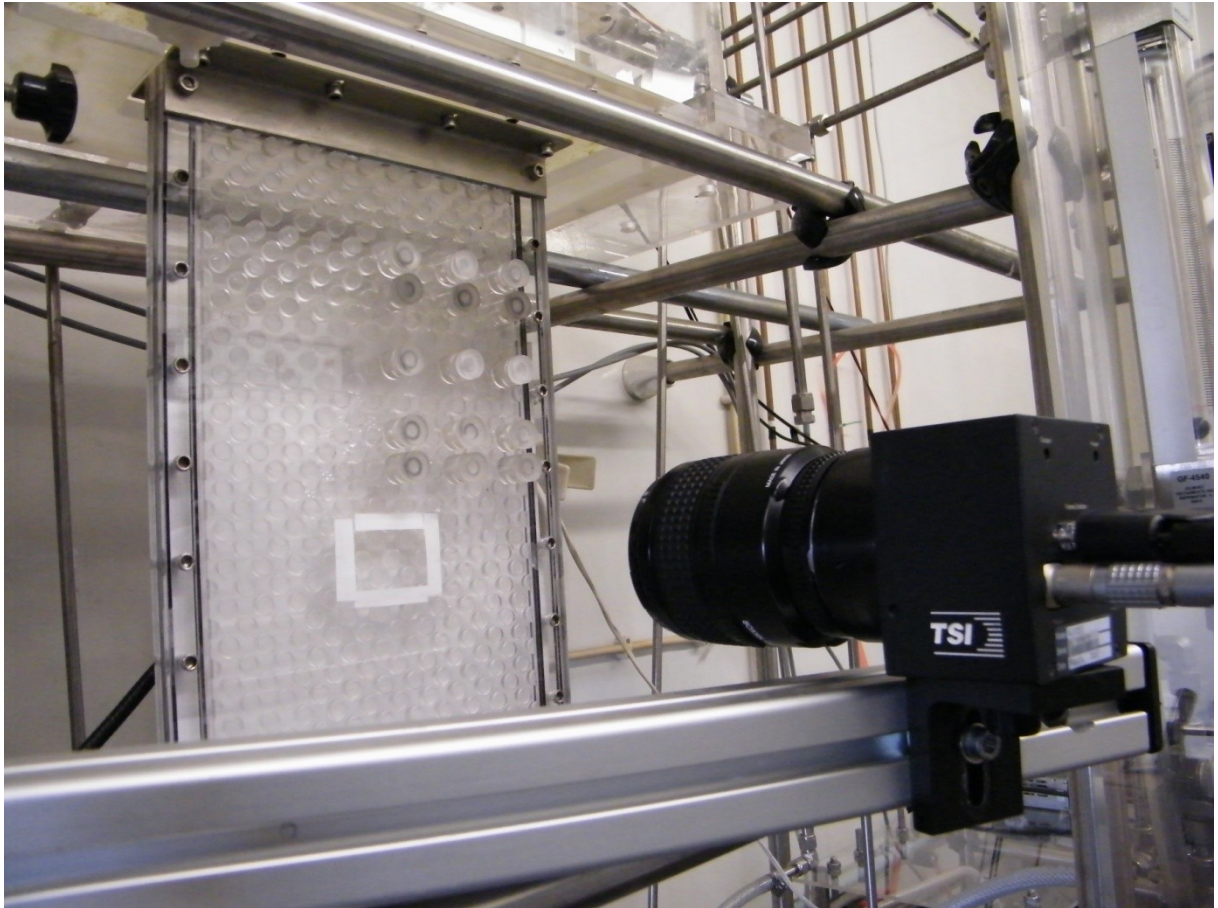


Figure 2.27 Image acquisition system.

2.5.5.2 Flow Regime Determination

Precise characterization of the flow dynamics, i.e. flow regime in the multiphase reactors, such as BCR, is important from the point of view of the application and operation of the reactor, as well as aeration process efficiency. Classification of the flow regimes in typical cylindrical column reactors is based mainly on the ratio of gas-liquid superficial velocities (Kantarci et al., 2005; Shaikh and Al-Dahhan, 2007; Spicka et al., 1999). In bubble column reactors, depending on the interactions of dispersed gas phase and continuous liquid phase, four different types of flow patterns are commonly observed: homogeneous (bubbly); heterogeneous (churn-turbulent); slug; and annular flows. These flow patterns occur also in the bubble columns of rectangular cross section, however the classification of

the flow regimes in channel and narrow flat channel reactors is more often based on the identification of the gas-liquid distributions in the reactor (Spicka, 2001).

In the present case of the gas-liquid flow in the 2D BCR of a high aspect ratio cross section, air bubbles tend to be flattened in narrow passages, therefore they can be considered two-dimensional. The flow regime determination may be based on the shape of the bubbles observed through the wider front wall of the BCR.

Homogeneous (bubbly) flow is characterized by circular or ellipsoidal bubbles of almost uniform size. At low gas rising and liquid velocities, there is almost no coalescence and break-up, hence the narrow bubble size distribution (Shaikh and Al-Dahhan, 2007; Takács, 2005). The size of the bubbles depends entirely upon the gas distribution and reactor characteristics, thus in case of BCR, dimensions of the sparger orifices, reactor cross section and the packing. If the bubbles released from the sparger are bigger than the gap thickness between the walls, they will be flattened (Spicka, 2001) and constantly deformed due to the collisions with the packing disks.

At low gas and relatively higher liquid velocities, increased turbulent forces break up large bubbles and prevent the coalescence of the smaller ones. The fluid phase imparts velocity to the small bubbles causing that the multiphase system behaves like a homogenous one, and such flow regime is referred as dispersed bubbly flow (Takács, 2005).

Slug flow occurs over a wide range of intermediate liquid and gas velocities small bubbles coalesce into the bigger elongated and unstable bubbly forms. Due to that, most of the gas phase is accumulating in large bubbles, while the contribution of the fine bubble fraction decreases. With the increase of liquid velocity, turbulent fluctuations break up large bubbles into the smaller ones and the transition from the slug into the dispersed bubbly flow occurs.

At the higher gas rates than those of slug flow, transition into a heterogeneous flow takes place. This turbulent flow regime is characterized by intense bubble-bubble interactions, leading to wide bubble size distribution. Next to the intense bubble coalescences and break up, existence of the high shear forces destabilize liquid slug structures. Collapsed liquid slugs are lifted by the larger bubbles of distorted shape followed by the clusters of smaller bubbles, forcing oscillatory motion of fluid in alternating directions. Since the large bubbles churn through the liquid, such heterogeneous flow is commonly referred as churn-turbulent flow (Shaikh and Al-Dahhan, 2007; Takács, 2005).

Annular flow occurs at the extreme high gas velocities and is characterized by the presence of the continuous gas flow core, containing dispersed droplets of liquid and surrounded by the wavy liquid film flowing upwards (Takács, 2005).

2.5.5.3 Determination of Volumetric Fraction of Air via Image Processing

Gas hold-up is one of the most important parameters characterizing hydrodynamics of the aeration systems (Coelho Pinheiro et al., 2000; Tang and Heindel, 2004). Gas hold-up is a dimensionless parameter, defined as the percentage fraction of the gas volume, such as gas bubbles, dispersed in the multiphase mixture in the reactor at any instant during gas-liquid contact process. Volumetric fraction of gas depends largely on the superficial gas velocity, however influence of the liquid velocity and the gas distributor have to be accounted.

Determination of the volumetric fraction of air in studied BCR involves application of the complex analysis of the grabbed images to measure the area (size) of the captured gas bubbles. In this work image analysis was performed using ImageJ, a public domain, Java-based image processing software developed at the U.S. National Institutes of Health (NIH). One of the options available in ImageJ, which is used for counting and measuring objects in binary images, is automatic determination of the particle size distribution. However, to obtain reliable results from the analysis, several steps of image processing must be followed.

A sample frame is shown in the Figure 2.28 and the sequence of the main steps of the image processing is presented in the Figure 2.29. As seen in the raw image, some of packing disks contain air bubbles trapped between the disk and the wall of the reactor, which cannot be accounted into the actual air fraction determination. Due to that, image pre-processing was made using Adobe® Photoshop® CS2 photo editing software and was based on the correction of the packing texture by simply creating a clipping mask with the white circles overlapping the disks, as seen in the Figure 2.29a. Enhanced in this way frames were consecutively processed using ImageJ.

In the first step, 16-bit image was converted into 256 shades of grey (8-bit). For convenience, the image scale was set to convert the pixels into the centimetres.

Various factors, such as limited number of grey scale levels, non-uniform background illumination and instability of the light source or room illumination affect the quality of the images. From the photographs shown in the Figure 2.28 and Figure 2.29a it is clear, that a dark to light gradient from the bottom right to the other upper left corner of the image, and some pixels affected by noise are scattered randomly within a frame. To correct non-uniform background illumination, background subtraction option was applied, and the result is presented in the Figure 2.29b.

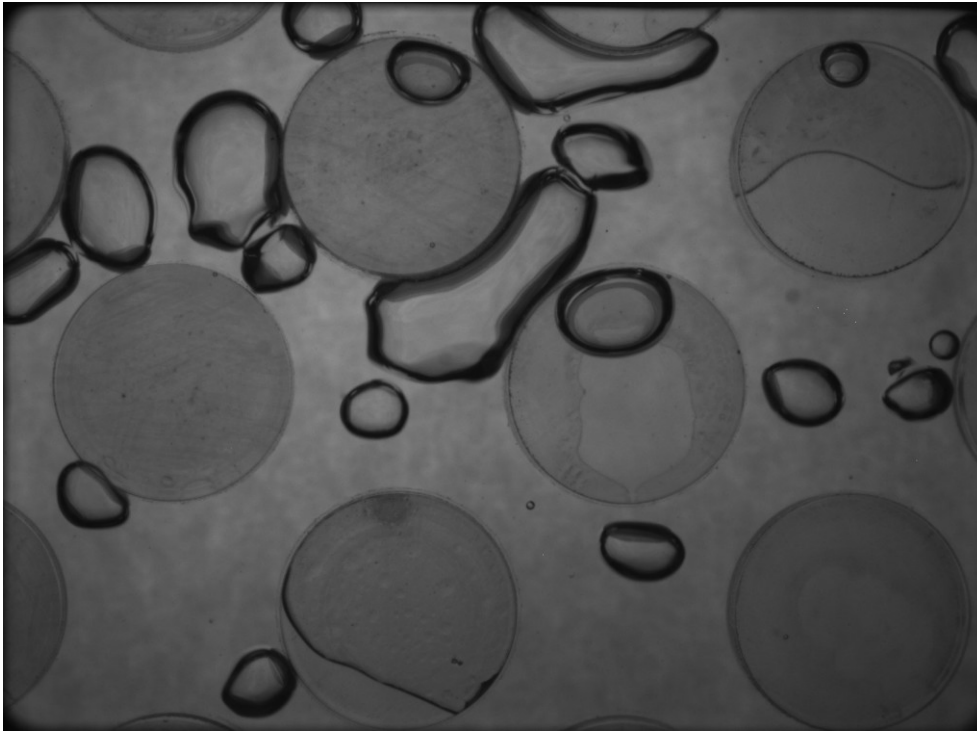


Figure 2.28 Example of the raw image captured by CCD camera.

Air phase identification was performed as the combination of two separate image processing algorithms, having different purposes, thus leading to either bubble edge detection or gaseous phase detection.

The edge tracing technique is based on the assumption that large intensity gradients are more likely to correspond to edges than the small intensity gradients. However, in most of the cases auto-thresholding operation is not sufficient to extract the gradients of the certain intensity, which might be directly associated with the particular boundaries. The common strategy to overcome that problem is to use *thresholding with hysteresis* (Canny, 1986; Olsson, 1993; Russ, 2011), based on the *double thresholding* of the image. The operation requires application of high and low thresholds to track the faint edges, recognised as the genuine ones and to generate gradients allowing for their identification. For that purpose, the original frame, named Image 1 was duplicated and a copy was labelled Image 2. In case of Image 1, threshold levels were adjusted in such a way, that only the etched boundaries of the bubbles of maximum pixel value were outlined, as seen in the Figure 2.29c. Image 2 was processed with the lower threshold in order to enhance the contours of bubbles, as seen in the Figure 2.29d and converted into binary image.

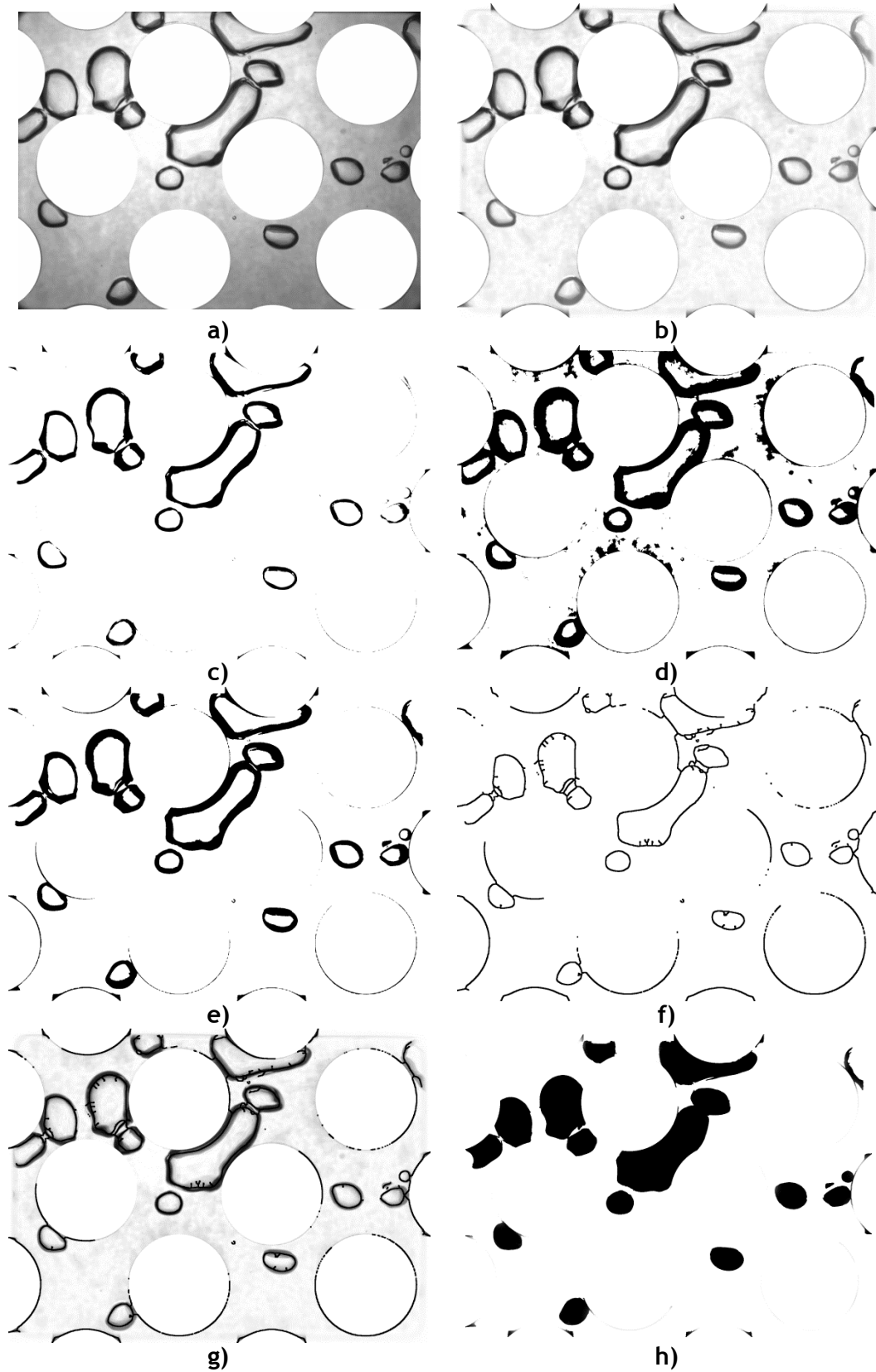


Figure 2.29 Image processing algorithm.

The noise generated during thresholding was consecutively removed using *Erode* algorithm (Russ, 2011), which eliminates black pixels in 3×3 white neighbourhood. The contours of the bubbles were additionally enhanced by applying *Dilate* algorithm (Russ, 2011), which adds black pixels to the edges of black objects. Image 1 and 2 were successively combined using *Binary Reconstruct* operation, referred also as the *Feature-AND* procedure (Russ, 2011), which reconstructs the outlined edges of the bubbles in the image called mask (Image 1), based on markers present in another image called seed (Image 2). The reconstructed image (Figure 2.29e) characterized by the thick edges was consecutively processed in binary thinning (*skeletonization*) algorithm (Lee and Kashyap, 1994), to extract the single pixel edges (centrelines), thus a topological skeleton of the bubbles, later enhanced in *Greyscale Dilation* algorithm (Figure 2.29f).

To identify air fraction the original image processed in equalization of the background illumination (background subtracting operation), was overlapped with the skeletonized image obtained in the edge detection train (Figure 2.29f). The result image (Figure 2.29g) was then auto-threshold and subjected to particle size distribution analysis, allowing disjoining within the image air bubbles from the water phase. This procedure is based on the identification of the bubbles' (particles) shapes, followed by measurement and characterization of their sizes (areas). The processed image may still contain some noise objects, such as small dots or the fragments of the disks outline. Because of that, the parameters of the particle size computing must be calibrated in such a way that the noise objects are excluded as much as possible, and thus by setting the limiting bubble area values in size filtering panel. Thus, taking into account visual inspection of the frames, the area of the filled, delineated air bubbles (masks) range was set from 0.05 cm^2 to infinity. Due to the diversity of the bubbles shapes, circularity range was set from 0 (elongated polygon) to 1 (perfect circle).

Finally, to determine volumetric fraction of air, it was assumed, that each bubble is a bi-dimensional thin object, characterized by projected area A_b with maximal thickness corresponding to the reactor gap width. Thus, for each frame, the volumetric fraction of air will be calculated as follows:

$$\varphi_{Air} = \frac{V_{Air}}{V_{mix}} \quad (2.76)$$

where φ_{Air} denotes volumetric fraction of air, V_{Air} is volume of air bubbles and V_{mix} is the volume of air-water mixture in the BCR. Knowing the bubble and the reactor thickness, and the reactor porosity, for each image with n bubbles φ_{Air} can be calculated as follows:

$$\varphi_{Air} = \frac{\sum_{i=1}^n A_b}{0.6 \cdot x_{img} \cdot y_{img}} \quad (2.77)$$

where A_b is total area of the bubbles, and x_{img} and y_{img} are image dimensions.

2.5.6 Clean Water Test

The procedure for the preparation of the test water using deoxygenating chemicals and stabilizing the whole aeration system was exactly the one described in Section 2.4.3. Characterization of the BCR as the aeration unit was performed using steady-state experiments, conducted in the open fluid flow system scheme. During experiment, BCR is continuously fed with deoxygenated water from the reservoir and the effluent from the outflow after passing through the DO flow cell is disposed in the drainage collector. The reaeration test is considered completed, once the DO effluent concentration reached a steady state value, maintained for at least 10 minutes.

To determine Oxygen Transfer Rate and aeration process parameters ($K_L a$, $SOTR$, $SOTE$ and SAE) clean water test was performed for each pair of water-air flow rates (Table 2.13). For each test, the value of oxygen saturation concentration, C_s , was determined on the base of the actual measurement of electrical conductivity (EC) and the temperature (T) (Tchobanoglous et al., 2003) of the test water in the reservoir.

Inlet (C_0), outlet (C_t) DO concentration and pressure drop (Δp) were continuously monitored and recorded with time intervals of 0.1 s.

2.5.6.1 Determination of the Process Parameters

To determine the $K_L a$ values using Equation (2.17), the volume of BCR and the oxygen flux must be computed. Knowing the porosity of the reactor, the active volume of the 2D reactor is $1.44 \cdot 10^{-4} \text{ m}^3$. The mass flux of oxygen is computed from the formula described by Equation (2.53). The standardized mass transfer coefficient $K_L a_{20}$ was computed from the formula described by Equation (2.20).

The Oxygen Transfer Rate for test and standard conditions was computed using Equations (2.23) and (2.24).

To assess AE and SAE values described by Equations (2.25) and (2.26), the power consumed by the whole aeration system, i.e. by water and air system must be considered. Power demand on water pumping was computed according to the Equation (2.56). Pressure drop in the multiphase (water-air) flow is higher than in single water phase. The main reason is not only reduction of flow area of both phases, but also the differences in the densities of both phases, yielding additional body force, resulting in different phase

velocities, non-uniform phase distribution and increase of shear rate in the denser water phase (Spicka, 2001). Design of the aeration systems considers device operation in the less favourable conditions, and thus Δp used in the computation of power demand for water pumping refers to the total pressure drop of the influent deoxygenated water and degassed oxygen rich water. The values of Δp measured during each experiment and recorded in the intervals of 0.1 s account for the local headloss at the entrance and discharge from the BCR, frictional and local headloss due to multiphase flow through a packed bed. The final Δp value considered in the computation is the average from all data registered during experiment.

Determination of power requirements for aeration in BCR was based on the determination of energy consumption by blower assessed from the adiabatic compression equation (2.28), considering blower efficiency of 70% and motor efficiency of 92%. Assumed blower inlet pressure equals 1.0 atm. For specific laboratory scale BCR system, computing power demand for blower requires proper blower sizing by prediction of the discharge pressure to give accurate values, which approximate experimental conditions to the real scale unit performance. Design discharge pressure of the blower, p_2 , is generally calculated for the worst case conditions and the higher operating air flow rate and needs to compensate: head losses for air piping from the blower location to the experimental installation considering high pipe roughness, partially throttled valves and fittings; head losses due to DWP of diffuser increased by additional losses due to device ageing, i.e. progressive fouling; peak high headloss during flow through the packed bed; safety factor and overpressure preventing surge conditions within the blower. On the other hand, actual operating discharge pressure is much lower than design pressure, thus calculation of the energy efficiency based only on the design pressure may impose misleading conclusions.

In this work, DWP of the fouled diffuser, safety factor and the overpressure, assumed according to blower design guidelines account for 0.3 bar. Pressure drop on the BCR is equivalent to the static head measured and determined for power demand for water pumping. The highest headloss accounts for frictional and local losses during flow through all devices and fittings, such as meters, blower's air filter and silencer, valvings and piping. Unfortunately, an exact analysis of air distribution system and blower's manufacturer data was not made, and from so, these losses have to be assumed accounting for the layout of a hypothetical full scale unit.

In this work, both, the worst and normal operating conditions were considered for blower sizing and power demand computation. For worst scenario, the assumed pressure head was 10.0 m H₂O and for the normal operation - 5 m, respectively. Therefore, the absolute values of discharge pressure for compressor used in the calculations are 2.0 and 1.5 bar,

respectively, representing typical values for the wastewater treatment installations (EPA, 2010; Quasim, 1999).

OTE and $SOTE$ are calculated from the Equations (2.29) and (2.30), where the influent and the effluent oxygen fluxes are computed from the modified formulas (2.61) and (2.62), accounting for the aeration system supplied by atmospheric air. Therefore considering mass fraction of oxygen in air of 23.2%, the oxygen flow rate expressed by Equation (2.59) the formula can be written as:

$$w_{O_2} = 0.232 \cdot \rho_{Air,N} \cdot Q_{Air} \quad (2.78)$$

where $\rho_{Air,N}$ is air density in normal conditions, i.e. 0 °C, which equals to 1.293 kg m³.

Therefore the Equations (2.29) and (2.30) can be written, as follows:

$$OTE = \frac{OTR}{0.232 \cdot \rho_{Air,N} \cdot Q_{Air}} \quad (2.79)$$

and assuming that $C_t = C_{S20}$

$$SOTE = \frac{SOTR}{0.232 \cdot \rho_{Air,N} \cdot Q_{Air}} \quad (2.80)$$

2.5.7 Results and Discussion

2.5.7.1 Flow Regime

In the present work, determination of the multiphase flow regimes was based on the visual analysis of the registered sequence of the images, for the specified air-water flow rates. The flow regimes are presented as contour maps as function of air and water superficial velocities, see Figure 2.30. Horizontal, layered distribution of the contour paths suggests that the character of the flow regime in BCR depends to a greater extent on the air velocity. Bubbly, homogenous flow regime (blue colour in the contour map) was observed for low values of the air velocity, up to 0.15 m s⁻¹, and characterized by the occurrence of the flat, rounded, oval, and drop-shaped bubbles, as can be seen in Figure 2.31a. The majority of the rounded bubbles have diameters up to 5 mm, while the drop shaped ones are up to 10 mm long. Dispersed flow (light blue colour) on the contour map was characterized by shredding bubble sizes due to the increased turbulence and coalescences

with the packing disks. This flow regime was observed at low air velocity range and with increasing water velocity. Slug flow (green colour) extends over relatively narrow gas velocity of the range 0.23-0.33 m s^{-1} when comparing with homogenous flow (bubbly and dispersed flow regimes). Slug flow regime is characterized by the passage of a sequence of slugs of liquid carrying dispersed bubbles of the diameter up to 3 mm, alternating with sections of separated flow within long bubbles, distorted due to the collisions with the packing disks, as seen in the Figure 2.31b.

As the air velocity increases, large bubbles are constantly ruptured into the smaller due to intense collisions with the reactor packing, and the flow regime shifts to dynamic and diverse churn regime (orange to red colour). This turbulent flow regime is characterized by intense bubble-bubble interactions, leading to wide bubble size distribution within the liquid phase, from the large elongated forms to the clusters of tiny (1 mm) to medium sized bubbles (4 mm), as can be seen in the Figure 2.31c.

Annular flow (dark red), was sporadically observed for the highest air velocity, 0.66 ms^{-1} , and the lowest water velocity in the range of 0.02 to 0.10 ms^{-1} . As seen in the Figure 2.31d, gas phase occupies nearly whole void space of the BCR and the liquid film flowing upwards forms thin bridges connecting neighboring packing disks.

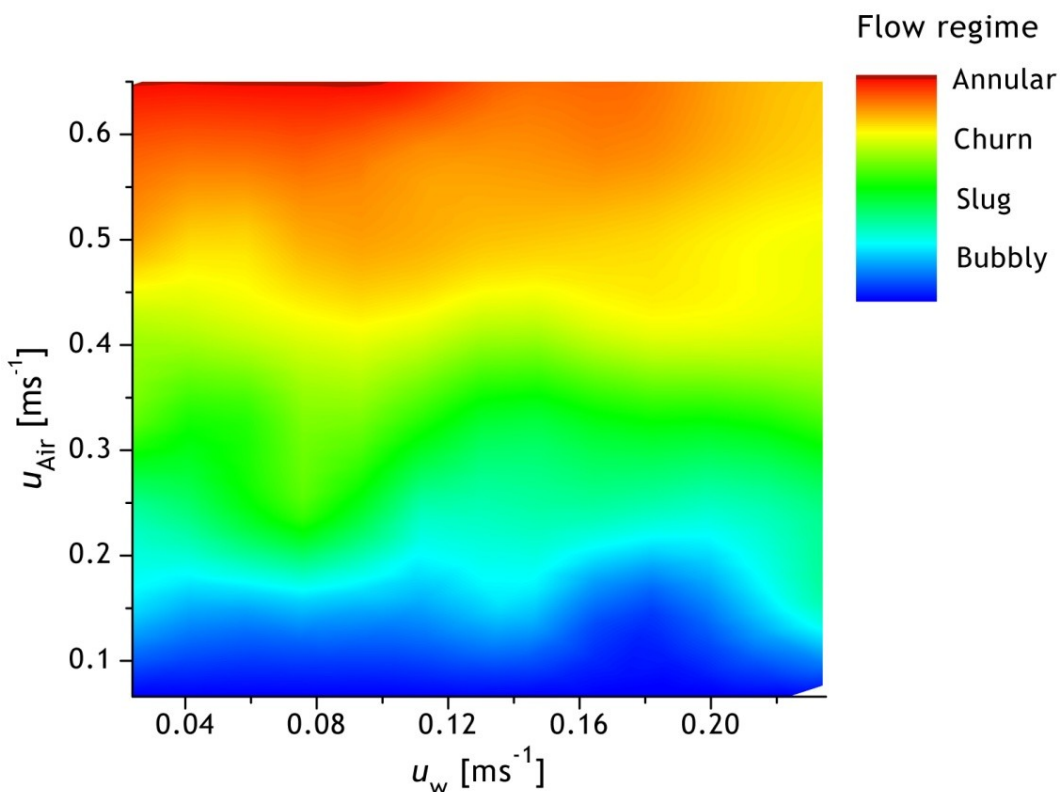


Figure 2.30 Flow regime contour maps obtained for the BCR.

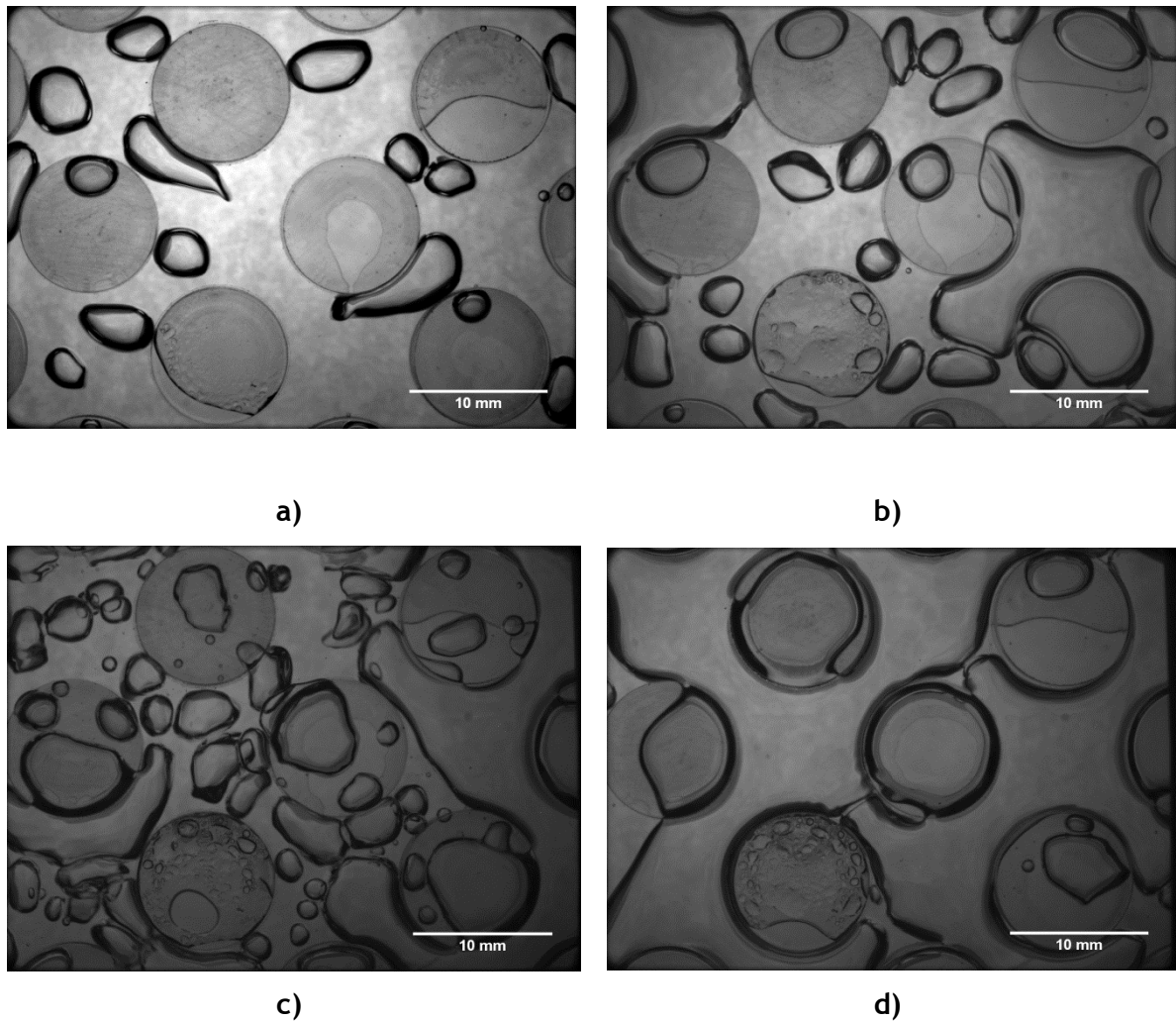


Figure 2.31 Different flow patterns observed in BCR: a) bubbly; b) slug; c) churn; and d) annular flow.

2.5.7.2 Gas Hold-up

Gas hold-up (φ_{Air}) was obtained *via* imaging technique coupled with computational procedure for different pairs of liquid-gas superficial velocities. Comparison of the results shown in contour maps of volumetric percentage of air (Figure 2.32) with flow regime (Figure 2.30) leads to the unambiguous conclusions, that in both cases, distribution pattern of the contour bands is mostly influenced by the surface air velocity, however the impact of the water flow rate on the gas hold-up is also visible in diagonal tendency of the contour bands.

The lowest volumetric air fraction, which constitutes 11-13% of the BCR volume, was observed for dispersed bubbly flow regime at low air and high water velocities. For developed homogenous flow at low air-water velocities, due to the presence of bubbles of larger area, φ_{Air} reaches values of 35-40%, but with increase of the water velocity, the bubbles content in the volume of fluid decreases to 24%. As the flow shifts to slug, due to

the presence of large bubble formations at low water velocities, high values of gas hold-up were obtained, ranging from 0.45-0.55. In churn flow, clusters of bubbles contribute to air volume fraction of the range 0.60-0.69, with the lower limit around 0.42. The highest values of φ_{Air} were almost 0.80 and were observed for the transition flow from churn to annular.

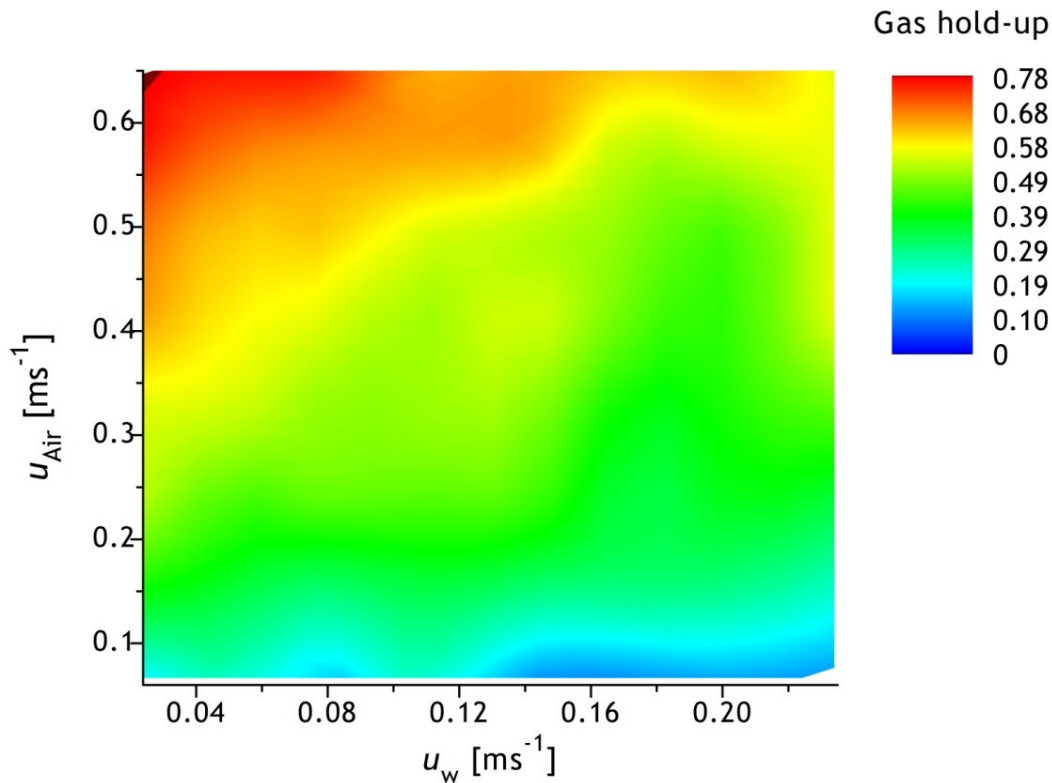


Figure 2.32 Contour map of gas hold-up obtained for different gas-fluid velocities.

2.5.7.3 Clean Water Test Results

When comparing the values of the aeration process parameters obtained from the steady-state clean water test experiments presented in Figures 2.33- 2.37 it is clear, that gas hold-up has strong impact on $k_L a_{20}$, $SOTR$, $SOTE$ and SAE . The maximal ranges of gas hold-up overlap the maxima of the transfer rate parameters, thus on the base of the volume fraction of air in BCR, optimal operating conditions in terms of air and water velocity ranges for the maximal efficiency of the aeration process can be defined.

When comparing the contour maps related to the changes of volumetric mass transfer coefficient and the oxygen transfer rate with air and water velocity, shown in Figure 2.33 and Figure 2.34, the same trend in values distributions are present, as $SOTR$ computations are based on the $k_L a_{20}$ value.

The maximal values of the volumetric mass transfer coefficient in the range of 37-55 s^{-1} were obtained for low water velocity of 0.08 ms^{-1} and high gas velocity ranging from 0.58

to 0.66 m s^{-1} , thus for the transition region from churn to annular flow. For the same conditions, the value of standard oxygen rate is ranging from 0.2 to $0.3 \text{ kgO}_2 \text{ h}^{-1}$.

For fully developed churn flow and the φ_{Air} above 50%, the values decrease to from 26 to 10 s^{-1} for $K_L a_{20}$ and $0.1 \text{ kgO}_2 \text{ h}^{-1}$ for $SOTR$.

For slug flow and φ_{Air} above 45% further decrease of $K_L a_{20}$ to 2 s^{-1} , and $0.02 \text{ kgO}_2 \text{ h}^{-1}$ for $SOTR$ was observed.

Further 50% decrease in values for both oxygen transfer parameters were observed for bubbly flow regime, and for the air hold-up up to 0.35.

At the lowest gas velocity and the highest water velocity the values, i.e. for dispersed flow with the air volume content of 0.11-0.13, the mass transfer is negligible.

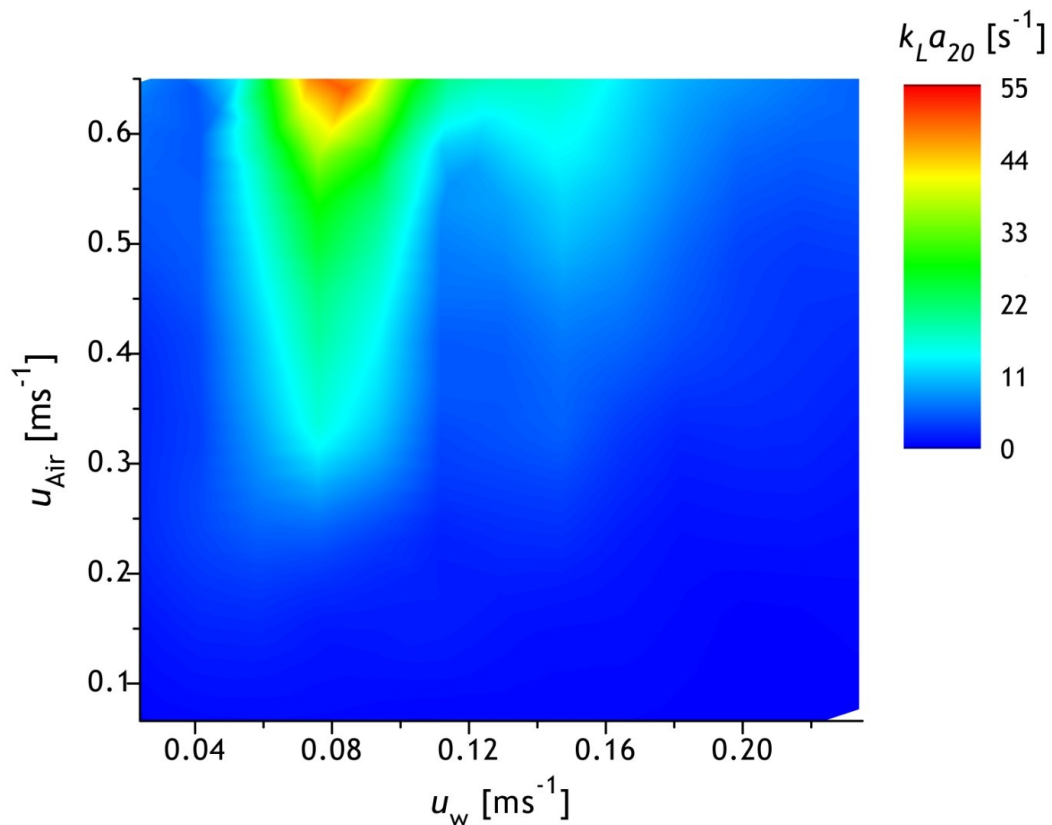


Figure 2.33 Standard volumetric mass coefficient $K_L a_{20}$ obtained in clean water test for different water and air velocities.

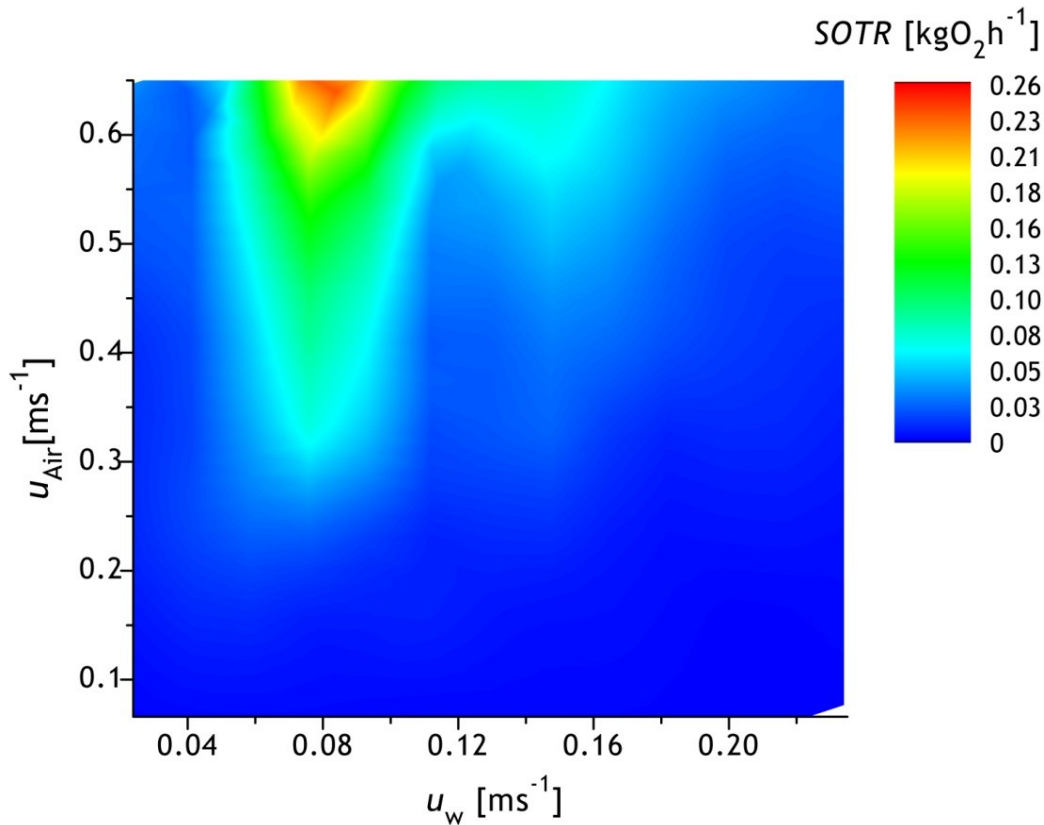


Figure 2.34 Standard Oxygen Transfer Rate $SOTR$ obtained in clean water test for different water and air velocities.

Contour map of standard oxygen transfer efficiency of BCR, computed for the equilibrium oxygen concentration in standard pressure and temperature conditions is shown in Figure 2.35. The impact of the flow regime and gas hold-up on the quantity of the oxygen absorbed results in identical distribution of the contour bands as in case of oxygen mass transfer parameters, $K_L a_{20}$ and $SOTR$. Thus the region of lowest $SOTE$ values, from 0-8% corresponds to dispersed flow regime. The highest $SOTE$ were obtained for the air-water flow rates characteristic for the transition from churn to annular flow, thus for the highest gas hold-up, yielding the average efficiencies in the range of 74-93%, with the maximal values from 121 to 150% for developed annular flow. For the wide band of churn flow, $SOTE$ values range from 37-51%, representing the maximal possible values obtained - for the top efficient state-of-the-art membrane diffusers, while for the slug flow, obtained efficiencies from 21-33% are comparable with the majority of the porous diffusers. For bubbly flow the percentage of oxygen absorbed is in average 13-16%.

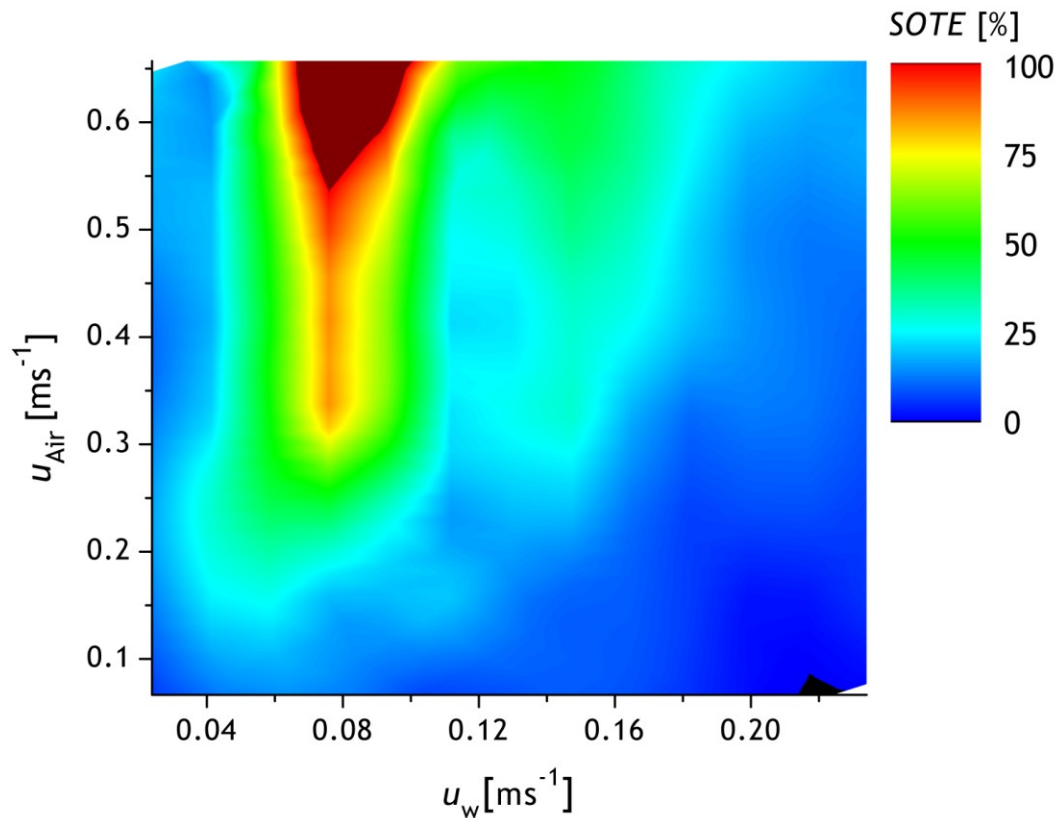


Figure 2.35 Standard Oxygen Transfer Rate *SOTE* obtained for different water and air velocities

The results obtained for standard aeration efficiency, *SAE*, are shown as contour maps in Figure 2.36 and Figure 2.37. *SAE* is the function of *SOTR* and the power expenditure of the aeration system. In BCR, power demand for water pumping depends on the pressure drop of the multiphase flow through the packed bed, which increases with the increase of the superficial velocities of the phases. Therefore P_w ranges from 0.03 to 0.90 W. Nonetheless, power demand on pumping is around one order lower than for air compression, P_{O_2} , which depends on the operating air flowrate and blower discharge pressure. Therefore, for blower operating in normal conditions, i.e. with typical values of headloss in the pipeline, valves, fittings, diffuser and other devices included in the aeration system, power expenditure ranges from 1.0 to 10.0 W, due to changes in air flow rate with constant blower discharge pressure of 1.5 bar. The most demanding operating conditions in terms of headloss for air flow through rough pipeline, throttled valves and fouled diffuser, yield in a blower discharge pressure of 2.0 bar, corresponding to the power expenditure ranging from 1.8 to 17.8 W. The tendency of *SAE* values is similar to contour maps of *SOTR*, as can be seen in the Figure 2.36 and Figure 2.37.

For the average operating conditions, the maximum values of *SAE* obtained for the peak hold-up and shift from churn to annular flow, range from 20 to 25 kgO₂ kW⁻¹ h⁻¹. These values are couple of times higher than the corresponding standard efficiencies of the

commercially used state of the art aeration devices, and are due to the optimal conditions for efficient mass transfer within packed structure of the bubble column. When the most challenging operating conditions are considered, SAE decreases to 12-14 $\text{kgO}_2 \text{ kW}^{-1} \text{ h}^{-1}$.

For fully developed churn flow and the φ_{Air} above 0.5, average SAE values from 4.2 to 8.6 $\text{kgO}_2 \text{ kW}^{-1} \text{ h}^{-1}$ were obtained for blower pressure of 1.5 bar. These efficiencies correspond to the upper range for membrane discs, panels and perforated EPDM membrane tubes (Mueller et al., 2002). The peak values from nearly 13.0 to 16.2 $\text{kgO}_2 \text{ kW}^{-1} \text{ h}^{-1}$ were observed for low water and high air velocities, contrary to the lowest values, from 2.0 to 3.6 $\text{kgO}_2 \text{ kW}^{-1} \text{ h}^{-1}$ obtained for the high water and low air flow rates. In that range, the efficiency are approximately equal to the low efficient porous diffusers or non-porous perforated tubes (Mueller et al., 2002). Increase of blower pressure due to more demanding operating conditions yields with the average SAE values for churn flow from 2.4 to 4.9 $\text{kgO}_2 \text{ kW}^{-1} \text{ h}^{-1}$, representing typical middle values for the majority for porous diffusers. Similarly, the maximum values from 7.0 to 9.2 $\text{kgO}_2 \text{ kW}^{-1} \text{ h}^{-1}$, were obtained for low water and high air velocities, and the minimum values from 1.1 to 2.1 $\text{kgO}_2 \text{ kW}^{-1} \text{ h}^{-1}$, which are in the range of typical values for nonporous, hybrid and mechanical devices, were observed for the high water- low air velocities.

For slug flow and φ_{Air} above 0.45, the average values of aeration efficiency, which range from nearly 3.0 to 6.9 $\text{kgO}_2 \text{ kW}^{-1} \text{ h}^{-1}$ are obtained for low to moderate water velocities and moderate air velocities. These values correspond to the wide range of ceramic, plastic and membrane diffusers. The lowest values of 0.9 -1.3 $\text{kgO}_2 \text{ kW}^{-1} \text{ h}^{-1}$ are observed for low air - high water flow rates, and are typical of nonporous, mechanic, and hybrid aeration units. In the worst case scenario in terms of blower operating pressure, the average aeration efficiency decrease to 1.2 to 3.9 $\text{kgO}_2 \text{ kW}^{-1} \text{ h}^{-1}$, characteristic for broad range of nonporous, hybrid and mechanical units, and also for lower limits for porous diffusers. The lowest values ranging from 0.5-1.2 $\text{kgO}_2 \text{ kW}^{-1} \text{ h}^{-1}$ correspond to aspirating aerators and low efficient high-speed devices.

For low gas hold-up of 0.35 and bubbly flow regime, the average SAE is 0.9-2.2 $\text{kgO}_2 \text{ kW}^{-1} \text{ h}^{-1}$, which represents typical values for nonporous diffusers, jet aerators, U-tube aerators and the whole range of the mechanical aeration devices. The maximal values obtained at the same conditions ranged from 2.7 to 4.6 $\text{kgO}_2 \text{ kW}^{-1} \text{ h}^{-1}$, corresponding to the lower efficiency limits of ceramic discs and domes. Considering the worsening of the blower operating conditions, the average values decrease to 0.5-1.3 $\text{kgO}_2 \text{ kW}^{-1} \text{ h}^{-1}$ shifting towards the efficiencies typical for aspirating and high-speed aerators, while the peak efficiencies from

1.6 to 2.6 $\text{kgO}_2 \text{ kW}^{-1} \text{ h}^{-1}$ correspond to nonporous, both hybrid and mechanical units performance. For both operating scenarios, low values up to 0.7 and 0.6 $\text{kgO}_2 \text{ kW}^{-1} \text{ h}^{-1}$, respectively, were obtained for the higher water flow rates. At the lowest gas velocity and the highest water velocity the values, i.e. for dispersed flow with the air volume content of 0.11-0.13, the standard aeration efficiency is almost zero.

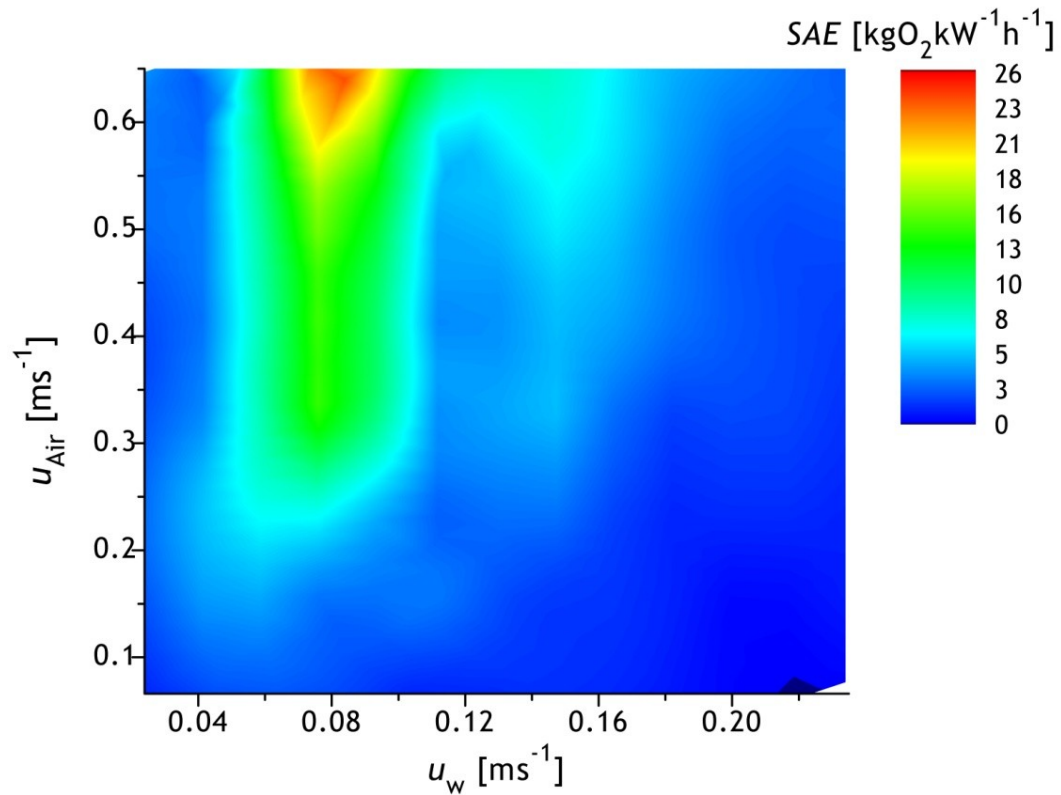


Figure 2.36 Standard Aeration Efficiency *SAE* obtained for different water and air velocities. for blower discharge pressure of 1.5 bar.

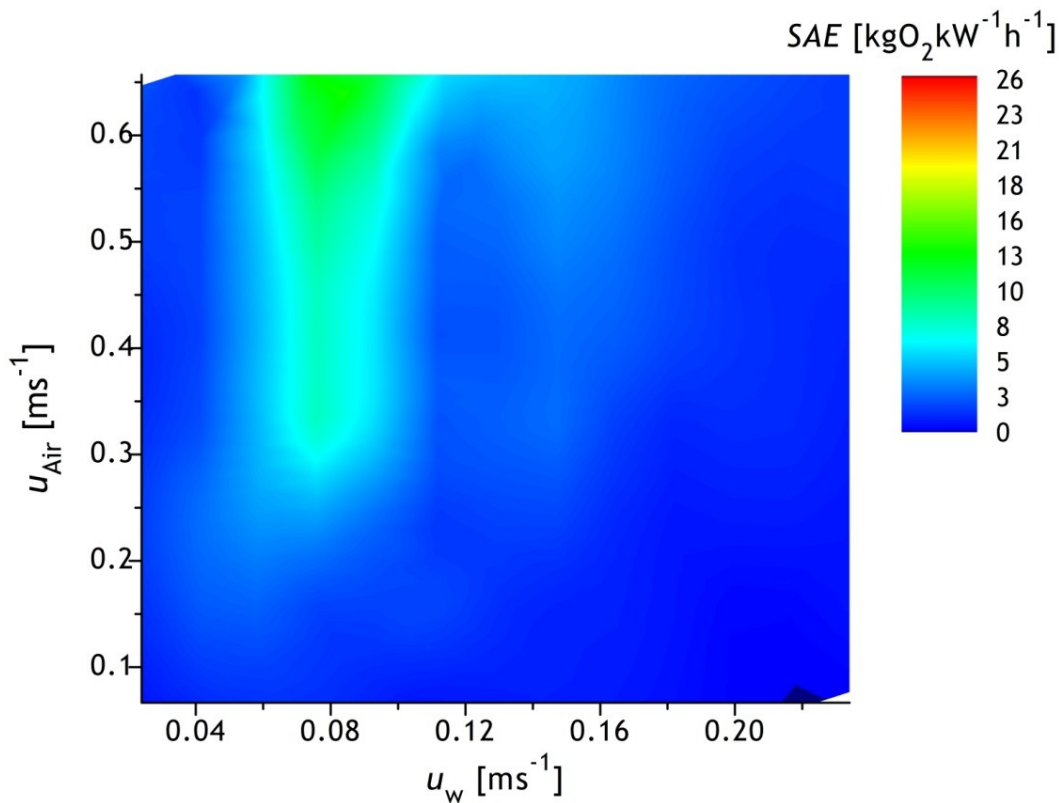


Figure 2.37 Standard Aeration Efficiency SAE obtained for different water and air velocities for blower discharge pressure of 2.0 bar.

2.6 Conclusions

In this chapter, the process principles, standard methods for device testing and the review of the recent trends in aeration of the AS systems were given.

A novel aeration device, Pressurized Aeration Chamber was introduced. 2D and 3D CFD studies of the PAC were made. The objective of 2D simulations was to represent the main trends in oxygen concentration distribution within all PAC layouts, pointing out the most efficient geometries in terms of oxygen transfer efficiency. Three out of seven geometries simulated outperformed the remaining ones, yielding higher DO content in the outflow, and consecutively were further studied with the 3D CFD simulations. It was shown, that PAC chamber with baffles placed in the bottom enhanced oxygen mass transfer up to 50%, when compared with the rectangular geometry. Further introduction of the baffles on the topwall yields negligible ca. 1% improvement of the outflow DO concentration. Efficient PAC geometry with baffles fixed at the bottom was constructed in lab-scale for reaeration tests, to determine oxygen transfer rate parameters in steady and unsteady clean water tests and validate results obtained from the CFD studies.

Steady-state aeration experiments were performed in a PAC, showing high process efficiencies. The lowest value of $SOTE$, 120%, determined for the oxygen pressure of

0.5 bar, is higher than the corresponding values of currently most efficient aeration systems, i.e. membrane diffusers, having the efficiencies up to 44%. With the increase of the operation pressure, *SOTE* increased to 200%. More energy efficient solutions were obtained for the lowest operating pressure, resulting in *SAE* of $8 \text{ kg O}_2 \text{ kW}^{-1} \text{ h}^{-1}$ that is higher than the most conventional mechanical and diffused aeration systems. Lowest average *SAE* of nearly $5 \text{ kg O}_2 \text{ kW}^{-1} \text{ h}^{-1}$ were obtained for the oxygen pressure of 1.5 bar, which corresponds to typical efficiencies of porous diffusers.

Both unsteady-state and steady-state reaeration tests were performed. Standard aeration efficiencies obtained from the unsteady-state experiments are lower than in steady approach, ranging from $0.7\text{-}1.2 \text{ kgO}_2 \text{ kW}^{-1} \text{ h}^{-1}$. These values are similar to the aeration efficiencies typical for nonporous diffusers, jet aerators, and a wide range of the mechanical units such as: submerged turbines, including devices equipped with draft tubes; high-speed aerators; and aspirating aerators. The lower values from unsteady-state tests may be explained from the fact that the experiments were run in a close loop, and with time the system is operated closer to the DO saturation conditions, which means that in the PAC there is a reduction of the area where steeper concentration gradients between gas and liquid phases occurs, which reduces the respective oxygen flux.

Simulated with CFD code 3D PAC complies with the process conditions of the steady state clean water test. The average value of the aeration efficiency obtained from the multiple reaeration experiments amounts $4.5 \text{ kgO}_2 \text{ kW}^{-1} \text{ h}^{-1}$, what is in good agreement with the *AE* obtained from the CFD simulations that is of almost $4.0 \text{ kgO}_2 \text{ kW}^{-1} \text{ h}^{-1}$.

BCR was also studied for aeration in AS processes. Impact of the flow regime on the gas hold-up in the reactor was determined. The lowest gas hold-up of 13% was observed for dispersed flow and with increase of the air velocity reaches values up to 80% for the transition flow from churn to annular regime.

In BCR gas hold-up has strong impact on aeration process performance, and can be used as a design parameter to set optimal operating conditions, i.e. air and water velocity ranges for the maximal oxygenation efficiency. Considering clean water test results it is clear, that the highest ranges of volumetric air content observed for transition from churn to annular flow regime overlap with the maxima of the transfer rate parameters, while in conditions of dispersed flow, the oxygen mass transfer is negligible. Thus the average values of *SOTE* obtained from the experiments are in the range of 37-93%, thus distinctly higher than the top state-of-the-art aeration devices, and may reach up to 150%.

The values of standard aeration efficiency, *SAE*, depend in greater extent from the power demand by blower and thus operating air flow rates. The maximal values of *SAE* obtained for the peak hold-up are up to $25 \text{ kgO}_2 \text{ kW}^{-1} \text{ h}^{-1}$ and thus higher than the corresponding standard efficiencies of the commercially used state of the art aeration devices. For the average operating conditions and hold-up of 50%, obtained *SAE* values were in the range of $5\text{-}9 \text{ kgO}_2 \text{ kW}^{-1} \text{ h}^{-1}$ corresponding to the upper range for membrane diffusers.

Adaptation of the BCR system to wastewater aeration imposes sharp limits, especially on the bubble regime involved. As the efficient aeration depends on the extended contact time between AS flocs and air bubbles, and later, delayed escape of the bubbles to the atmosphere, thus oxygenated stream should contain in majority fine bubbles. Therefore instead of operating in the air-water velocity ranges characteristic for annular flow, which characterizes with highest oxygen transfer rates, heterogeneous churn flow with the efficiencies corresponding to wide range of porous diffusers seems to be reasonable solution. Additionally, aerated effluent should have momentum sufficient to impart velocity to the wastewater volume, which allow for at least local mixing and mass transfer between the fluid layers in the aeration tank due to ascending pathlines of the bubbles. While PAC performance combines high efficient aerating with mixing due to energy of the discharged fluid plume, low pressure conditions in BCR may require implementation of additional momentum sources, such as pumps and mixers (flow boosters), which may have, to a greater or lesser extents, further adverse effects on power expenditure of the whole aeration system. In addition to that, application of BCR in activated sludge systems may be limited due to clogging of the column packing, which increases pressure drop in the system and requires frequent maintenance procedures, such as pressurized backflow washing.

3 Hydrodynamics of the Oxidation Ditch

3.1 Introduction

The main objective of the experimental studies was to assess the hydrodynamics of two different oxidation ditches, namely pilot-scale tubular piston flow reactor and full-scale oxidation ditch in municipal wastewater treatment plant. The chapter is divided in three parts concerning: literature review, pilot- and full-scale experimental studies.

The main objective of the literature review section is the brief presentation of the oxidation ditch process and operation characteristics. A literature review considering studies performed on several ditches and the variety of methods used in these systems to assess flow characteristics is also given.

Second section considers experimental studies carried out on a pilot-scale tubular closed-loop reactor during system start-up. The obtained hydrodynamic data was the velocity, dissolved oxygen (DO), mixed liquor suspended solids and nutrients concentration (COD , ammonia, nitrates and orthophosphates) profiles along the reactor. Additionally, reactor performance was evaluated from the results of Residence Time Distribution (RTD) experiments using pulse and step tracer techniques.

Third part of this chapter considers experimental studies carried out on a real-scale oxidation ditch of the municipal wastewater treatment plant situated in Viana do Castelo. Here, to assess the overall flow patterns within the ditch, DO content was measured at various depths of the tank, and the profiles along the ditch were made for intermittently operated aeration system. Additionally, to complete hydrodynamic data, horizontal

velocity close to the wastewater surface, nutrients (*COD*, ammonia, nitrates and orthophosphates) and total solids content were determined for all sampling points along the ditch.

3.2 Literature Review

An oxidation ditch is a fully demonstrated secondary wastewater biological treatment technology and one of the well known modifications of Activated Sludge (AS) processes (Benefield and Randall, 1980; EPA, 2000), operated in the extended aeration mode and with long solids retention times (SRTs). This technology was developed in 1950s in the Netherlands (Pasveer, 1962), and although it has been the focus of relatively few publications, the process is widespread and it is still commonly used in new Wastewater Treatment Plants (WWTPs) serving small to medium-sized municipalities, due to its robustness and efficiency in terms of Biological Oxygen Demand (BOD) and nutrients removal up to 75-95 % (Benefield and Randall, 1980). The oxidation ditch can be operated as a continuous or intermittent process, due to its buffer capacity against variable flows, loadings and also unfavorable environmental temperatures.

By the late 1970s and mid 1980s in Europe, over 2000 municipal WWTPs were using Pasveer ditches, alongside with over 200 Carrousel™ systems. Only in the U.S., by the year 2000, oxidation ditches found application in more than 9200 municipal WWTPs (EPA, 2000). Extended aeration process in oxidation ditches is also commonly used in WWTPs in Portugal, e.g. in Vila Nova de Gaia- Febros, Viana do Castelo- Areosa, Guimarães- Serzedelo II, Óbidos- Charneca, Resende- Mirão, Faro, Ponte de Lima, Seia, and more.

A typical oxidation ditch is a closed loop system, consisting of a single or multi- channel configuration within a ring, oval or horseshoe shaped basin, equipped with aeration and mixing devices. Besides the original Pasveer-type oxidation ditches with the horizontal aeration, and the Carrousel, where the aerators are vertical (Potier et al., 2005), other type of systems with different channel, aeration and propulsion devices configurations had been developed, such as Orbal, Total Barrier Oxidation Ditch, or Jet Aeration Channel (Mandt and Bell, 1984). Due to such specific tank configuration, the oxidation ditches are classified as racetrack type reactors, in which the aeration and mixing devices promote unidirectional channel flow with average velocities in the range of 0.25-0.40 m s⁻¹ (Abusam et al., 2002; Tchobanoglous et al., 2003), sufficient to maintain the activated sludge biomass suspended in the mixed liquor, and assuring high dilution of the influent stream.

Biological wastewater treatment efficiency in such closed-loop continuous flow reactors, as the oxidation ditches, depends to a great extent on the overall flow patterns.

Therefore, overall mixing inside the ditch determines the distribution of the oxygen within the mixed liquor volume, creating aerobic and anoxic zones. Nonetheless, in the design of most activated sludge units, the assumption of ideal reactor model is used, and thus the actual reactor hydrodynamics is not taken into account (Stamou, 2008). Considering slow biochemical reactions in the activated sludge, oxidation ditches are usually classified as completely mixed systems over the hydraulic residence time (EPA, 2000), however when considering multi-channel configuration, strong plug flow characteristics are observed along one loop - channel, without accounting for the effects of internal recirculation (Barnes et al., 1983; Tchobanoglous et al., 2003). According to that, characteristic feature is occurrence of large DO gradients along the ditch while the other components, such as ammonia or COD concentrations are spatially homogenized (Nakamachi et al., 2012). From this reason the theoretical analysis of the flow regime within the oxidation ditch involves following types of ideal reactor models: Plug Flow Reactor with Recirculation (PFRR); and Continuous Stirred Tank Reactors (CSTRs) in Series with recirculation from the last reactor to the first one (Potier et al., 2005). However in most of the practical cases, none of the ideal assumptions corresponds to the actual flow conditions during operation of the real scale oxidation ditch. Therefore the knowledge about the actual flow behaviour, thus hydrodynamics, is of crucial importance to assess and evaluate design, reactor performance and for the troubleshooting (Levenspiel, 1999; Wolf and Resnick, 1963).

In engineering practice, assessment of flow regime, and thus overall mixing phenomena can be achieved with an experimental approach by determination of the complete velocity distribution map within the tank, which is not a feasible task most of the times, considering dimensions of real scale units (Pereira et al., 2012; Stamou, 2008). The alternative approach to characterize non-ideal flow and mixing in the tank is determination of the residence time distribution (RTD) of the fluid. The RTD is the probability function, which describes the length of time a fluid element spends inside the reactor before the exit. The distribution of the times for the stream of fluid exiting the reactor system is defined as the exit age distribution, known as $E(t)$ function or the RTD of the fluid (Levenspiel, 1999). Considering different paths of the fluid elements within the continuous flow reactors, such as oxidation ditches, the RTD data can be used to predict such adverse phenomena, as channeling and recycling of the flow, or formation of the dead zones, and finally to assess the mixing time, which can be crucial regarding to the chemical or biochemical reaction yield, troubleshooting of the reactor and improved design of the future vessels. The experimental approach to assess RTD through non-reactive tracer technique is based on the measurement of the system response to a disturbance applied to the reactor inlet, where the inert tracer is introduced as a pulse,

impulse, step or periodic function and its concentration is measured at the outlet in function of time (Wolf and Resnick, 1963).

Within all the work published on the oxidation ditch performance, only few consider assessment of the hydrodynamics based on the RTD experiments. One of the works (Potier et al., 2005) considered determination of the impact of geometrical and operational parameters on the axial dispersion in bench-scale and full scale oxidation ditches through pulse tracer experiments using lithium chloride (LiCl). Follow-up studies (Le Moullec et al., 2008b) in the same bench-scale oxidation ditch (Potier et al., 2005) consisted of over 80 RTD experiments carried out by injecting pulses of a sodium chloride (NaCl) solution. From these experiments the mean residence time and axial dispersion coefficients were determined, and were used to validate RTD data obtained from the CFD simulations. To complete the hydrodynamic data, velocity field was additionally measured using Laser Doppler Velocimetry (LDV). In the other work carried out in a full scale oxidation ditch process, the CarrouselTM (Nakamachi et al., 2012), besides the measurements of the three-dimensional velocity field, the RTDs data were obtained from the impulse tracer experiments using fluorescent uranium dye. Here, the assessment of the flow regime, which was strong plug flow, was used to optimize operation of the diffused aeration system and flow boosters, which could lead to energy savings.

Most of the experimental work carried on the full-scale oxidation ditches considered flow field assessment based on the measurements of the horizontal velocity. It was proven that even small changes in the axial velocity may have dramatic effect on the oxygen profiles, and thus on the nitrogen removal in oxidation ditches. Therefore, the horizontal velocity should be treated as an important process variable to control total nitrogen removal efficiency. Furthermore it was stated, that decoupling of aeration and propulsion functions allows maintaining robust and energy efficient plant operation in such AS systems, and thus mechanical aeration should be replaced by air diffusers cooperating with flow boosters (Abusam, 2002).

In the recent decade, an important input into the scientific achievements on the knowledge of oxidation ditch flow field was made by Cemagref (today Irstea) research group. The subject of several publications was development of the measurement methods for characterization of the hydrodynamics in the oxidation ditches with the degree of required accuracy to calibrate and validate CFD models (Fayolle et al., 2007; Fayolle et al., 2010; Fayolle et al., 2006; Gillot and Héduit, 2000). The experiments were carried on pilot to full scale ditches having various configurations within oblong and annular shaped tanks, and where the aeration process was dissociated from mixing by introduction of

membrane diffusers and slow speed mixers. The hydrodynamics of the oxidation ditch was obtained from the on-site measurements of the axial liquid velocity and the bubble size distributions within the tanks, aiming determination of the flow impact, the local gas hold-ups and the oxygen transfer efficiency. It was shown, that the hydrodynamics of the channel reactors aerated with the bottom diffusers is controlled by the competition between the vertical bubble plume and the horizontal fluid flow. Thus, for the specific diffuser grid configuration, the influence of the air flow rate on the oxygen transfer coefficient can be distinctly higher with an absence of the horizontal motion of the fluid (Gillot and Héduit, 2000). Similar studies carried on the pilot scale oxidation ditch aerated with fine pore bottom diffusers and agitated with impeller (Vermande et al., 2007), concerned the impact of the agitator position and rotating speed on the horizontal velocity and oxygen profiles within the tank. Here it was also found, that with the absence of the horizontal velocity, an increasing, linear relationship can be obtained between the local mass transfer and air flow rate. Under such conditions a vertical liquid flow loop, known as spiral flow is generated by rising bubbles. Although spiral flow increases local gas hold-up, it is counteracted by increased absolute velocity of the gas bubbles and larger interfacial area. Under conditions of horizontal liquid motion induced by rotating impeller, increase of the wastewater velocity causes neutralization of the spiral flow patterns and decrease of the gas hold-up. Nonetheless, greater dispersion of the air plumes results in higher local mass transfer coefficient due to longer contact times between both liquid and gaseous phases. Thus, application of the axial velocity of 0.4 m s^{-1} may enhance oxygen transfer coefficient for up to 30% (Fayolle et al., 2007; Fayolle et al., 2010; Fayolle et al., 2006; Vermande et al., 2007).

Another work (Diamantis et al., 2010) focus on flow behaviour in the oval, single channel oxidation ditch having uniform field of the bottom diffusers allowing for development of the aerated and anoxic zone within one tank. General rule of thumb is assumption that aeration system operating at high aeration rates ensures high DO content and adequate, “good” mixing. Nevertheless, the authors proved, that in oxidation ditches with incorrect aerators arrangement, even slight changes of the operating parameters, namely increase of the aeration rate may lead to undesirable consequences affecting mixing within the tank, such as strong stratification and short-circuiting of the flow, and creation of local zones in the mid-depth where the velocities drop to zero. As the result, distinctly reduced volume of the ditch was actually available for the effective biological wastewater treatment.

The examples of different approach of the hydrodynamics assessment from the velocity and concentration profiles within the wastewater tank can also be found in the literature (Le Moullec et al., 2010a; Lesage et al., 2003). Several works consider numerical studies on coupling of the hydrodynamics with mass transfer and biokinetics models to simulate activated sludge reactor and validation of the results on pilot and real scale oxidation ditches (Le Moullec et al., 2010a, b; Lesage et al., 2003). In agreement with the conclusions from previous work (Abusam et al., 2002) it was found, that DO and nutrient concentration profiles along the ditch depend on the horizontal liquid velocity. Furthermore, as the oxygen transfer capacity depends also on the horizontal liquid motion thus the hydrodynamics of oxidation ditch has an impact on overall nutrient conversion rates within the bioreactor.

The knowledge of the accurate system hydrodynamics found practical application in design of new utilities and modification of the existing activated sludge systems aiming not only enhancement of the treatment process performance, but also maximal reduction of the exploitation costs allowing to maintain high quality effluent. And thus, one of the works (Yang et al., 2011) considered study on the hydrodynamics in multichannel Carrousel™ ditch simulated with CFD codes and validated experimentally on the full scale tank. Determination of the velocity and dissolved oxygen patterns within the ditch led to modification of the mechanical aerator placement, resulting in significant energy savings and maintain high effluent quality.

Measurement of the flow characteristics in full-scale oxidation ditches is generally difficult, due to the presence of solid, liquid and gaseous phase and predominantly involves application of the flow disturbing measurement methods, based on the introduction into the system different sensors and sampling devices. At the same time, increasing popularity of the CFD-aided design requires application of advanced, non-intrusive techniques to assess multiphase flow behaviour in the lab-scale models of the oxidation ditches. Thus, several works considered application of Laser Doppler Anemometry (LDA) to validate CFD simulations of the airlift oxidation ditch system (Xu et al., 2010) and oxidation ditch equipped with inversed umbrella surface aerators (Fan et al., 2010). Another work, which also focused on solid-liquid flow in oxidation ditch used Particle Image Velocimetry (PIV) to study settling velocity of the activated sludge (Chen et al., 2006). Here, the aim of LDA and PIV experiments, besides the overall flow patterns characterization, was to evaluate the influence of the aerator performance and tank geometry on the efficient dispersion of the particles mimicking the motion of the suspended activated sludge flocs within the ditch.

At the same time, other works consider validation of the simulated gas-liquid flow field in the oxidation ditches aerated with porous diffusers and agitated with slow speed mixers using Standard Imaging technique combined with LDA (Le Moullec et al., 2010a, b; Le Moullec et al., 2008b), aiming the assessment of the oxygen mass transfer and wastewater treatment efficiency.

3.3 Pilot Scale Studies

The aim of the experimental studies is characterization of the hydrodynamics of the pilot scale oxidation ditch. The experiments were conducted on a closed-loop tubular piston flow reactor with recirculation (PFRR ditch), which configuration is an approximation of the oxidation ditch system.

In this work, hydrodynamics of the pilot scale oxidation ditch was assessed in two experimental approaches: by determination of the velocity, *DO*, *TSS* and nutrients concentration profiles along the ditch; and determination of the RTD of the fluid from tracer experiments.

3.3.1 Piston Flow Reactor Set-up

The pilot scale experimental system was built in the WWTP Pavilion, situated in the Faculty of Engineering campus (Porto, Portugal). The experimental set-up, shown in the Figure 3.1 consists of a tubular piston flow reactor with recirculation (PFRR); storage tank; feed and recirculation pump; secondary settler; and tubing connecting all components.

The PFRR reactor was designed as 4.40 m long closed-loop reactor made of PVC tube with internal diameter 0.1 m. The total volume of the reactor is 35 L. A detailed view of the PFRR reactor is shown in Figure 3.2. Nine sampling points were made in the length of the reactor's body, allowing for multi-sensor probe placement during measurements (Figure 3.3). The distribution of the sampling points was chosen to give the best representation of the mixing and biokinetics along the ditch. Numbering of the sampling points was in accordance with the flow direction (counter-clockwise), starting with the first one located downstream the paddlewheel aerator. The scheme of the distribution of the numbered sampling points is presented in Figure 3.4. Point 1 is the ditch inlet, where feed tubing is placed. Outlet tube is located in the ditch bottom, between Point 1 and paddlewheel impeller, allowing for controlled gravitational discharge of the effluent into the clarifier. The recirculation pipe from the clarifier is connected to the feed pipe from the influent storage tank.



Figure 3.1 Pilot installation of the tubular closed-loop PFRR with feed tank and the secondary settler.

The circulation of the mixed liquor within the PFRR in the counter-clockwise direction is kept by means of horizontal paddlewheel aerator, shown in detail in Figure 3.5. The device is made of stainless steel and consists of four paddles fixed to the horizontal shaft. The impeller is fitted with geared motor (Panasonic, model M9MC90GKP4W1) with variable speed drive (Panasonic, model MZ9G15B) and the propulsion rate is controlled by frequency inverter (Sinamics G110). During operation the reactor is filled with mixed liquor up to approximately 57% of the cross-section to avoid excessive splashing of the liquid out of the reactor by the paddlewheel aerator. Thus, the active volume of the vessel is 20 L. Besides surface aeration unit, the PFRR ditch is additionally equipped with the diffused air unit (Figure 3.6), consisting of five porous diffusers, each with 8 cm long connected in series to the air pipeline. The diffusers are placed in the bottom of the reactor in Point 4, opposite side to the paddlewheel rotor. Atmospheric air is supplied through distribution manifold connected to an outdoor air compression module mounted on the roof of the building. Air pressure is regulated by pressure reducer equipped with air filter (Pneumax, model FIMET), operating in the range from 0 to 4 bar, connected directly to the indoor air manifold below shut-off valve.

3 Hydrodynamics of the Oxidation Ditch

The PFRR ditch was fed by the synthetic influent stored in the polyethylene container having 500 L capacity and the effluent was directed to the radial secondary clarifier made of acrylic, having active volume of 40 L. As the mean hydraulic retention time of the fluid is 4 h, thus the influent, effluent and sludge recirculation flow rates were regulated by means of constant flowrate peristaltic pump (Watson Marlow SciQ 300), connected to the timer. The waste sludge was directed from the clarifier to the sewer drainage.

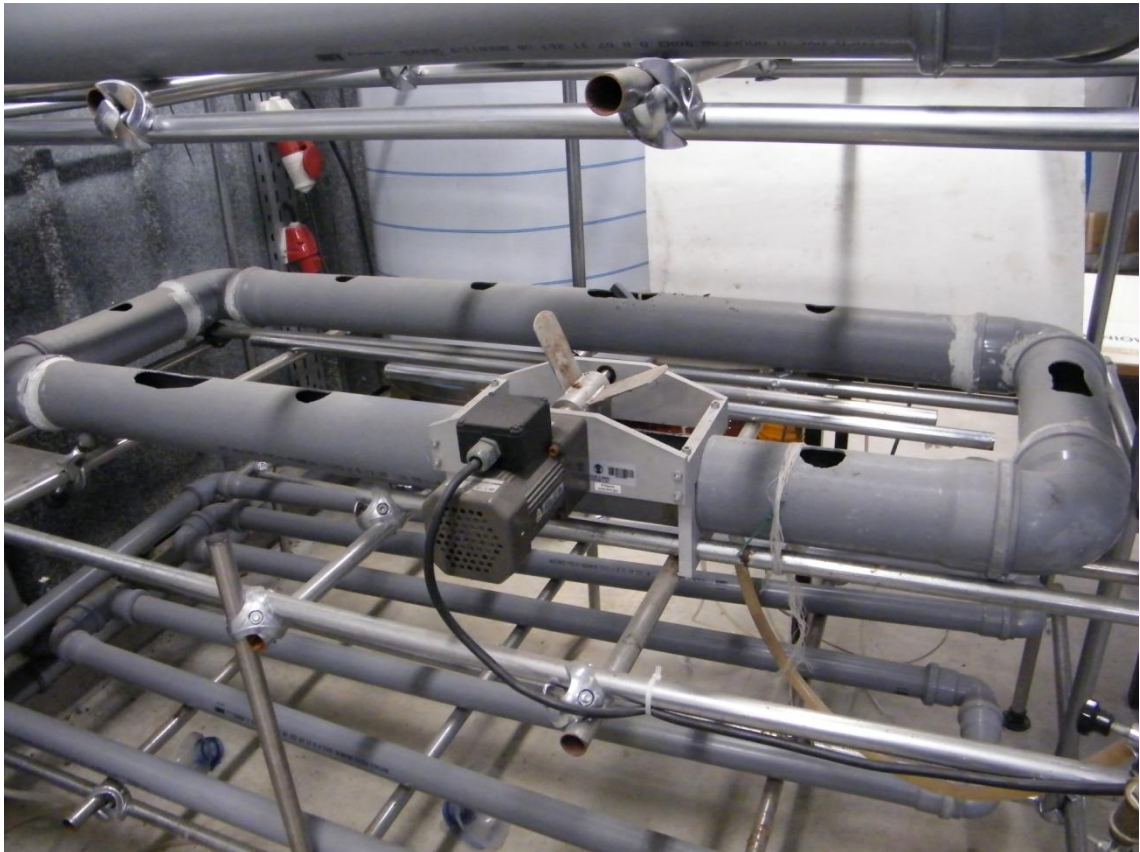


Figure 3.2 Pilot scale closed-loop PFRR reactor.

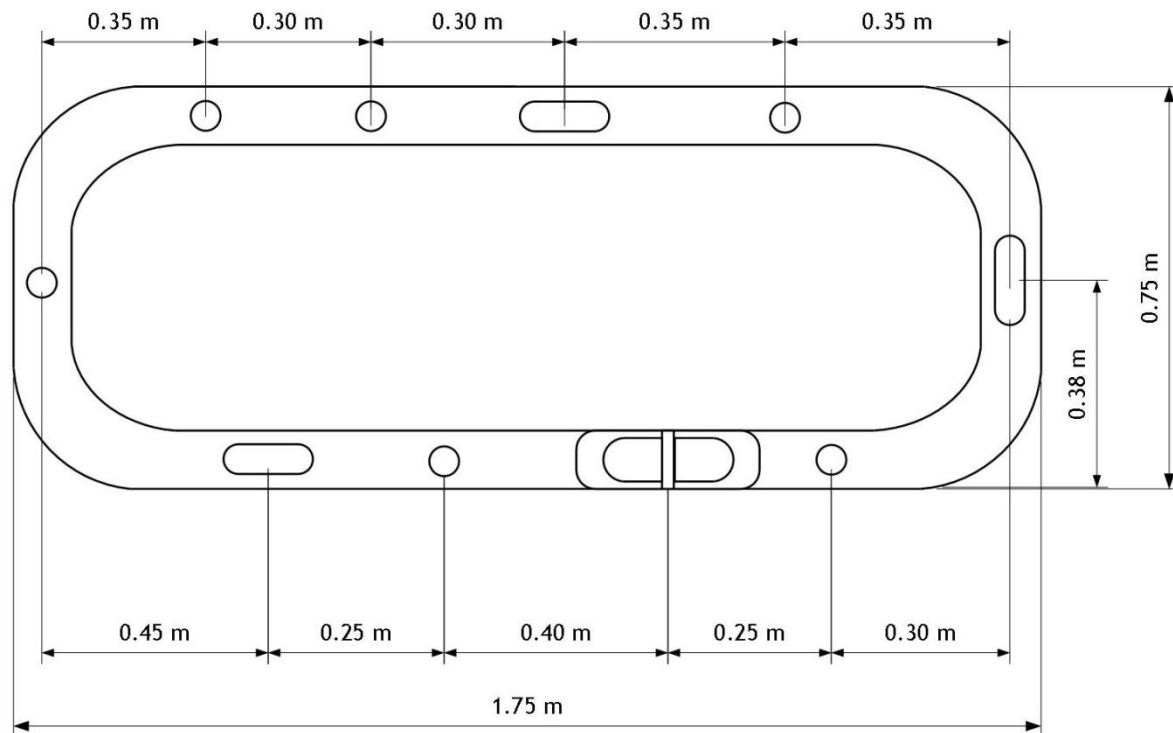


Figure 3.3 Schematic layout of the PFRR reactor.

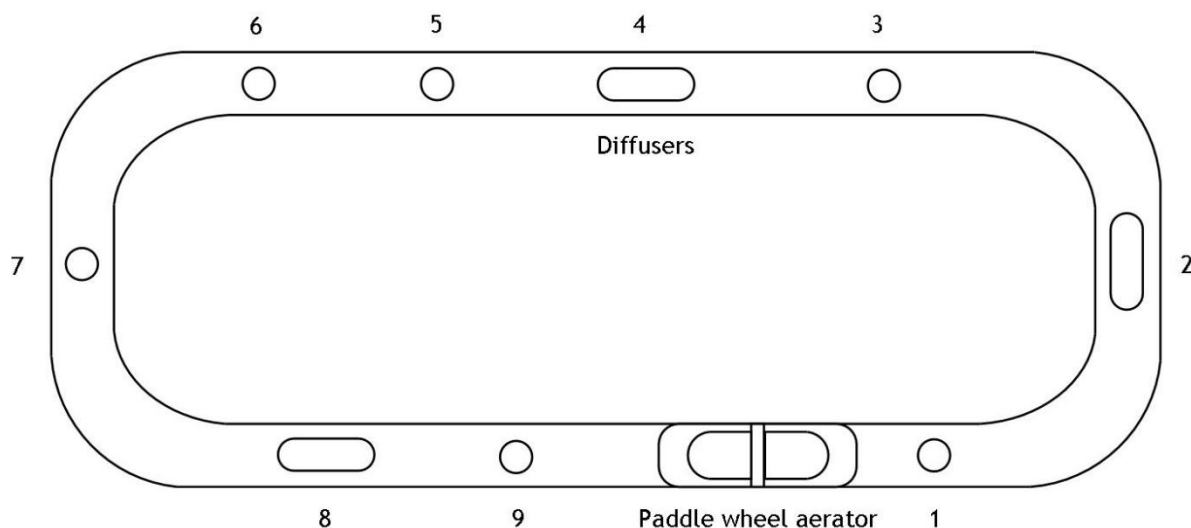


Figure 3.4 Distribution of the sampling points along the PFRR ditch.

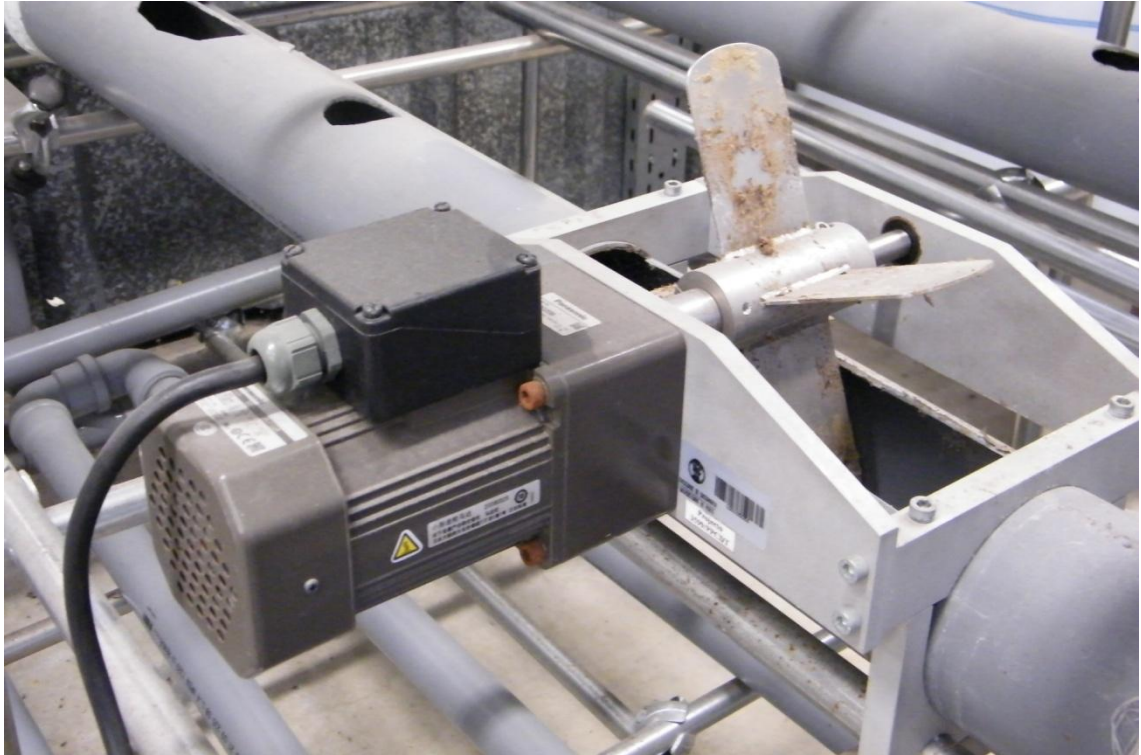


Figure 3.5 Horizontal paddlewheel impeller.

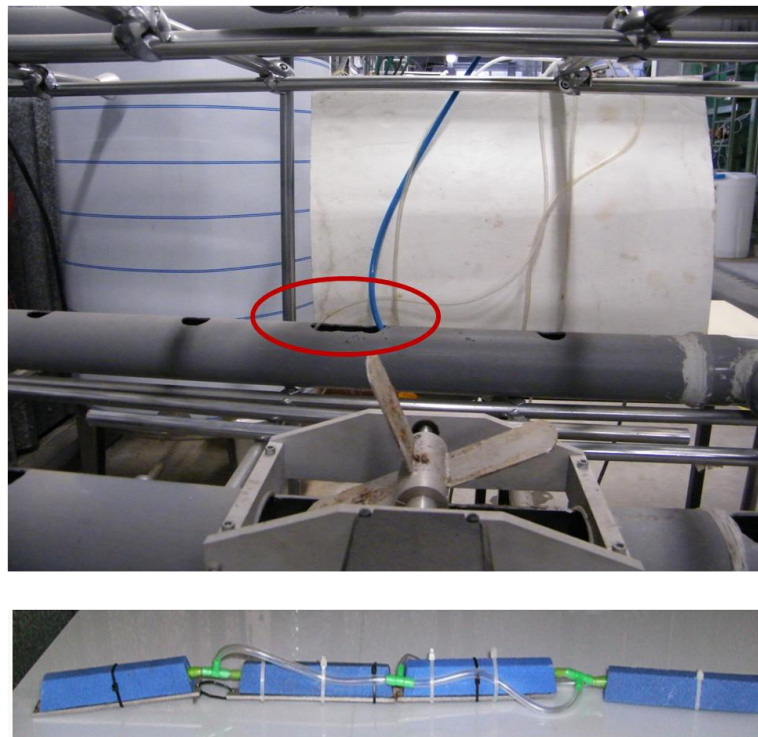


Figure 3.6 Bottom diffused air system.

3.3.2 PFRR Start-up and Operation

The PFRR ditch filled with 10 L of synthetic wastewater was inoculated with 10 L of activated sludge. The synthetic wastewater was prepared according with the formula described in Activated Sludge Simulation Test (OECD/OCDE, 2001) and the list of the ingredients necessary to prepare synthetic feed in 1 L of tap water is shown in Table 3.1. The quality of the synthetic wastewater corresponds to the parameters characteristic to the typical municipal wastewater. Fresh inoculum was brought from the aerobic tank of the Sobreiros WWTP (Porto, Portugal).

For assumed hydraulic retention time τ of 4 h, the inlet flow rate, Q_{in} equals the outlet flowrate (Q_{out}) and is 5.0 L h^{-1} (120 L d^{-1}). Moreover, Q_{in} is the sum of feed (Q_{feed}) and recirculation (Q_{rec}) flow rates and $Q_{feed} = Q_{rec} = 2.5 \text{ L h}^{-1}$ (60 L d^{-1}). Considering operating flow rates, weekly demand for reactor feed was 420 L, thus the synthetic wastewater was prepared in large quantities and stored in 500 L feed tank. The aeration was switch on to ensure that level of DO within the tank did not drop below 2.0 mg L^{-1} . The rotation of the paddlewheel aerator was adjusted to reach the values of the velocity in the reactor approximated to the velocities in the real scale oxidation ditches. The operation of the pilot reactor was monitored on the daily basis. The samples withdrawn from the feed, recirculation, and Point 2 were analyzed for COD , $NH_4 - N$, $NO_3 - N$, $PO_4 - P$, and TSS to assess progress of AS acclimatization.

Table 3.1 Composition of the synthetic wastewater.

Substance	mg per L water
Peptone	160
Meat extract	10
Urea	30
NaCl	7
CaCl ₂ · 2H ₂ O	4
MgSO ₄ · 7H ₂ O	2
K ₂ HPO ₄	28

3.3.3 Materials and Methods

3.3.3.1 Sampling

The list of the sampling points along the PFRR ditch and measured parameters at each point are shown in Table 3.2. During the pilot ditch operation, axial liquid velocity and *DO* concentrations in the sampling points were determined directly by on-site measurements using digital sensors with incorporated memory for data storage. Nutrient concentrations were determined indirectly, by analysis of the mixed liquor samples withdrawn carefully via a silicone tube suctioning in the middle depth of the reactor in the specified sampling points (Figure 3.4). The collected mixed liquor aliquots of 50 mL were immediately transferred into the labelled plastic containers and transported to the laboratory for *COD*, *NH₄ – N*, *NO₃ – N*, *PO₄ – P*, and *TSS* assays. To minimize errors, duplicate analyses were run on each sample tested and the results were compared.

Table 3.2 Spatial distribution of sampling points with assigned to them measurements.

Sampling Point	Analysis	Distance (m)
Paddle wheel aerator	-	0
1	<i>DO</i>	0.25
2	<i>v, DO, COD, NH₄ – N, NO₃ – N, PO₄ – P, TSS</i>	0.85
3	<i>DO</i>	1.45
4 (Bottom Diffusers)	<i>v, DO, COD, NH₄ – N, NO₃ – N, PO₄ – P, TSS</i>	1.8
5	<i>DO</i>	2.1
6	<i>DO</i>	2.4
7	<i>DO</i>	3
8	<i>v, DO, COD, NH₄ – N, NO₃ – N, PO₄ – P, TSS</i>	3.75
9	<i>DO</i>	4
Paddle wheel aerator	-	4.4

3.3.3.2 Measurement of the Axial Velocity

Axial liquid velocity in the tubular pilot scale PFRR ditch was measured with the acoustic Doppler velocimeter Nivus PVM-PD, equipped with telescopic wading rod. The equipment accuracy is 1% of the measurement range in water. The measurements were performed for the three oval sampling points, as shown in the Figure 3.7. During measurement, sensor body was placed in counter-current to the flow direction in three different positions: near the bottom, in the mid-depth and below the fluid surface. The mean value of the experimental axial velocity was calculated as the arithmetic average of the instantaneous velocities measured in the sampling point. Two different operating frequencies of the paddlewheel rotor of 24 and 38 RPMs, measured with Hofbauer digital hand tachometer, were considered aiming selection of the one which ensure the most effective mixing of the reactor content.

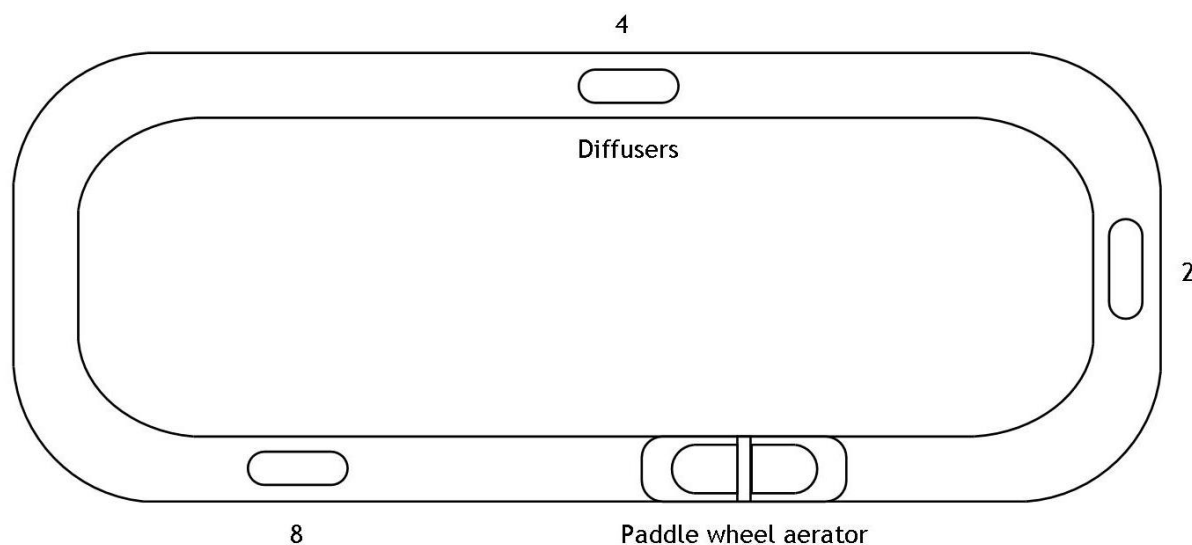


Figure 3.7 Distribution of the sampling points for velocity measurement.

3.3.3.3 Measurement of Dissolved Oxygen

For the selected rotor operating conditions and with the diffusers switched on, *DO* concentration was measured in all sampling points along the ditch (Figure 3.4) by means of portable multi-meter (Hach Lange HQ40D) equipped with digital luminescent *DO* probe (IntelliCAL™ LDO10103). The precision of the equipment is $0.01 \text{ mg L}^{-1} \text{ O}_2$ or 0.1% of *DO* saturation.

3.3.3.4 Determination of *COD*

COD in each of the samples was determined using Merck Spectroquant® *COD* Cell Test (1.14690.0001 and 1.14895.0001), according to the spectrophotometric method described by EPA Method 410.4, US Standard Methods 5220 D and ISO 15750. The sample was filtered through 1.0- μm -pore-diameter borosilicate glass fiber membrane filter (A/E Pall). 3 mL of the filtered sample was run from the pipette down into the cell with reagent. Afterwards, the cell was tightly screwed, vigorously mixed and placed in the preheated thermoreactor (Merck Spectroquant TR 420) in $148 \text{ }^\circ\text{C}$ for 120 min. After that time, the test vials were removed from the digester and placed in the test tube rack for cooling to room temperature for around 30 min. Finally, the cell was placed in the spectrophotometer (Merck Spectroquant® Pharo 100) for *COD* value reading using the internal calibration curves of the spectrometer for the 1.14690.0001 and 1.14895.0001 *COD* tests.

3.3.3.5 Determination of $NH_4 - N$

$NH_4 - N$ in each of the samples was determined using Merck Spectroquant® Ammonium Cell Test (1.14559.0001), according to the spectrophotometric method described by EPA 350.1, US Standard Methods 4500-NH₃ D and ISO 7510/1. The sample was filtered through 1.0- μ m-pore-diameter borosilicate glass fiber membrane filter (A/E Pall). 0.1 mL of the sample was pipetted into the cell and 1 dose of the NH_4 -1K reagent was added. The cell was closed tightly mixed vigorously until the complete dissolution of the reagent. After 15 min-reaction time, the cell was placed in the spectrophotometer (Merck Spectroquant® Pharo 100) for $NH_4 - N$ reading using the internal calibration curve of the spectrometer for the 1.14559.0001 Ammonium test.

3.3.3.6 Determination of $NO_3 - N$

$NO_3 - N$ in each of the samples was determined using Merck Spectroquant® Nitrate Cell Test (1.14563.0001). The sample was filtered through 1.0- μ m borosilicate glass fiber membrane filter (A/E Pall). 1.0 mL of the sample was pipetted into the cell and 1 mL of the NO_3 -1K reagent was added, closed tightly with the cap, mixed and left to stand for 10 min for reaction. Afterwards the cell was placed in the spectrophotometer (Merck Spectroquant® Pharo 100) for $NO_3 - N$ reading using the internal calibration curve of the spectrometer for the 1.14563.0001 Nitrate test.

3.3.3.7 Determination of $PO_4 - P$

$PO_4 - P$ in each of the samples was determined using Merck Spectroquant® Cell Test (1.14546.0001), according to the spectrophotometric method described by US Standard Methods 4500-P C. The sample was filtered through 1.0- μ m borosilicate glass fiber membrane filter (A/E Pall). 5.0 mL of the filtered sample was pipetted into the reaction cell, closed and mixed vigorously. Afterwards the cell was placed in the spectrophotometer (Merck Spectroquant® Pharo 100) for $PO_4 - P$ reading using the internal calibration curve of the spectrometer for the 1.14546.0001 Phosphate test.

3.3.3.8 Determination of TSS

TSS of the wastewater sample is determined according to the ESS Method 340.2. 1.0 μ m glass microfiber filter disc of 4.7 cm diameter without organic binder (Whatman GF/A) was weighted, placed in the base, clamp on the funnel which was mounted on the 1 L suction flask. While the vacuum pump was on (KNF Neuberger Aeromat), the filter was rinsed with distilled water. A well-mixed sample of 20 mL was transferred to the filter using a volumetric pipette. After removal of all traces of water, the filter is carefully

transferred from the base to a watch glass and dried in preheated oven at 103-105 °C for the time of 1 h. Subsequently the filter was placed in the desiccator for cooling and weighted. The *TSS* concentration in mg L⁻¹ was computed from the following formula:

$$TSS = \frac{(m_{F,S} - m_F) \cdot 1000}{V_{sample}} \quad (3.1)$$

where $m_{F,S}$ is the weight of filter with residue dried in 105 °C in mg, m_F is the weight of the filter, mg, and V_{sample} is the sample volume in mL.

3.3.4 RTD Determination

RTDs of the fluid in the pilot scale oxidation ditch were obtained from a pulse and step tracer experiment. Both experiments required usage of non-reactive tracer substance, which is introduced into the reactor through the inlet and the response of the system was found by measurement of the tracer concentration at the PFRR ditch measurement point located in the neighbourhood of the outlet tubing. Design of the optimal system to measure the RTDs was based on proper selection of both mutually inert tracer and working fluid. It was assumed, that introduction of the tracer substance into the system cannot trigger changes in physical properties of the fluid medium, which might further modify the hydrodynamics of the flow within the vessel. Thus both materials should have similar physical properties, such as density, viscosity, and diffusion coefficient. Another crucial feature was the ease of the tracer detectability. From this reason, the experiments were conducted using clean, tap water as the working fluid and an aqueous solution of sodium chloride, NaCl, as the non-reactive tracer. Electrical conductivity, *EC*, was measured to assess the content of Cl⁻ and Na⁺ equivalents in the water, and therefore to determine tracer concentration at the outlet of the PFRR ditch.

3.3.4.1 Pulse Tracer Experiment

The experimental conditions consider reactor filled with 20 L of clean tap water and operating in the steady-state for the assumed τ of 2 h (Q_{in} is 10.0 L h⁻¹) with the constant velocity of the flow ensured by the paddlewheel aerator operating with 38 RPMs. The experiment was carried out excluding the recirculation loop to the settler, therefore assuming that the reactor system has only one inlet and one outlet. NaCl solution was prepared by dissolving 18 g of salt in 75 mL of tap water. At time $t = 0$, the tracer was injected instantaneously into the reactor feed (Point 1) and at the same time at the outlet (Point 9) the concentration of the salt was measured and recorded in function of time by

means of the digital multi-sensor (HI 769828 Multiparameter Probe). EC of background, was $350 \mu\text{S cm}^{-1}$. The scheme of the experiment is shown in Figure 3.8

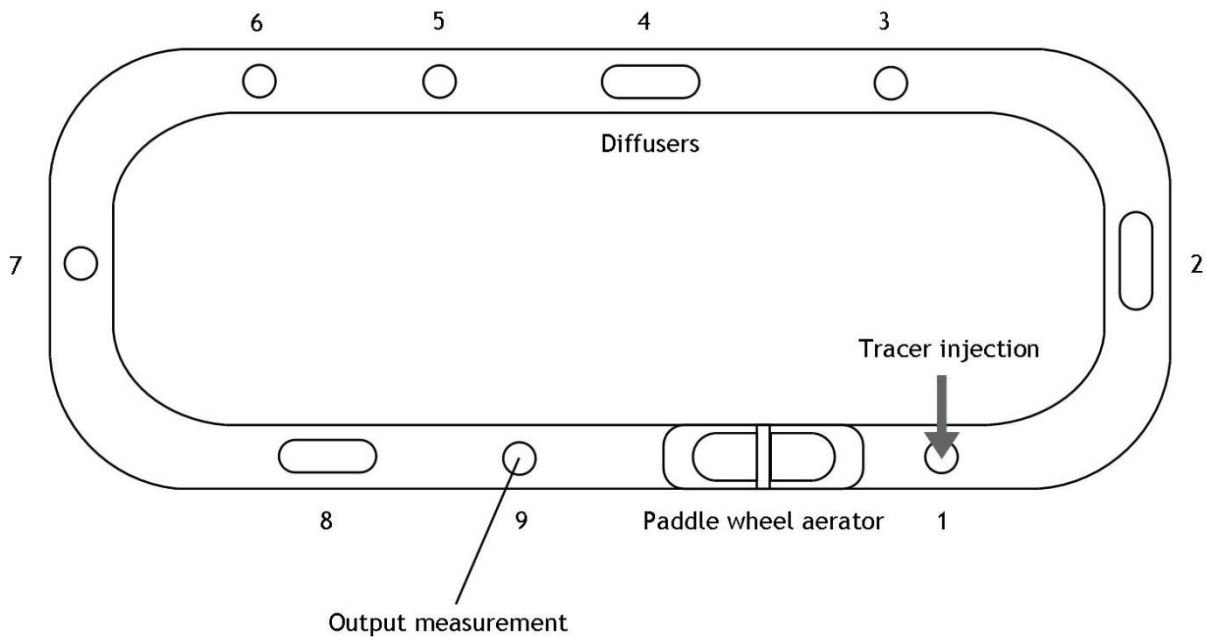


Figure 3.8 Scheme of the RTDs experiments.

3.3.4.2 Step Tracer Experiment

In this approach we are considering PFR ditch filled with 20 L of clean tap water and operating at steady flow conditions, as described in section 3.3.4.1. The brine solution was prepared in a container by dissolving 62 g of NaCl in 100 L of tap water. EC of the tracer solution was $1240 \mu\text{S cm}^{-1}$ and of the clean water- $140 \mu\text{S cm}^{-1}$. At the time $t = 0$ the input of the fluid is switched from tap water to the tracer solution. The concentration of the tracer at the reactor outlet is measured until the level of initial concentration in feed is reached. The measurement data is recorded over time by means of multi-sensor (HI 769828 Multiparameter Probe).

3.3.5 Results and Discussions

3.3.5.1 Wastewater Characteristics

The quality of the synthetic wastewater prepared to feed the PFRR ditch during first 14 days of the system start-up is shown in Figure 3.9. The feed characterizes with *COD* content in the range 300 - 350 mg L⁻¹, *NH₄ - N* from 20 to 30 mg L⁻¹ and *PO₄ - P* from 6 to 10 mg L⁻¹. Only in the case of *COD* content in feed, variability over time can be observed. Low concentrations of *NO₃ - N* and the absence *TSS* in the synthetic feed were also observed.

3.3.5.2 Reactor Start-up and Treatment Efficiency

Figure 3.9 - Figure 3.14 show the changes in the concentration of nutrients and *TSS* in the influent (recirculation + feed) and within the reactor during 14-days. During this period, the values of *COD* stabilized after 100 h of operation, yielding the effluent *COD* concentration in the range from 15 to 60 mg L⁻¹ (Figure 3.10). At the same time, mutual changes in conversion of the nitrogen compounds are observed. Thus, with the increase of ammonia level within the reactor to 37 mg L⁻¹ (Figure 3.11), the decrease of the nitrates from almost 4.0 to 1.0 mg L⁻¹ is observed (Figure 3.12). On the other hand, slight increase of the orthophosphates from 3.5 to nearly 10 mg L⁻¹ *PO₄ - P* is also seen (Figure 3.13).

When considering treatment efficiency, the effluent meets the quality standards in terms of *COD* and the nitrates concentration. Nonetheless, at the end of the considered in this work start-up time, the worsening of the effluent quality in terms of the ammonia and orthophosphates content is noticeable. Here, the lowest observed *NO₃ - N* concentration occur simultaneously with the successive *NH₄ - N* and *PO₄ - P* build-up within the reactor. In the typical aerobic activated sludge system, the optimum ratio of C : N : P in the mixed liquor is thought to be as 100 : 5 : 1. In PFRR ditch, this ratio is not met in case of the mixed liquor quality, due to low carbonaceous nutrient content. From this reason despite of the excellent aeration conditions, poor treatment effects, inhibition of the ammonia uptake and the nitrification breakdown in the PFRR ditch could be explained as: the effects of the activated sludge starving, caused by low carbon content in feed; suspected instability of the feed composition; and changes in pH due to decrease of alkalinity. Variable *TSS* content in the pilot ditch and thus in the recirculation stream was observed during system start-up (Figure 3.14), which ranged from 5 to 360 mg L⁻¹. Lowering tendency in the total suspended solids concentrations contributes also to the worsening of the reactor performance. Possible cause of the suspected sludge “washout” was the

operation of the recirculation loop resulting in observed excessive accumulation of biomass in secondary settler during start-up.

The 14-days start-up time was too short to achieve the pseudo-steady state within the PFRR reactor, which is crucial to assess biochemical process efficiencies. Nonetheless, the considered period of time is sufficient to study local-scale phenomena, and thus hydrodynamics of the pilot ditch based on the determination of the velocity and nutrient profiles.

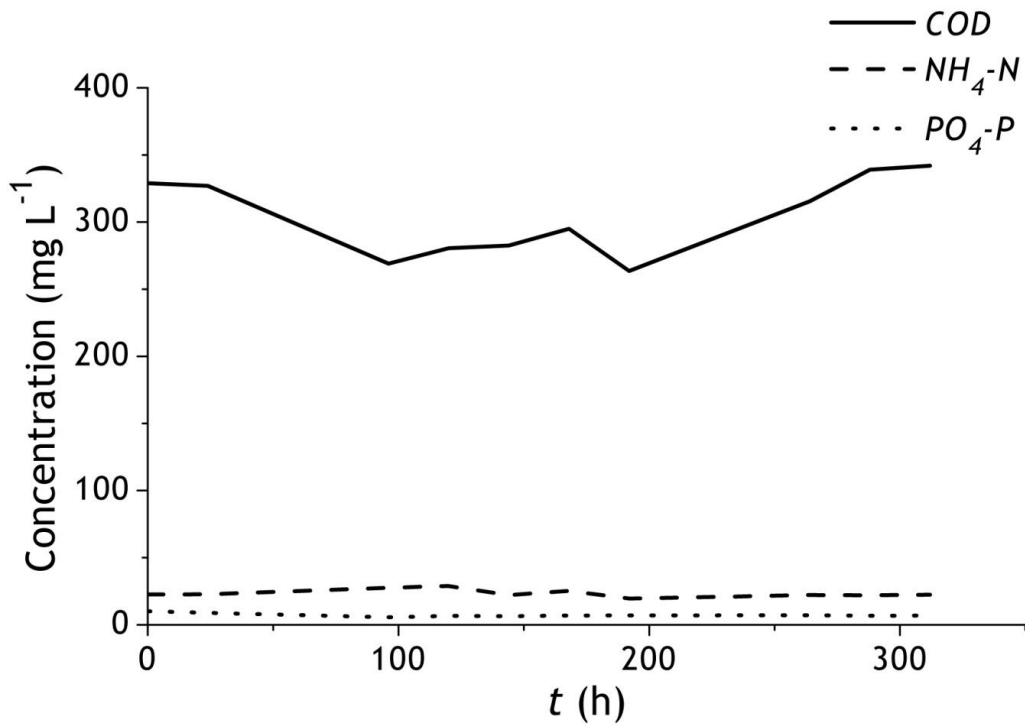


Figure 3.9 Quality parameters of the synthetic wastewater during system start-up.

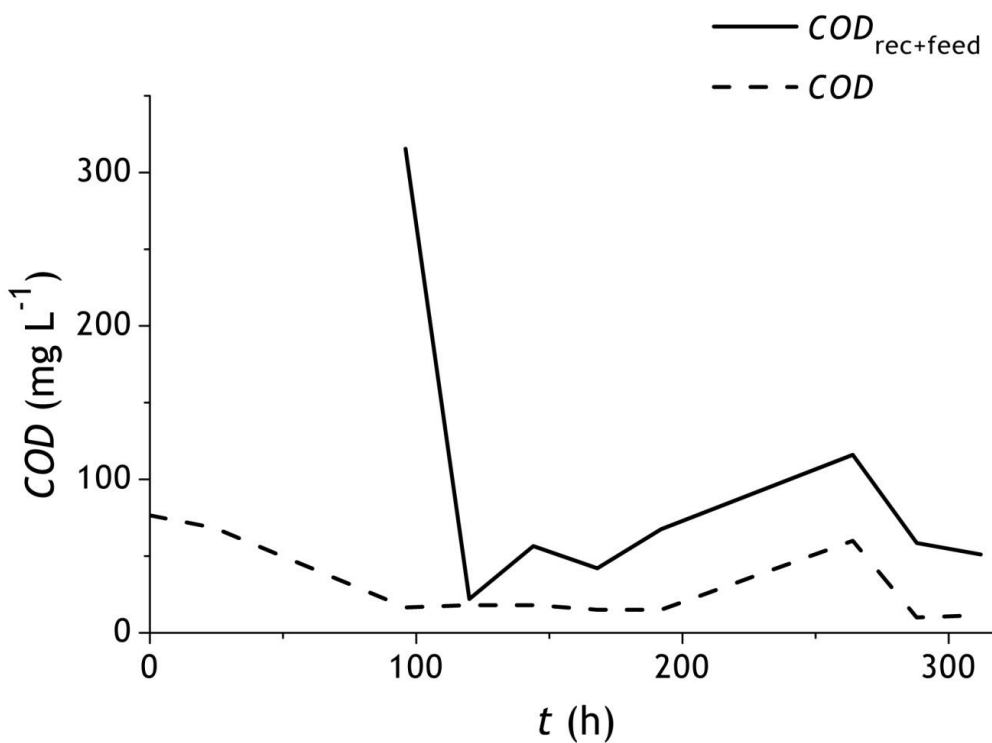


Figure 3.10 COD concentration in the influent and within the PFRR reactor during start-up.

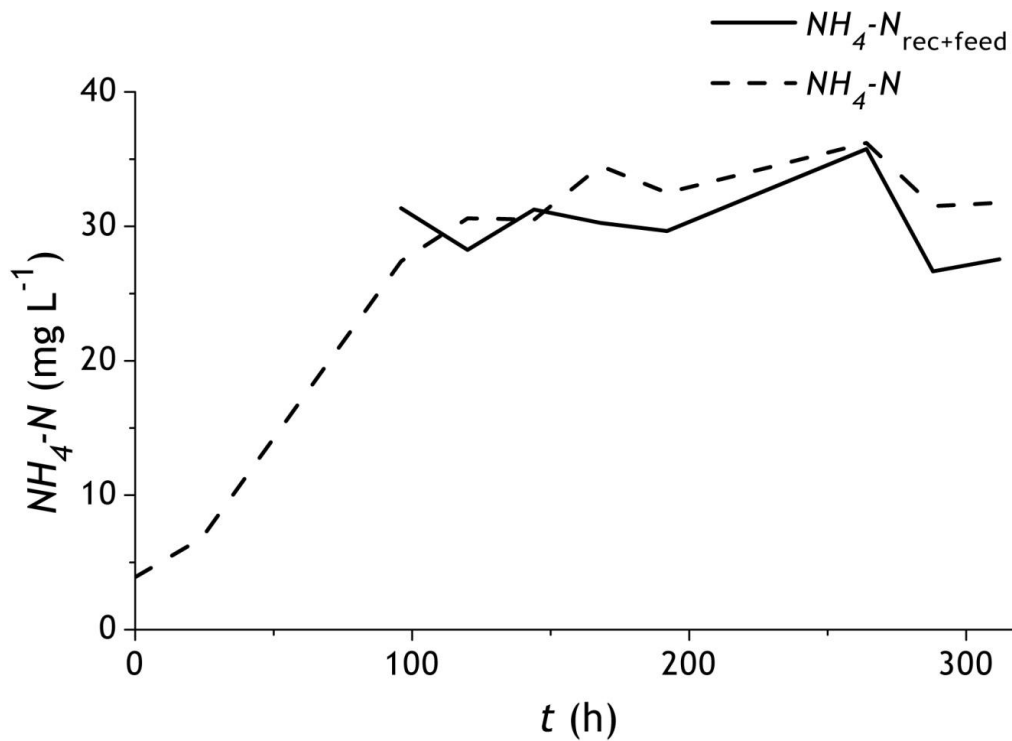


Figure 3.11 NH_4-N concentration in the influent and within the PFRR reactor during start-up.

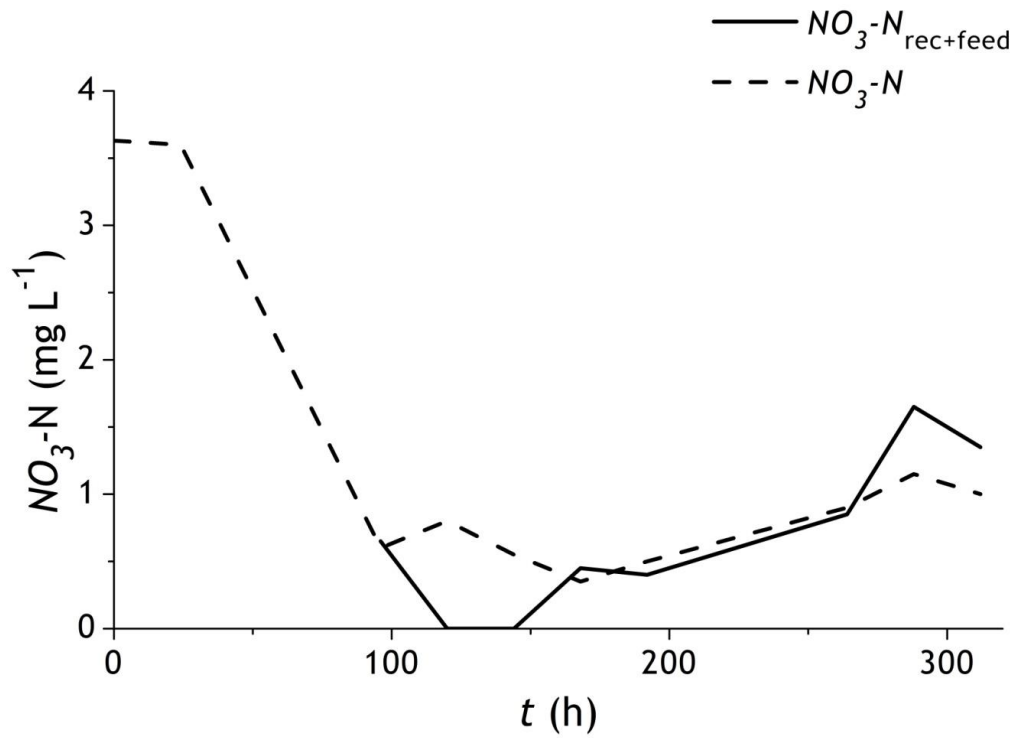


Figure 3.12 $NO_3 - N$ concentration in the influent and within the PFRR reactor during start-up.

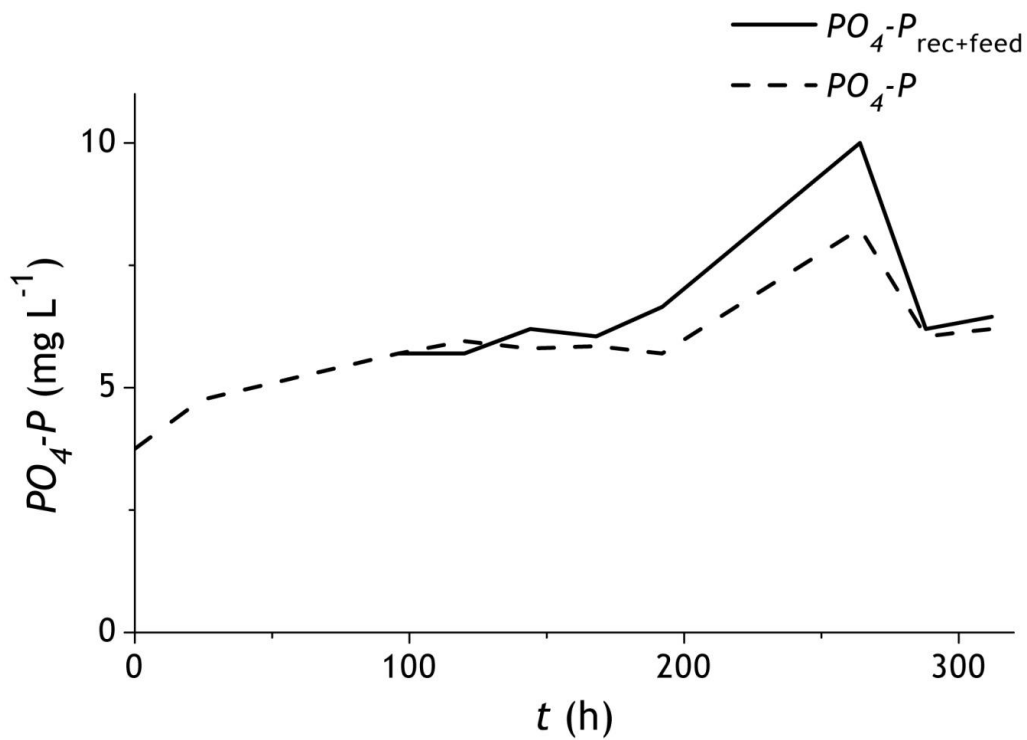


Figure 3.13 $PO_4 - P$ concentration in the influent and within the PFRR reactor during start-up.

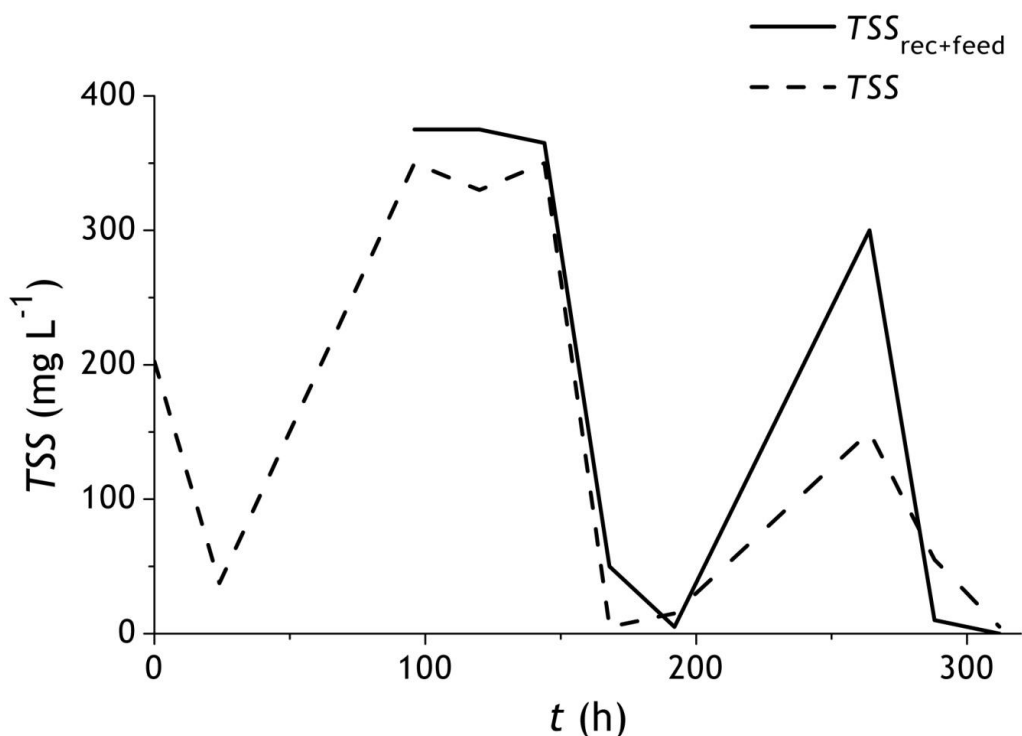


Figure 3.14 TSS concentration in the influent and within the PFRR reactor during start-up.

3.3.5.3 Velocity Profiles along the PFRR Ditch

Evolution of the horizontal, axial velocity profiles along the pilot PFRR ditch obtained for two different rotor frequencies, namely 24 and 38 RPMs, are presented in Figure 3.15. The vertical lines on the plots mark the distance from the centre of the paddlewheel aerator in the counter-clockwise direction, i.e. 0.2 m, 1.8 m (diffused air unit), and 4.2 m, which is at the same time 0.2 m away from the paddlewheel aerator. In both cases, the highest velocities due to the paddlewheel aerator action were measured in Point 2 and 8. The lowest velocities are observed near the bottom and in the measurement point downstream diffused air system, i.e. at the distance 1.8 m from the paddlewheel rotor. Here, the axial fluid velocity profile is strongly impacted when the flow crosses bubble plume released from the diffusers. Fluid velocities obtained for the lower paddlewheel rotations were in the range from 0.5 near the bottom to 1.0 m s⁻¹ near the surface. With increase of the rotor frequency, velocities in the reactor cross-section tend to be more uniform, without clear distinction between low velocity at the near-bottom zone and high velocity at the near-surface region. Here, the average mixed liquor velocity along the ditch is from 1.1 to 1.4 m s⁻¹ and drops to the value 1.0 m s⁻¹ downstream the diffusers. Considering the choice of such operating conditions, providing efficient mixing of the pilot reactor content

(wastewater, activated sludge and air) and preventing formation of the local dead zones, the rotor frequency allowing for higher velocities, i.e. 38 RPMs, was used for further studies.

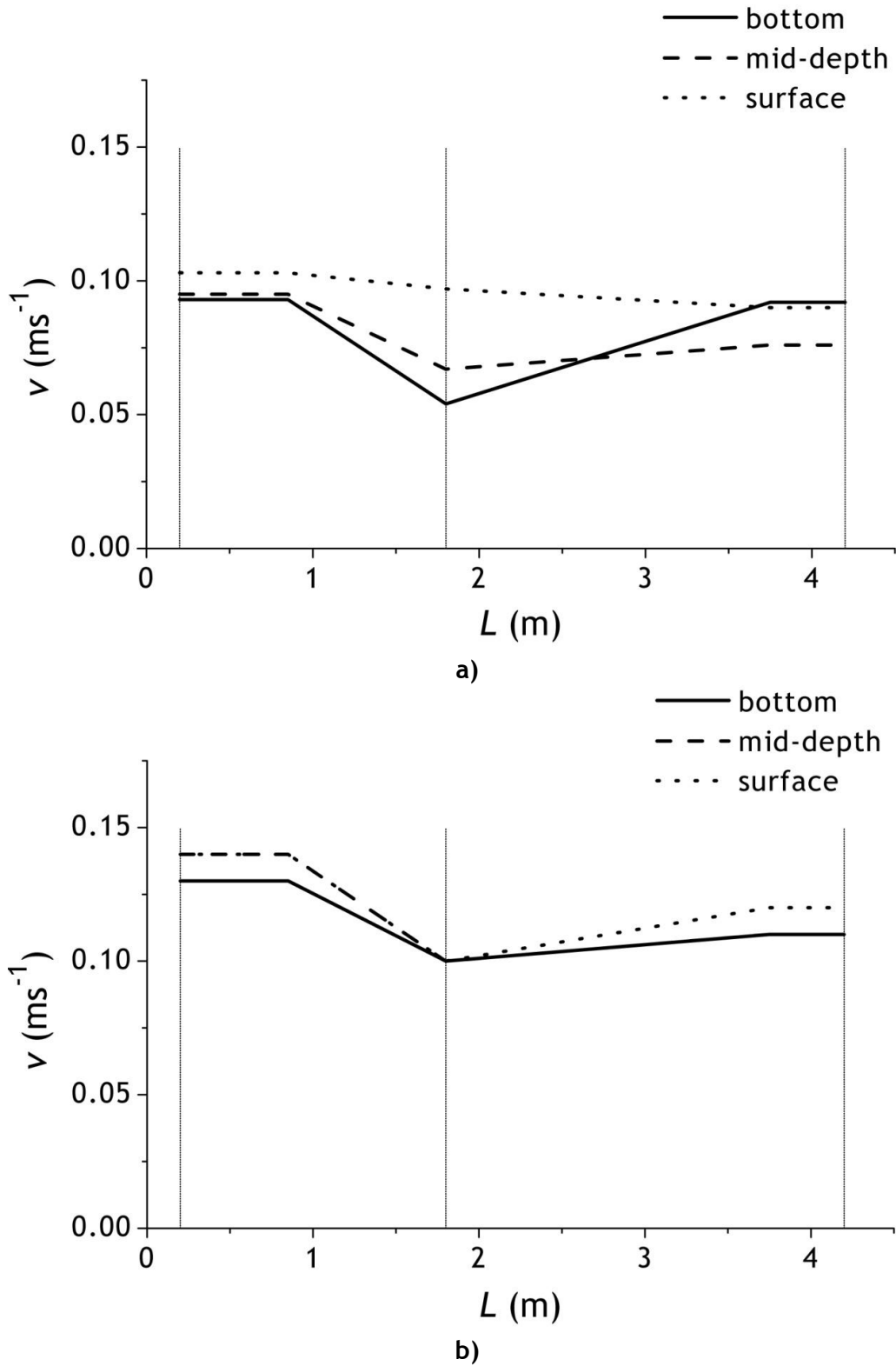


Figure 3.15 Velocity profiles along the PFRR ditch obtained for the paddlewheel rotation obtained with frequency of a) 24 RPMs and b) 38 RPMs.

3.3.5.4 Dissolved Oxygen Profiles along the PFRR Ditch

DO content was measured in the mid-depth along the reactor several times for the wastewater temperatures varying from 17 to 22.2 °C. Figure 3.16 shows the concentration profiles obtained from the measurements obtained in six different measurement campaigns. It is clearly seen, that regardless of the diffuser and paddlewheel aerator placement, and for the constant rotor frequency of 38 RPMs, DO concentration along the pilot ditch is almost constant. The factors affecting DO content in the PFRR reactor are wastewater temperature, which has an influence on the oxygen solubility and the synthetic feed quality. It can be assumed, that for the studied tubular PFRR ditch, the oxygen profiles and the constant concentration within the reactor and at the outflow make this system very closed to a completely mixed system.

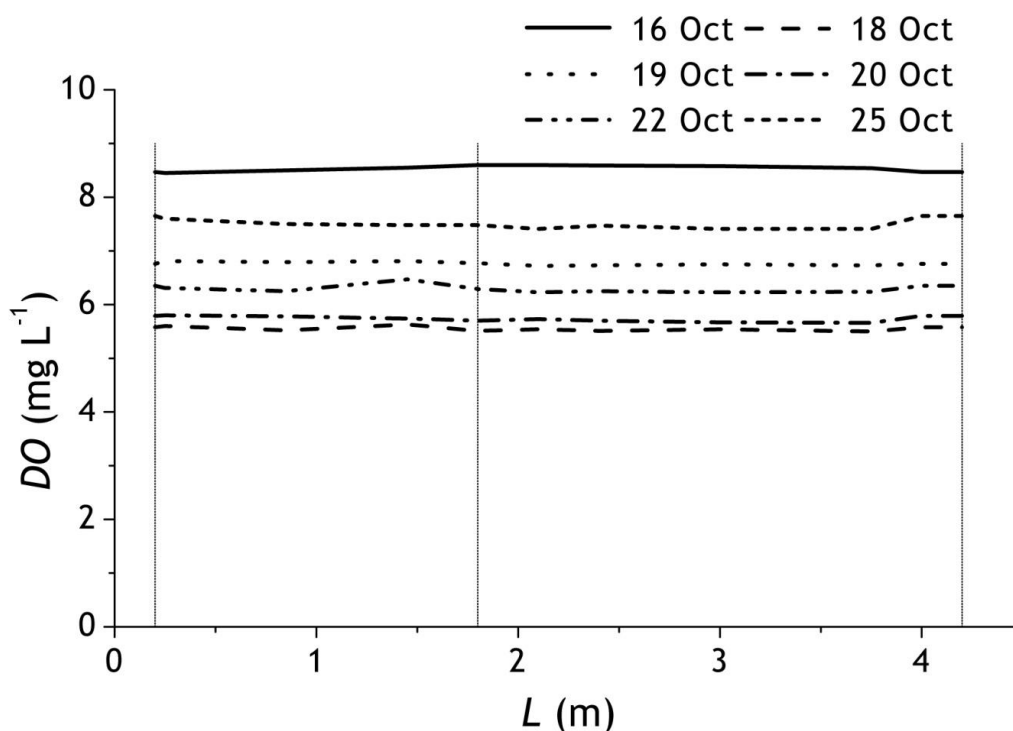


Figure 3.16 DO profile along the pilot PFRR ditch.

3.3.5.5 Nutrients Profiles along the PFRR Ditch

The sampling campaign aiming determination of the changes in nutrients content within the pilot PFRR ditch took place three times during reactor start-up. The plots showing the concentration profiles along the tubular reactor are presented in Figures 3.17 - 3.21.

Similarly to the *DO* distribution along the ditch, for most of the cases, concentrations of the *COD* (Figure 3.17), $NH_4 - N$ (Figure 3.18), $NO_3 - N$ (Figure 3.19), $PO_4 - P$ (Figure 3.20) and *TSS* (Figure 3.21) are constant, suggesting complete mixing of the reactor content. Isolated cases of decrease of *COD* and *TSS* content in the reactor section between paddlewheel aerator and diffuser may be explained by the local influence of the neighbouring influent injection point, supplying the PFRR ditch with synthetic feed mixed with the recirculated sludge from the clarifier.

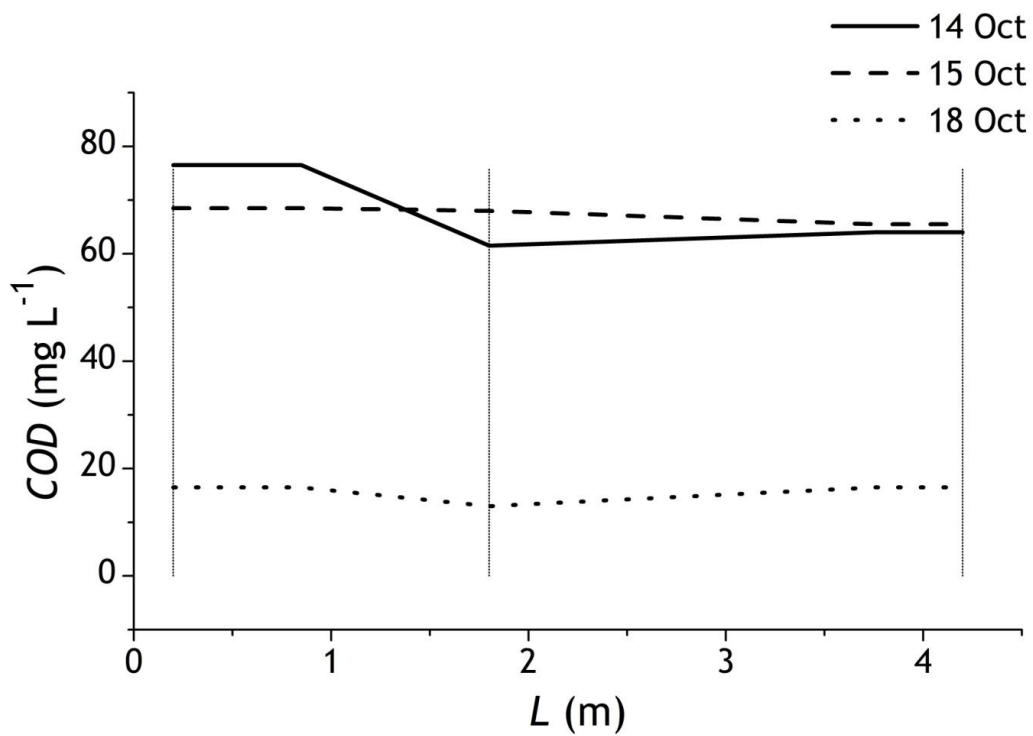


Figure 3.17 *COD* profile along the pilot PFRR ditch.

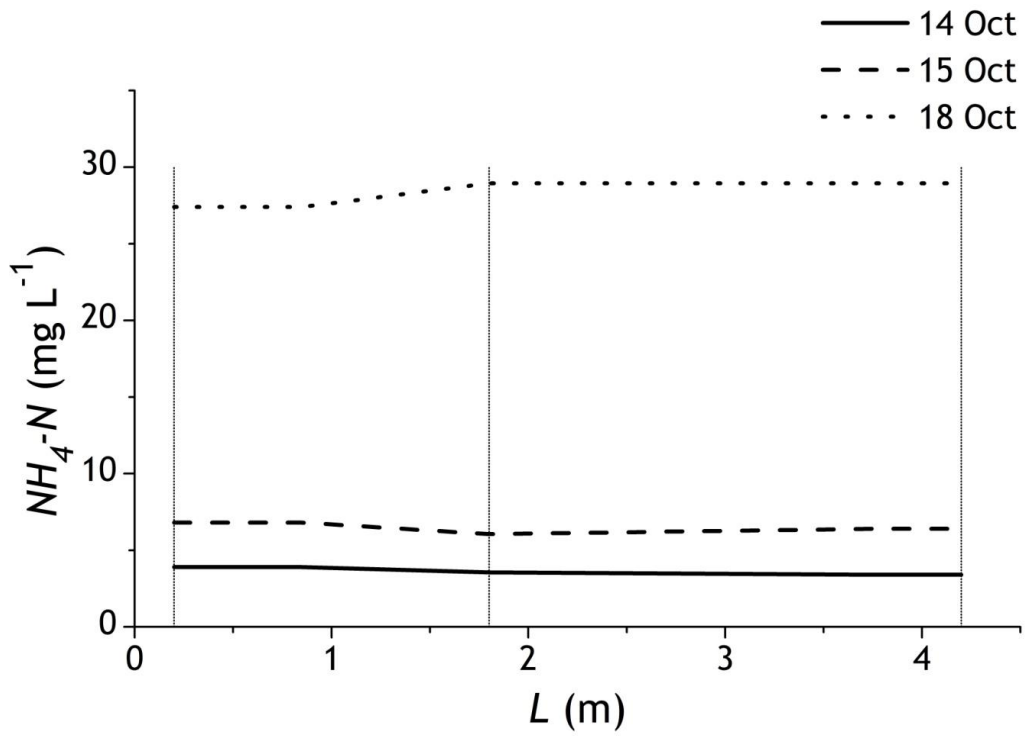


Figure 3.18 $NH_4 - N$ profile along the pilot PFRR ditch.

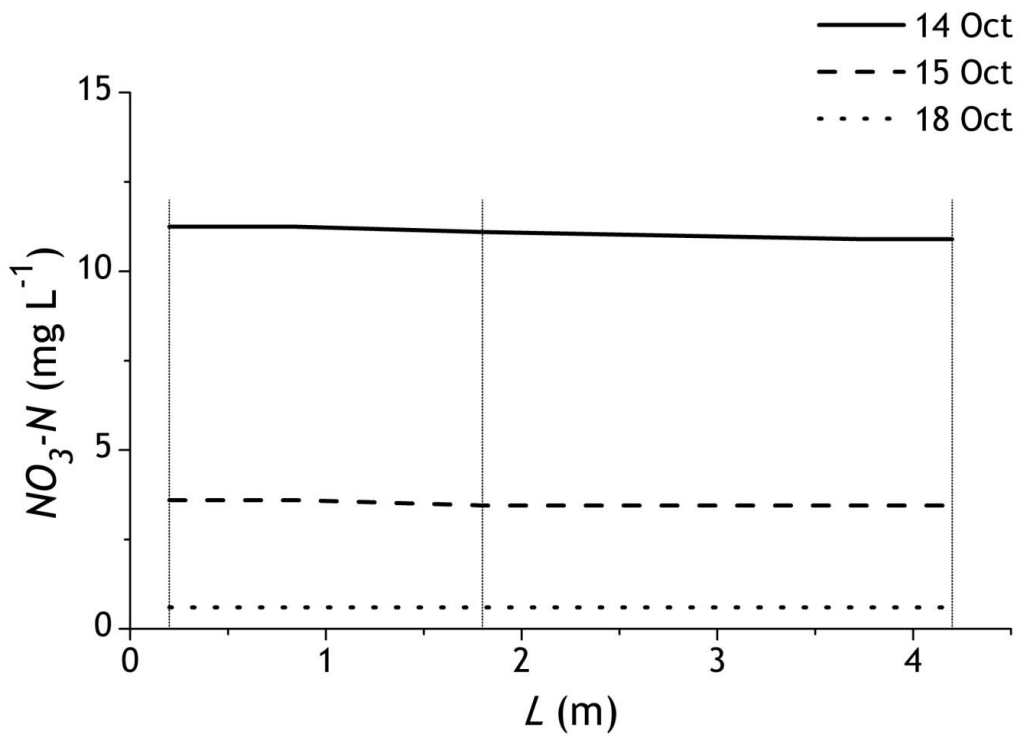


Figure 3.19 $NO_3 - N$ profile along the pilot PFRR ditch.

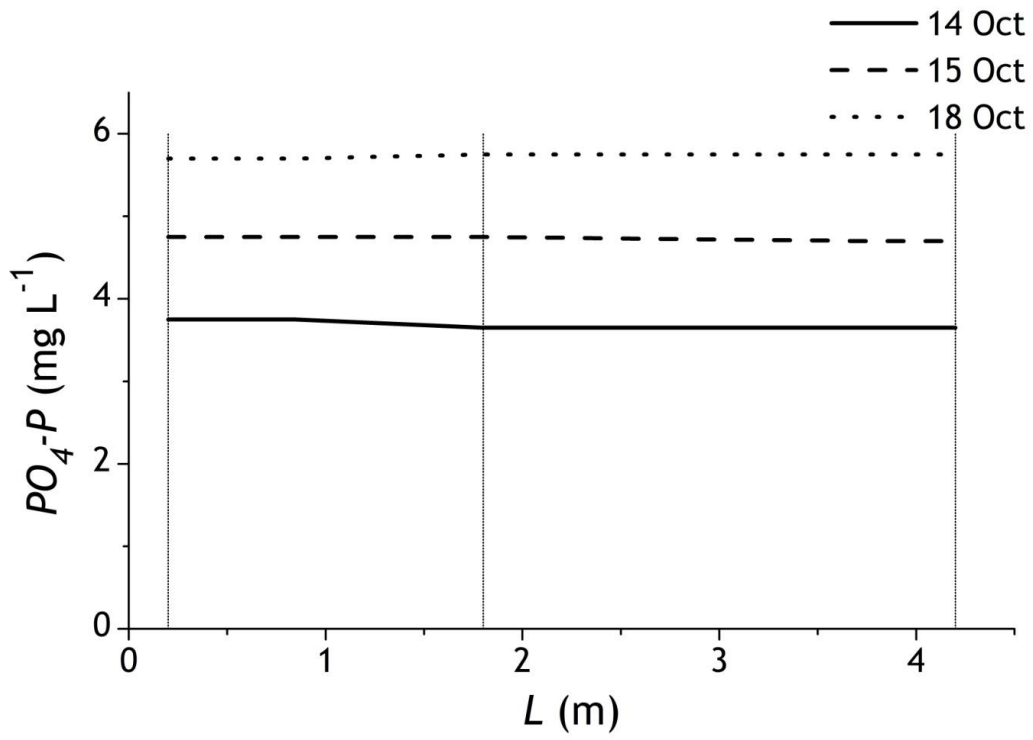


Figure 3.20 $PO_4 - P$ profile along the pilot PFRR ditch.

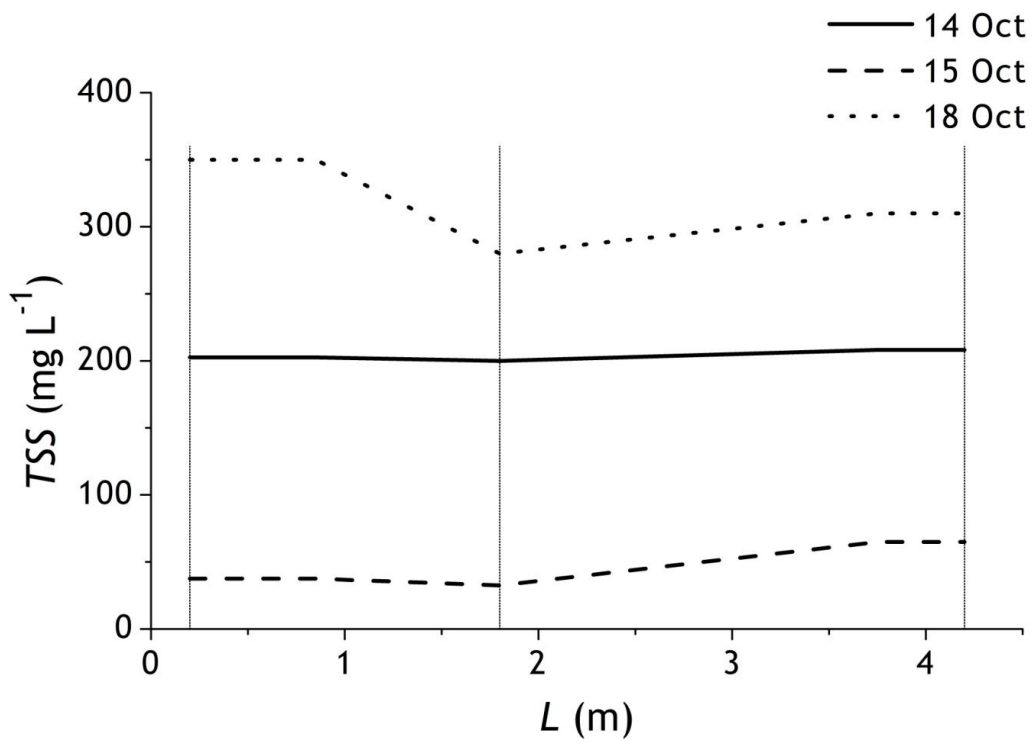


Figure 3.21 TSS profile along the pilot PFRR ditch.

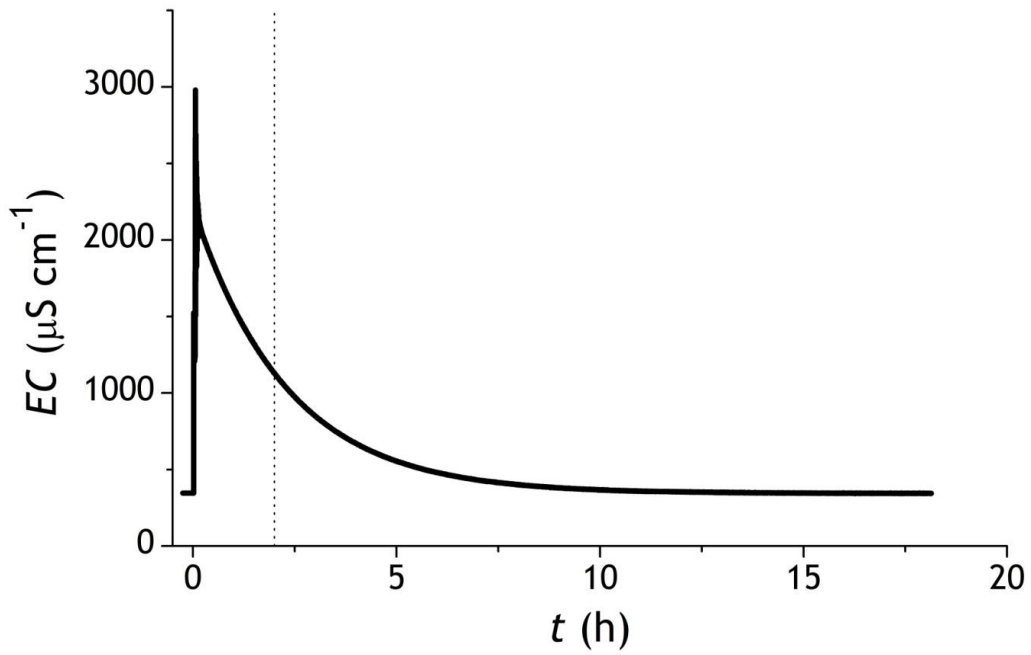
3.3.5.6 RTD of the PFRR Ditch

The RTDs of the fluid in the PFRR reactor obtained in the pulse tracer experiment are plotted as a C_{pulse} curve (Figure 3.22a) describing changes in the water conductivity over time and as the exit age distribution curve, normalized by expression $\sum C(t)\Delta t$ (Figure 3.22b). In both plots, the vertical dashed line designates the assumed mean retention time (τ) of 2 h.

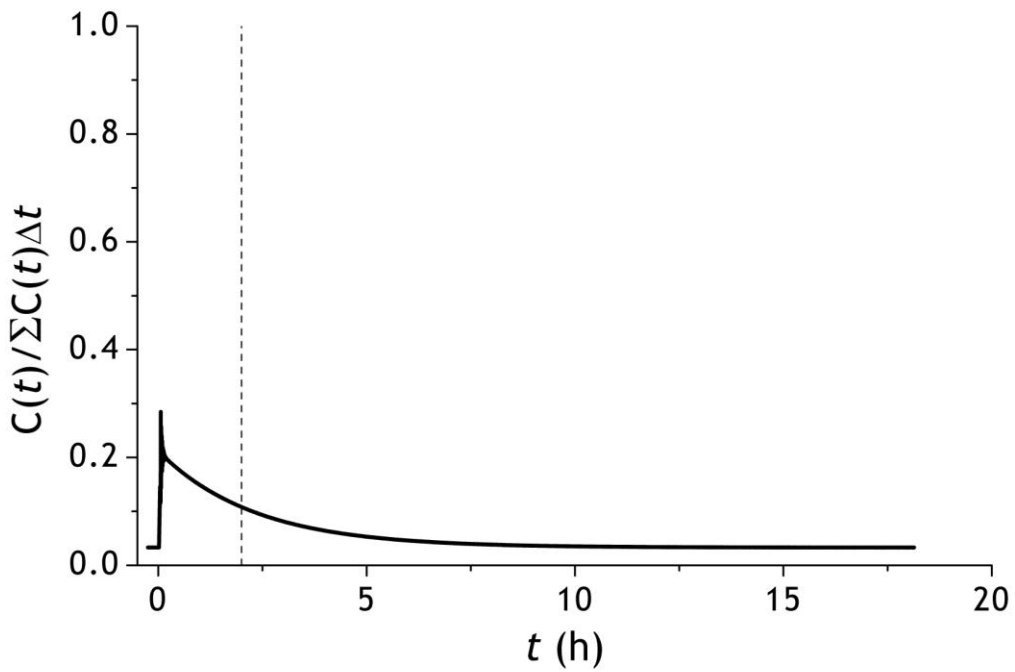
The distance between inlet and outlet of the reactor is 4.4 m, and the average velocity of the fluid within the pilot vessel of 0.12 m s^{-1} . As the PFRR system is operated without recirculation loop, the statistical fluid particle introduced through the inlet makes the first lap and reaches the outlet in around 37 seconds ($\sim 0.01 \text{ h}$) and for the assumed τ the fluid will make in average 200 laps before exiting from the pilot ditch system.

Conductivity of the tap water was $350 \mu\text{S cm}^{-1}$ corresponding to the 175 ppm TDS (NaCl). The shape of both concentration curves plotted in Figure 3.22 resembles the output profiles characteristic for the ideal CSTR vessel, consisting of a sharp peak with tail. Here, the large peak observed in the RTD plots might be associated to the large amount of the tracer particles detected at the ditch outlet- measurement point at early time instants equal to twenty laps around the ditch. However, when observing detailed plot made for first 20 laps (0.20 h) shown in Figure 3.23, it turns out, that the early large peak is actually made up of several peaks occurring in the identical time intervals, due to conductivity probe response time of 20 seconds (0.006 h). Furthermore, taking into account the fact, that the probe was actually placed in the sampling point, not in the outflow stream from the reactor, the PFRR ditch behaviour cannot be straightforwardly assessed. Nevertheless some observations can be made, such as the occurrence of the early peaks that may be due to the short-circuiting from inlet to outlet, and multiple decaying peaks that can be associated with internal fluid recirculation. Moreover, shortening of the observed mean residence time and the characteristic shallow tail of the early pulse curves can suggest the occurrence of stagnant fluid regions.

Consequently, after 1 h ($\tau/2$) the conductivity of the water in the outflow point decreased from the peak value of $3000 \mu\text{S cm}^{-1}$ (1500 ppm TDS) for around 50%. After 2 h, and thus the flow time equivalent in value to the assumed τ , the EC is still over twice the initial value of the clean water. As suspected, due to the existence of the dead zones in the reactor, the complete washout of the tracer from the PFRR ditch occurred only after 15 h (7.5τ).



a)



b)

Figure 3.22 The plots of the response curves of the fluid in the pilot reactor obtained from the pulse tracer experiment presented as the a) conductivity curve b) normalized concentration curve.

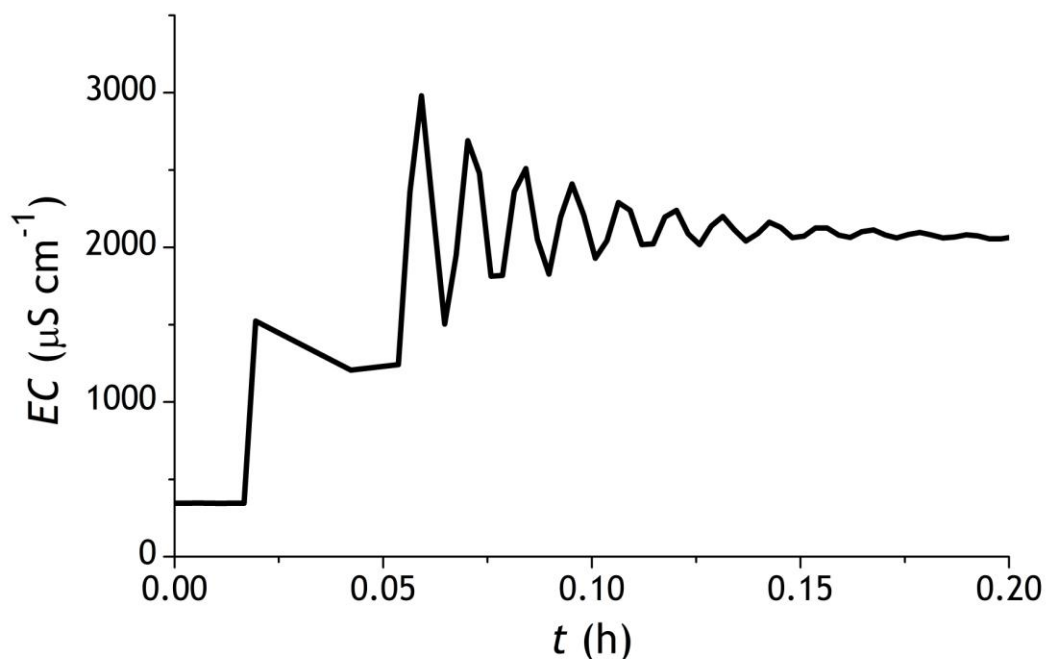


Figure 3.23 Plot of the conductivity of the fluid in the pilot reactor obtained from the pulse tracer experiment.

The RTDs of the fluid in the pilot ditch were further investigated in the step tracer approach. The experiment was conducted in the same conditions in terms of the flow rate, assumed τ and the fluid velocities as for the pulse tracer experiment. The EC of tap water was $140 \mu\text{S cm}^{-1}$ (70.0 mg L^{-1}) and the conductivity of the tracer solution was $1240 \mu\text{S cm}^{-1}$ (620 mg L^{-1}). The plots of the step response curve C_{step} and the curve normalized by initial concentration of the tracer solution are presented in the Figure 3.24. Once again, the shape of the both curves, namely the slope of the curve and the presence of the long tail confirm the findings obtained from the pulse experiment results. After the observed time of $\tau/2$ the conductivity of the fluid within the pilot ditch constitutes only 34% of the initial value in tracer solution. After flow time corresponding to τ , EC measured in the outflow from the reactor reaches 56% of the initial value. After 10 h the TDS content within the reactor is 99% of the tracer solution, however due to the presence of the stagnant flow regions inhibiting efficient mixing and exchange of the fluid within the vessel, the complete substitution of the tap water by brine solution occurs only after 16 h (8τ).

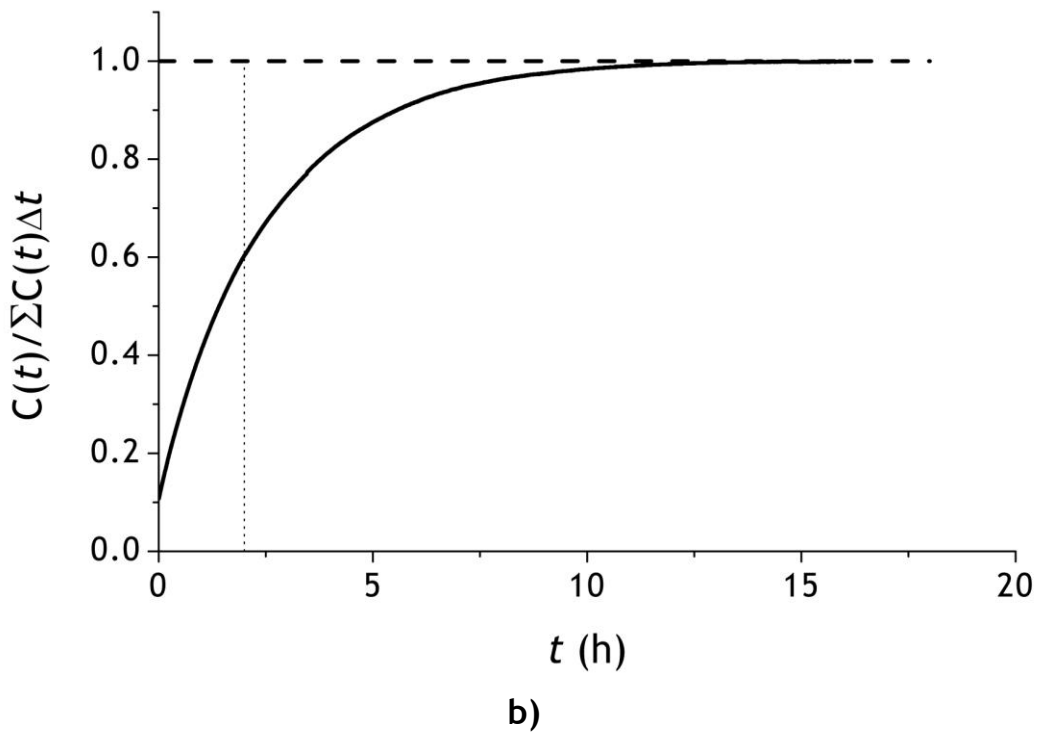
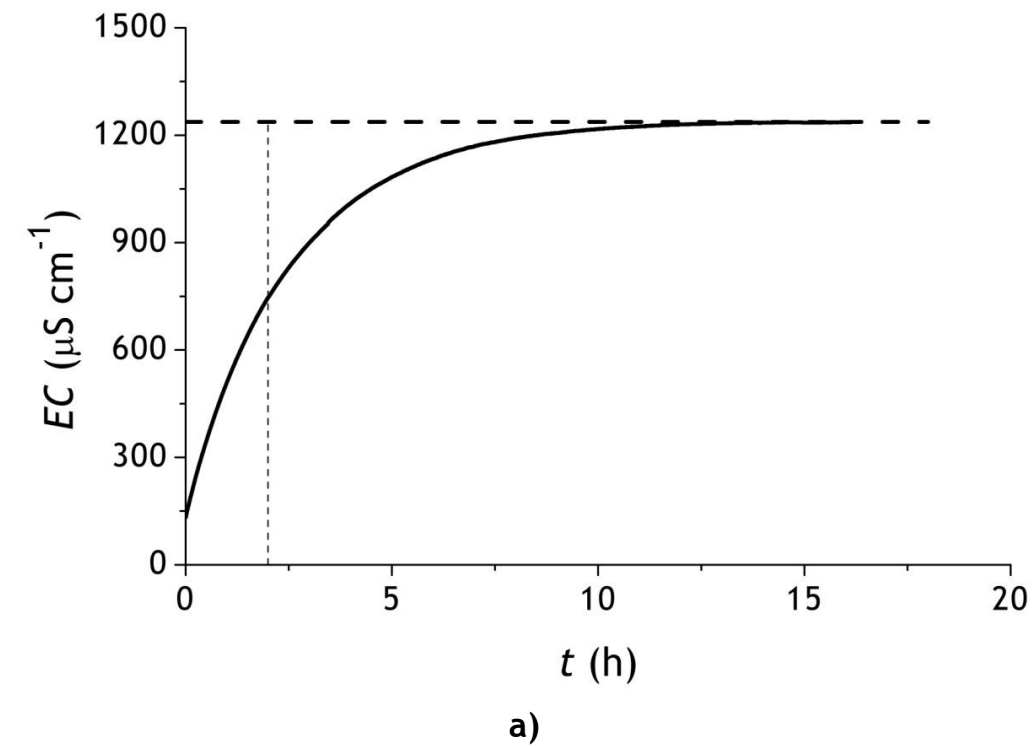


Figure 3.24 The plots of the response curves of the fluid in the pilot reactor obtained from the step tracer experiment presented as the a) C_{step} curve b) normalized concentration curve.

3.4 Real Scale Experiments

The aim of the real scale experiments was to assess the hydrodynamics of the real scale oxidation ditch on the base of the velocity, DO , and nutrient concentration profiles along the tank. To evaluate aeration performance, the DO profiles were determined for several depths of the ditch.

3.4.1 Areosa WWTP - Viana do Castelo

Areosa WWTP serving Viana do Castelo city is located in the North - West coast of Portugal, at a distance of 50 m from the Atlantic Ocean. A bird's eye view of the Areosa WWTP is shown in the photo in Figure 3.25. The plant, which was built and inaugurated in 1999 and later modernized in 2008, was designed for ca. 45260 PE (population equivalent). The maximal capacity of the WWTP is $8580 \text{ m}^3 \text{ d}^{-1}$ of medium strength wastewater. The wastewater is treated in three stages. Primary treatment train consists of the screens, grit chamber, flotation tank equipped with skimming devices and radial primary settler. Secondary treatment of wastewater involves activated sludge process, based on the intermittent operation of the extended aeration process. The treatment train consists of the oxidation ditch and the radial secondary clarifier. The final effluent is disinfected with UV and discharged to the Atlantic Ocean.



Figure 3.25 Areosa WWTP - Viana do Castelo (www.adnoroeste.pt).

3.4.2 Oxidation Ditch System

The oxidation ditch system at the Areosa WWTP consists of the two single channel tanks each having dimensions of 50.0 x 10.0 x 4.0 m, as shown in Figure 3.26. This work concerns performance of one of the two oxidation ditches, where aeration and mixed liquor circulation is carried on by means of four opposite-sided horizontal brush aerators that extend throughout the whole channel width. The flow circulation in the clockwise direction is ensured by eccentric guiding walls placed in opposite corners of the ditch. The aeration process is operated intermittently, with the times of aeration on and off controlled by DO level set point of 2.0 mg L^{-1} , measured by galvanized DO sensor mounted on float. Second ditch is additionally equipped with fine pore diffusers, which are switched on occasionally, in conditions of extreme overloading. The inlet pipe supplies the ditch with mechanically treated wastewater from the primary settler. Biologically treated effluent from the ditch is discharged through overflow weir downstream to the pipe feeding the secondary settler. The inlet of the sludge recirculation pipe is placed in the bottom of the ditch. The top view of the oxidation ditch layout considered in this work is shown in Figure 3.27.

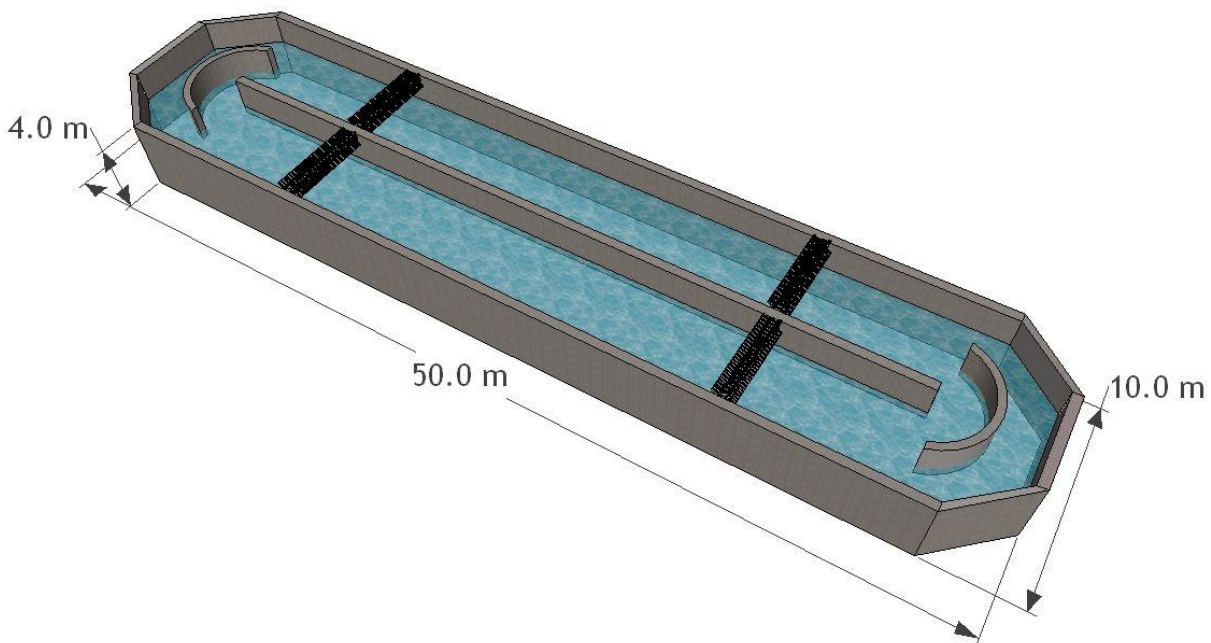


Figure 3.26 Scheme of the oxidation ditch in the Areosa WWTP.

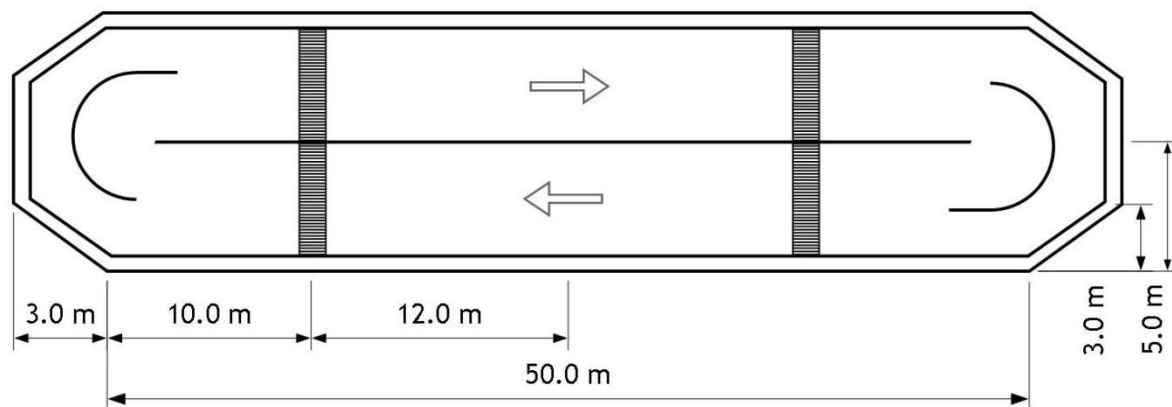


Figure 3.27 Scheme of the oxidation ditch of Areosa WWTP - top view.

3.4.3 Materials and Methods

3.4.3.1 Sampling

Sampling campaign took place four times during the period from July to October 2010, for the different weather conditions and the temperatures from 20 to 33 °C. The experimental studies of the oxidation ditch required selection of the measurement area allowing for the best possible representation of the mixing and biokinetics along the entire ditch. It was considered that the ditch is symmetric and so, the section of straight channel with two brush aerators and the bend were considered. Ten sampling points, numbered from P0 to P9 were distributed along the 44 m long measurement section, as shown in Figure 3.28. The numbers assigned to the sampling points are in accordance with the flow direction, which is clockwise.

Stainless steel support with a 3.0 m telescopic arm was used to attach the sensors and sampling tube allowing for measurements and withdrawal of the samples from various depths and at various distances from the lateral wall of the ditch channel.

Velocity and *DO* concentrations in the sampling points were measured on-site using portable digital sensors with incorporated memory for data storage. The nutrients and *TSS* content determination required a sequence of procedures associated with mixed liquor sampling, material storage, transport and finally, the analysis to obtain these data. The samples were withdrawn from the pre-defined position within the ditch, namely middle depth (2.0 m) in each sampling point (Figure 3.28) via suction tube connected to a peristaltic pump (Watson Marlow SciQ 300). The sampling tube, fixed to the submersed extended rod was positioned in the distance of 1.0 m from the lateral wall of the ditch. Each sample consisted of 50 mL aliquot transferred directly into the plastic labelled container. The collected samples in containers were stored for a short period of time in

the portable ice cooler box to endure the transport from the WWTP to the laboratory (in Faculdade de Engenharia da Universidade do Porto) for further analysis of COD , $NH_4 - N$, $NO_3 - N$, $PO_4 - P$, and TSS assays. To minimize errors, duplicate analyses were run on each sample tested and the results were compared with the within-laboratory precision statements for each parameter.

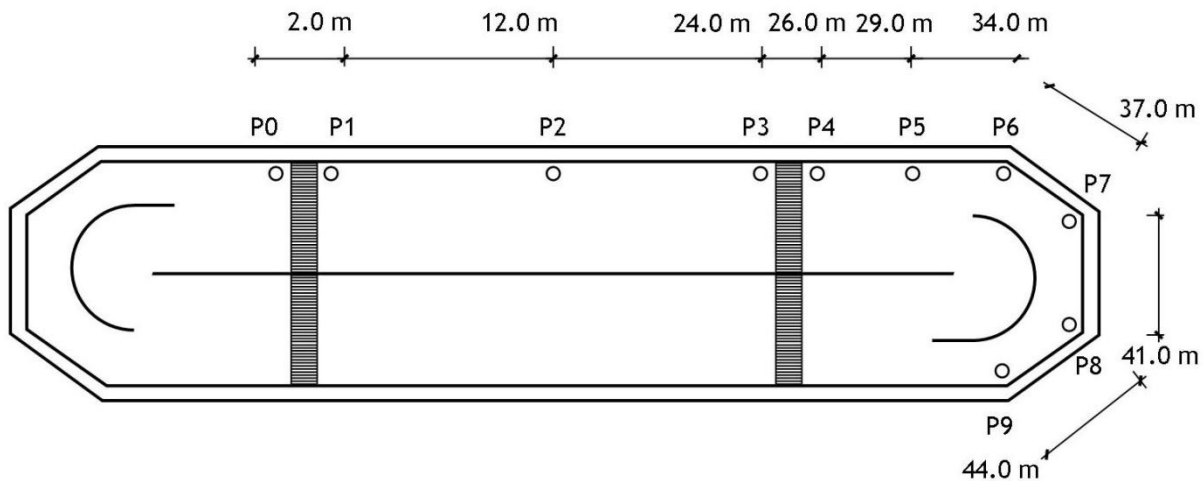


Figure 3.28 Distribution of the sampling points along the oxidation ditch.

3.4.3.2 Measurement of the Surface Velocity

Horizontal velocity in the oxidation ditch was measured with acoustic Doppler velocimeter Nivus PVM-PD, equipped with telescopic wading rod and fixed to the extended arm of the support. The equipment accuracy is 1% of the measurement range in water. To assess the axial surface velocity, the sensor body was positioned in counter-current to the flow direction, in approximately middle width of the ditch channel at the distance of 2.5 m from the lateral wall. The sensor was submersed around 0.15 m below the fluid surface. The measurements were performed in all sampling points shown in Figure 3.28.

3.4.3.3 Measurement of Dissolved Oxygen

Dissolved oxygen concentration was measured in all sampling points along the ditch (Figure 3.28) by means of portable multi-meter (Hach Lange HQ40D) equipped with digital luminescent DO probe (IntelliCAL™ LDO10103). The precision of the equipment is $0.01 \text{ mg L}^{-1} \text{ O}_2$ or 0.1% of DO saturation. Optic sensor was fixed to the extended rod of the support allowing for measurement of the DO content at several depths: below wastewater surface at 0.1 m, what corresponds to the submersion of the sensor head; 0.5 m; 1.0 m; 1.5 m; and 2.0 m equivalent to the mid-depth of the ditch. As the extended aeration process is

operated intermittently, the oxygen level was also measured during the aeration system switched-off. Here, the measurements considered the straight channel zone between the aerators, between the points P1 and P3.

3.4.3.4 Determination of Nutrients and TSS Content

Detailed procedures of COD , $NH_4 - N$, $NO_3 - N$, $PO_4 - P$ and TSS determinations in each collected sample were described in sections 3.3.3.4 - 3.3.3.8 of this chapter.

3.4.4 Results and Discussions

3.4.4.1 Velocity Profiles along the Oxidation Ditch

Evolution of the horizontal velocity profiles along the outer wall of the real scale oxidation ditch obtained during four sampling and measurement campaigns are presented in Figure 3.29. The vertical lines on the plots mark the location of the brush aerators, positioned at the distance of 1.0 m and 25.0 m relatively to the first measurement point P0 (Figure 3.28). All plots reveal similar tendency, thus the common feature for all profiles is the occurrence of the peaks associated with increase of the surface velocities downstream the aerators due to the action of brushes. Considering straight channel section, the peak corresponding to the increase of the local axial velocity up to 1.5 m s^{-1} occurs at the distance of 1.0 m downstream the brush aerator. With the increase of the distance, surface velocity decreases to the value of $0.7\text{-}1.1 \text{ m s}^{-1}$ in the flow area upstream the second aerator. The region of the ditch bend is characterized by sudden increase of the velocity up to 1.5 m s^{-1} and immediate decrease to 0.5 m s^{-1} , as can be seen in Figure 3.29 for the ditch length starting from 37.0 m. Here, the main factor contributing to the features of the horizontal velocity profile is increased turbulence, associated with the presence of the guiding wall redirecting the flow and causing uneven velocity distribution in the channel, making it slower close to the inner wall and faster close to the outer wall. This effect is not so pronounced in the bend region due to the middle baffle.

Additional feature of the full scale system performance is the operation that is made with almost four times higher average flow velocities than the typical values for the oxidation ditches, which lies in the range of $0.20\text{-}0.40 \text{ m s}^{-1}$.

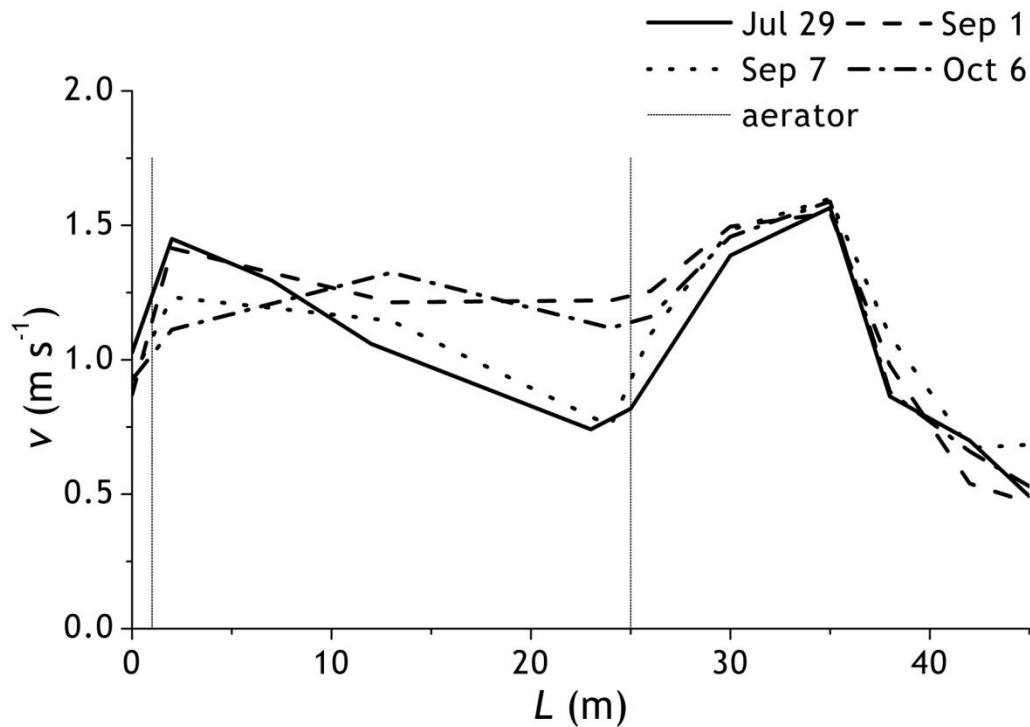


Figure 3.29 Velocity profiles along the oxidation ditch.

3.4.4.2 Dissolved Oxygen Profiles along the Oxidation Ditch

The climate has an influence on the wastewater temperature especially in the open tanks with large surface area, such as the oxidation ditch. As the wastewater temperature is a decisive factor in the solubility of oxygen in liquid medium and in the metabolic activity of the species, which constitute the activated sludge, thus it has an impact on the efficiency of the biological treatment process. During *DO* measurement campaign, which took place four times in the period from July to October, wastewater temperature was measured simultaneously with *DO* concentration by means of the same LDO sensor. The temperature data are presented in Table 3.3.

The *DO* profiles were made to investigate the changes of the concentrations along and within the oxidation ditch. The horizontal profiles of the oxygen concentration measured for different LDO sensor submergences and in conditions of the aerators switched on and off, are shown in Figures 3.30- 3.37. Regardless of the tank depth and wastewater temperatures, small variations of *DO* content are observed in the straight section of the ditch downstream and upstream the aerators. Larger *DO* gradients in the bend and in the neighbouring area are due to dynamic mixing of more or less oxygen enriched fluid layers, from the top to the bottom of the tank.

Table 3.3 The environment and wastewater temperature during sampling campaign.

Sampling date	Environment temperature (°C)	Wastewater temperature (°C)
July 29	32.5	30.0
September 1	29.7	27.0
September 7	26.2	23.5
October 6	22.0	20.0

Considering oxygen stratification within the ditch, it is clear, that elevated temperatures of the wastewater impede efficient oxygen transfer into the ditch. Thus in the days with the temperatures above 27 °C (Figure 3.30 and Figure 3.32), the *DO* concentration just below the surface is around 2.0 mg L⁻¹ with slight increase in the turbulent zone of the bend. For the wastewater temperature of 30 °C, at the mid-depth of the ditch the level of oxygen decreases to zero, while for slightly lower wastewater temperature of 27 °C, the *DO* level drops below 1.0 mg L⁻¹. Such conditions lead to formation of oxygen-poor to oxygen-deficit volumes in the lower parts of the straight channel sections. In these cases, despite intensification of the surface aeration process leading to higher fluid velocities, the unique zones along the ditch characterized with presence of *DO* at half of the ditch depth, are bends. Such phenomena can be explained as the effect of oxygen solubility in the wastewater, which decreases drastically with the increase of the temperature. Thus the atmospheric air introduced into the wastewater due to rotating action of the brushes is consumed before being transported to the deeper parts of the ditch. With the aeration switched off, almost constant zero-*DO* profiles extend through the section between the aerators, as can be seen in Figure 3.31 and Figure 3.33. Here, due to the backward order of the measurement points, slightly higher *DO* content was registered upstream the second aerator (first measurement point since switching off the brushes).

Considering the temperatures below 25 °C, the improvement of the oxygenation capacity of the aeration system is visible. Here, for wastewater temperature of 23.5 °C, the average *DO* concentration below the fluid surface is around 3.5 mg L⁻¹ and decreases to around 2.0 mg L⁻¹ at the depth of 2.0 m (Figure 3.34). For wastewater temperature of 20.0 °C (Figure 3.36), the average *DO* concentration measured below the fluid surface is slightly below 6.0 mg L⁻¹. In this case, considering the distribution of the *DO* concentration

with the depth of the tank, small variation up to 1.0 mg L^{-1} between the values in the mid-depth and below the surface are observed. Therefore, it can be concluded, that the distribution of DO within the whole volume of the ditch is uniform with the negligible differences in concentrations, and thus the DO profile corresponds to a completely mixed tank.

When comparing the oxygen profiles obtained during aeration-off time (Figure 3.35 and Figure 3.37) it is clear, that the backward order of measurement points (from the second brush aerator to the first) and the time intervals between measurements for support and sensor transporting allowed to assess DO decay due to progress of endogenous respiration in time rather than actual DO profiles along the ditch section. Such tendency was also observed in Figure 3.31 and Figure 3.33, however due to close to zero DO content the effects of endogenous respiration were also negligible.

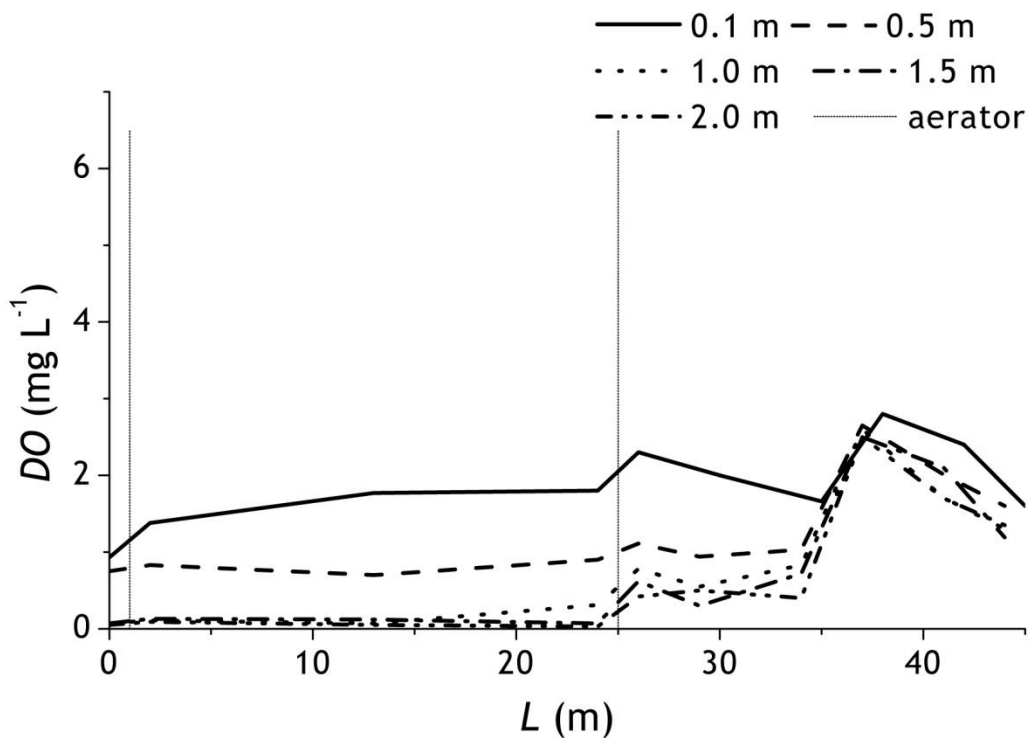


Figure 3.30 DO concentration profile obtained for the wastewater temperature of $30 \text{ }^\circ\text{C}$.

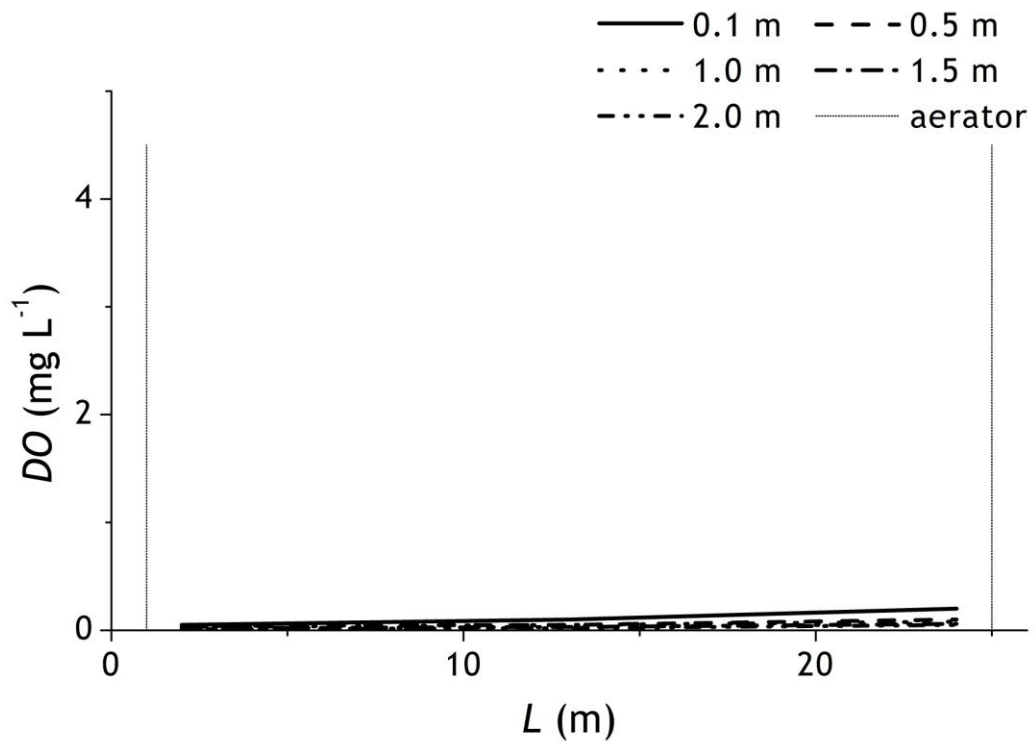


Figure 3.31 *DO* concentration profile under non-aeration period obtained for the wastewater temperature of 30 °C.

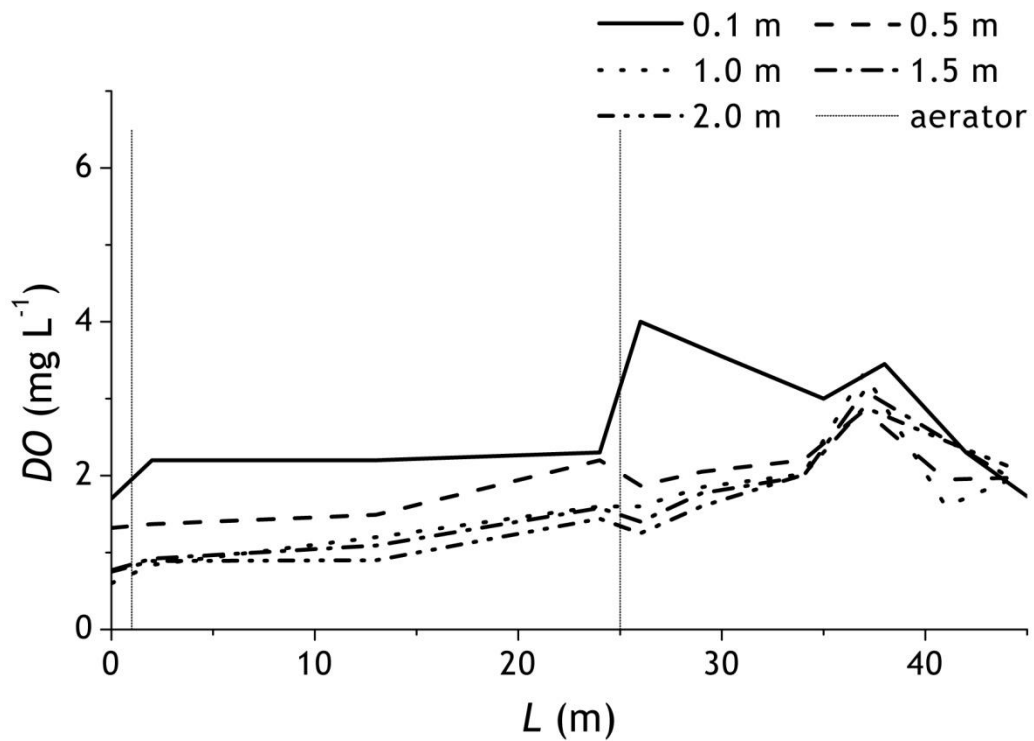


Figure 3.32 *DO* concentration profile obtained for the wastewater temperature of 27 °C.

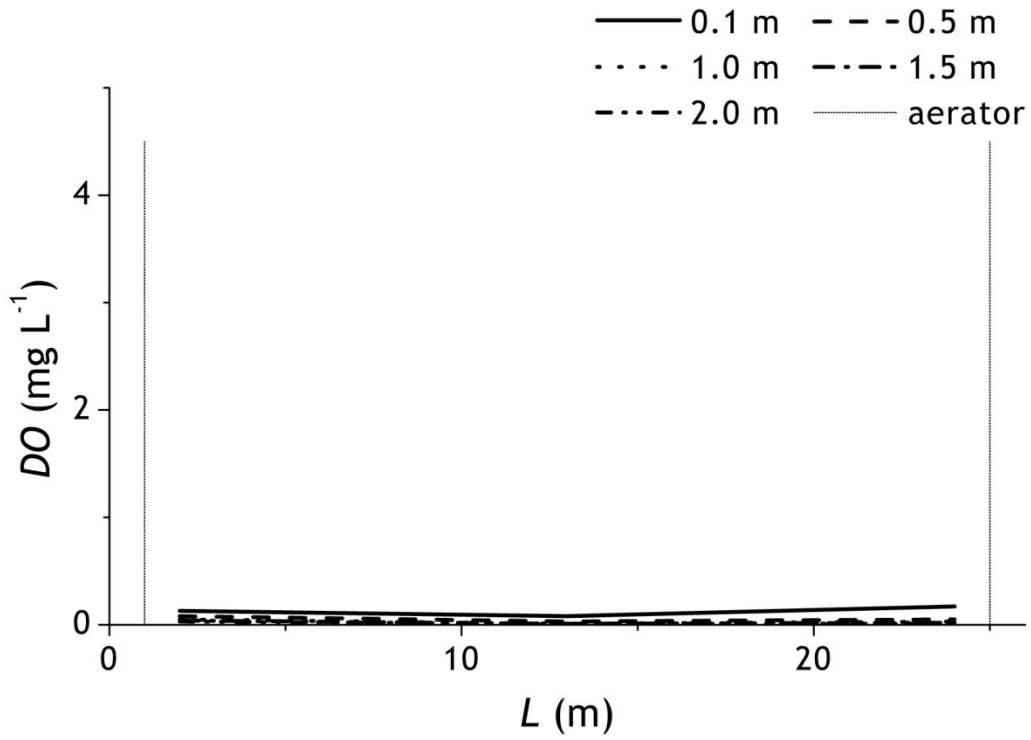


Figure 3.33 *DO* concentration profile under non-aeration period obtained for the wastewater temperature of 27 °C.

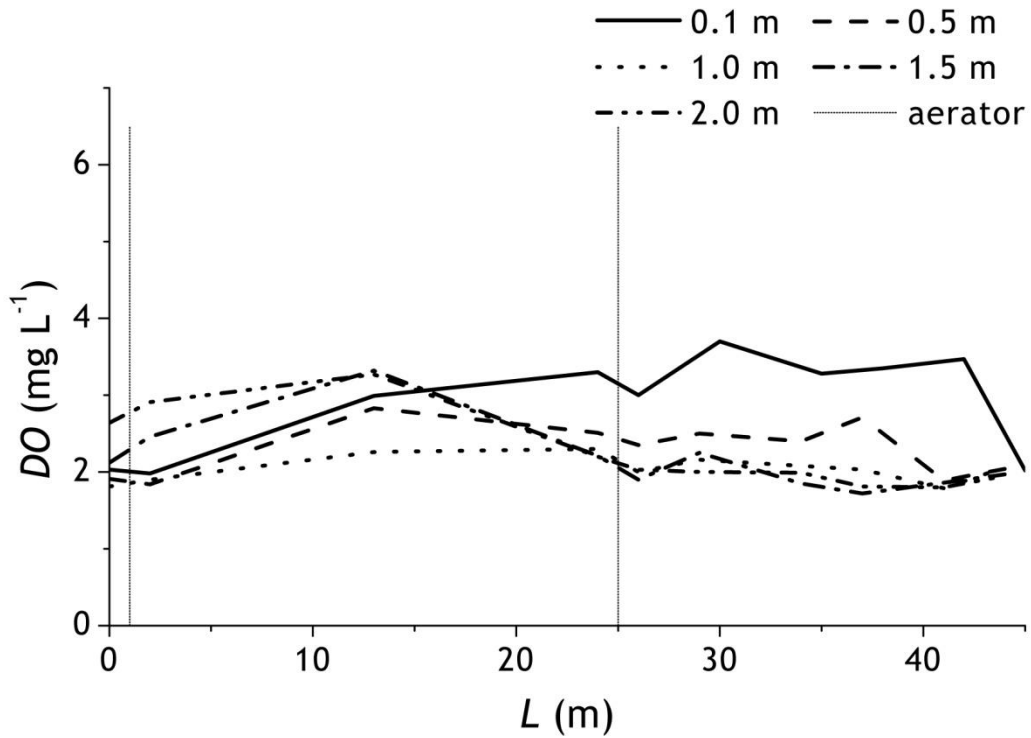


Figure 3.34 *DO* concentration profile obtained for the wastewater temperature of 23.5 °C.

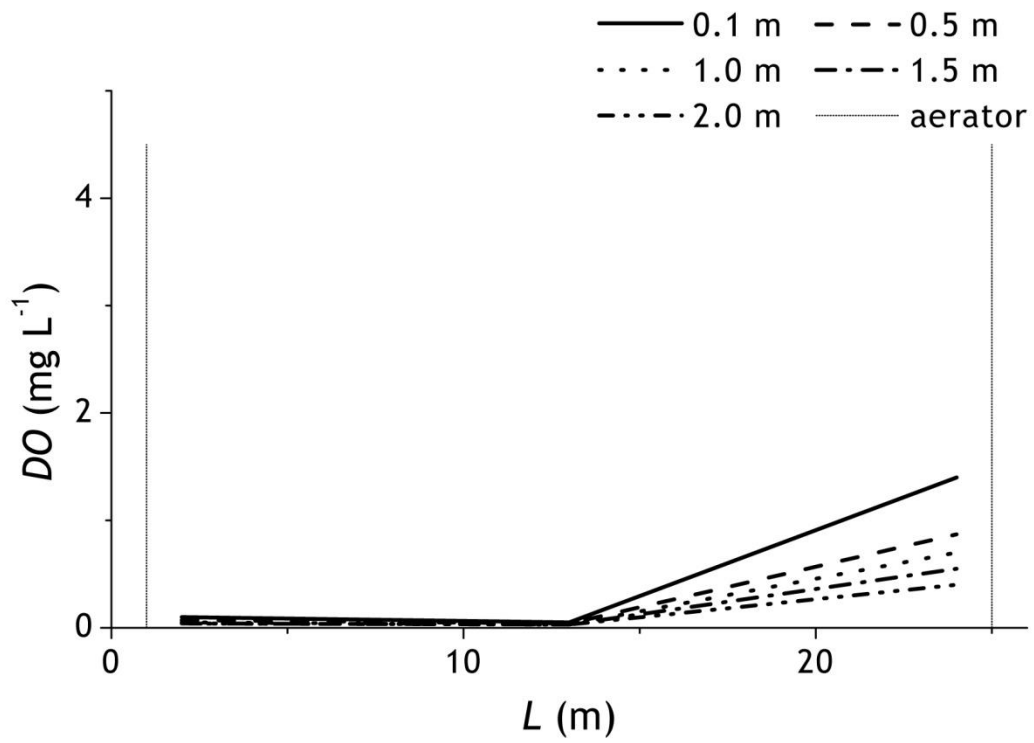


Figure 3.35 *DO* concentration profile under non-aeration period obtained for the wastewater temperature of 23.5 °C.

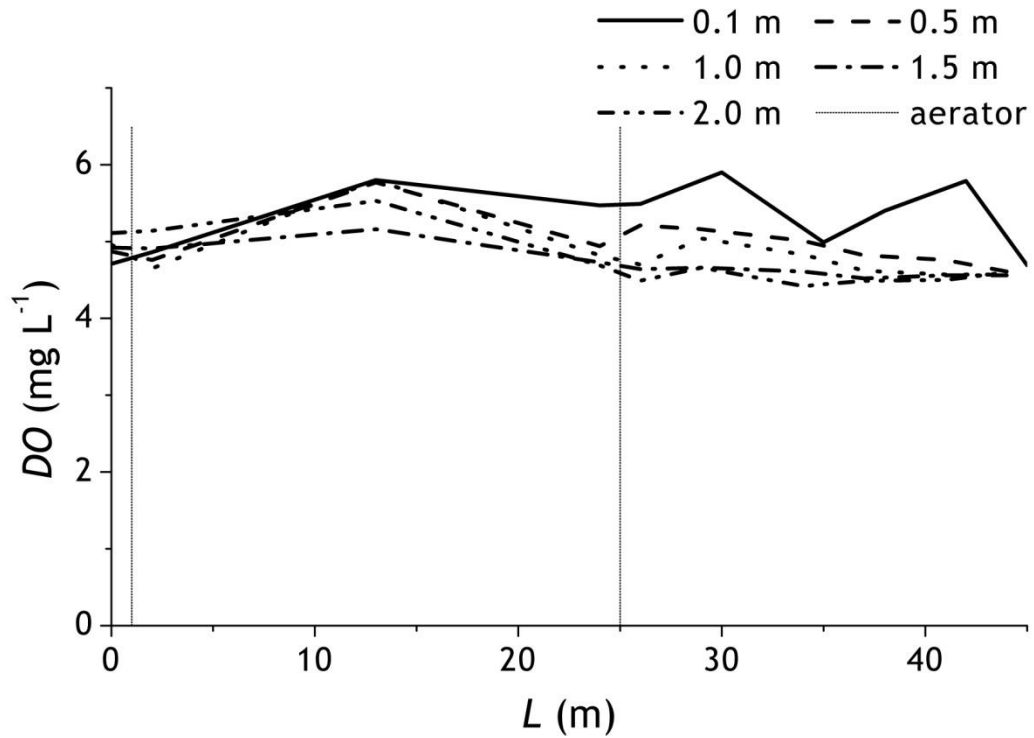


Figure 3.36 *DO* concentration profile obtained for the wastewater temperature of 20 °C.

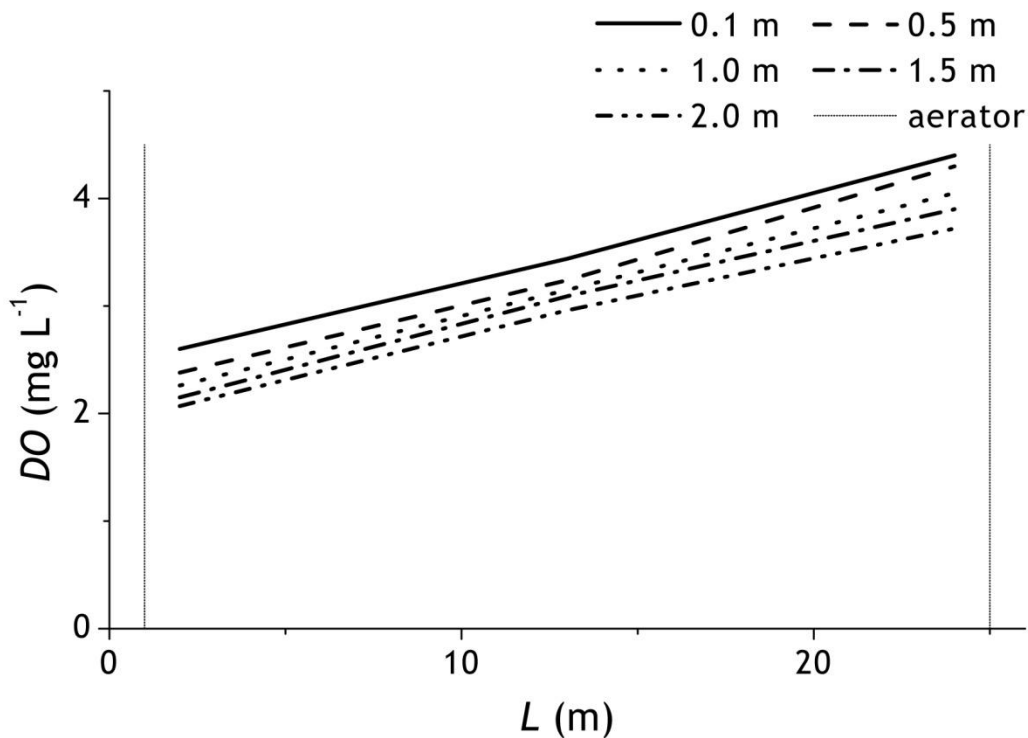


Figure 3.37 *DO* concentration profile under non-aeration period obtained for the wastewater temperature of 20 °C.

3.4.4.3 Nutrients Profiles along the Oxidation Ditch

Nutrients concentration profiles along the real scale oxidation ditch obtained during four sampling campaigns conducted in varying weather conditions are shown in Figures 3.38-3.41.

Distribution of the *COD* concentration along the ditch is almost uniform, with the maximal gradients up to 10 mg L⁻¹, as can be seen in Figure 3.38. The lower values in all four profiles are concentrated in the ditch area characterized by higher *DO* content, thus the section between the second aerator and the bend. Nonetheless, since the differences in concentrations do not exceed 8% it can be assumed, that the *COD* profiles are as for a completely mixed system. During sampling campaign, the influent quality was not determined, due to that it can only be assumed that the differences in the *COD* concentrations obtained in different sampling days could be due to the variable characteristics of the raw wastewater. Nonetheless, if one plots the average values of *COD* and nutrient concentrations as functions of the average value of *DO* as shown in Figure 3.42, it is clear that this parameter is probably the main responsible for the variability of data with time. According to that, for higher *DO* concentration more efficient nutrient conversion in the oxidation ditch was observed. Thus for average *DO* content from 1.9 to 2.6 mg L⁻¹, the average *COD* is up to 56.0 mg L⁻¹. With increase of *DO* to 5.3 mg L⁻¹, the average *COD* is 33.0 mg L⁻¹.

The constant concentration values of the $NH_4 - N$ profiles along the ditch (Figure 3.39) are as for the ideal CSTR. Nonetheless, during sampling days characterized by the elevated temperatures and the poor aeration conditions, the values of $NH_4 - N$ content within the tank ranging from 40-60 $mg L^{-1}$. In conditions of the wastewater temperature of 20 °C, the outflow $NH_4 - N$ concentration lowers distinctly to around 7.0 $mg L^{-1}$. The content of $NH_4 - N$ in the ditch depends to a larger extent on the oxygen conditions, as can be seen in Figure 3.42. Thus for the increase of DO content from 2.6 to 5.3 $mg L^{-1}$, the average ammonia concentration decreased from 56.0 to 6.0 $mg L^{-1}$.

Distribution of the nitrates concentration along the oxidation ditch is presented in Figure 3.40. As far as the profile obtained from the data related to the highest wastewater temperature and the lowest DO concentration differs from the other profiles with the higher $NO_3 - N$ content up to 4.2 $mg L^{-1}$ and the occurrence of the concentration gradient up to 1.0 $mg L^{-1}$ in the straight part of the ditch channel. The remaining profiles obtained for the lower wastewater temperatures revealed the constant nitrate concentrations along the considered section of the ditch. Considering extremely high values of ammonia and low concentration of nitrates, one could conclude that the nitrifying capacity of the activated sludge is low due to poorer aeration conditions, particularly at higher temperatures. In contrary to that, for lower wastewater temperatures and better oxygenation conditions, as the result of the intermittent aeration process, low COD and low nitrates concentrations seen in Figure 3.42, suggest intense biodegradation and denitrification processes occurring during the anoxic periods, however the course of partial nitrification should also be considered.

The profiles of the $PO_4 - P$ content along the ditch are presented in Figure 3.41. Here, one can also conclude that the distribution of the orthophosphates along the considered ditch section is linear and characteristic for the complete mixed systems. Slight increase of the $PO_4 - P$ concentration downwards the first aerator was only observed for the highest wastewater temperatures. When comparing the average orthophosphates, COD and $NO_3 - N$ concentrations in function of DO (Figure 3.42), it can be furthermore concluded, that intense denitrification process occurring during the anoxic periods are followed by re-aeration are accompanied by intensified $PO_4 - P$ uptake. And thus, for increasing dissolved oxygen content, the average $PO_4 - P$ decreases from almost 10.0 $mg L^{-1}$ and to 3.0 $mg L^{-1}$. The profiles of the TSS content along the oxidation ditch are show in Figure 3.43. Regardless of the wastewater temperature, the mixed liquor suspended solids levels are constant along the ditch. Determined range of the TSS concentration which varies from 2500 to 3500 $mg L^{-1}$ is representative for the oxidation ditch process.

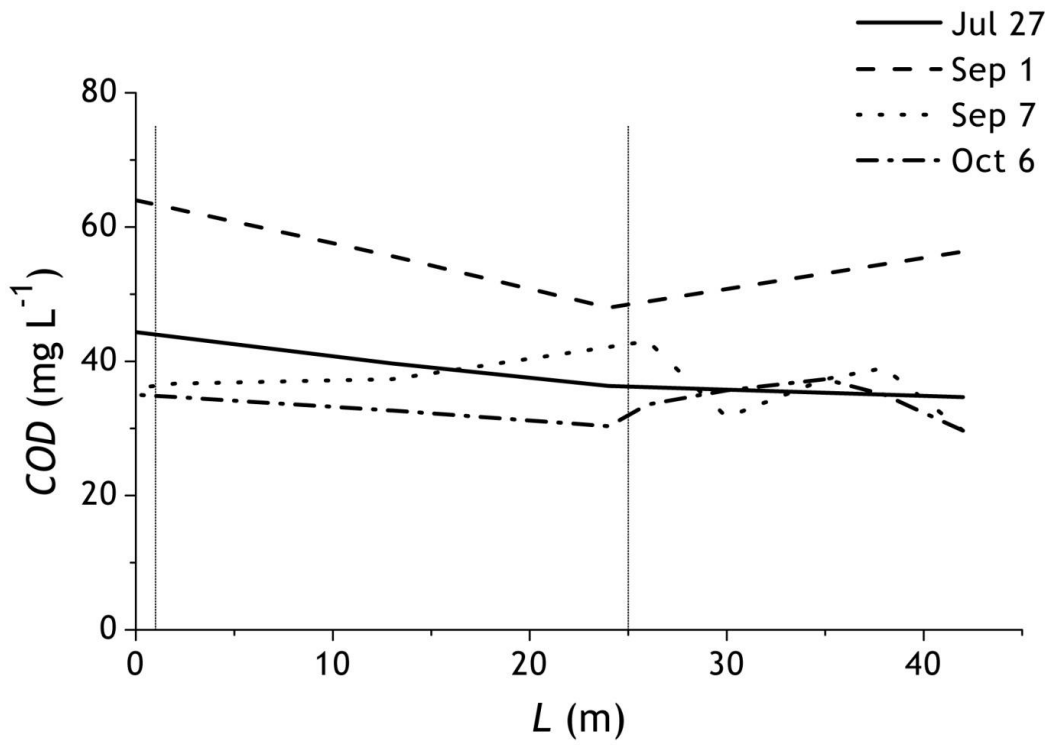


Figure 3.38 COD profile along the real scale oxidation ditch.

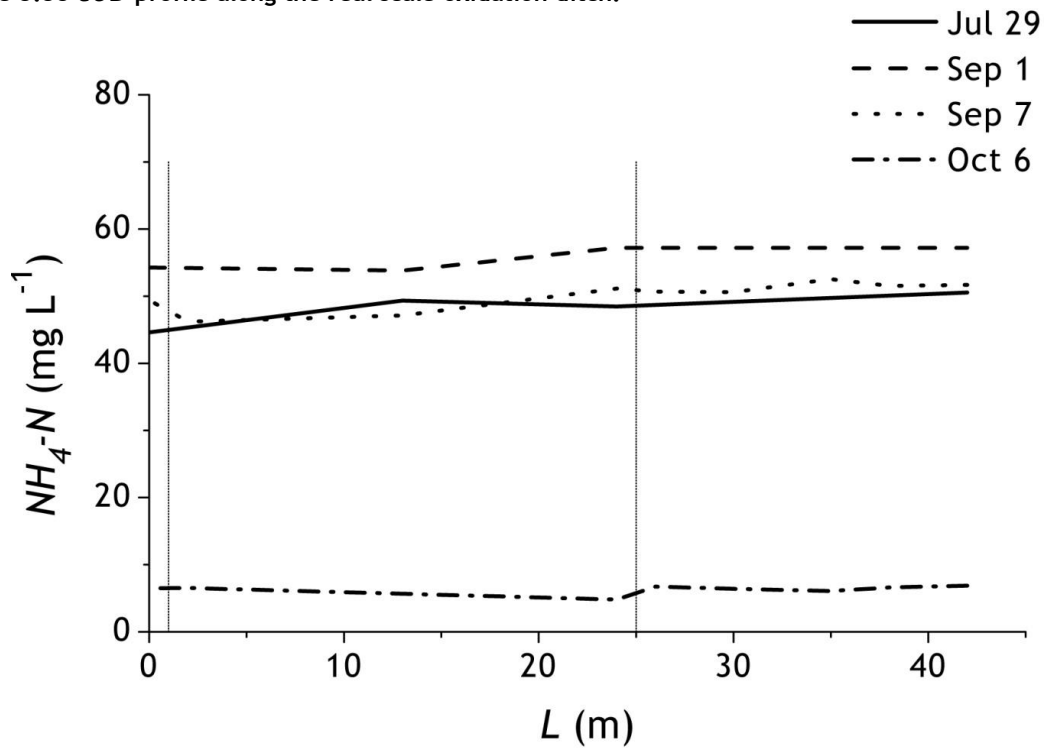


Figure 3.39 NH₄ - N profile along the real scale oxidation ditch.

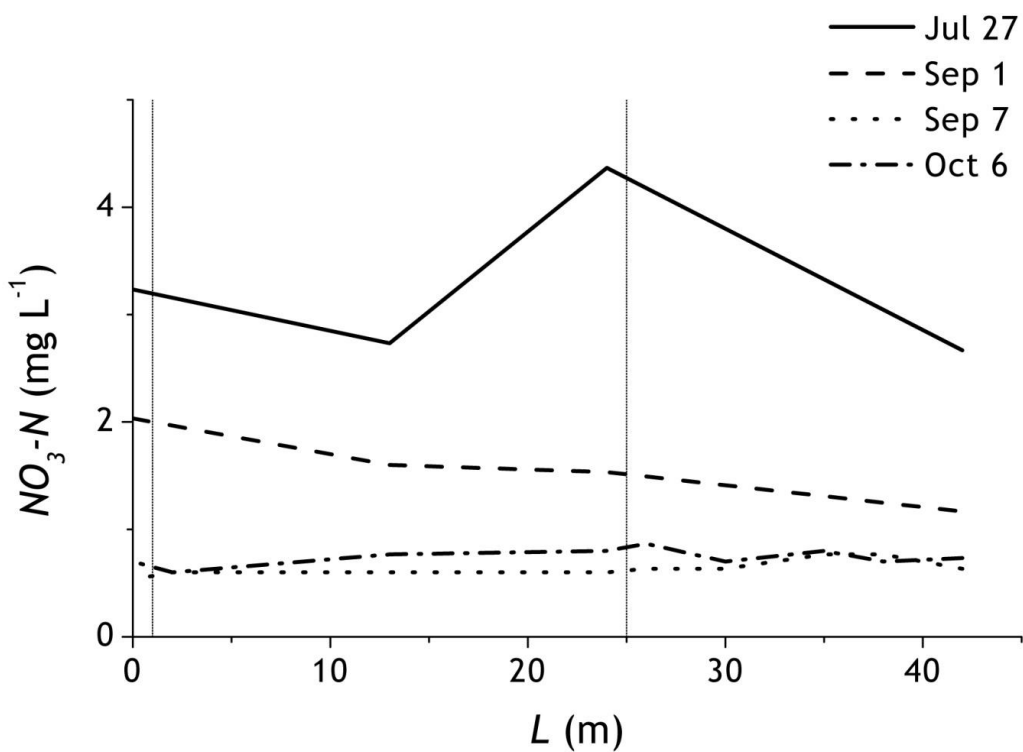


Figure 3.40 $NO_3 - N$ profile along the real scale oxidation ditch.

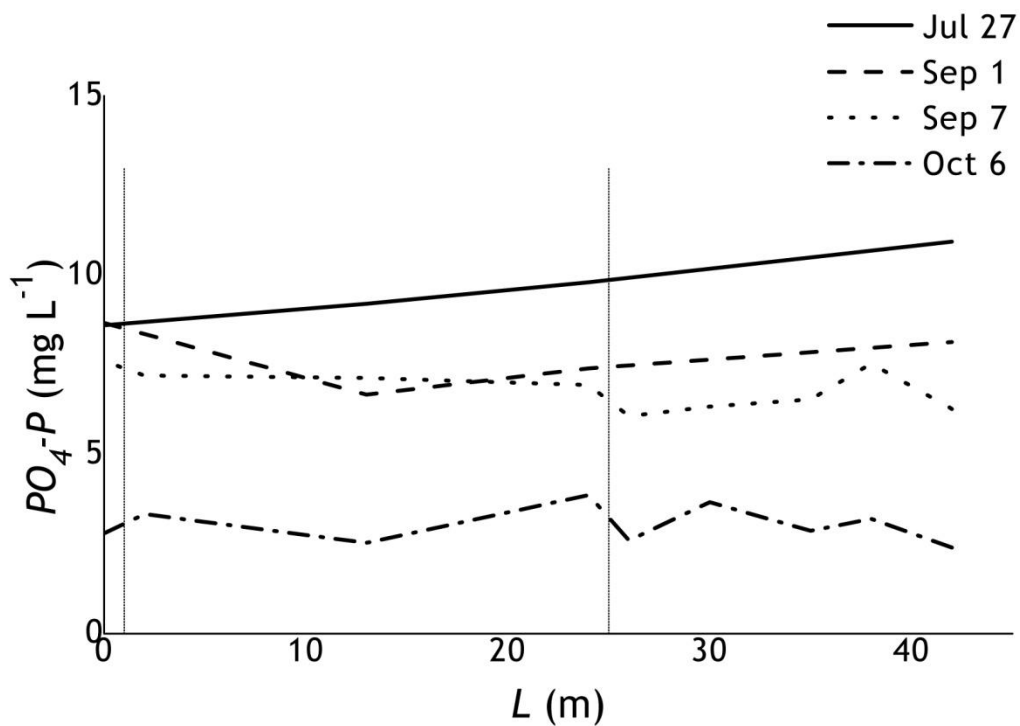


Figure 3.41 $PO_4 - P$ profile along the real scale oxidation ditch.

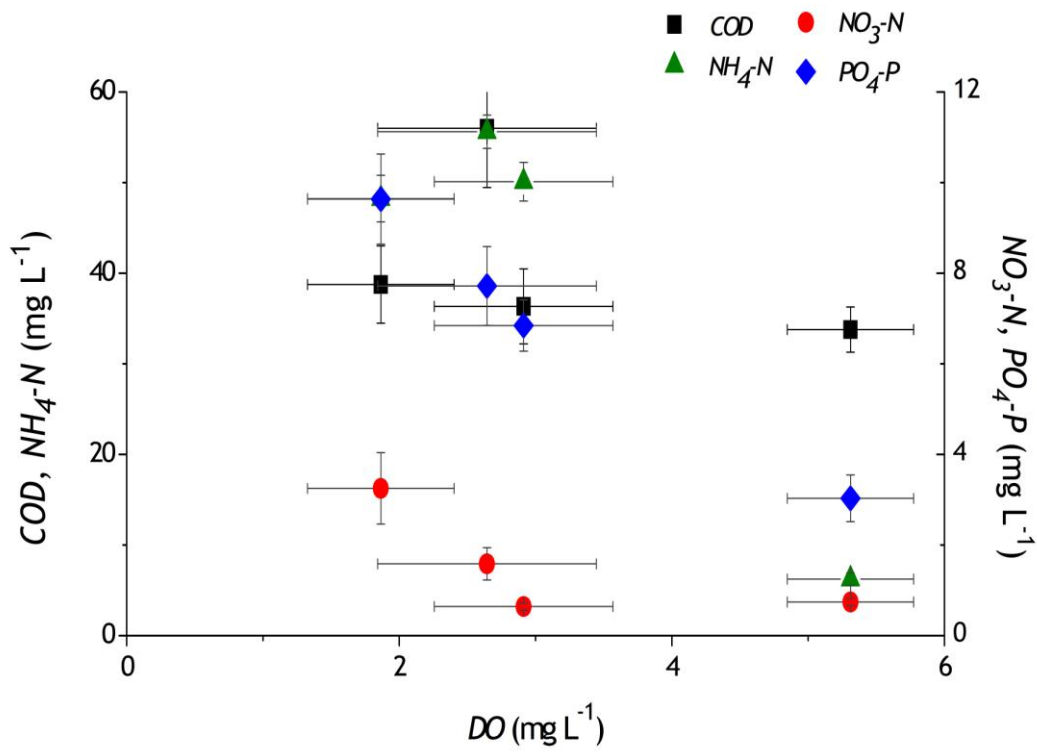


Figure 3.42 Nutrient concentration in function of DO content in real scale oxidation ditch.

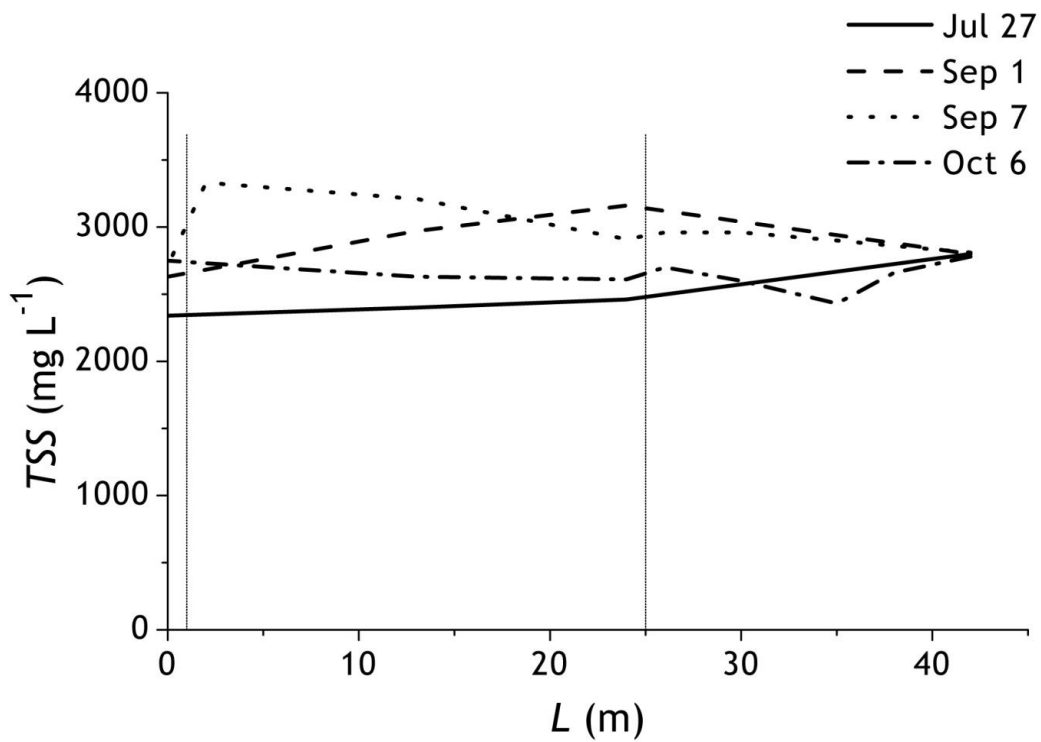


Figure 3.43 TSS profile along the real scale oxidation ditch.

3.5 Conclusions

The aim of this chapter was to study the hydrodynamics in two different oxidation ditches, the pilot PFRR ditch and the real scale oxidation ditch at Areosa WWTP.

The hydrodynamics in the pilot scale tubular ditch was assessed by determination of the horizontal velocity, DO , solids and nutrients profiles along the reactor. It was observed that for the selected rotor frequency, and regardless of the distance from the paddlewheel aerator, average velocities are uniform in the reactor cross-section, without clear distinction between low velocity near-bottom zone and high velocity near-surface region. On the other hand, velocity decreases with the distance from the paddlewheel aerator, reaching the minimum in the bottom diffusers region. Regardless of the wastewater temperature, diffuser and paddlewheel aerator placement, DO and nutrients concentrations were nearly constant along the pilot ditch yielding linear profiles. The only factor affecting DO level in the PFRR reactor is wastewater temperature, which has an influence on the oxygen solubility. Sporadic gradients in COD and TSS concentrations observed in the ditch zone affected by the proximity of the feed inlet, were caused only by varying quality of the influent and recirculation stream over time. Nonetheless one can conclude that for the studied tubular PFRR ditch, linearity of the profiles and the constant concentrations within the reactor and at the outflow are as for the complete mix system, characteristic for the flow conditions in the CSTR.

Hydrodynamics of the PFRR reactor was further investigated through determination of the RTDs of the fluid via pulse and step tracer experiments. Both experimental techniques involved using the clean tap water as the fluid medium and the aqueous solution of NaCl as the inert tracer and were conducted for identical conditions the constant flow rate, fluid velocity within the reactor and τ . The shape of both RTD curves obtained from the tracer experiments approach resembles the output profiles characteristic for the ideal CSTR vessel. Nonetheless, early peaks and the shallow tail observed in the normalized pulse curve and the slope and the long tail of the normalized step curve suggested the occurrence of the possible channelling, internal recirculation and stagnant fluid regions, which may have serious consequences in wastewater treatment efficiency.

As the performance of the tracer experiments in the real scale tanks is not a feasible task, the hydrodynamics of the oxidation ditch at the Areosa WWTP was assessed on the base of the velocity, DO , TSS and nutrients profiles, determined along the wastewater tank.

The distribution of the horizontal surface velocities along the oxidation ditch depends on the ditch geometry and aerators placement and performance. It was found that the fluid

velocities in the studied activated sludge system are nearly four times higher than the typical operating ranges for the oxidation ditches.

For such operating velocities, distribution of the DO concentration downstream and upstream the aerators in the straight section of the ditch is almost constant, as in the complete mix system. Wastewater temperature has a large influence on the DO transfer within these sections. In conditions of the elevated temperatures above $27\text{ }^{\circ}\text{C}$ only surface fluid layers are aerated. Despite higher operating capacities of the aerators yielding higher velocities, low solubility of air in wastewater causes formation of steep oxygen stratification in the ditch with the oxygen deficit zone ranging from the mid-depth of the ditch constituting 50% of the ditch volume. In such conditions, required DO concentration at the point of introduction should be increased.

Larger DO gradients occur in the area of the ditch bend due to dynamic mixing of more or less oxygen enriched fluid layers. Thus, even for high wastewater temperatures, the bends are unique zones along the ditch characterized with presence of DO at half of the ditch depth. Significant improvements of the aeration efficiency were observed for the temperatures around $20\text{ }^{\circ}\text{C}$, yielding slight changes of the DO content along the ditch and between the values measured below the surface and in the mid-depth of the ditch, that are around 5.0 mg L^{-1} . For such conditions, the considered ditch section behaves like CSTR.

The differences in COD concentration along the ditch, and thus considering values obtained for the straight channel section and for more intense oxygenated bend, do not exceed 8%. According to that it can be assumed, that the COD profiles are as for a completely mixed system. Similar to COD patterns, the concentration profiles obtained for the remaining nutrients: $NH_4 - N$, $NO_3 - N$, and $PO_4 - P$ along the oxidation ditch are constant and thus complete mixed tank conditions can be assumed.

When evaluating treatment efficiency during sampling days characterized by the elevated temperatures, high values of ammonia within the tank are observed. As variable $NO_3 - N$ concentrations are low it can be suspected, that due to poor aeration, nitrifying capacity of the activated sludge is low. In lower wastewater temperatures and optimal oxygenation conditions within the ditch, the final $NH_4 - N$ concentration drops nearly ten times. Low COD and nitrates contents suggested efficient biodegradation and denitrification processes, which occur during anoxic periods, but at the same time, possibility of accumulation of nitrites should be taken into account. As in case of ammonia, decrease of $PO_4 - P$ concentration within the ditch is observed. According with the above one can conclude, that the biological reactor performance, thus intensity of the biodegradation,

3 Hydrodynamics of the Oxidation Ditch

denitrification and P uptake and bioaccumulation depend on the DO concentration within the ditch.

The mixed liquor suspended solids levels are in the typical ranges for the oxidation ditches, and their content is constant along the studied ditch, suggesting complete mixing characteristic for the flow conditions, as in the CSTR.

4 CFD Simulations of the Oxidation Ditch

4.1 Introduction

This chapter is divided in two main sections: in the first section, a literature review on the use of CFD modelling in wastewater treatment engineering is done; while the second refers to a development of a CFD based model to simulate hydrodynamics in a specific wastewater treatment bioreactor- an oxidation ditch.

The review aims to present the typical trends in design of Activated Sludge systems and rationale behind the use of CFD modelling approach to optimize wastewater treatment operation and process efficiencies.

Second part of the chapter concerns the implementation of various configurations of slot jet aeration devices in oxidation ditched, compromising the functions of aerator and mixer. The design considerations and the CFD model are described with detail. Furthermore, the fundamental concepts of the flow field and macromixing simulations with the description of different approaches commonly used in turbulence modelling are given. The impact of the turbulence model on the flow patterns evolution within the oxidation ditch channel is assessed. Additionally, the influence of the aeration system geometry on the hydrodynamics and the energy expenditure for mixing in the oxidation ditch is evaluated. Further studies concerned the study of the hydrodynamics in the near-wall region of the oxidation ditch. The influence of the mesh and the near-wall treatment coupled to the turbulence models on the accuracy of the boundary layer representation, and the energy expenditure is also made. Finally, the analysis of the effect of the

turbulence models on the macromixing data, which can be furthermore incorporated into the Activated Sludge Models (ASM), is also assessed.

4.2 Literature Review

One of the major challenges in wastewater sector is successful design and reliable operation, which ensure that the treatment efficiency will comply with the outflow quality restrictions, while keeping the investment and operating cost as low as possible (Brouckaert and Buckley, 1999; Do-Quang et al., 1999). Although the design of wastewater treatment plants (WWTPs) is a key step to assure these goals, it is usually based on the general guidelines and both the designers and operators experience, dominated often by the rule of thumb (Bosma and Reitsma, 2007; Pereira et al., 2012; Stamou, 2008). Thus, in majority of the designs, the assumption of the ideal reactor model is imposed to predict flow behaviour in the unit process tanks, while the actual reactor hydrodynamics is not taken into account (Stamou, 2008). The classical example is the assumption of complete mixed flow regime in aerobic, anoxic and anaerobic tanks. Other commonly practiced rules of thumb are (Tchobanoglous et al., 2003): the assumption that in AS basins equipped with diffused aeration systems, the air requirement to ensure good mixing will vary from 1.2 - 1.8 m³ h⁻¹ per cubic meter of tank volume; and typical power requirements for maintaining a completely mixed flow regime with mechanical aerators varies from 13 to 26 W per cubic meter of tank volume. None of these assumptions consider influence of the tank hydraulics (depth), energy input, or any variable affecting mixing. The one commonly used criterion for “good mixing” in AS process control is such, that the variations of solids concentration across the complete mixed tank profile is less than 10%. However, the proper design of such “well mixed” system requires use of sophisticated analysis of flow behavior accounting for mixing patterns in the tank, distribution of solids and determination of local densities.

In engineering practice, assessment of flow regime, and thus overall mixing phenomena can be achieved in experimental derivation of local flow velocities through a tracer technique, which is not a feasible task most of the times, considering dimensions of real scale units (Pereira et al., 2012; Stamou, 2008). Several factors contribute to the increasing popularity of the modelling in engineering practice. Modelling is cost and time efficient risk-free solution, which allows: to evaluate whether a new unit or modification will operate properly; to foreseen the consequences before implementation; to isolate and quantify bottlenecks in liquid or solid handling lines in the AS system. In modelling practice, RTD determination allows to obtain these data by deriving the main convective and diffusive characteristics of the flow (Stamou, 1997, 2008). Thus, prediction of RTDs of

fluid is a fundamental tool to understand and analyze flow system allowing therefore realistic information on the hydrodynamics of the tanks (Nauman, 2007). Moreover, the RTD yields information about the macromixing within the reactor, allowing the recognition of mixing conditions that are not plug flow or complete mixing regimes, and that are usually described by tank-in-series models or even more complex arrangements of reactors (Pereira et al., 2012). Due to that, successful biological wastewater treatment modelling combining hydrodynamics, mass transfer and biochemical reactions kinetics remains one of the major goals in chemical engineering (Le Moullec et al., 2010a, b; Pereira et al., 2012).

Nowadays, due to increasing availability of computational resources, dynamic modelling of the AS tanks involves different approaches, providing relevant and mutually complementary information (Karpinska et al., 2012a). Systemic approach is based on well-established Activated Sludge Models (ASM), focused mainly on the reactions of biochemical conversion within the ideal reactors: one or a cascade of Continuous Stirred Tank Reactors (CSTRs) or plug flow reactor (PFR) (Abusam and Keesman, 1999; Abusam et al., 2001; Le Moullec et al., 2010b; Pereira et al., 2009). The results allow for prediction of quantitative oxygen consumption, nutrients removal and qualitative biomass growth and decay; however, the ideal reactor models do not account for the actual influence of the reactor hydraulics, temperature and oxygen spatial distribution on the treatment efficiency (Karpinska et al., 2012a). Additionally, since overall biochemical conversion reactions in AS occur at a significant rate, the wastewater treatment efficiency will depend on the hydrodynamics of the biological reactor (Le Moullec et al., 2008b). Consequently, to model accurately biological wastewater treatment in AS process and determine correct pollutant removal rates, biokinetic reactions have to be coupled to the reactor hydrodynamics.

With the recent developments in multiphase flow research area (Kochevsky, 2004), CFD has been extensively used as a powerful tool allowing for precise analysis of the hydrodynamics in AS tanks which enables prediction of the influences of the operating parameters and of local scale phenomena, such as flow field coupled with mass transfer and chemical reactions. Behaviour of aeration tanks is complex, mainly due to the presence of multiphase (gas-liquid-solid) flow and the interactions between nano-, micro- and macro-scale elements of the system, such as between AS flocs, air/oxygen bubbles introduced by aerator and finally, geometry of the tank. Considering the sizes of the aeration tanks and the typical values of fluid velocity of 0.3 m s^{-1} , the Reynolds numbers in the AS processes are turbulent (Pereira et al., 2012). Although the complete simulation of such biological system is difficult to handle due to the complexity of the hydrodynamics, resulting in long computational times involved and massive computer resources usage,

some few examples of complete modelling of wastewater treatment tanks with CFD codes, accounting for flow field, oxygen mass transfer and biokinetics can be found in the literature (Brannock et al., 2010b; Fayolle et al., 2007; Gresch et al., 2011; Le Moullec et al., 2010a; Zima et al., 2009).

A more common engineering practice is to model the whole process with reasonable computational resources usage, by simulating separately with CFD codes its individual parts, such as aeration performance or flow field and afterwards couple the results (Pereira et al., 2012). Literature offers handful examples of the CFD application to study AS process in wastewater tanks. Here, CFD can be used as a hi-tech tool for design of the new efficient and energy minded unit processes at WWTPs or for optimization and retrofit of the existing systems. Thus, two-phase gas-liquid flow simulations enable prediction of oxygen mass transfer and gas hold-up in activated sludge tanks aiming both, process design and optimization through “tune-for-benefit” operating parameters of aeration devices (Cockx et al., 2001; Dhanasekharan et al., 2005; Do-Quang et al., 1999; Fayolle et al., 2007; Gresch et al., 2011; Talvy et al., 2007). The focus of other works is on the aerator design, number of units and configuration within the AS basin, allowing for effective mixing and process performance (Bhuyar et al., 2009; Gresch et al., 2011; Le Moullec et al., 2010a, b; Luo and Al-Dahhan, 2008; Moraveji et al., 2012; Wu et al., 2012; Xu et al., 2010). Two-phase, turbulent solid-liquid flow simulations enable representation of the main flow currents within the oxidation ditches considering the impact of aerators and propellers performance on mixing patterns, solids distribution and sludge settling (Fan et al., 2010; Zhang et al., 2010). Recently, CFD has been also successfully implemented in hydrodynamics modelling of specific gas-solid-liquid systems, namely Membrane Bioreactors (MBRs), allowing for optimization of mixing regime within full-scale units through RTD of the fluid determination. Until recently, desired mixing regime in MBRs, although being of crucial importance for overall process performance, was designed only from empirical techniques (Brannock et al., 2010a; Brannock et al., 2010b)). Nowadays numerous examples of hydrodynamics studies based on the RTD determination for various AS process modifications can be found in the literature (Brannock et al., 2010a; Brannock et al., 2010b; Fan et al., 2010; Glover et al., 2006; Le Moullec et al., 2008b; Stamou, 2008; Wu et al., 2012; Zhang et al., 2010; Zima et al., 2009). Furthermore, the procedures of coupling AS hydrodynamics data obtained from CFD simulations into the ASM simulations have been also intensively studied (Glover et al., 2006; Le Moullec et al., 2010b; Pereira et al., 2012). Here the RTDs computed from CFD simulations are used to generate reactor model in which ASM can be applied.

Nowadays an alternative modelling approach to AS, namely compartmental model approach, is emerging, which is based on the description of the wastewater reactor as a network of interconnected compartments. The flowrates between the compartments are computed from the flow field obtained in the CFD simulations and accounting for local velocities and mixing due to turbulence (Le Moullec et al., 2010b; Pereira et al., 2012).

This chapter considers the use of CFD to simulate hydrodynamics and macromixing in one of the well-known modifications of the AS process- the oxidation ditch. Typical oxidation ditch system consist of a ring, oval or horseshoe shaped basin, where the liquid phase, mixed liquor is circulated around the ditch by means of mechanical impellers. In the ditch there are aerated regions, where the air is introduced into the mixed liquor either through the surface by brush rotors or into the fluid volume, by bottom diffusers. Prediction of the flow regime with systemic approach in oxidation ditches is not straightforward. Usually, both, single- and multi-channel ditches are considered to be completely mixed over the hydraulic residence time (EPA, 2000), but simultaneously show strong plug flow characteristics, when observed over one loop (Barnes et al., 1983). Additional feature is occurrence of large DO gradients along the ditch while the other components, such as ammonia or COD concentrations are spatially homogenized (Nakamachi et al., 2012). Thus, simulation for such AS system has been mostly based on ideal reactor models: Continuous Stirred Tank Reactor (CSTR) or in a cascade of CSTRs (Karpinska et al., 2008).

According to that, only CFD based modeling allows to reproduce the actual conditions of the ditch performance, based on the dynamic fluid circulation by the propellers and intense aeration with surface rotors or diffused aeration units. Several works on CFD modeling consider and oxidation ditch as a showcase to assess the system hydrodynamics, the paths of biochemical reactions represented by concentration profiles, and to optimize aeration and agitation devices (Chen and Wu, 2010; Do-Quang et al., 1999; Fan et al., 2010; Fayolle et al., 2007; Glover et al., 2006; Karpinska et al., 2012a; Pereira et al., 2012; Wu et al., 2012; Xia and Liu, 2004; Xu et al., 2010; Yang et al., 2011; Zhang et al., 2010).

4.3 CFD Model

This section analyses the use of a specific slot jet aeration system in oxidation ditches, comprising the functions of aerator and mixer. CFD is used as the design and analysis tool to study oxidation ditch aerated with hydrojets, taking into consideration aeration and mixing performance, the influence of geometry (hydrojet placement) and the wall effects on the energy expenditure of the simulated system. The analysis of the effect of the

turbulence models on the macromixing data, which can be further incorporated into the ASM models, is also made. Moreover, the results obtained from the CFD simulations of the oxidation ditch are further used to set some guidelines of the application of CFD tools on AS processes design.

All simulations of the oxidation ditch used Finite Volume Method and were performed using ANSYS Fluent 14 commercial CFD code in a HP Workstation with Intel® Xeon® 2.33 GHz 8-Core PC with 16.0 GB RAM memory.

4.3.1 Design Consideration

Hydraulic design of the proposed oxidation ditch system (Figure 4.1) consists of: an oxidation ditch; a jet aeration device; an external aeration unit - Pressurized Aeration Chamber (PAC), introduced in Chapter 2 of this dissertation; mixed liquor recirculation pump; feed and discharge tubes; and a pipeline connecting all equipments. In such system, the increase of *SOTE* and *AE* is obtained through introduction of an external aeration unit- PAC cooperating with the mixing and propulsion devices- slot injector modules (hydrojets). Mixed liquor is recirculated from the ditch to PAC, where is saturated with oxygen up to 18 mg L^{-1} . The DO enriched stream is recirculated by pump and reinjected into the ditch by the hydrojets with the energy accelerating fluid flow throughout the tank with the velocities keeping the AS flocs suspended, and ensuring efficient mixing of the ditch content.

In oxidation ditch systems, the average concentration of the Mixed Liquor Suspended Solids (MLSS) is in the range of $3000\text{-}5000 \text{ mg L}^{-1}$ (0.3 - 0.5 % w/w). The main purpose of this work is to explore the use of CFD in the design of oxidation ditches, and so water was defined as the working fluid, which is not so accurate as far as viscosity is regarded. However, for the purposes of present studies a model fluid that enables a faster setup of the lab validation of CFD results will serve better considering the near future plans of this research.

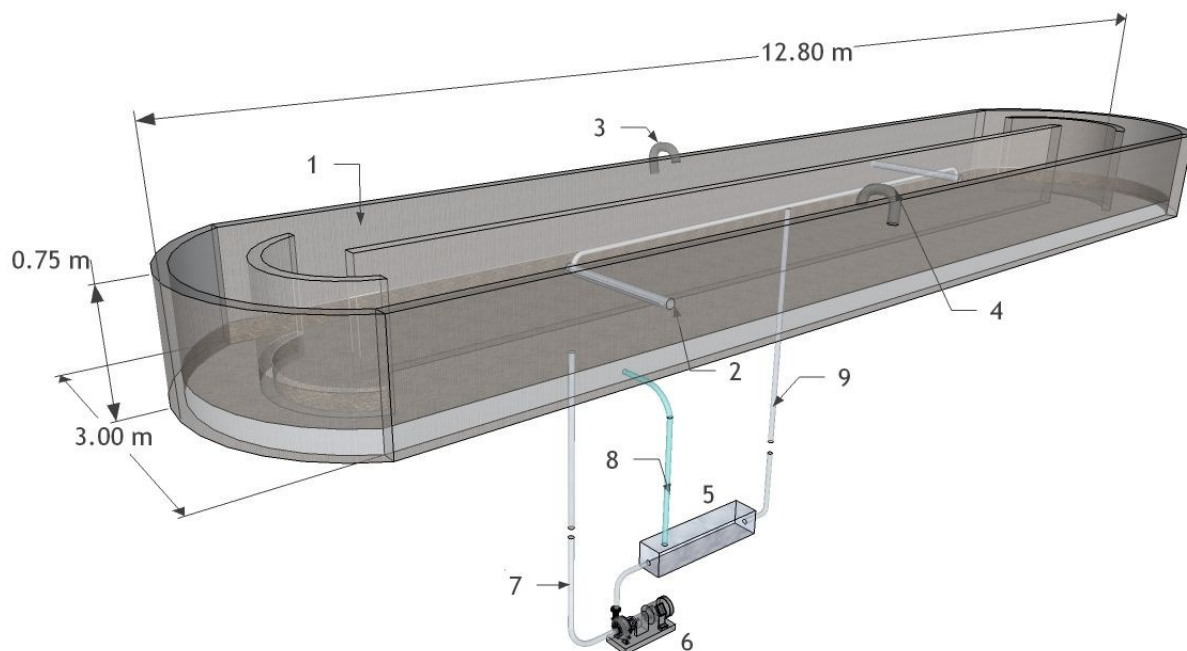


Figure 4.1 Oxidation ditch system scheme: 1- oxidation ditch; 2- hydrojets; 3- inlet; 4- outlet; 5- PAC; 6- recirculation pump; 7- recirculated mixed liquor from the ditch; 8- air/oxygen manifold; 9- oxygen rich mixed liquor.

4.3.2 3D Geometry

The simulated ditch system consists of a closed-loop oval open channel filled with liquid (mixed liquor), and equipped with two jet aeration devices placed at opposite positions in the oxidation ditch. The 3D ditch geometry, which outline is shown in Figure 4.1, was designed for further laboratory scale applications and has the following dimensions: 12.8 m long, 3.0 m wide and 0.75 m deep. The surfaces of the oxidation ditch inlet and outlet are rectangular sections with 1.44×0.25 m, which are located on the top of the ditch. Inlet, outlet and hydrojets are distanced from each other by half of the ditch length. The hydrojets devices are designed as slot injectors extended throughout the ditch and have 0.1 m height. Schematic design of what an actual hydrojets would be, is shown in the Figure 4.2. In this work it is assumed that the flow rate has a constant distribution at hydrojet suction face and outlet, i.e. a flat velocity profile. In this study, three different geometry scenarios were taken into consideration: hydrojets fixed near the bottom, at $1/3$ depth, in the middle of the ditch and below the fluid surface, at $2/3$ depth. Inlet and outlet are located on the fluid surface.

Geometries of the oxidation ditch with various hydrojets positions were made using ANSYS Workbench Design Modeller pre-processing software. An example of the ditch geometry, with hydrojets positioned in the middle depth is shown in Figure 4.3.

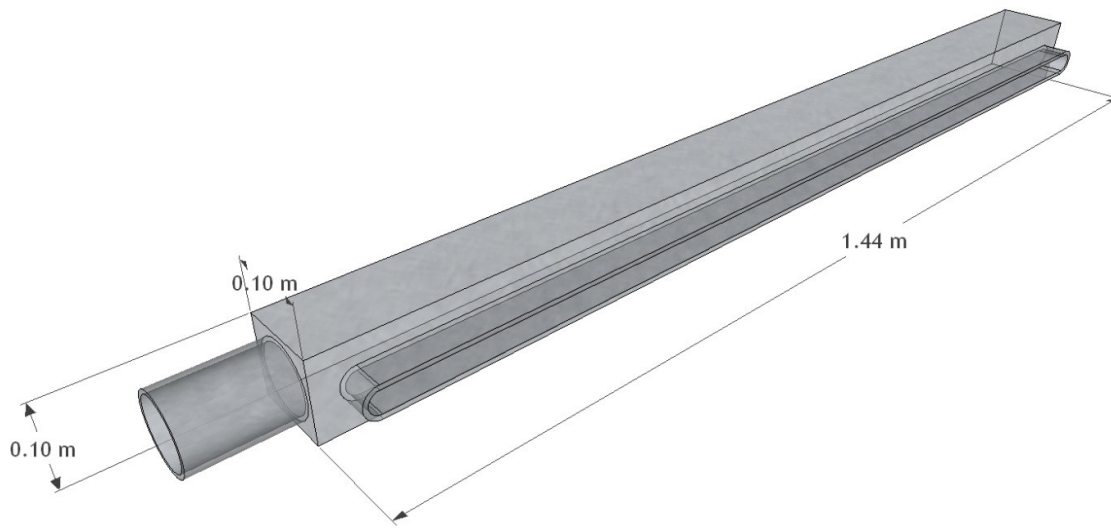


Figure 4.2 Schematic design of the hydrojet device.

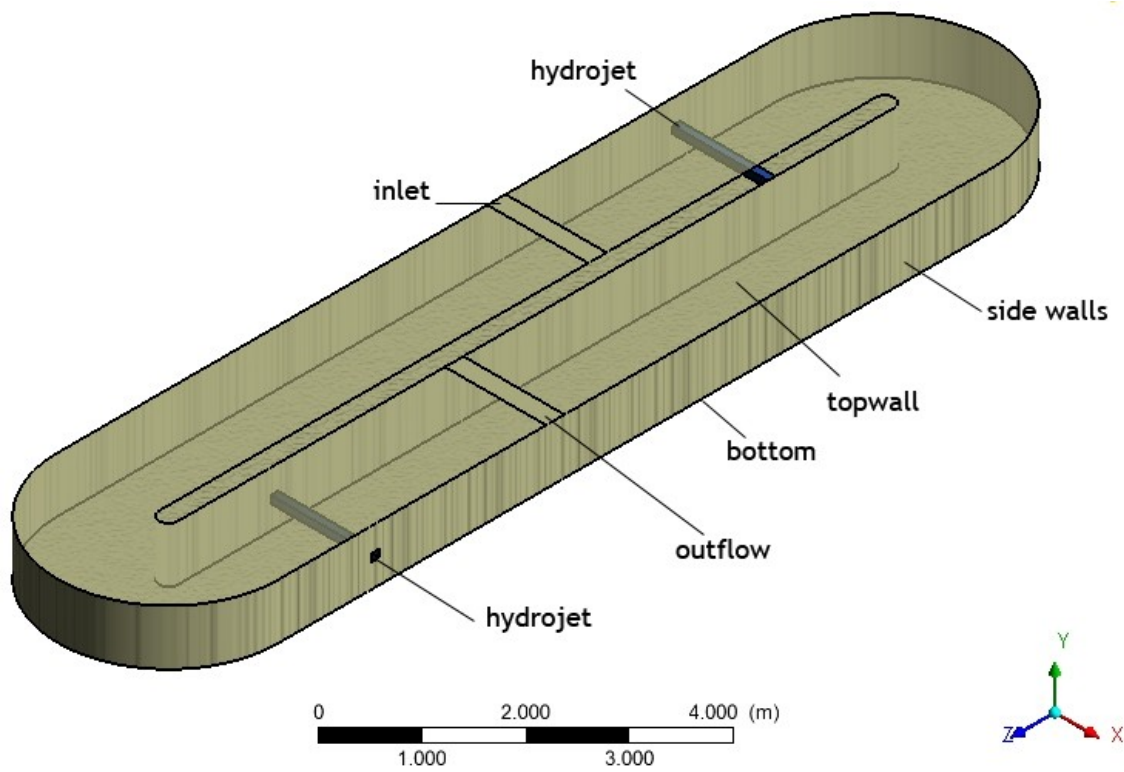


Figure 4.3 Geometry of the oxidation ditch with hydrojets placed in the middle depth of the tank.

In all geometries, the computational grid was generated by sweeping algorithm based on the projection of the source surface mesh created for the topwall onto the target surface of the ditch bottom. Different features of the source surface mesh, such as additional inflation of the lateral edges or defining of the sweep bias, yield six meshes composed of from 0.6×10^6 to 5.6×10^6 hexahedral cells. The rationale behind using meshes of different characteristics was their further application in simulations having different purposes and level of complexity, and thus requiring for more or less computational resources. The details concerning geometry of the oxidation ditch, meshing algorithm, number of generated mesh elements, average element size and the application to specific CFD studies, are listed in the Table 4.1. For each mesh several preliminary simulations were made to test grid independence.

4 CFD Simulations of the Oxidation Ditch

Table 4.1 Characteristics of the meshes used in the simulations of the oxidation ditch.

Mesh n°	Mesh features	N° of mesh elements	Average element size	Application
		Million	m	
1	Sweep; surface mesh consisted of mapped/paved grid of quadrilateral elements	0.6	0.0304	Hydrodynamics and macromixing simulations using different turbulence models; energy expenditure and boundary layer determination
2	Sweep; surface mesh consisted of mapped quadrilateral and triangular elements; size function in the hydrojets zone	1.7	0.0250	Hydrodynamics simulations using different turbulence models; geometry studies; energy expenditure and boundary layer determination
3	Sweep; surface mesh consisted of mapped quadrilateral and triangular elements; 24 inflation layers with 1.1 growth rate factor, 25 sweep bias	4.7	0.0013	Hydrodynamics simulations; energy expenditure and boundary layer determination
4	Sweep; surface mesh consisted of mapped quadrilateral and triangular elements; 24 inflation layers with 1.1 growth rate factor, 32 sweep bias	4.7	0.0011	Hydrodynamics simulations; energy expenditure and boundary layer determination
5	Sweep; surface mesh consisted of mapped quadrilateral and triangular elements; 24 inflation layers with 1.1 growth rate factor, 25 sweep bias; boundary refined in Fluent using y^+/y^* adapt algorithm	5.4	0.0007	Hydrodynamics simulations using different turbulence models; energy expenditure and boundary layer determination
6	Sweep; surface mesh consisted of mapped quadrilateral and triangular elements; 24 inflation layers with 1.1 growth rate factor, 25 sweep bias; boundary refined twice in Fluent	5.6	0.0063	Hydrodynamics simulations; energy expenditure and boundary layer determination

4.3.3 Hydrodynamics Modelling

The hydrodynamics of the oxidation ditch is obtained from single-phase flow field simulations. For all ditch geometries the flow field was simulated using steady Reynolds Averaged Navier-Stokes (RANS) simulations and Unsteady RANS (URANS) with different turbulence models and Large Eddy Simulation (LES) with Smagorinsky's subgrid-scale model (SGS).

4.3.3.1 Reynolds Averaged Navier-Stokes Simulations

In most of the CFD related engineering practice, time-averaged properties of the flow provide the needed information. RANS simulations focus on the representation of the effects of turbulence on the mean flow properties by solving transport equations for the averaged flow quantities with whole range of the turbulent scales being modelled. Thus this modelling approach greatly reduces required computational effort and resources, and is widely adopted for practical engineering applications.

In both approaches, RANS and URANS, flow is governed by the following mass conservation equation:

$$\frac{\partial \rho \bar{v}_i}{\partial x_i} = 0 \quad (4.1)$$

and momentum conservation equation, which for RANS is:

$$\frac{\partial}{\partial x_j} (\rho \bar{v}_i \bar{v}_j) = -\frac{\partial \bar{p}}{\partial x_i} + \frac{\partial}{\partial x_j} \left[\mu \left(\frac{\partial \bar{v}_i}{\partial x_j} + \frac{\partial \bar{v}_j}{\partial x_i} - \frac{2}{3} \delta_{ij} \frac{\partial \bar{v}_l}{\partial x_l} \right) \right] + \frac{\partial}{\partial x_j} (-\rho \overline{v'_i v'_j}) \quad (4.2)$$

and for time dependent, transient flow (URANS) is:

$$\frac{\partial \bar{v}_i}{\partial t} + \frac{\partial}{\partial x_j} (\rho \bar{v}_i \bar{v}_j) = -\frac{\partial \bar{p}}{\partial x_i} + \frac{\partial}{\partial x_j} \left[\mu \left(\frac{\partial \bar{v}_i}{\partial x_j} + \frac{\partial \bar{v}_j}{\partial x_i} - \frac{2}{3} \delta_{ij} \frac{\partial \bar{v}_l}{\partial x_l} \right) \right] + \frac{\partial}{\partial x_j} (-\rho \overline{v'_i v'_j}) \quad (4.3)$$

where \bar{p} is the averaged pressure field, ρ and μ are the fluid density and viscosity, respectively, t is the time, x_i , x_j and x_l are the spatial coordinates, v_i , v_j and v_l are the velocity components and δ_{ij} is the Kronecker delta.

Here, the turbulent mean velocity field is described by *Reynolds decomposition* of the velocity using time averaged term, \bar{v}_i , and a fluctuating term, v'_i :

$$v_i = \bar{v}_i + v'_i \quad (4.4)$$

RANS and URANS equations are linearized and solved, however originated from the momentum transfer by the fluctuating velocity field flow structures, which are smaller than the numerical grid discretization- represented by the term $-\rho \overline{v'_i v'_j}$ - Reynolds stresses, are unclosed, and thus they must be modelled. In this work, three turbulence models are used for $-\rho \overline{v'_i v'_j}$ closure, namely standard $k - \varepsilon$ model, standard $k - \omega$ model and Reynolds stress model.

Standard $k - \varepsilon$ Model

The standard $k - \varepsilon$ model (Launder and Spalding, 1974), incorporated in most commercial CFD codes is likely to be one of the simplest complete turbulence models. Due to its robustness, economy in terms of computational effort and satisfactory accuracy in diverse turbulent flow issues, standard $k - \varepsilon$ model found the broadest range of applicability in both, academia and industrial sectors. The $k - \varepsilon$ model belongs to two equations models, which solves model transport equation for two turbulence quantities: k - the kinetic energy of the velocity fluctuation (turbulence kinetic energy) and ε - its dissipation rate (Pope, 2000). Reynolds stresses modelling employs Boussinesq hypothesis relating these stresses to the mean deformation rates, thus mean velocity gradients, as follows (ANSYS, 2011):

$$-\rho \overline{v'_i v'_j} = \mu_t \left(\frac{\partial \bar{v}_i}{\partial x_j} + \frac{\partial \bar{v}_j}{\partial x_i} \right) - \frac{2}{3} \left(\rho k + \mu_t \frac{\partial v_k}{\partial x_k} \right) \delta_{ij} \quad (4.5)$$

where μ_t is the turbulent viscosity computed as a function of k and ε :

$$\mu_t = \rho C_\mu \frac{k^2}{\varepsilon} \quad (4.6)$$

where C_μ is a constant and amounts 0.09.

The transport equations for turbulence kinetic energy, k and its dissipation rate, ε are represented by the following equations:

$$\frac{\partial}{\partial t}(\rho k) + \frac{\partial}{\partial x_i}(\rho k \bar{v}_i) = \frac{\partial}{\partial x_j} \left[\left(\mu + \frac{\mu_t}{\sigma_k} \right) \frac{\partial k}{\partial x_j} \right] + G_k + G_b - \rho \varepsilon - Y_M \quad (4.7)$$

and

$$\frac{\partial}{\partial t}(\rho \varepsilon) + \frac{\partial}{\partial x_i}(\rho \varepsilon \bar{v}_i) = \frac{\partial}{\partial x_j} \left[\left(\mu + \frac{\mu_t}{\sigma_\varepsilon} \right) \frac{\partial \varepsilon}{\partial x_j} \right] + C_{1\varepsilon} \frac{\varepsilon}{k} (G_k + C_{3\varepsilon} G_b) - C_{2\varepsilon} \rho \frac{\varepsilon^2}{k} \quad (4.8)$$

In these equations, the term G_k represents the generation of turbulence kinetic energy due to the mean velocity gradients and G_b is the generation of turbulence kinetic energy due to buoyancy; Y_M is the contribution of the fluctuating dilatation in compressible turbulence to the overall dissipation rate; $C_{1\varepsilon}$, $C_{2\varepsilon}$ and $C_{3\varepsilon}$ are model constants - default values for $C_{1\varepsilon}$ and $C_{2\varepsilon}$ are 1.44 and 1.92, and $C_{3\varepsilon}$ is -0.33 ; σ_k and σ_ε are the turbulent Prandtl numbers for k and ε , and amount 1.0 and 1.3 respectively.

The production of turbulence kinetic energy, G_k , is approximated in a manner consistent with Boussinesq hypothesis by:

$$G_k = -\overline{\rho v'_i v'_j} \frac{\partial \bar{v}_j}{\partial x_i} = \mu_t S^2 \quad (4.9)$$

where S is the modulus of the mean rate-of-strain tensor, defined as follows:

$$S \equiv \sqrt{2S_{ij}S_{ij}} \quad (4.10)$$

and

$$S_{ij} = \frac{1}{2} \left(\frac{\partial \bar{v}_j}{\partial x_i} + \frac{\partial \bar{v}_i}{\partial x_j} \right) \quad (4.11)$$

Effect of buoyancy, G_b , is described by the following formula:

$$G_b = \beta g_i \frac{\mu_t}{Pr_t} \frac{\partial T}{\partial x_i} \quad (4.12)$$

where β is the coefficient of thermal expansion, g_i is the component of the gravitational vector in the i -th direction, Pr_t is the turbulent Prandtl number for energy and T is the temperature. For the standard $k - \varepsilon$ model the default value of Pr_t is 0.85.

The coefficient of thermal expansion, β , is defined as:

$$\beta = -\frac{1}{\rho} \left(\frac{\partial \rho}{\partial T} \right)_p \quad (4.13)$$

Contribution of the fluctuating dilatation in compressible turbulence, Y_M , is defined as follows:

$$Y_M = 2\rho\varepsilon M_t^2 \quad (4.14)$$

where M_t is the turbulent Mach number, defined as:

$$M_t = \sqrt{\frac{k}{v_s^2}} \quad (4.15)$$

where v_s is the speed of sound.

The values of k and ε can be used to determine the quantities, representative for the large scale turbulence, i.e. velocity scale: $\vartheta = k^{1/2}$, and the length scale: $\ell = \frac{k^{3/2}}{\varepsilon}$.

Standard Wall Functions approach involved in $k - \varepsilon$ model, specify wall boundary condition for velocity by determination of the flow resistance on the wall and diffusion coefficient. This approach relies on universal behaviour of the near-wall flows rather than direct integration of the modelled equations with the wall boundary and thus, for more complex wall bounded flow issues, viscous near-wall region modelling requires enhanced wall treatment approach.

Standard $k - \omega$ Model

The second widely used 2-equation model, introduced by Wilcox (Wilcox and Traci, 1976), is $k - \omega$ model, based on the model transport equations for k and the specific dissipation rate ω referred as the turbulence frequency and expressed as the ratio of ε and k , i.e. $\omega \equiv \varepsilon/k$.

Analogically to the standard $k - \varepsilon$ model, Reynolds stresses in $k - \omega$ model are modelled using Boussinesq hypothesis described by the Equation (4.5). Here, the turbulent viscosity is computed as a function of k and ω :

$$\mu_t = \alpha^* \frac{\rho k}{\omega} \quad (4.16)$$

where α^* is a coefficient related to the use of functions damping the turbulent viscosity causing a low-Reynolds-number correction.

Transport equation for the turbulence kinetic energy, k , is computed as follows:

$$\frac{\partial}{\partial t}(\rho k) + \frac{\partial}{\partial x_i}(\rho k \bar{v}_i) = \frac{\partial}{\partial x_j} \left(\Gamma_k \frac{\partial k}{\partial x_j} \right) + G_k - Y_k \quad (4.17)$$

where Γ_k is the effective diffusivity for k , G_k is production of turbulence kinetic energy, defined previously by Equation (4.9) and Y_k is dissipation of k , due to the average velocity gradients.

Here, the effective diffusivity for k is computed from the following formula:

$$\Gamma_k = \mu + \frac{\mu_t}{\sigma_k} \quad (4.18)$$

where σ_k is a constant Prandtl number for k equal to 2.0.

Dissipation of k is given by the following equation:

$$Y_k = \rho \beta_\infty^* f_{\beta^*} k \omega \quad (4.19)$$

where β_∞^* is a model constant equal to 0.09, and f_{β^*} is defined as:

$$f_{\beta^*} = \begin{cases} 1, & \chi_k \leq 0 \\ \frac{1 + 680\chi_k^2}{1 + 400\chi_k^2}, & \chi_k > 0 \end{cases} \quad (4.20)$$

and where χ_k equals:

$$\chi_k \equiv \frac{1}{\omega^3} \frac{\partial k}{\partial x_j} \frac{\partial \omega}{\partial x_j} \quad (4.21)$$

The transport of the turbulent frequency ω , is expressed by the following:

$$\frac{\partial}{\partial t}(\rho \omega) + \frac{\partial}{\partial x_i}(\rho \omega \bar{v}_i) = \frac{\partial}{\partial x_j} \left(\Gamma_\omega \frac{\partial \omega}{\partial x_j} \right) + G_\omega - Y_\omega \quad (4.22)$$

In these equations, G_ω stands for generation of ω ; Γ_ω represents effective diffusivity of ω and Y_ω is the dissipation of ω due to turbulence.

The value of effective diffusivity Γ_ω is given by the following equation:

$$\Gamma_\omega = \mu + \frac{\mu_t}{\sigma_\omega} \quad (4.23)$$

where σ_ω is the turbulent Prandtl number for ω and its default value is 2.0.

Production of ω is given by:

$$G_\omega = \alpha_\omega \frac{\rho}{k} G_k \quad (4.24)$$

where α_ω coefficient is

$$\alpha_\omega = \frac{\alpha_\infty}{\alpha^*} \left(\frac{\alpha_0 + Re_t/Re_\omega}{1 + Re_t/Re_\omega} \right) \quad (4.25)$$

In this equation, Re_ω , α_∞ and α_0 are model constants equal 2.95, 0.52 and $\frac{1}{9}$, respectively, and Re_t is:

$$Re_t = \frac{\rho k}{\mu \omega} \quad (4.26)$$

Dissipation of ω due to turbulence is given by:

$$Y_\omega = \rho \beta_i f_\beta \omega^2 \quad (4.27)$$

Here β_i is model constant equal to 0.072, and

$$f_\beta = \frac{1 + 70\chi_\omega}{1 + 80\chi_\omega} \quad (4.28)$$

The variable χ_ω is obtained from the following:

$$\chi_\omega = \left| \frac{\Omega_{ij}\Omega_{jk}S_{ij}}{(\beta_\infty^*\omega)^3} \right| \quad (4.29)$$

where β_∞^* is the model constant and β_∞^* is 0.09, and Ω_{ij} is the mean rate-of-rotation tensor is defined as:

$$\Omega_{ij} = \frac{1}{2} \left(\frac{\partial \bar{v}_i}{\partial x_j} - \frac{\partial \bar{v}_j}{\partial x_i} \right) \quad (4.30)$$

The values of k and ω can be used to determine representative for the large scale turbulence length scale: $\ell = \sqrt{k}/\omega$. Contrary to the $k - \varepsilon$ model, standard $k - \omega$ model uses enhanced wall treatment approach to model wall boundary condition in flows characterized by high and low Reynolds numbers. Therefore it accounts for viscous effects in boundary layer and the streamwise pressure gradients and is applicable for both, wall-bounded separated flows and fully turbulent flows.

Reynolds Stress Model

The Reynolds stress model (RSM) (Launder et al., 1975) is most elaborate and complex turbulence model, referred as Second Order Closure. In RSM the isotropic eddy-viscosity hypothesis is discarded, the RSM closes the Reynolds-averaged Navier-Stokes equations by solving transport equations for the Reynolds stresses, together with an equation for the dissipation rate, yielding seven additional transport equations to be solved in 3D scheme. Thus, the transport equation of the Reynolds stresses, $\overline{\rho v'_i v'_j}$, can be written in the simplified form as (ANSYS, 2011; Versteeg and Malalasekera, 1995):

$$\frac{\partial}{\partial t} \left(\overline{\rho v'_i v'_j} \right) + C_{ij} = -D_{T,ij} + D_{L,ij} - P_{ij} - G_{ij} + \phi_{ij} - \varepsilon_{ij} - F_{ij} \quad (4.31)$$

where $\frac{\partial}{\partial t} \left(\overline{\rho v'_i v'_j} \right)$ is local time derivative; C_{ij} is transport by convection, $D_{T,ij}$ and $D_{L,ij}$ are transport due to turbulent and molecular diffusion; P_{ij} and G_{ij} are stress and buoyancy productions; ϕ_{ij} transport due to pressure strain interactions; ε_{ij} is dissipation rate; and F_{ij} is production by system rotation.

From all components of the Reynolds stress transport equation, the terms concerning turbulent diffusion, buoyancy production, pressure-strain and dissipation rate require further modeling to close equation set.

Transport by convection is defined by:

$$C_{ij} = \frac{\partial}{\partial x_k} \left(\overline{\rho \bar{v}_k v'_i v'_j} \right) \quad (4.32)$$

Turbulent diffusive transport $D_{T,ij}$ is expressed as:

$$D_{T,ij} = -\frac{\partial}{\partial x_k} \left[\rho \overline{v'_i v'_j v'_k} + \overline{p(\delta_{kj} v'_i + \delta_{ij} v'_j)} \right] \quad (4.33)$$

Transport due to molecular diffusion, $D_{L,ij}$ equals

$$D_{L,ij} = \frac{\partial}{\partial x_k} \left[\mu \frac{\partial}{\partial x_k} \left(\overline{v'_i v'_j} \right) \right] \quad (4.34)$$

Stress production is expressed as follows:

$$P_{ij} = -\rho \left[\overline{v'_i v'_k} \frac{\partial \bar{v}_j}{\partial x_k} + \overline{v'_j v'_k} \frac{\partial \bar{v}_i}{\partial x_k} \right] \quad (4.35)$$

Buoyancy production is defined as:

$$G_{ij} = -\rho\beta \left(\overline{g_i v'_j \theta_T} + \overline{g_j v'_i \theta_T} \right) \quad (4.36)$$

where $\bar{\theta}_T$ is mean potential temperature.

Transport due to pressure strain interactions is:

$$\phi_{ij} = \overline{p \left(\frac{\partial v'_i}{\partial x_j} - \frac{\partial v'_j}{\partial x_i} \right)} \quad (4.37)$$

Dissipation rate ε_{ij} is:

$$\varepsilon_{ij} = -2\mu \overline{\left(\frac{\partial v'_i}{\partial x_k} \frac{\partial v'_j}{\partial x_k} \right)} \quad (4.38)$$

Finally, production by system rotation is:

$$F_{ij} = -2\rho\Omega_k \left(\overline{v'_j v'_m \varepsilon_{ikm}} + \overline{v'_i v'_m \varepsilon_{jkm}} \right) \quad (4.39)$$

It is clear, that as the RSM model accounts for such effects, as streamline curvature, rotation, and rapid changes in strain rate in a more exact manner than both 2-equation models, thus it has greater potential to give accurate predictions for complex flows, however, as in case of standard $k - \varepsilon$ model, it is based on the standard wall treatment approach. Nevertheless, the reliability of RSM predictions is still limited by the closure assumptions employed to model pressure-strain and dissipation-rate terms. The other

shortcomings are the problems with model convergence due to numerical issues associated with coupling of mean velocity and turbulent stress field through user-defined source terms resulting in distinctly higher computational costs (Versteeg and Malalasekera, 1995).

4.3.3.2 Large Eddy Simulation

LES was used as an alternative approach in hydrodynamics modelling. In this model, large, three dimensional unsteady scale motions affected by the flow geometry large eddies, are directly and explicitly solved in time-dependent simulation using space-filtered Navier-Stokes equations. LES is one of the most expensive simulation options and requires a refined grid to accurately resolve eddies in the boundary layer. A filtering operation, analogously to the Reynolds decomposition in RANS, is based on the decomposition of the velocity into the resolved (filtered) component $\bar{v}(x, t)$ and the residual, so called subgrid-scale (SGS) component, $v'(x, t)$ (Pope, 2000). Thus, the velocity field in LES can be written as:

$$v(x, t) = \bar{v}(x, t) + v'(x, t) \quad (4.40)$$

Thus, the filtered incompressible continuity equation can be written as:

$$\frac{\partial \bar{v}_i}{\partial x_i} = 0 \quad (4.41)$$

Filtering yields momentum equation of the following form:

$$\frac{\partial \bar{v}_i}{\partial t} + \frac{\partial}{\partial x_j} (\bar{v}_i \bar{v}_j) = -\frac{1}{\rho} \frac{\partial \bar{p}}{\partial x_i} + \frac{\partial}{\partial x_j} \left(\nu \frac{\partial \bar{v}_i}{\partial x_j} \right) + \frac{1}{\rho} \frac{\partial \tau_{ij}}{\partial x_j} \quad (4.42)$$

where \bar{p} , is the filtered pressure field: $p = \bar{p} + p'$

Filtering operation results in introduction of a residual, subgrid-scale stress tensor term, τ_{ij} :

$$\tau_{ij} = \overline{v_i v_j} - \bar{v}_i \bar{v}_j \quad (4.43)$$

The term τ_{ij} cannot be directly solved and thus it must be modelled. The accuracy of the LES models is the result of modelling only the subgrid-scale motions, i.e. the smallest eddies, which tend to have more universal properties. In this approach, small eddies are modelled with the Smagorinsky's subgrid-scale model, of the following form:

$$\tau_{ij} - \frac{1}{3}\tau_{kk}\delta_{ij} = -2\mu_{t,SGS}\bar{S}_{ij} \left(\frac{\partial v_i}{\partial x_j} + \frac{\partial v_j}{\partial x_i} \right) \quad (4.44)$$

where τ_{kk} is isotropic component of the subgrid-scale stresses $\mu_{t,SGS}$ is the dynamic subgrid-scale viscosity and \bar{S}_{ij} is the rate-of-strain tensor for the resolved scale defined as:

$$\bar{S}_{ij} \equiv \frac{1}{2} \left(\frac{\partial \bar{v}_j}{\partial x_i} + \frac{\partial \bar{v}_i}{\partial x_j} \right) \quad (4.45)$$

Due to the large mesh requirements and high computational costs, wide application of LES approach to solve flow related issues is still limited.

4.3.4 Channel Flow

Performance of biological raceway reactors, such as oxidation ditches, is characterized by a fully developed turbulent flow through a long, open channel of rectangular cross-section. Most of the turbulent flows are bounded to at least one solid surface. Numerous examples of the bounded flows include: internal flows, e.g. flow through pipes or ducts; external flows, such as air/water flow around aircraft or ships' wings and hulls; and the flows occurring in the natural environment, as e.g. atmospheric boundary layer or the river flow (Libby, 1996; Pope, 2000). The common feature of all the above-mentioned cases is that despite high Re numbers and relatively low fluid viscosity, during fluid flow along solid surface at the regions adjacent to the stationary wall develops thin viscous boundary layer (Prandtl, 1904), while with the distance from the wall develops substantial quase-inviscid core flow, dominated by inertia forces.

Over the last decades, extensive experimental and numerical studies have been conducted on the mean flow variables turbulence structure and the viscous boundary layer in fully developed open channel flow (Czernuszenko and Rylov, 2002; Farrell and Ioannou, 1998; Khosronejad et al., 2007; Kim et al., 1987; Moser et al., 1999; Nezu and Rodi, 1986; Salim and Cheach, 2009). A scheme of the fluid flow through the rectangular ditch cross-section is shown in Figure 4.4. The dimensions of the ditch channel are: height $h = 2\delta$; length L and $L/\delta \gg 1$; width b , and $b/\delta \gg 1$. The mean flow currents dominate in the axial x -direction, while the mean velocity fluctuations occur in the crosswise y -direction to the main current.

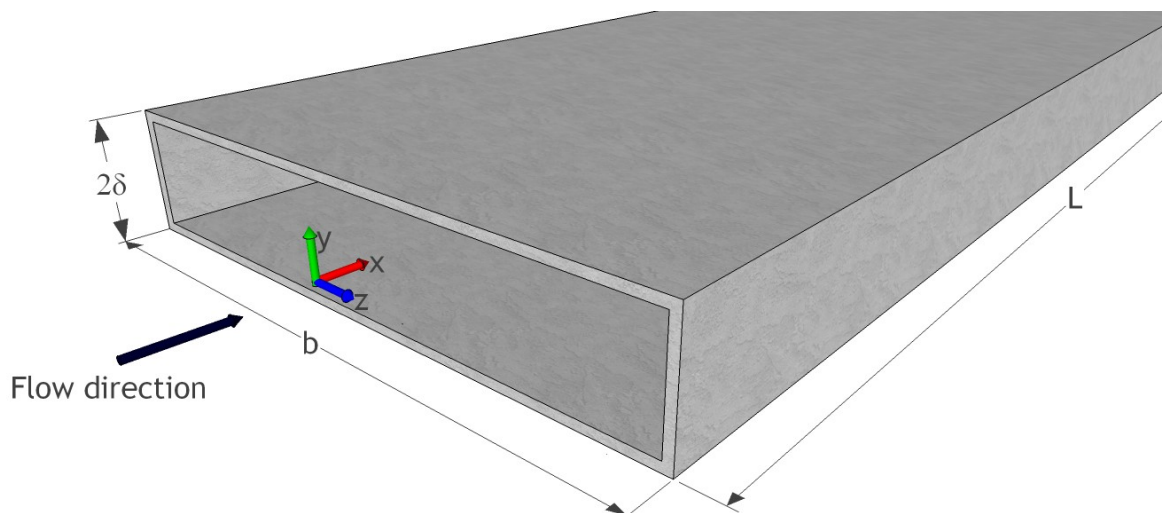


Figure 4.4 Sketch of a channel flow (Pope, 2000).

It can be assumed, that the Reynolds number is:

$$Re \equiv \frac{2\delta\bar{U}}{\nu} \quad (4.46)$$

where \bar{U} denotes bulk velocity, m s^{-1} and ν is kinematic viscosity, $\text{m}^2 \text{s}^{-1}$.

In turbulent flows, Re number based on length scales is always high and of the order 10^5 , due to the inertia forces. During fluid flow through the ditch, the total shear stress on the wall in the crosswise direction to the flow, $\tau_s(y)$ is determined as follows:

$$\tau_s(y) = \rho\nu \frac{d(U)}{dy} - \rho(u'v') \quad (4.47)$$

where the term $\rho\nu \frac{d(U)}{dy}$ denotes viscous shear stress; $-\rho(u'v')$ is Reynolds shear stress; and ρ is fluid density in kg m^{-3} .

At the stationary wall ($y = 0$), no-slip boundary condition must be satisfied, and since turbulent velocity fluctuations are zero, all the Reynolds stresses also need to be zero (Pope, 2000). According to that, the wall shear stress τ_w , is purely viscous and defined as:

$$\tau_w = \rho\nu \left(\frac{d(U)}{dy} \right)_{y=0} \quad (4.48)$$

Consequently, close to the wall, turbulent flow is influenced by viscous effects and does not depend on the free stream parameters. With the given values of ν , ρ and τ_w , viscous scales, and thus velocity scales and length scales, can be determined.

The friction velocity is defined as follows:

$$u_\tau = \sqrt{\frac{\tau_w}{\rho}} \quad (4.49)$$

where u_τ denotes friction velocity and τ_w is the wall shear stress, Pa.

The viscous length scale is defined by:

$$\delta_\nu \equiv \nu \sqrt{\frac{\rho}{\tau_w}} = \frac{\nu}{u_\tau} \quad (4.50)$$

The friction Reynolds number is:

$$Re_\tau \equiv \frac{u_\tau \delta}{\nu} = \frac{\delta}{\delta_\nu} \quad (4.51)$$

The distance from the wall is measured in viscous lengths, non dimensional “wall units” y^+ defined as:

$$y^+ = \frac{y}{\delta_\nu} = \frac{y \cdot u_\tau}{\nu} = \frac{y \cdot \sqrt{\tau_w/\rho}}{\mu/\rho} \quad (4.52)$$

where y denotes distance from the wall in m.

Close to the wall boundary, in *inner layer* region dominated by friction forces, mean velocity of the fluid depends only on y , μ , ρ and τ_w , and therefore, solely on y^+ (Prandtl, 1925), what can be written as follows:

$$u^+ = \frac{(U)}{u_\tau} \quad (4.53)$$

From the earlier work (Kim et al., 1987) it was proven, that in viscous sub-layer region, i.e. for $y^+ < 5$, the values of u^+ and y^+ are in linear relation, thus $u^+ = y^+$. The departures from this linearity become significant with increase $y^+ > 12$ (Pope, 2000).

In the distance from the wall such, that $y^+ > 30$, the influence of the viscosity forces weakens and the mean velocity is described by the logarithmic law of the wall (log-law) of the following form:

$$u^+ = \frac{1}{\kappa} \ln y^+ + B \quad (4.54)$$

where κ is von Kármán constant and $\kappa = 0.41$, and B is constant and typically $B = 5.2$.

The transient zone between viscosity dominated viscous layer and inertia dominated log-law region, for which $5 > y^+ > 30$, is called the buffer layer. In the outer layer, for $y^+ > 50$ holds velocity defect law (von Kármán, 1930), which states, that the velocity-defect, i.e. the difference between the mean and the centreline velocity value, normalized by the friction, depends upon the ratio y/δ :

$$\frac{U_0 - (U)}{u_\tau} = F_D \left(\frac{y}{\delta} \right) \quad (4.55)$$

where U_0 is the centreline velocity and $F_D(y/\delta)$ depends on the flow characteristics.

In overlap region between inner and outer layer, both law of the wall and velocity-defect law are valid and for $\delta_v \ll y \ll \delta$:

$$\frac{y}{u_\tau} \frac{d(U)}{dy} = \frac{1}{\kappa} \quad (4.56)$$

As can be seen, the value of y^+ is a criterion to determine layers in near-wall flow, influenced by predominance of friction or inertia forces. The wall regions characteristic for the wall bounded flow are listed in the Table 4.2 (Pope, 2000).

Application of the $k - \varepsilon$ turbulence model with Standard Wall Functions to model near-wall phenomena is limited by mesh resolution. Nonetheless, literature offers handful examples of successful application of the RANS closed by standard $k - \varepsilon$ model to simulate fluid flow and sediment transport in the curved open channels and laboratory 180° bends, both with rectangular cross-sections, and also, meandering river systems (Baghalian et al., 2012; Demuren, 1993; Demuren and Rodi, 1986; Khosronejad et al., 2007; Leschziner and Rodi, 1979; Wilson et al., 2007). Therefore, to obtain reliable results and for validity of the logarithmic law for the mean velocity parallel to the wall (von Kármán, 1930), non-dimensional distance from the wall to the first mesh node referred as the wall unit y^+ , should be in the range from 30 to 300. For this range of y^+ the viscous effects in the adjacent to the wall boundary cells are neglected. Due to that, modeling of near-wall region in wall bounded flows characterized by strong adverse pressure gradients or flow separation requires application of Enhanced Wall Treatment approach. Here, due to application of near-wall model, the viscosity-affected near-wall region is completely resolved all the way to the viscous sublayer. The two-layer approach is an integral part of

the enhanced wall treatment and is used to specify both and the turbulent viscosity in the near-wall cells. In this approach, the whole domain is subdivided into a viscosity-affected region and a fully-turbulent region.

Table 4.2 Wall regions and layers and their properties.

Region	Location	Properties
Inner layer	$y/\delta < 0.1$	Mean velocity is defined by u_τ and y^+ , independent from U_0 and δ
Viscous sub-layer	$y^+ < 5$	The Reynolds stress is negligible comparing with the shear stress
Buffer layer	$5 < y^+ < 30$	Transition between viscous layer and log-law layer
Log-law region	$y^+ > 30,$ $y/\delta < 0.3$	Log-law holds
Viscous wall region	$y^+ < 50$	The contribution of viscous forces is significant
Overlap region	$y^+ > 50,$ $y/\delta < 0.1$	Region of overlap between inner and outer layers at high Re
Outer layer	$y^+ > 50$	The effects of viscosity is negligible comparing to inertia forces

4.3.5 Residence Time Distribution Computing

The dynamic particle tracking in Discrete Phase Model (DPM) was used to determine the distribution of residence times in the oxidation ditch. RTD is computed from the time history of a continuous tracer concentration or from the rate at which discrete particles leave the oxidation ditch though the outlet deconvoluting the function of the tracer/particles injection. In this approach, fluid is simulated as a continuum by solving time-averaged Navier-Stokes equations in an Eulerian reference frame. The particle tracking is simulated using random-walk Lagrangian trajectory calculations for dispersed phase through the flow field of the continuous phase. The particles' trajectories are

predicted by integrating the force balance on the single particle and recording the particle position.

Here, the force balance, which equates the particle inertia with the forces acting on the particle, for the x direction in Cartesian coordinates, can be written as:

$$\frac{\partial v_p}{\partial t} = F_D (v - v_p) + \frac{g_x(\rho_p - \rho)}{\rho_p} + F_x \quad (4.57)$$

In this equation, term $F_D (v - v_p)$ represent drag force per unit particle mass; v denotes fluid phase velocity, which in prediction of particles' trajectories in turbulent flows equals the average velocity; v_p is the particle velocity; ρ_p and ρ are particle and fluid densities, respectively; and F_x is additional acceleration term, expressed as force per unit particle mass.

Particle trajectory equations are solved by stepwise integration of the Equation (4.57) over discrete time steps, yielding velocity of particle at each point along the trajectory:

$$\frac{\partial x}{\partial t} = v_p \quad (4.58)$$

Assuming constant body forces over small time step interval, particle density which is the same as of the fluid, and linearizing the remaining forces acting on the particle, the simplified form of equation (4.57) can be written as:

$$\frac{\partial v_p}{\partial t} = \frac{1}{t_p} (v - v_p) \quad (4.59)$$

where t_p is particle relaxation time.

4.4 Boundary and Operating Conditions

In this study water was set as a working fluid. The physical properties of water, density $\rho = 998.2 \text{ kg m}^{-3}$ and dynamic viscosity $\mu = 1.003 \times 10^{-3} \text{ Pa s}$ are constant. Particle tracking requires introduction of additional dispersed phase - inert particles. The physical characteristics of the particles were chosen to enable them to follow with water the flow eliminating deviations due to the particles inertia, i.e. their density is identical to the density of the working fluid, and they are spherical with a uniform diameter of 10^{-6} m .

The simulations consider operating pressure of 101325 Pa, set at the ditch surface and the acceleration due to gravity is 9.81 m s^{-2} . As the changes in density of the flow are assumed to be negligible, Boussinesq model was set to relate density as a function of temperature:

$$(\rho - \rho_0)g \approx -\rho_0\beta(T - T_0)g \quad (4.60)$$

where ρ_0 is constant density of water, T_0 is operating temperature set at 288.16 K, β denotes thermal expansion coefficient, and the term $\rho = \rho_0(1 - \beta\Delta T)$ is known as Boussinesq approximation.

The mean hydraulic residence time of the fluid in tank was 4 h.

Velocity inlet boundary condition was imposed on the ditch inlet surface. The local velocity of the water at the inlet, in the normal direction to the boundary was set as $6 \times 10^{-3} \text{ m s}^{-1}$. The turbulence at the inlet was specified by setting values of turbulent kinetic energy k equal to $1.0 \text{ m}^2 \text{ s}^{-2}$ and its dissipation rate, ε equal to $1.0 \text{ m}^2 \text{ s}^{-3}$. The turbulent length-scale at the inlet was assumed half of the inlet width and equal to 0.125 m.

In DPM simulations, 10 thousand particles were introduced through the inlet in a very short time of 0.001 s and in the normal direction to the inlet surface. Total flux of the particles injected through the inlet is $10^{-11} \text{ kg s}^{-1}$.

It was assumed, that there is no backflow during fluid discharge from the ditch and the diffusion fluxes in the direction normal to the exit plane are zero, therefore a parallel outflow boundary condition was imposed at the ditch outlet.

The hydrojets were set as two fluid zones with a momentum source, each zone having a volume of 0.014 m^3 and. The volumetric momentum source of the hydrojets in the flow direction having value of 450 N m^{-3} forces circulation of the fluid throughout the ditch with an average speed of 0.1 m s^{-1} .

At the top surface of the oxidation ditch a free surface flow condition was defined by setting the shear stress components to zero. No slip condition was imposed on the lateral walls of the ditch and the bottom, and thus the velocity component of the working fluid at fluid-solid boundary is equal to that of the solid boundary, i.e. zero.

4.5 Flow Solver

In RANS, URANS and LES simulations, flow and pressure fields are obtained using pressure-based coupled algorithm, which solves a coupled system of equations comprising the momentum equations and the pressure-based continuity equation. The remaining equations, thus energy, turbulence or discrete phase equations are solved in a decoupled fashion using the current values of the solution variables. Gradients necessary for

constructing scalar values at the cell faces, computing secondary diffusion terms and velocity derivatives are computed using Green-Gauss Cell based method. Standard scheme was enabled for pressure interpolation. Momentum, turbulence, k , ε , ω and Reynolds stresses are interpolated using *Third-Order MUSCL* (Monotone Upstream-Centered Schemes for Conservation Laws) scheme.

4.5.1 Solution Controls

In all simulation schemes, to stabilize the convergence Courant Number value equal to 50 was set. Explicit Relaxation Factors of 0.75 for the momentum and pressure were set, and all remaining Under-Relaxation Factors were accepted with the default value of 1.0, except from the k and ε and ω for which the factor is 0.8 whereas, discrete phase sources and Reynolds stresses were set to 0.5. Convergence criteria for the solutions were accepted for the scaled residuals to decrease below 10^{-6} . All flow variables were initialized with a value equal to zero.

4.5.2 Numerical Simulation Set-up

Converged steady- state solution obtained in RANS with the stabilized flow patterns within the oxidation ditch was set as the initial state for the transient URANS and LES simulations. In all simulations, the momentum equation was discretized with Second Order Implicit formulation.

Time step size, Δt between the iterations was computed from the following:

$$\Delta t = \frac{\bar{x}}{\bar{v}} \quad (4.61)$$

where \bar{x} denotes the average finite element cell size and \bar{v} represents local average velocity.

For all geometries studied, Δt considered was 0.001 s. For each time step 20 iterations were done.

The RTD simulations in steady-state flow conditions (RANS) allowed disabling flow simulation while only unsteady particle tracking is performed. In URANS and LES, ten continuous phase iterations were made per one discrete phase iteration. The size of Δt considered for particle tracking was 0.0001 s. The output record for DPM concentration at the outflow in function of flow time was set.

With the stabilization of the flow patterns during both, URANS and LES simulations, time step size, Δt between the iterations was increased to 0.01 s, 0.1 s and finally to 1 s.

4.6 Results and Discussion

4.6.1 Hydrodynamics of the Oxidation Ditch

The hydrodynamics of the oxidation ditch was obtained for single phase flow field simulations using different models, namely RANS and URANS with $k - \epsilon$ turbulence models and LES with Smagorinsky's SGS model. The simulations were performed for the geometries with different hydrojets' placement. Computational grid generated for all geometries consists of 1.7 million cells (mesh 2). The detailed properties of the mesh are listed in Table 4.1.

Figure 4.5 shows the contour maps of the velocity in the vertical planes obtained from RANS, URANS and LES, for the geometry with hydrojets placed in the middle depth. The same overall distribution of the flow patterns within the oxidation ditch was obtained from RANS and URANS. For RANS and URANS the hydrojets create an average flow with great stratification inside the volume of the ditch, characterized by poor vertical transport. The only difference between the two models is the smooth waving of the injected stream in URANS while in RANS the jets are steady and straight. In LES (Figure 4.5), the presence of eddies changes the hydrojet plume into a sinuous path evolving dynamically throughout the ditch, promoting convective transport between the fluid layers, i.e. vertical transport.

Figure 4.6 shows the velocity maps obtained for different hydrojets' placement. The values of the average fluid velocity within the ditch are presented in the Table 4.3. For RANS and URANS the horizontal profiles of the velocity reveal the same tendency. Flow field obtained with different models and for the hydrojets fixed near-bottom is characterized by lowest average velocities of 0.10 m s^{-1} . 10% increase of average velocities in RANS and URANS and 20% in LES, respectively, are observed for the mid-depth configurations. Regardless of the turbulence modelling, for the same momentum conditions imposed on the hydrojets, those placed at the surface exhibit average velocity values up to 30% larger than the others, however they lead to generation of the extended zones near the ditch bottom with the velocities close to zero, which in such biological reactor as oxidation ditch, may be related with the occurrence of the DO deficit zones or zones that promote the settling of the activated sludge flocks.

The differences between the averaged and actual flow fields obtained from the simulations became clear, when comparing contour plots of the velocity magnitude on the surface of the ditch (Figure 4.7) obtained from URANS and LES. The isovelocity contours have maximum values near the outer wall zones, and minimum near the inner walls,

furthermore the features of the dynamic flow velocity distribution are close to the few values reported in literature for open channel flow in 180° bends (Chow, 1959; Khosronejad et al., 2007; Liu and Shen, 2010; Shukry, 1950). The zones distanced from each other for half of the ditch length are characterized by recurrent flow patterns as can be seen in Figure 4.7. Two zones of different turbulence scales can be distinguished, namely inlet - outlet neighbouring zones having more linearized flow currents and the ditch bends, characterized by the higher contribution of the transverse flow components.

Regardless to the turbulence model, the same tendency as of the velocity magnitude can be seen in distribution of the gauge pressure on the surface of the ditch (Figure 4.8). The simulations were not made with free surface, but with a zero stress wall, so normal pressure components would account in an actual oxidation ditch as variations in the free surface quota. Thus during the fluid flow through the straight part of the ditch, linear distribution of the pressure iso-regions with slight increased values towards the outer walls can be seen, while increase degree of the turbulence in the ditch bend is accompanied by formation of large pressure gradients.

To investigate further flow characteristics in these zones for different turbulence models, two control sections were created: one in the centre of the ditch at 0.0 m from the reference point and another one between the hydrojets and the bend, at the distance of 4.8 m from the centre, as can be seen in an example image shown in Figure 4.9.

Figure 4.10 shows the velocity maps in the central section through the ditch for the mid-depth hydrojets' placement. For RANS and URANS the main flow currents of the highest velocity extend to the third part of the cross-section area. As suspected, there is no mixing across the fluid layers due to flow channelling, contrary to the results obtained with LES, exhibiting dynamic mixing in the transversal direction to the flow current.

Figure 4.11 shows the velocity maps obtained with RANS, URANS and LES for the cross-sections through the ditch channel located at 4.8 m from the centre of the ditch. The left section shows the velocity profile of the fluid accelerated by hydrojet and approaching the ditch bend and the right section concerns fluid flow after passing through the bend. From RANS and URANS it is seen, that as the fluid is accelerated by hydrojets, the flow core with velocity exceeding 1.1 m s^{-1} spreads uniformly through whole cross-section from interior to exterior wall, and after passing the bend the high velocity vertical layer bounds to the outer wall and extends to 2/3 of the channel cross-section. In LES wavy transversal jet plume having velocities higher than 0.15 m s^{-1} promotes intense vertical mixing. After passing the bend, flow core consists of high velocity large eddies bounded to the outer wall

and expanded towards the fluid surface. The zone of lower velocity constitutes around 10% of the section area and is bonded to the bottom and inner wall. From Figure 4.10 and Figure 4.11 it is clear, that as it is typical in wall bound flow through open channels, fluid flow in the oxidation ditch is characterized by presence of large velocity gradients near-wall regions due to friction forces, while the flow core is predominated by inertia forces.

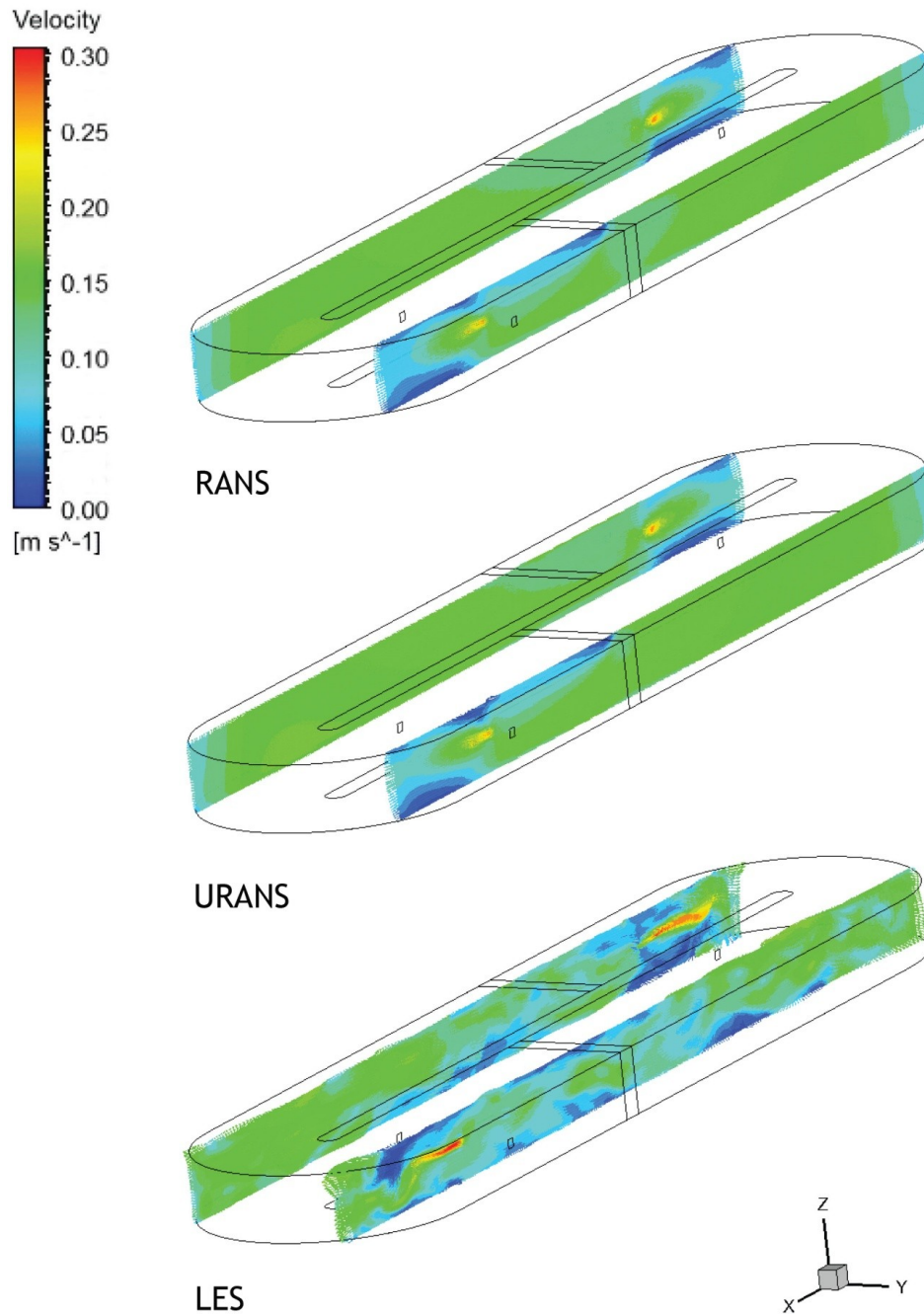


Figure 4.5 Velocity vector maps in the oxidation ditch using RANS, URANS and LES.

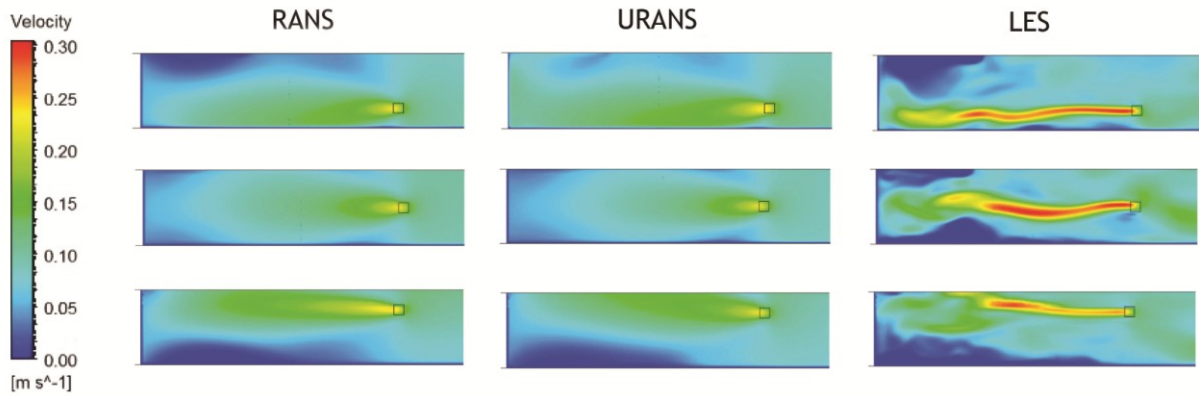


Figure 4.6 Velocity maps in the oxidation ditch obtained from RANS, URANS and LES for different hydrojets' placement.

Table 4.3 Average velocity of the fluid obtained with different turbulence models.

Simulation	Hydrojet placement	\bar{v} (m s ⁻¹)
RANS	bottom	0.10
	surface	0.13
	middle	0.11
URANS	bottom	0.10
	surface	0.13
	middle	0.11
LES	bottom	0.10
	middle	0.12

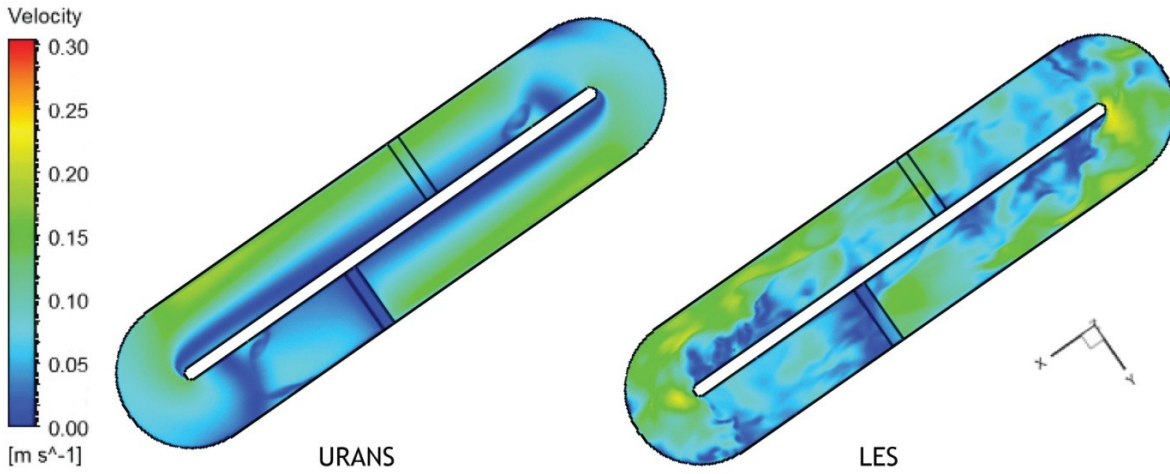


Figure 4.7 Velocity distribution maps on the surface obtained from the simulations with URANS and LES.

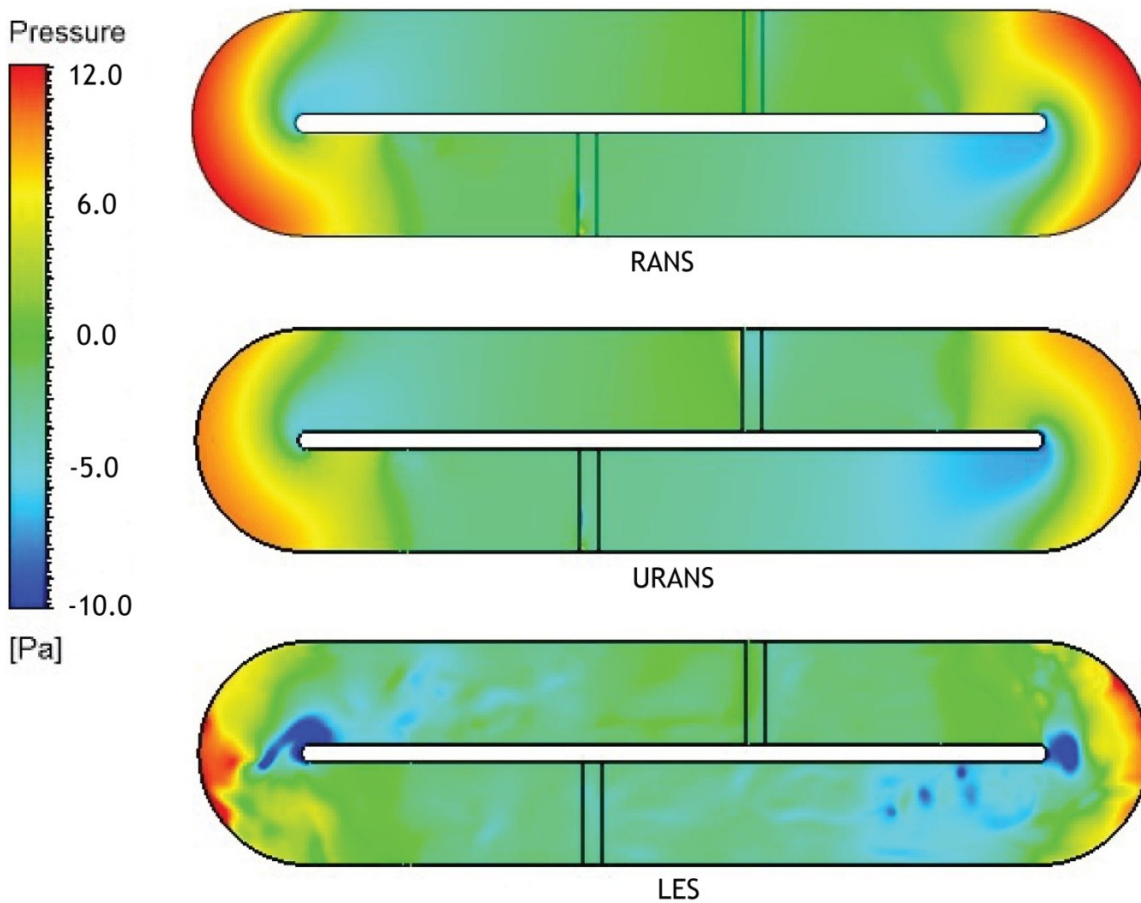


Figure 4.8 Maps of pressure field obtained from the simulations of the oxidation ditch with different models.

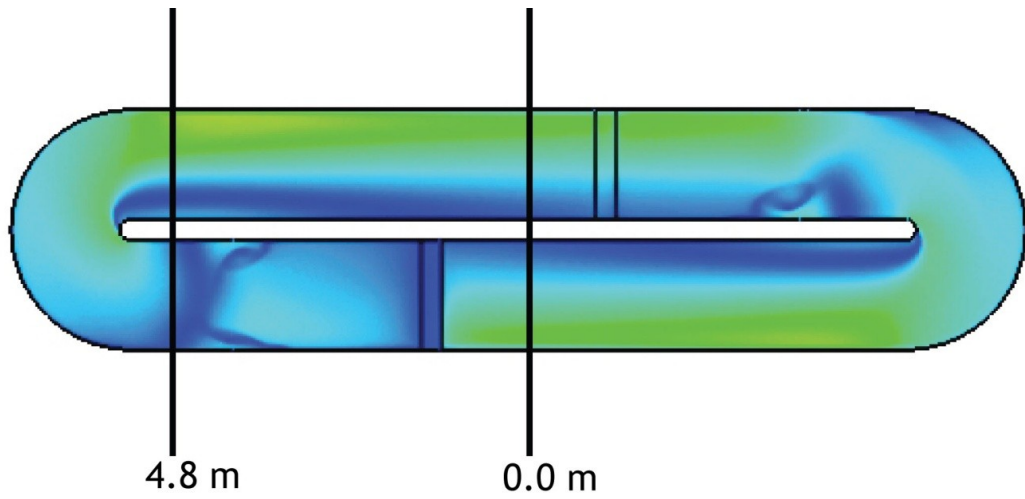


Figure 4.9 Location of the control section in the oxidation ditch.

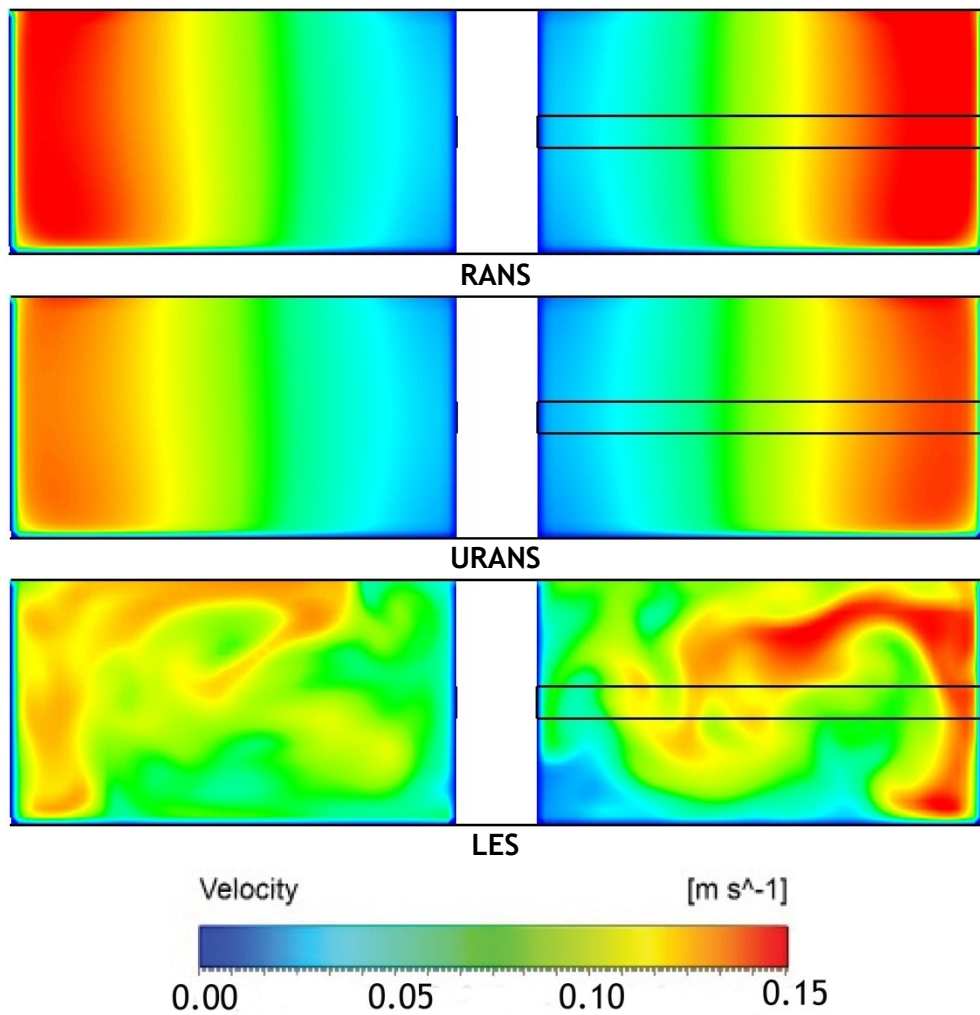


Figure 4.10 Velocity maps obtained with different models for the cross section located in the centre of the ditch.

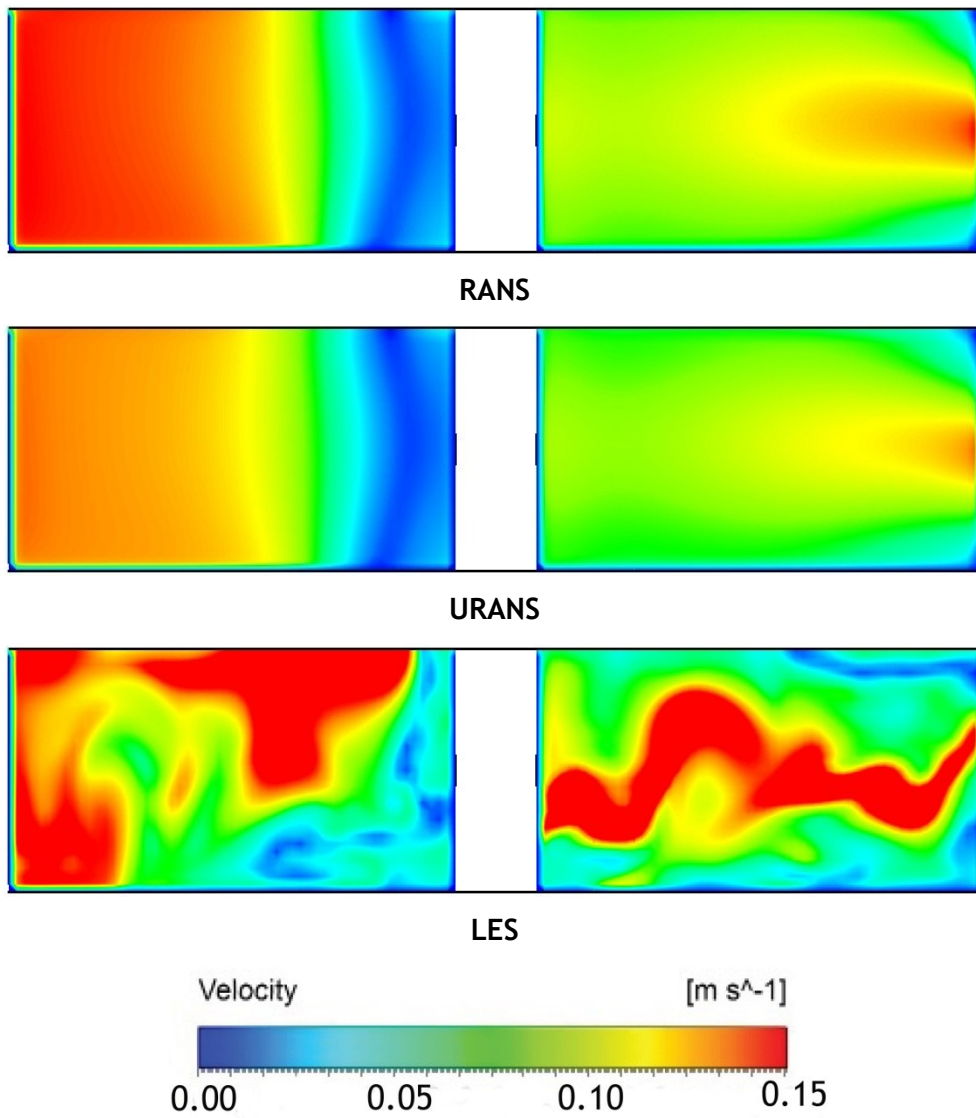


Figure 4.11 Velocity maps obtained with different models for the cross-section through the bend, located at 4.8 m from the centre of the ditch.

4.6.2 Energy Expenditure for Mixing

The energy expenditure associated with keeping the fluid flowing inside the ditch and mixing its content is determined directly from the boundary condition inside the hydrojets volume that was set in RANS, URANS and LES as a volumetric momentum source. Thus, the power demand for mixing is defined as a product of momentum by volume integral of the velocity in the hydrojets, as follows:

$$P_{mix} = M \int v dV \tag{4.62}$$

where P_{mix} is power demand for mixing in W, M denotes momentum source of the hydrojets and equals 450 N m^{-3} .

For each hydrojets configuration, power supplied to a fluid, P_u , to give its kinetic energy is computed as follows:

$$P_u = \frac{1}{2} \rho \bar{v}^2 Q \quad (4.63)$$

where ρ is water density and \bar{v} is average velocity and Q is the flowrate.

Energy efficiency was assessed as ratio of the power flow supplied for each hydrojets positions to power associated with their mixing performance. Table 4.4 shows the data set obtained from the fluid flow simulations with different turbulence models and for all hydrojets' configurations. Regardless of the turbulence modelling, for the same momentum conditions in the hydrojets, those placed near the bottom demand for less than 5% energy for mixing when comparing with mid-depth and near-surface configurations, but also yield lower average velocities, what affects overall mixing in the ditch. The power supplied to the fluid is also the lowest and constitutes 46% of the amount delivered to the near-surface configurations. Such configuration is most energy-intensive allowing use of only 24% of the total energy supplied. On the other hand, location of the hydrojets close to the surface improves fluid circulation and energy efficiency, which is in the range of 46-52% and fluid circulation only, however in this case the DO profiles are not being considered. Therefore, when considering design guidelines aiming to prevent formation of the oxygen deficit or settling zones in the aeration tank, geometry scenario with the hydrojets fixed in the mid-depth of the ditch seems to be well justified choice, in terms of both, mixing and energy efficient performance allowing use of up to 38% of supplied power.

The difference in energy efficiency obtained from all simulations with RANS, URANS and LES and for each specific placement of the hydrojets is 2-7%. Considering power expenditure for mixing this difference is up to 8%, and taking into account all hydrojets' configurations, less than 13%. Therefore, the model that requires less computational resources, RANS, can be applied to analyse the effects of the geometry on the power demand and energy efficiency.

Table 4.4 Power demand and energy efficiency obtained with different turbulence models.

Simulation	Hydrojet placement	P_{mix}	P_u	P_u/P_{mix}
		(W)		(%)
RANS	bottom	2.33	0.56	24
	surface	2.37	1.23	52
	middle	2.42	0.75	31
URANS	bottom	2.36	0.56	24
	surface	2.35	1.23	52
	middle	2.41	0.75	31
LES	bottom	2.57	0.56	22
	surface	2.69	1.23	46
	middle	2.56	0.97	38

4.6.3 Modelling of the Boundary Layer

As in the case of the fully developed turbulent flow in the open channel, fluid flow in the oxidation ditch is characterized by large velocity gradients in the neighbourhood of the solid wall boundaries, as can be seen from the maps in two regions of interest- cross-sections through the ditch, shown in Figure 4.12.

The focus of the hydrodynamics studies of the oxidation ditch was on the description of the phenomena related to inertia dominated regions. This section concerns the study of the turbulent shear flow near the oxidation ditch wall, based on determination of the wall unit parameter, y^+ , and the wall shear stress, τ_w , for several meshes while simulating fluid flow with different turbulence models. The objective of the simulations was also to assess the effect of different mesh resolutions and different turbulence models on the energy expenditure computation. All simulations consider hydrojets' placement in the middle depth of the ditch.

Boundary layer studies considered simulations of the single phase flow with the model accounting for less computational efforts, RANS with Reynolds stresses being modelled

with the following turbulence models: standard $k - \varepsilon$ with Standard Wall Functions; standard $k - \varepsilon$ with Enhanced Wall Treatment; standard $k - \omega$; and RSM with Standard Wall Functions.

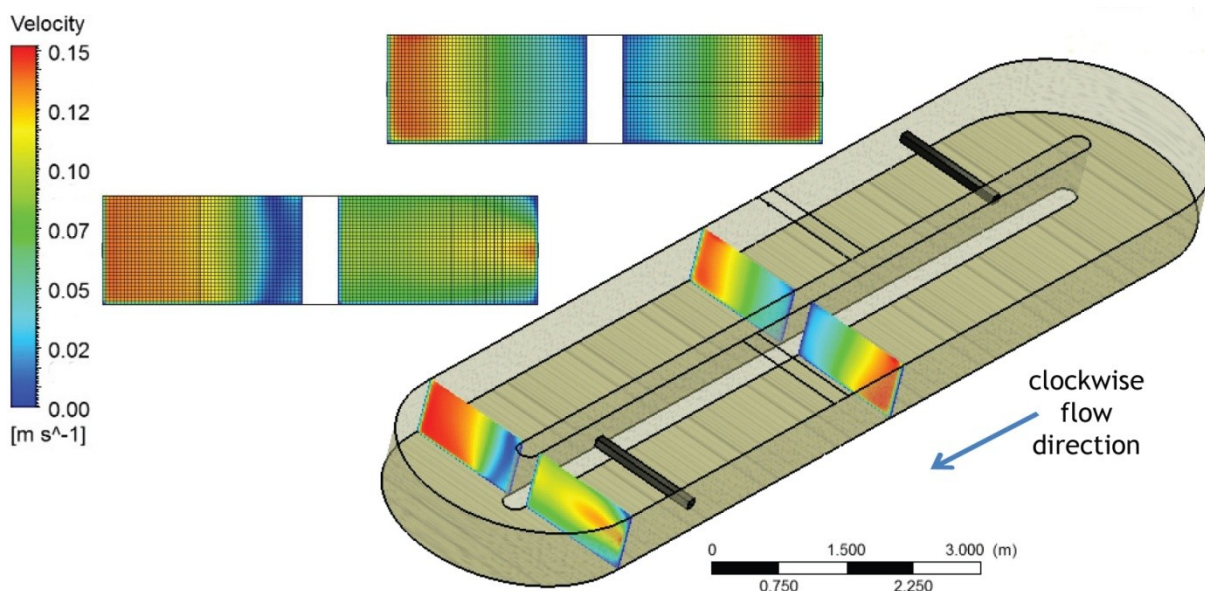


Figure 4.12 Velocity maps in the control cross-sections considered in the near-wall region modelling.

4.6.3.1 Grid Configuration in Near-wall Region Treatment

As application of the $k - \varepsilon$ turbulence model with Standard Wall Functions to model viscosity-affected region is limited by mesh resolution. From this reason, grid independence test was performed for six meshes having different resolution and configurations (Table 4.1), aiming selection of the most robust mesh allowing for accurate presentation of the flow in the near-wall region. The section planes through the ditch channel (Figure 4.9) having different meshes considered in the simulations are shown in Figure 4.13. For each mesh, the distances of the first cell from the wall boundaries: bottom, Δy_B ; outer wall, Δy_O ; and inner wall Δy_I , correspond to the element sizes in the boundary zone, and are shown in the Table 4.5.

Within the selected control planes, located in the distance of 0.0 m and 4.8 m from the centre of the ditch, horizontal and vertical lines connecting opposite located wall points were defined, as can be seen in the Figure 4.14. The wall points were located in the middle length of each wall: bottom, inner and outer wall. For each point, the values of y^+ of first grid cell, adjacent to the wall and τ_w were obtained directly from the CFD

simulations. The values of the mean streamwise velocity magnitude associated to the grid nodes along the lines were also obtained from the simulations. The values of y^+ along the lines were determined following the Equation (4.52) for the constant value of the viscous velocity, u_τ , assessed from the Equation (4.49). For $y^+ < 30$ the values of the u^+ were calculated from the Equation (4.53), i.e. law of the wall, and for $y^+ > 30$, log-law of the wall, described by (4.54) was used.

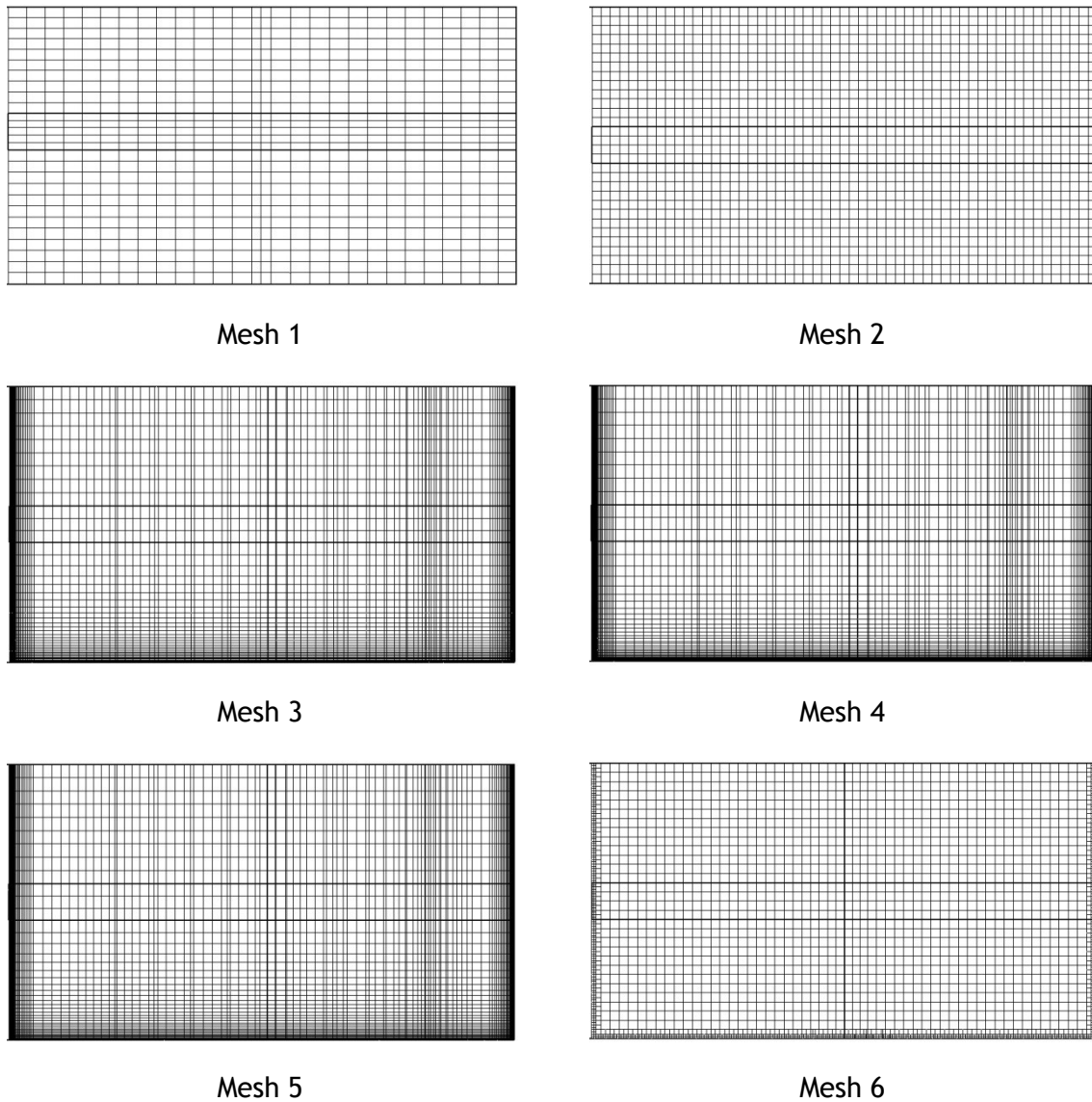


Figure 4.13 Cross-section through the ditch channel geometry having different mesh.

4 CFD Simulations of the Oxidation Ditch

Table 4.5 Element sizes of the meshes used in the CFD simulations of the boundary layer.

Mesh n°	N° of mesh	Δy_B	Δy_O	Δy_I
	elements	m		
	$\times 10^6$			
1	0.6	30.4×10^{-3}	51.4×10^{-3}	48.6×10^{-3}
2	1.7	25.0×10^{-3}	25.0×10^{-3}	25.0×10^{-3}
3	4.7	1.3×10^{-3}	0.8×10^{-3}	0.7×10^{-3}
4	4.7	1.1×10^{-3}	0.8×10^{-3}	0.7×10^{-3}
5	5.4	0.7×10^{-3}	0.4×10^{-3}	0.3×10^{-3}
6	5.6	6.3×10^{-3}	6.3×10^{-3}	6.2×10^{-3}

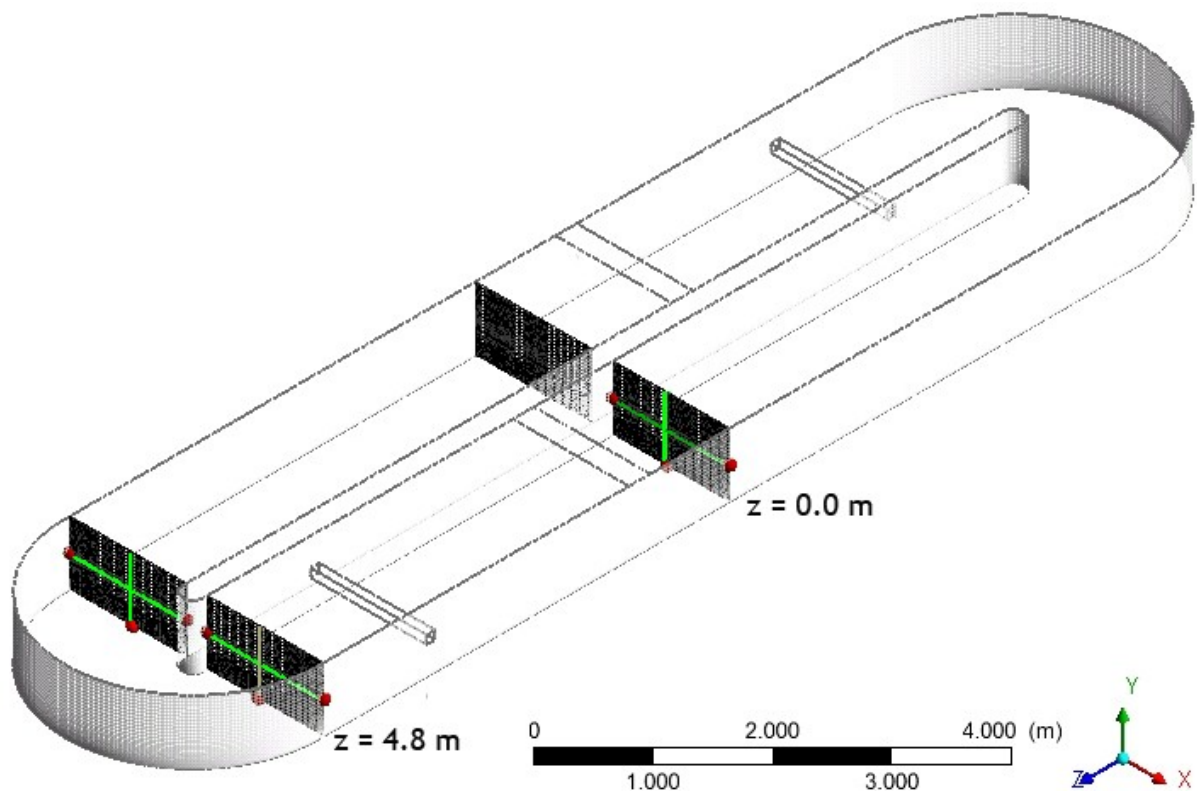


Figure 4.14 Determination wall points and lines within the control cross-sections in the oxidation ditch.

Figure 4.15 and Figure 4.16 show the velocity maps obtained from RANS with standard $k - \varepsilon$ model in the cross-sections through the central part and the bend of the oxidation ditch. It is clearly seen, that the grids of varying density, i.e. Mesh 3, 4 and 5, which are coarser in the flow core part and refined along the boundaries characterized by the presence of the large gradients. The algorithms incorporated into the simulation of the fluid flow in the volumes with coarser, structured mesh slightly refined along the wall boundaries, i.e. Mesh 1, 2 and 6, yield higher velocity values in the near wall zones, but do not account for wider-scale phenomena, such as transversal distribution of the jet plume.

As the velocity maps in left and right channel in the central part of the ditch correspond to each other, thus only one section was consider to study viscous interactions in the near-wall region.

Figure 4.17, Figure 4.18 and Figure 4.19 present the near-wall profiles of the mean streamwise velocity expressed as a function of a wall distance: $u^+ = f(y^+)$ for the cross-section in the central part of the ditch and through the bend. When comparing results obtained from the modelling of the wall region it is clear, that in case of dense meshes, independently to a certain extent on the number of computational cells, the finer the mesh at the considered boundaries, the higher accuracy of the reported results defining the flow in the near-wall region. Refinement of the Mesh 3, 4 and 5 at the inner, outer and bottom wall boundaries yielding mesh element sizes smaller than 1 mm, lead to the wall units values in the considered cross-sections smaller than 10, therefore corresponding to the boundary sublayer. Mesh 5 allowed obtaining the lowest y^+ being in the range from 1 to 2, corresponding to the inner layer zone.

Applicability of the $k - \varepsilon$ model coupled with Standard Wall Functions to simulate boundary layer is limited due its validity only for the region distanced from the wall (Salim and Cheach, 2009). Here, for the cells adjacent to the wall where determined y^+ are smaller than 11, laminar stress-strain relationship is applied, so that $y^+ \approx u^+$ (Nezu and Rodi, 1986). As the $k - \varepsilon$ model uses always wall functions, it is generally not recommended to model boundary layer in flows with advert pressure gradients, as in case of bend region in the oxidation ditch (Figure 4.8). Due to that, the enhanced wall treatment should be applied to solve with high accuracy viscosity dominated flow in the cells adjacent to the wall.

Structured grid of the highest total number of cells (Mesh 6), but distinctly coarser at the walls than Meshes 3, 4 or 5, revealed to be less efficient in terms of accuracy in representation of the results in the near-wall region, and yielding $10 < y^+ < 30$

corresponding to blending region between viscosity affected sublayer and inertia dominated turbulent flow. These values of wall units are sufficient to solve with high level of accuracy log-law region, considering lower limits of logarithmic law of the wall applicability, which is 30.

For Mesh 1 and 2, the distance from the walls to the first node is in the range of $50 \leq y^+ \leq 250$. Here, the viscous effects of the flow in the cells adjacent to the boundaries are neglected as in case of the finer mesh, however the log-law region is still solved with reasonable reliability.

Table 4.6, Table 4.7 and Table 4.8 show the parameters related to the viscous wall region in the considered sections through the oxidation ditch. Different mesh properties and y^+ revealed to have influence on the computed wall friction coefficients, such as wall shear stress, τ_w . The increase of the mesh resolution yields higher values of τ_w and thus lower values of the streamwise velocity in the wall adjacent cells.

When comparing the values of wall shear stress and the velocity parallel to the wall in the central section through the ditch it is observed, that the outer wall and the bottom are characterized by higher τ_w , which depending on the mesh refinement along the boundaries ranges from 0.08 Pa for the outer wall to 0.02 Pa for the inner wall and for the average streamwise velocity ranging from 0.07 to 0.09 m s⁻¹.

Considering the cross-section through the ditch channel at the entrance to the bend, as the fluid flow through this section is accelerated by the hydrojets, the flow resistance at the walls increases and the boundaries affected by the highest shear stress of 0.2 Pa are both, inner and outer wall, with the average streamwise velocity of 0.1 m s⁻¹. The lowest τ_w in the range of 0.03 to 0.08 Pa is observed for the bottom wall, where the average streamwise velocity equals around 0.1 m s⁻¹.

Considering the cross-section following the bend, the shear stress in the low velocity zone of inner wall is the lowest and ranges from 0.003 to 0.01 Pa. The highest mean velocity of 0.12 m s⁻¹ was observed in the near-bottom zone, while the highest τ_w values, up to 0.14 Pa were observed for the exterior wall.

According to the results obtained from the grid tests, Mesh 5 revealed to be the most accurate to represent the flow in both, viscous sublayer and inertia dominated flow core. One of the drawbacks is high computational cost, which is largely determined by resolution requirements, i.e. grid density and the time intervals (Δt) defined in simulation set-up. In this work, the highest computational effort was required for Mesh 6, having the highest number of cells. On the other hand, in conditions of limited CPUs and computational

times, and with negligence of the detailed modelling of the laminar sublayer, application of adequate wall treatment functions make coarser Meshes 1 and 2 suitable to solve accurately both, log-law and fully developed turbulent flow regions.

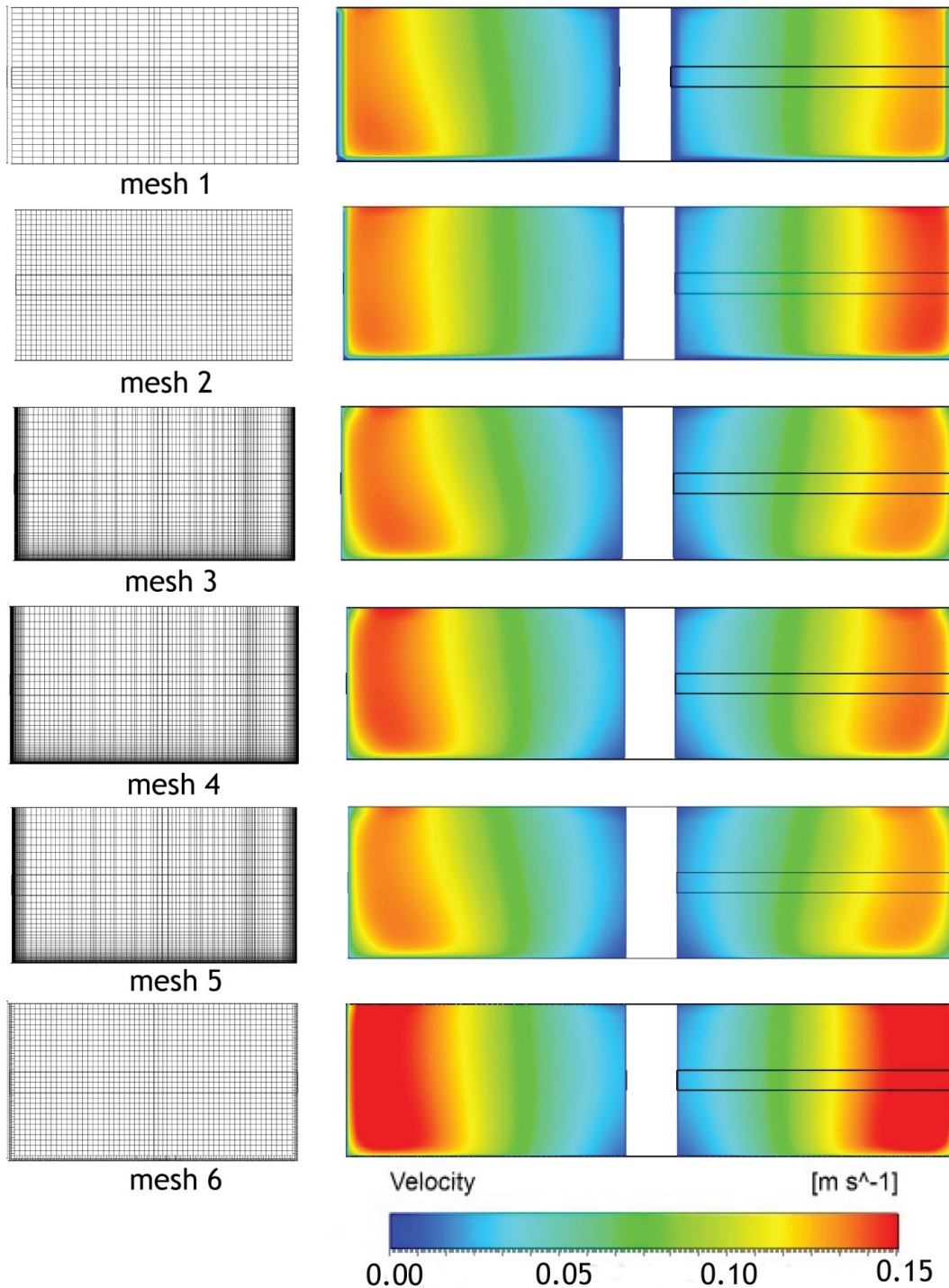


Figure 4.15 Velocity maps in the section planes for $z = 0.0$ m obtained for different meshes.

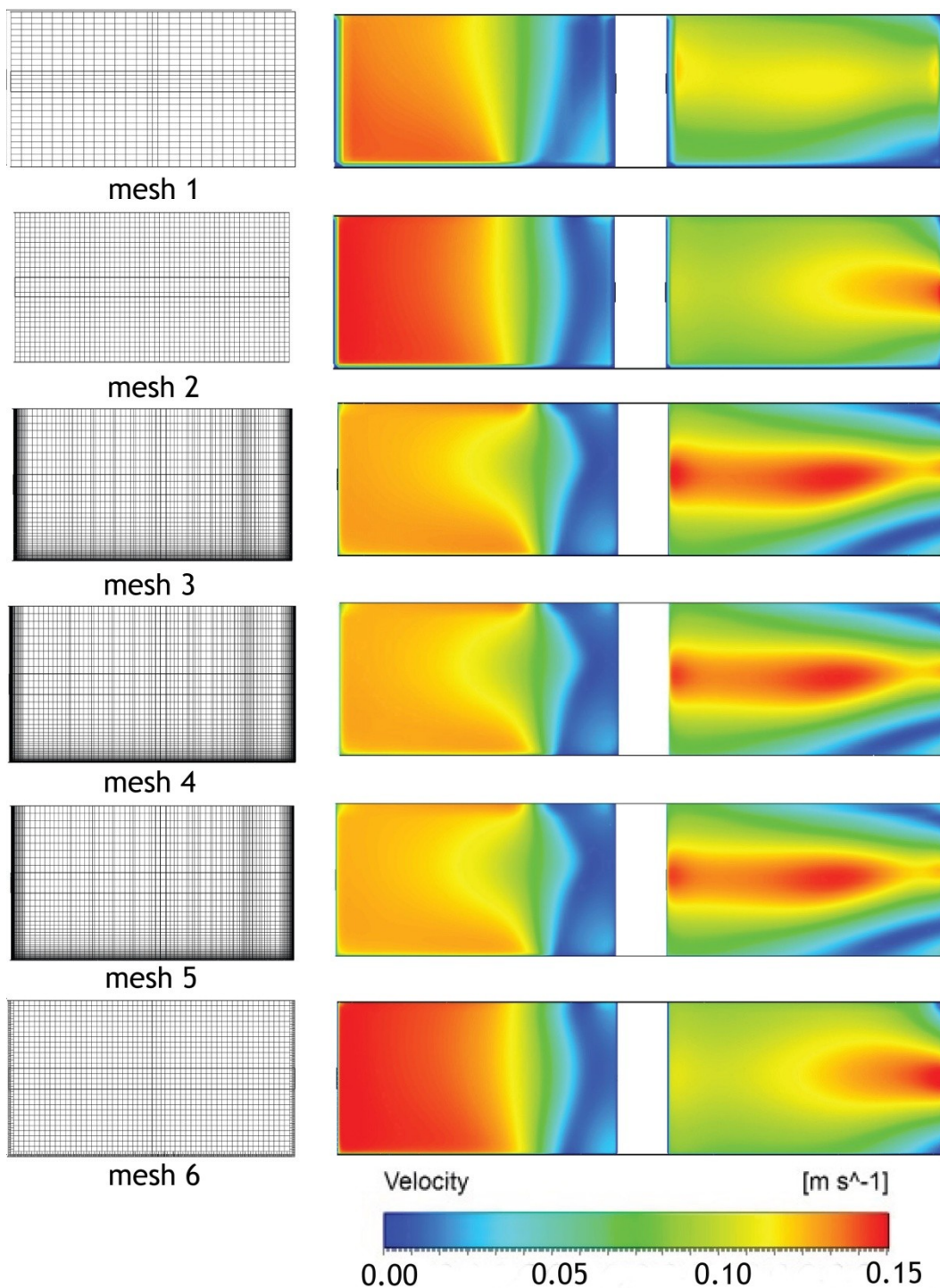


Figure 4.16 Velocity maps in the section planes for $z = 4.8$ m obtained for different meshes.

4 CFD Simulations of the Oxidation Ditch

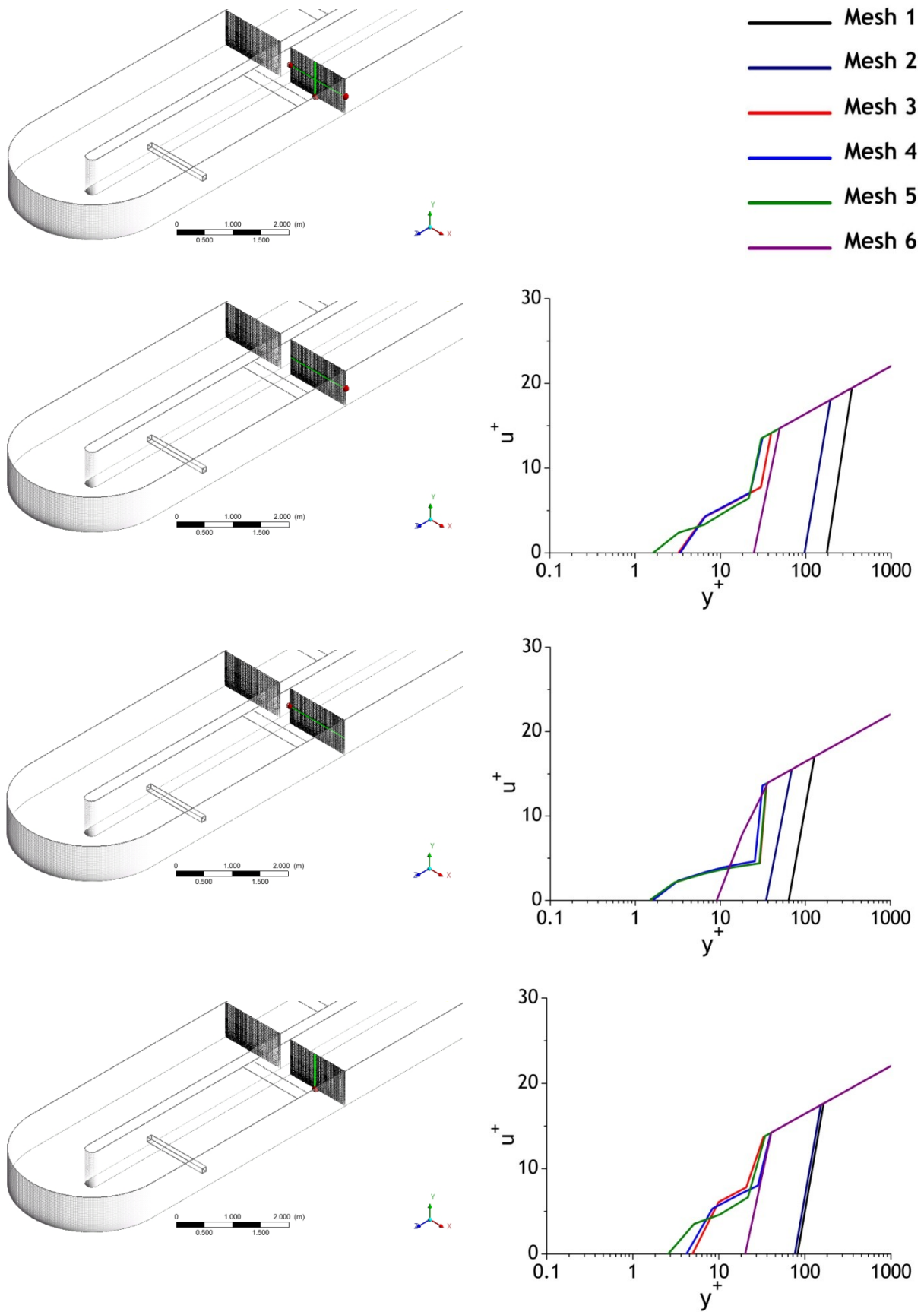
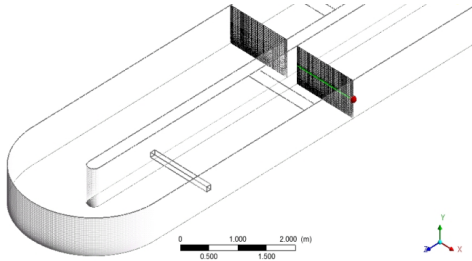
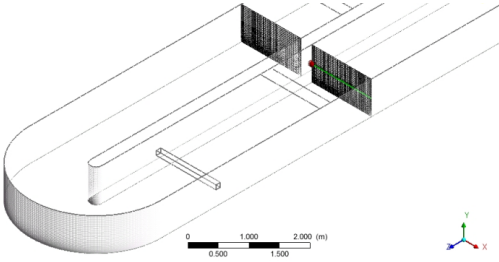
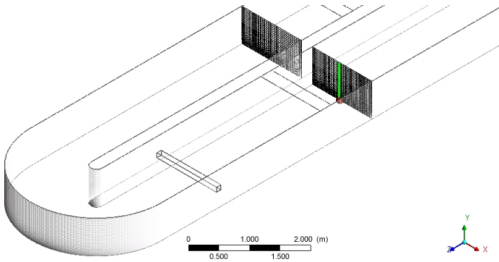


Figure 4.17 Streamwise mean velocity near-wall profiles in the central cross-section through the oxidation ditch.

4 CFD Simulations of the Oxidation Ditch

Table 4.6 Viscous flow parameters in the near-wall region in the central cross-section through the oxidation ditch.

Wall point	Mesh n ^o	τ_w (Pa)	\bar{u} (m s ⁻¹)
 <p>x = 1.50 m, y = 0.375 m, z = 0 m</p>	1	0.048	0.076
	2	0.061	0.090
	3	0.072	0.079
	4	0.079	0.083
	5	0.073	0.076
	6	0.063	0.092
 <p>x = 0.125 m, y = 0.375 m, z = 0 m</p>	1	0.007	0.076
	2	0.008	0.090
	3	0.016	0.079
	4	0.019	0.083
	5	0.016	0.076
	6	0.009	0.092
 <p>x = 0.75 m, y = 0 m, z = 0 m</p>	1	0.030	0.074
	2	0.038	0.084
	3	0.055	0.079
	4	0.058	0.079
	5	0.060	0.075
	6	0.042	0.089

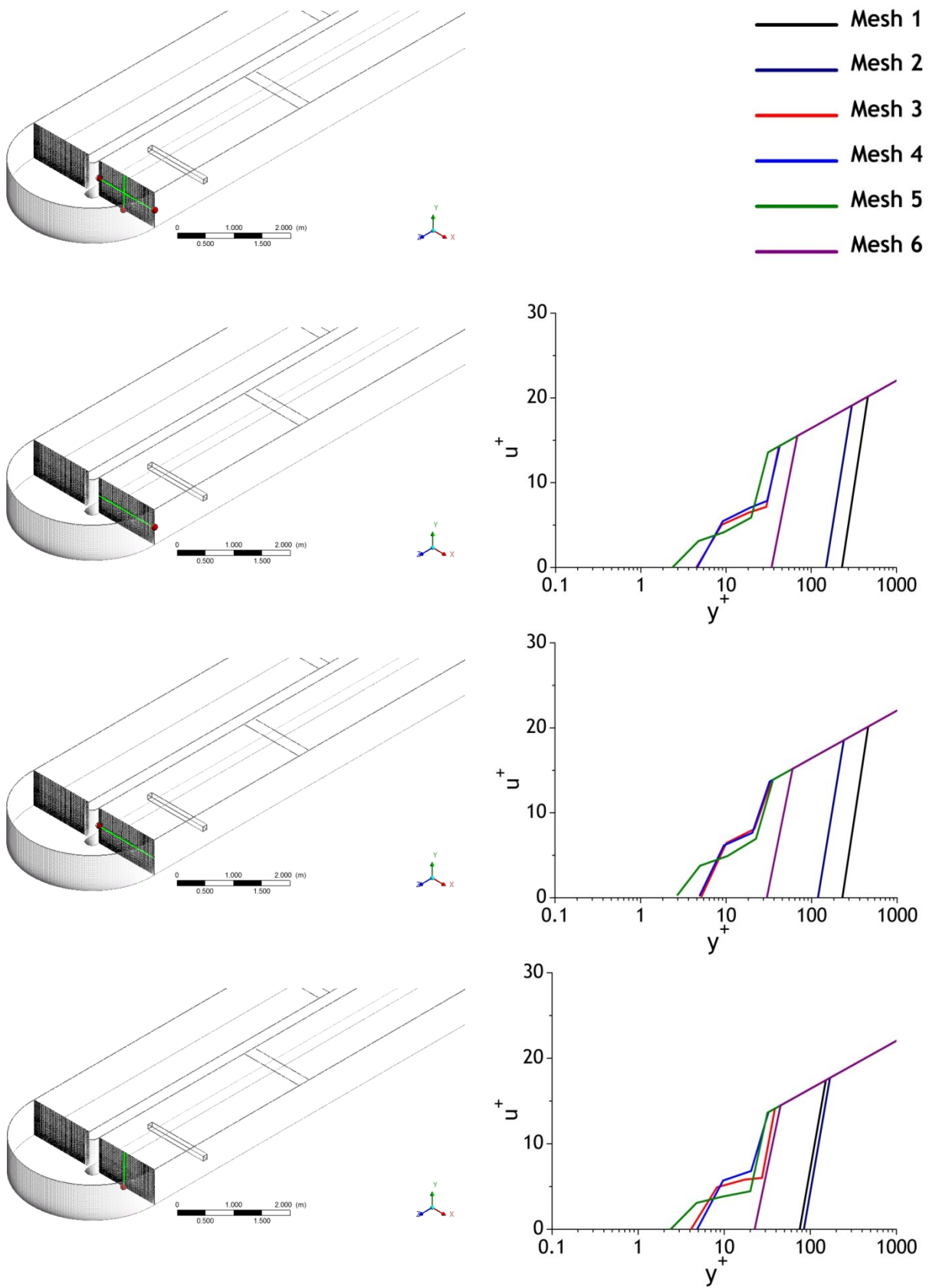
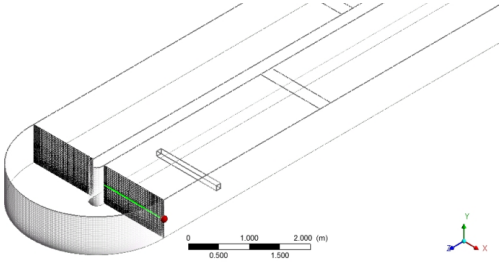
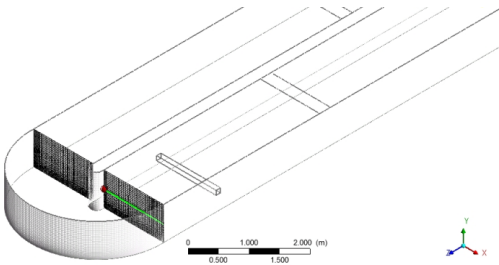
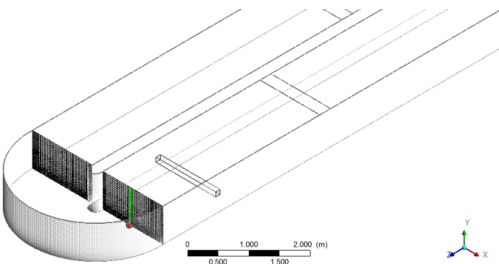


Figure 4.18 Streamwise mean velocity near-wall profiles in the cross-section through the entrance to the bend.

4 CFD Simulations of the Oxidation Ditch

Table 4.7 Viscous flow parameters in the near-wall region in the cross-section through the entrance to the bend.

Wall point	Mesh n°	τ_w (Pa)	\bar{u} (m s ⁻¹)
 <p>x = 1.50 m, y = 0.375 m, z = 4.80 m</p>	1	0.081	0.100
	2	0.143	0.118
	3	0.142	0.125
	4	0.149	0.112
	5	0.156	0.121
	6	0.121	0.126
 <p>x = 0.125 m, y = 0.375 m, z = 4.80 m</p>	1	0.089	0.100
	2	0.091	0.118
	3	0.189	0.125
	4	0.172	0.112
	5	0.208	0.121
	6	0.093	0.126
 <p>x = 0.750 m, y = 0 m, z = 4.80 m</p>	1	0.025	0.090
	2	0.046	0.097
	3	0.038	0.074
	4	0.077	0.083
	5	0.051	0.070
	6	0.052	0.100

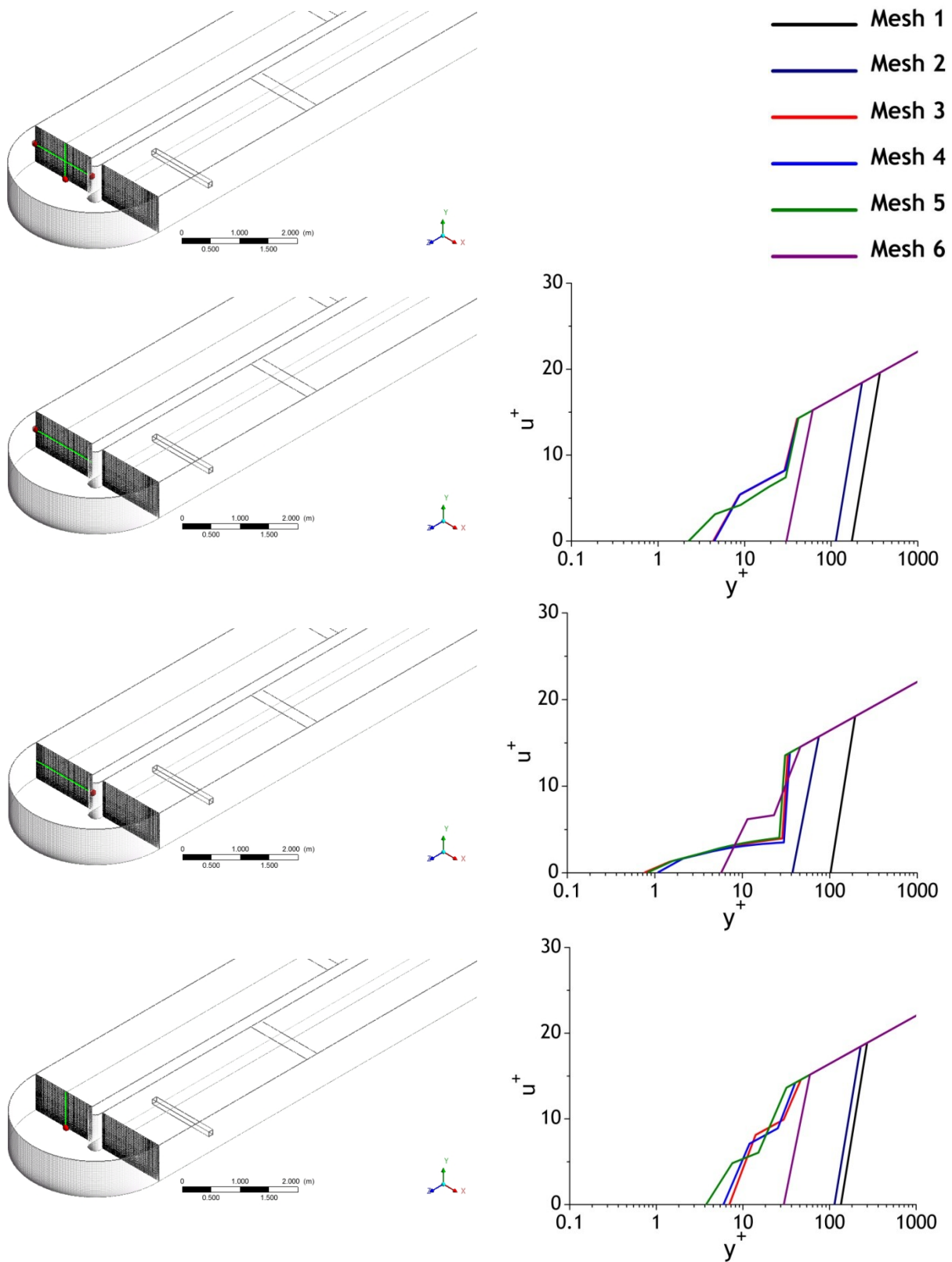
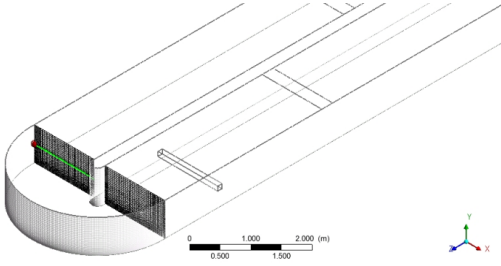
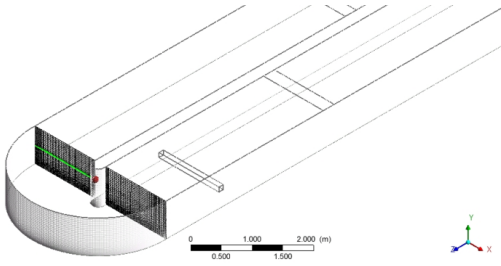
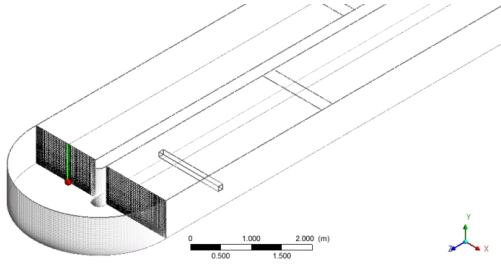


Figure 4.19 Streamwise mean velocity near-wall profiles in the cross-section through the exit from the bend.

4 CFD Simulations of the Oxidation Ditch

Table 4.8 Viscous flow parameters in the near-wall region in the cross-section through the exit from the bend.

Wall point	Mesh n ^o	τ_w (Pa)	\bar{u} (m s ⁻¹)
 <p>x = -1.50 m, y = 0.375 m, z = 4.80 m</p>	1	0.066	0.085
	2	0.082	0.102
	3	0.133	0.079
	4	0.140	0.083
	5	0.143	0.076
	6	0.096	0.104
 <p>x = -0.125 m, y = 0.375 m, z = 4.80 m</p>	1	0.013	0.085
	2	0.009	0.102
	3	0.004	0.079
	4	0.009	0.083
	5	0.005	0.076
	6	0.003	0.104
 <p>x = 0.750 m, y = 0 m, z = 4.80 m</p>	1	0.080	0.111
	2	0.084	0.125
	3	0.111	0.119
	4	0.117	0.120
	5	0.129	0.113
	6	0.090	0.132

4.6.3.2 Turbulence Model in Near-wall Region Treatment

In this section the impact of the turbulence model and associated wall treatment method on the boundary layer modelling was determined. As application of the turbulence models with Standard Wall Functions to model near-wall region is limited by mesh resolution, thus the most dense mesh, which enables lower values of y^+ determined in the previous section of this study (4.6.3.1), Mesh 5, was used in the simulations.

As previously described and according to Figure 4.14, horizontal and vertical lines connecting opposite located wall points were defined within the control cross-section. The wall points were located in the middle length of each wall: bottom, inner and outer wall. For each point, the values of y^+ of first grid cell adjacent to the wall and τ_w were obtained directly from the CFD simulations, as well as the node values of the average streamwise velocity magnitude along the lines. The node values of y^+ were determined following the Equation (4.52) for the constant value of the viscous velocity, u_τ , assessed from the Equation (4.49). For $y^+ < 30$ the values of the u^+ were calculated from the law of the wall described by Equation (4.53) and for $y^+ > 30$, log-law of the wall, expressed by Equation (4.54) was applied.

Figure 4.20 and Figure 4.21 show the velocity maps obtained from RANS with different turbulence models in the cross-sections through the central part and the bend of the oxidation ditch. It is clearly seen, that both models using Enhanced Wall Treatment, i.e. $k - \varepsilon$ and $k - \omega$ yield almost identical velocity distribution in the central part of the ditch, as can be seen in Figure 4.20. The different maps were obtained for models based on Standard Wall Functions, the $k - \varepsilon$ and RSM. Here the differences in the average velocity distributions and the presence of the vortices in the flow core obtained from RSM are due to the model completeness and accuracy in the direct solution with 7-equation approach of the small scales, i.e. Reynolds stresses, which in $k - \varepsilon$ approach are only modelled with two equations.

For the cross-section through the entrance and exit of the bend, the maps obtained with both $k - \varepsilon$ models revealed the same tendency, with slight differences resulting from the fact, that while the model with Standard Wall Function solves directly the turbulent flow core, Enhanced Wall Treatment splits the solved flow domain on wall-affected region and fully turbulent region. The difference in maps obtained with the $k - \varepsilon$ and $k - \omega$ model are due to poor sensibility of the $k - \varepsilon$ model to the streamline curvature and adverse pressure gradients, which occur in the ditch bend zone, as it was shown in Figure 4.7 and Figure 4.8. Contrary to the 2-equation models, the RSM model accounts for many effects, i.e. streamline curvature, rotation, and rapid changes in strain rate, thus it has greater potential to give accurate predictions for complex flows, however, as in case of standard $k - \varepsilon$ model, it is still based on the standard wall treatment approach, and due to that, both models are primary valid for turbulent core flows. Thus the velocity maps obtained from RSM (Figure 4.20 and Figure 4.21) are comparable with the model which accounts for the actual flow hydrodynamics, i.e. LES, as can be seen when comparing these results with those in Figure 4.10 and Figure 4.11.

When comparing the profiles of average streamwise velocity in function of wall distance in all cross-sections through the ditch, which are presented in Figure 4.22, Figure 4.23 and Figure 4.24 it is also clear, that the lowest values of $0.7 < y^+ < 2$ were obtained with the $k - \omega$ turbulence model. This model is applied throughout the boundary layer to solve directly viscous flow region, thus it requires sufficient near-wall mesh resolutions. The accuracy of the model is increased as the cell sizes are closer to $y^+ = 1$, which enables to capture detailed flow features in the inner layer during computation.

The values of wall y^+ obtained from other models, $k - \varepsilon$ and RSM with the standard near-wall treatment coupled to them, are almost identical and slightly higher, in the range of 2-4, due to use of wall functions instead of direct solution flow in near wall cells.

In a few cases, for lower velocities close to inner wall or the bottom, $k - \varepsilon$ model with Enhanced Wall Treatment yields values of y^+ close to those obtained with $k - \omega$. This is due to application of two layer approach, which divides whole domain on viscosity affected near wall region and inertia dominated turbulent flow region. For the accurately inflated mesh in the wall region with y^+ close to 1, application of two layer model allows that the viscosity-affected near-wall region is completely resolved all the way to the viscous sublayer, as well as turbulent flow far from the wall.

When comparing the values of wall shear stress and the average streamwise velocity in the viscous wall region for different section planes through the ditch, shown in Table 4.9, Table 4.10 and Table 4.11 it is clear, that $k - \omega$ and $k - \varepsilon$ model with Enhanced Wall Treatment yield almost identical values. The differences in values of streamwise velocities and τ_w obtained with $k - \varepsilon$ and RSM with wall functions are also minor. The \bar{u} values are only slightly higher than those obtained with other turbulence models but the wall shear stress in many cases is more than 50% higher. Therefore considering suitability of the all models to represent the flow close to the wall, the validity of $k - \omega$ and $k - \varepsilon$ model with Enhanced Wall Treatment was assumed.

In the middle section plane through the straight ditch channel, the highest τ_w is for the outer wall and equals 0.06 Pa, while for the inner wall is almost zero. The values of \bar{u} are almost constant in the cross-section and equal 0.1 m s^{-1} . The section through the entrance to the ditch bend is characterized by the highest shear stress, which on the inner and outer wall is 0.1 Pa. The average velocity in the section at the inner and outer wall equals 0.14 m s^{-1} and decrease in the middle of the channel towards to 0.09 m s^{-1} . After passing the bend, the higher τ_w of 0.1 Pa is for the bottom and outer wall, while on the inner wall

is almost zero. The highest \bar{u} of 0.13 m s^{-1} are in the middle of the channel, while close to the walls decrease to around 0.1 m s^{-1} is observed.

In this study, the simulation of the fluid flow within the ditch using fine mesh allowing for detailed computation of the quantities in the near wall region accounts for relatively high computational cost and long computational times involved, that for 7-equation RSM are the highest.

4.6.3.3 Surface Roughness

The concept of existence of laminar sublayer in turbulent boundary layer explains the behaviour of surface roughness, which is a measure of the wall texture. If the average roughness height, k_s , is smaller than the height of the laminar sublayer, it can be said that the roughness elements are completely submerged in the viscous near-wall region. As the default value of wall k defined in the boundary conditions is zero, thus in such conditions, the roughness has no effect upon the inertia dominated flow region extending outside the laminar sublayer and the surface is defined as hydraulically smooth (Chadwick and Morfett, 1998; Chow, 1959).

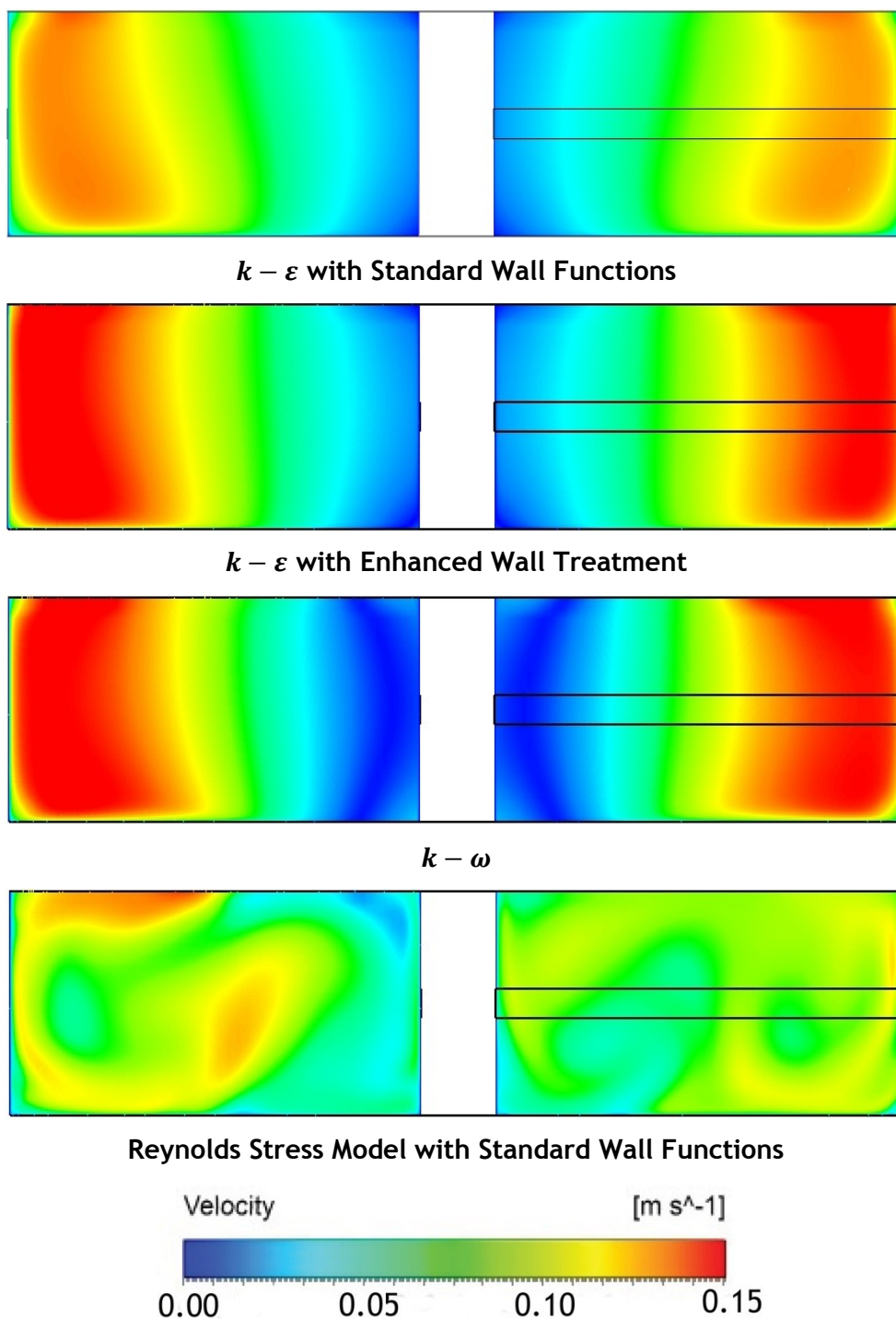


Figure 4.20 Velocity maps obtained from RANS with different turbulence models for the ditch cross-section at $z = 0$ m.

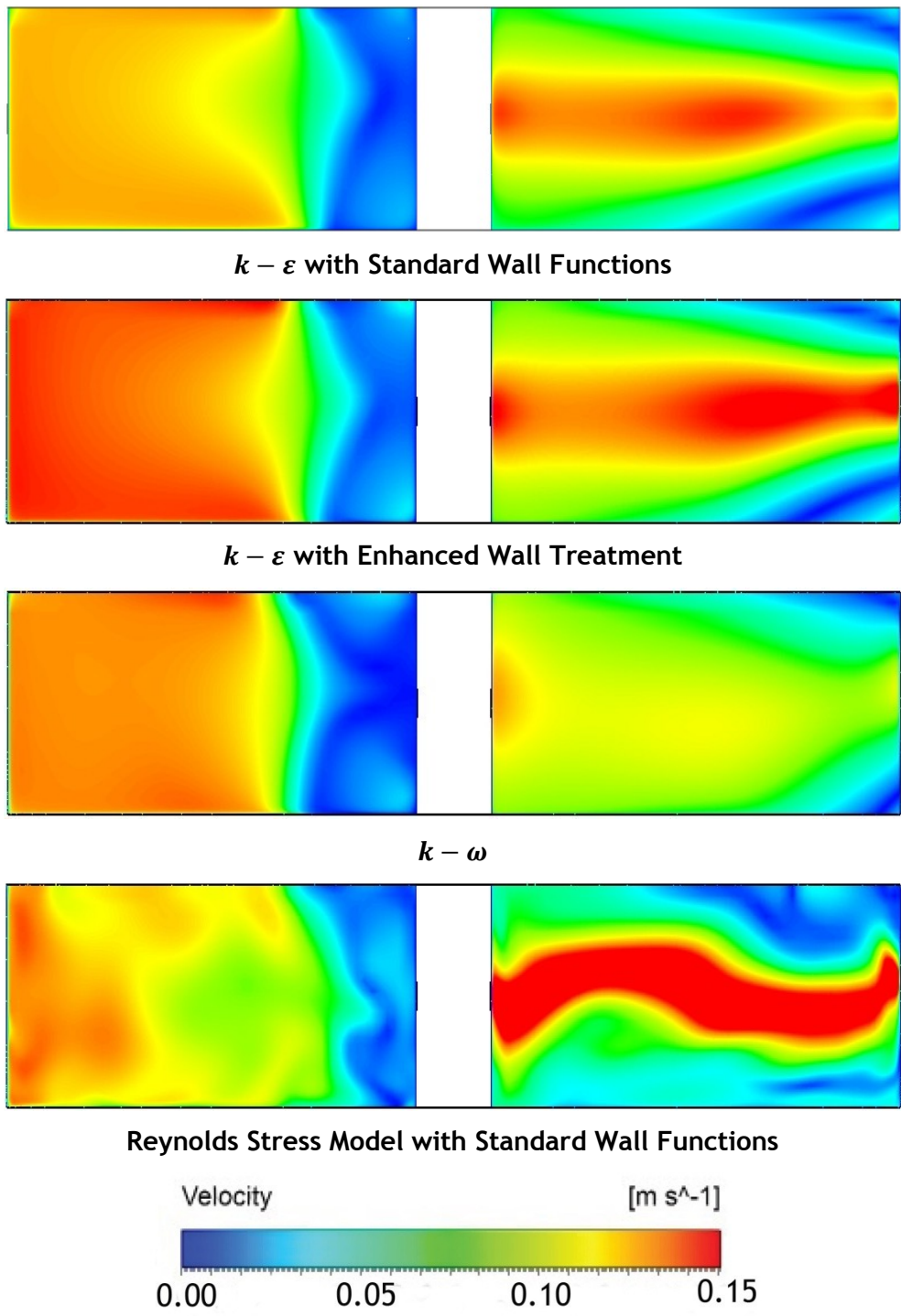


Figure 4.21 Velocity maps obtained from RANS with different turbulence models for the ditch cross-section at $z = 4.8$ m.

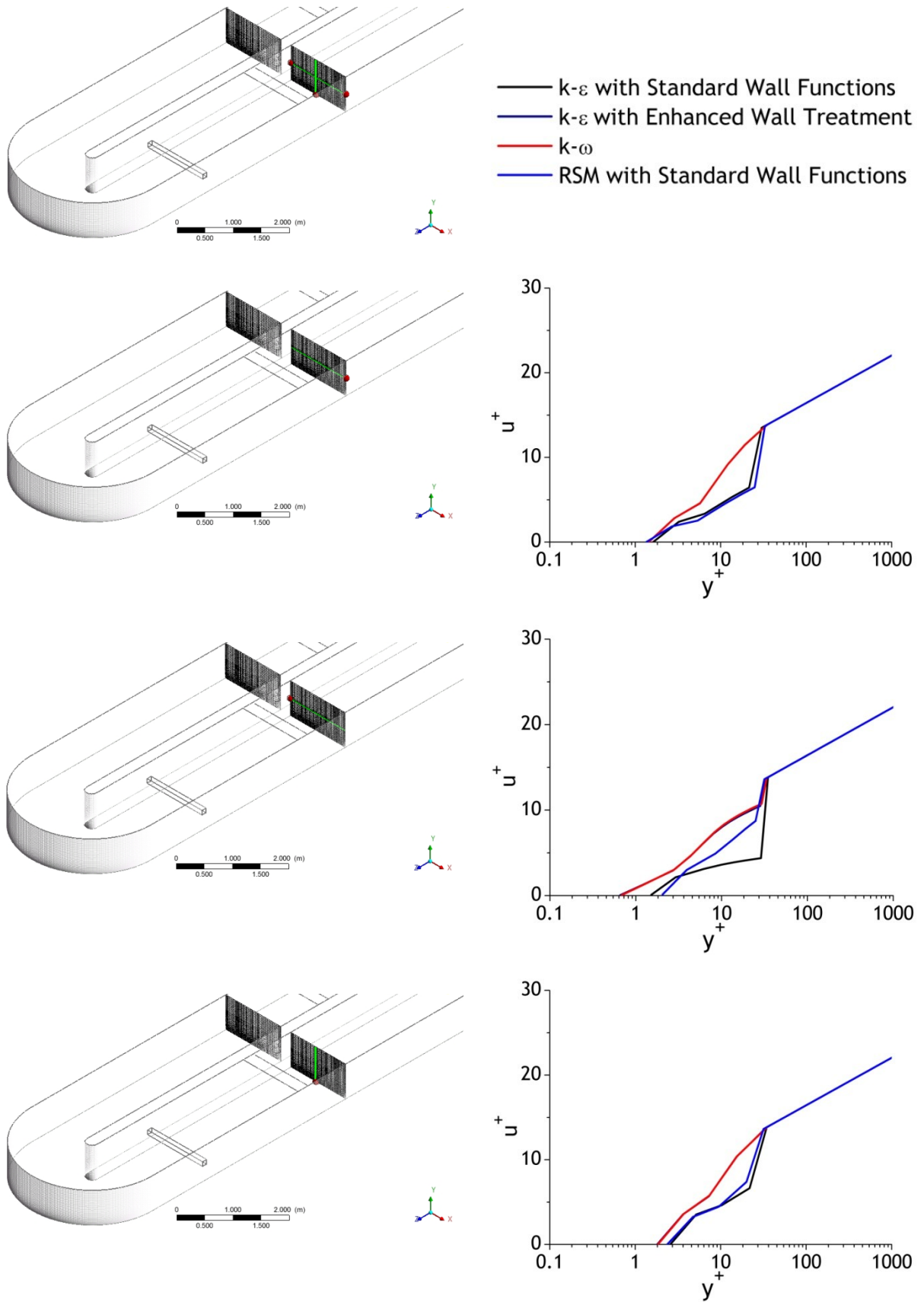
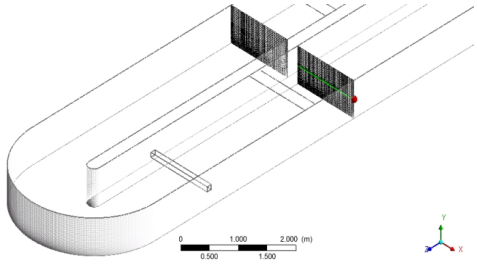
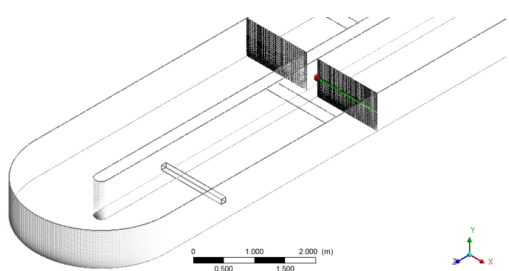
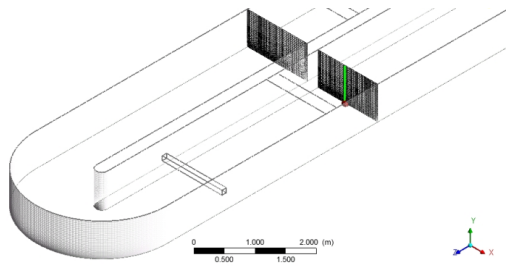


Figure 4.22 Streamwise mean velocity near-wall profiles in the central cross-section through the oxidation ditch obtained with different turbulence models.

4 CFD Simulations of the Oxidation Ditch

Table 4.9 Viscous flow parameters in the near-wall region in the central cross-section through the oxidation ditch obtained with different turbulence models.

Wall point	Model	τ_w (Pa)	\bar{u} (m s ⁻¹)
 <p>x = 1.50 m, y = 0.375 m, z = 0 m</p>	$k - \varepsilon$ with SWF	0.073	0.076
	$k - \varepsilon$ with EWT	0.057	0.086
	$k - \omega$	0.057	0.087
	RSM with SWF	0.050	0.073
 <p>x = 0.125 m, y = 0.375 m, z = 0 m</p>	$k - \varepsilon$ with SWF	0.016	0.076
	$k - \varepsilon$ with EWT	0.003	0.086
	$k - \omega$	0.003	0.087
	RSM with SWF	0.029	0.073
 <p>x = 0.75 m, y = 0 m, z = 0 m</p>	$k - \varepsilon$ with SWF	0.060	0.075
	$k - \varepsilon$ with EWT	0.030	0.078
	$k - \omega$	0.031	0.080
	RSM with SWF	0.051	0.070

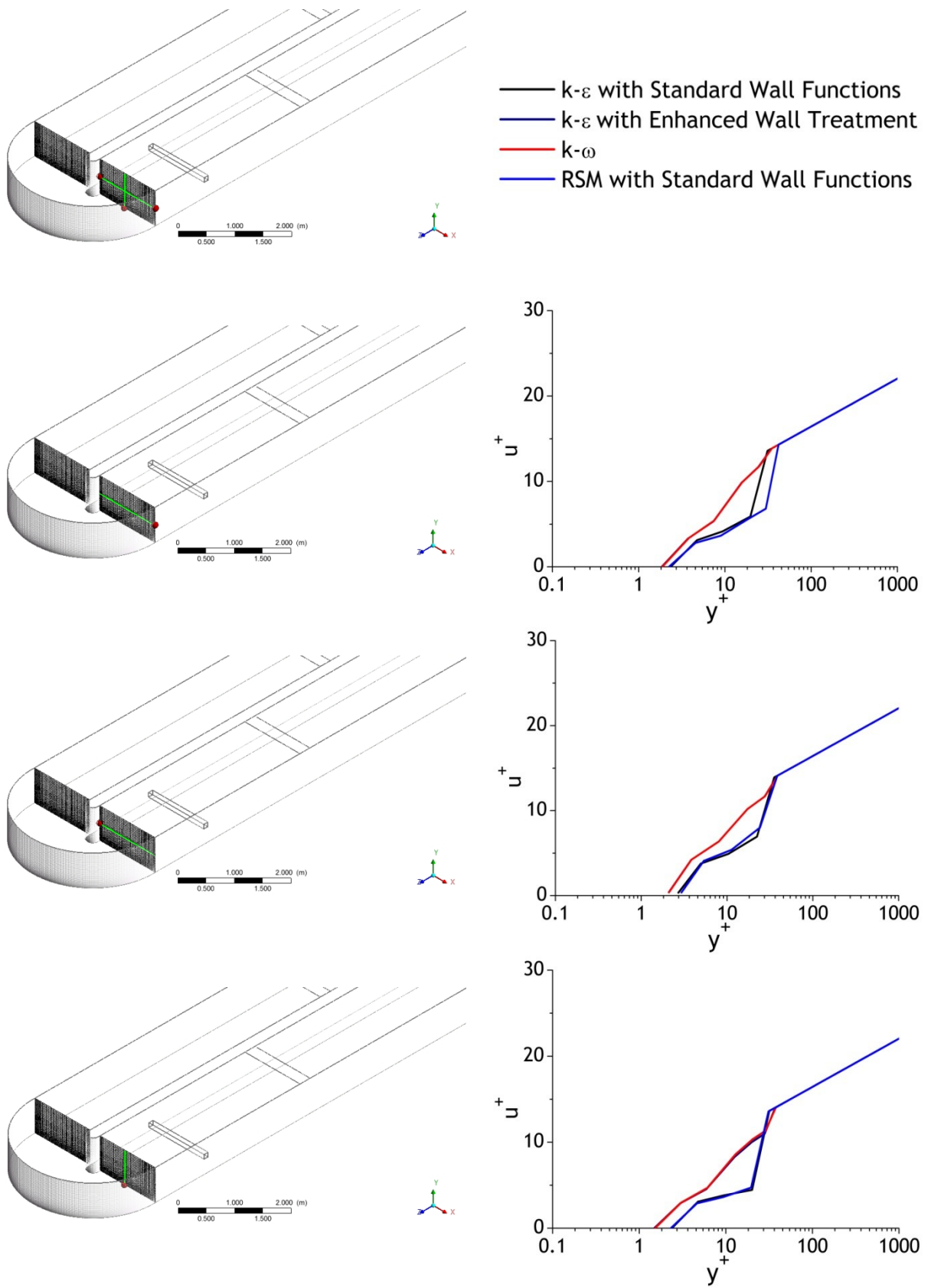
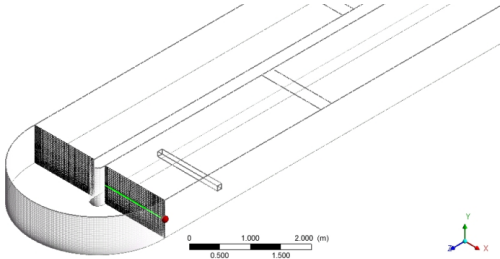
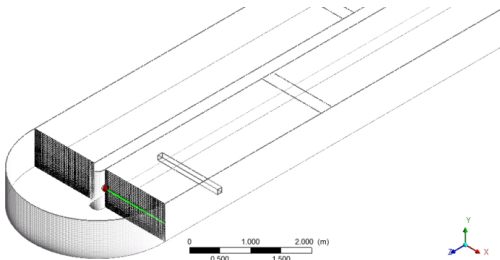
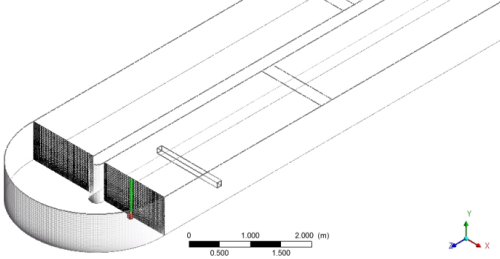


Figure 4.23 Streamwise mean velocity near-wall profiles in the cross-section through the entrance to the bend obtained with different turbulence models.

4 CFD Simulations of the Oxidation Ditch

Table 4.10 Viscous flow parameters in the near-wall region in the cross-section through the entrance to the bend obtained with different turbulence models.

Wall point	Model	τ_w (Pa)	\bar{u} (m s ⁻¹)
 <p>$x = 1.50$ m, $y = 0.375$ m, $z = 4.80$ m</p>	$k - \varepsilon$ with SWF	0.156	0.121
	$k - \varepsilon$ with EWT	0.097	0.134
	$k - \omega$	0.100	0.135
	RSM with SWF	0.143	0.151
 <p>$x = 0.125$ m, $y = 0.375$ m, $z = 4.80$ m</p>	$k - \varepsilon$ with SWF	0.208	0.121
	$k - \varepsilon$ with EWT	0.124	0.134
	$k - \omega$	0.126	0.135
	RSM with SWF	0.245	0.151
 <p>$x = 0.750$ m, $y = 0$ m, $z = 4.80$ m</p>	$k - \varepsilon$ with SWF	0.051	0.070
	$k - \varepsilon$ with EWT	0.020	0.081
	$k - \omega$	0.021	0.083
	RSM with SWF	0.049	0.068

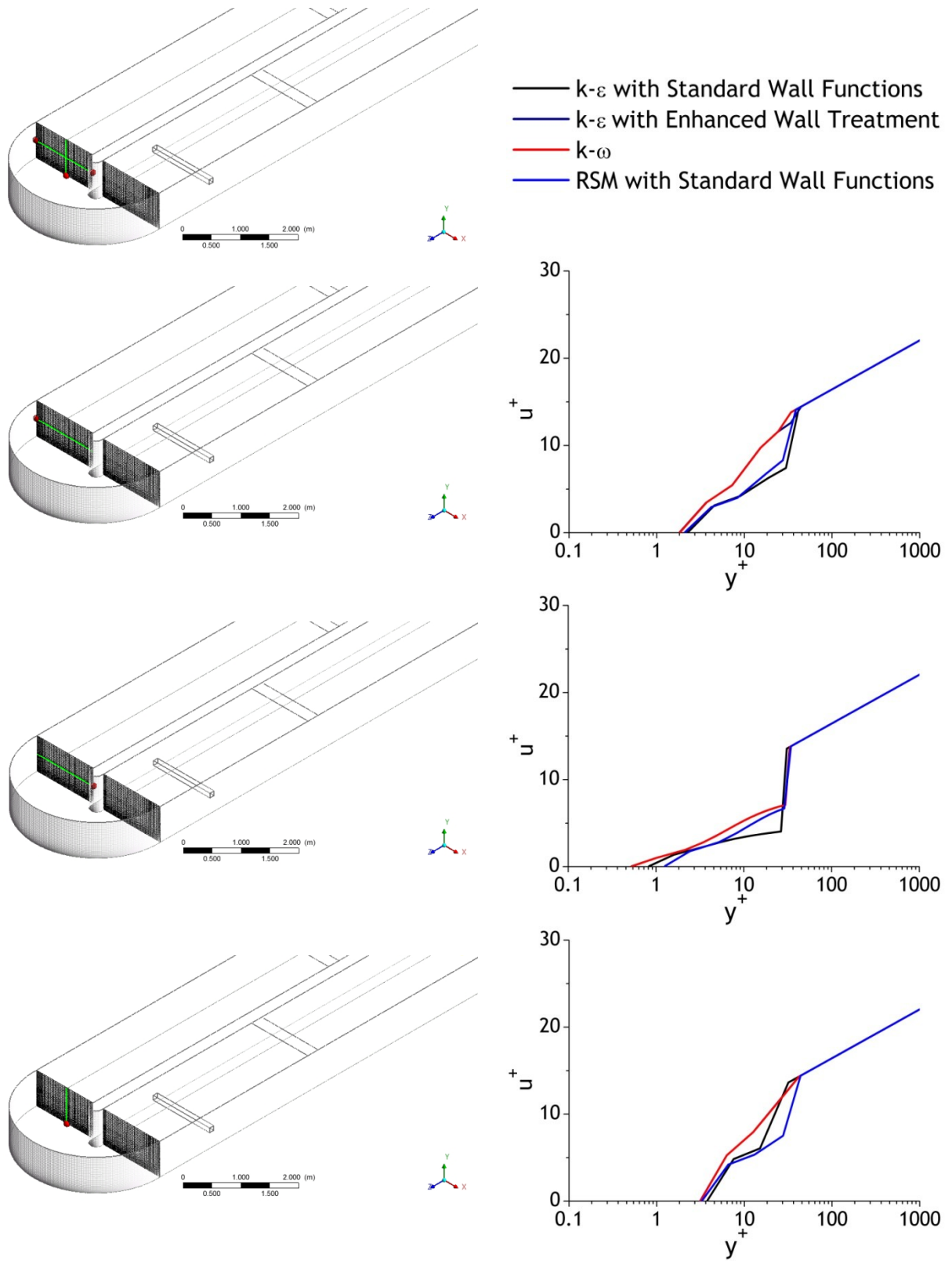
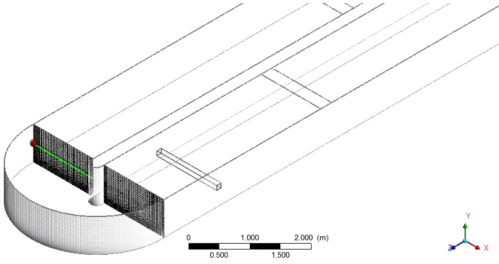
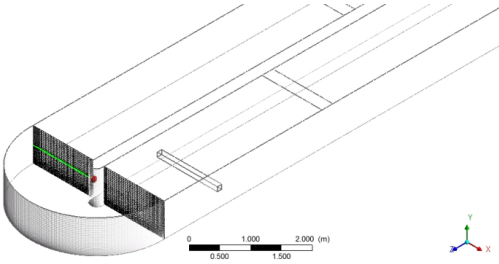
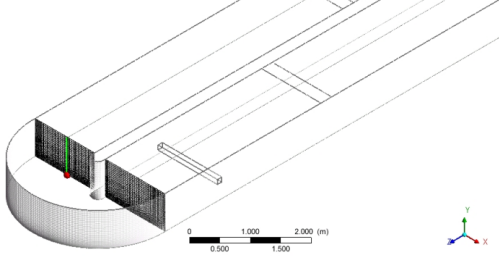


Figure 4.24 Streamwise mean velocity near-wall profiles in the cross-section through the exit from the bend obtained with different turbulence models.

4 CFD Simulations of the Oxidation Ditch

Table 4.11 Viscous flow parameters in the near-wall region in the cross-section through the exit from the bend obtained with different turbulence models.

Wall point	Model	τ_w (Pa)	\bar{u} (m s ⁻¹)
 $x = -1.50$ m, $y = 0.375$ m, $z = 4.80$ m	$k - \varepsilon$ with SWF	0.143	0.076
	$k - \varepsilon$ with EWT	0.093	0.087
	$k - \omega$	0.095	0.088
	RSM with SWF	0.123	0.082
 $x = -0.125$ m, $y = 0.375$ m, $z = 4.80$ m	$k - \varepsilon$ with SWF	0.005	0.076
	$k - \varepsilon$ with EWT	0.002	0.087
	$k - \omega$	0.002	0.088
	RSM with SWF	0.011	0.082
 $x = 0.750$ m, $y = 0$ m, $z = 4.80$ m	$k - \varepsilon$ with SWF	0.129	0.113
	$k - \varepsilon$ with EWT	0.089	0.127
	$k - \omega$	0.090	0.128
	RSM with SWF	0.097	0.093

4.6.4 Energy Expenditure for Different Mesh Properties and Turbulence Models

The energy expenditure associated with keeping the fluid flowing inside the ditch and mixing its content is determined directly from the boundary condition inside the hydrojets volume that was set in RANS as a volumetric momentum source. The simulations considered the hydrojets configuration in the mid-depth of the ditch. Power demand was computed taking into consideration various mesh configurations and different turbulence models. The formulas used to determine power demand for mixing, P_{mix} , and power supplied to the fluid, P_u , were described in section 4.6.2 with the Equation (4.62) and (4.63). Energy efficiency was determined as the ratio of P_u to P_{mix} .

Table 4.12 shows the data set obtained from the fluid flow simulations with different turbulence models and for varying mesh cells numbers. For comparison, the values of power of the hydrojets, obtained with transient models, URANS and LES, were also shown. It is seen that with increase of the grid density and the refinement on the wall boundaries, the power for mixing increases due to the increase of the accuracy in flow solution. Nonetheless, the difference between the highest power demand value obtained for Mesh 4 and Mesh 5, and the lowest value, obtained for the coarsest grid 1 is of 5%.

Considering turbulence model involved in computations of fully developed flow region and viscosity affected boundary layer, increase of the power demand for the hydrojets zone with the solution accuracy was observed. Thus the highest value of power demand was obtained for $k - \omega$ turbulence model, and the lowest for $k - \varepsilon$ with Enhanced Wall Treatment and the difference in these values is of 5%. Nonetheless, when comparing these values with the results obtained with unsteady-state models, as far as for URANS the values of power and energy expenditure are equal to those obtained with RANS, whereas LES yield the higher power numbers, only 2% lower than those obtained with $k - \omega$ model. The values of power demand for mixing obtained for all grid configurations and turbulence models used in the simulations are shown in Figure 4.25.

On the other hand when comparing the data presented in Table 4.12 it is clear, that average velocity of the fluid has large impact on values of power supplied to the fluid and thus on energy efficiency of the oxidation ditch system. Here, regardless of the turbulence model and mesh density, increase of the average velocities by 10%, yields 25% increase of power of the fluid, resulting in 6-8% increase of energy efficiency. Therefore the energy efficiency computed for the lowest velocity of 0.10 m s^{-1} , obtained from simulations with standard $k - \varepsilon$ model using coarser mesh and RSM model using refined mesh, is only 23%. At the same time, the highest average velocity of 0.12 m s^{-1} , obtained with RANS and standard $k - \varepsilon$ model using the finest grid, as well as with LES and much coarser grid, yielded energy efficiency of 39%. Nonetheless, seven out of eleven cases of simulations with RANS and URANS and using both, coarse and refined in different algorithms meshes yielded the average velocity of 0.11 m s^{-1} and energy efficiency of 31%, which was accepted as the most reliable value for further assessments.

4 CFD Simulations of the Oxidation Ditch

Table 4.12 Power demand and energy efficiency obtained from RANS simulations with different turbulence models and for different mesh configurations.

Mesh n°	N° of mesh elements	Turbulence model	\bar{u}	P_{mix}	P_u	P_{mix}/P_u
	$\times 10^6$		(m s ⁻¹)	(W)	(W)	(%)
6	5.6	RANS $k - \varepsilon$ with SWF	0.12	2.49	0.97	39
5	5.4	RANS $k - \varepsilon$ with SWF	0.11	2.55	0.75	29
4	4.7	RANS $k - \varepsilon$ with SWF	0.11	2.55	0.75	29
3	4.7	RANS $k - \varepsilon$ with SWF	0.11	2.49	0.75	30
2	1.7	RANS $k - \varepsilon$ with SWF	0.11	2.42	0.75	31
1	0.6	RANS $k - \varepsilon$ with SWF	0.10	2.42	0.56	23
5	5.4	RANS $k - \varepsilon$ with EWT	0.11	2.49	0.75	30
5	5.4	RANS $k - \omega$	0.11	2.61	0.75	29
5	5.4	RANS RSM with SWF	0.10	2.51	0.56	22
2	1.7	URANS $k - \varepsilon$ with SWF	0.11	2.41	0.75	31
2	1.7	LES Smagorinsky's SGS	0.12	2.56	0.97	38

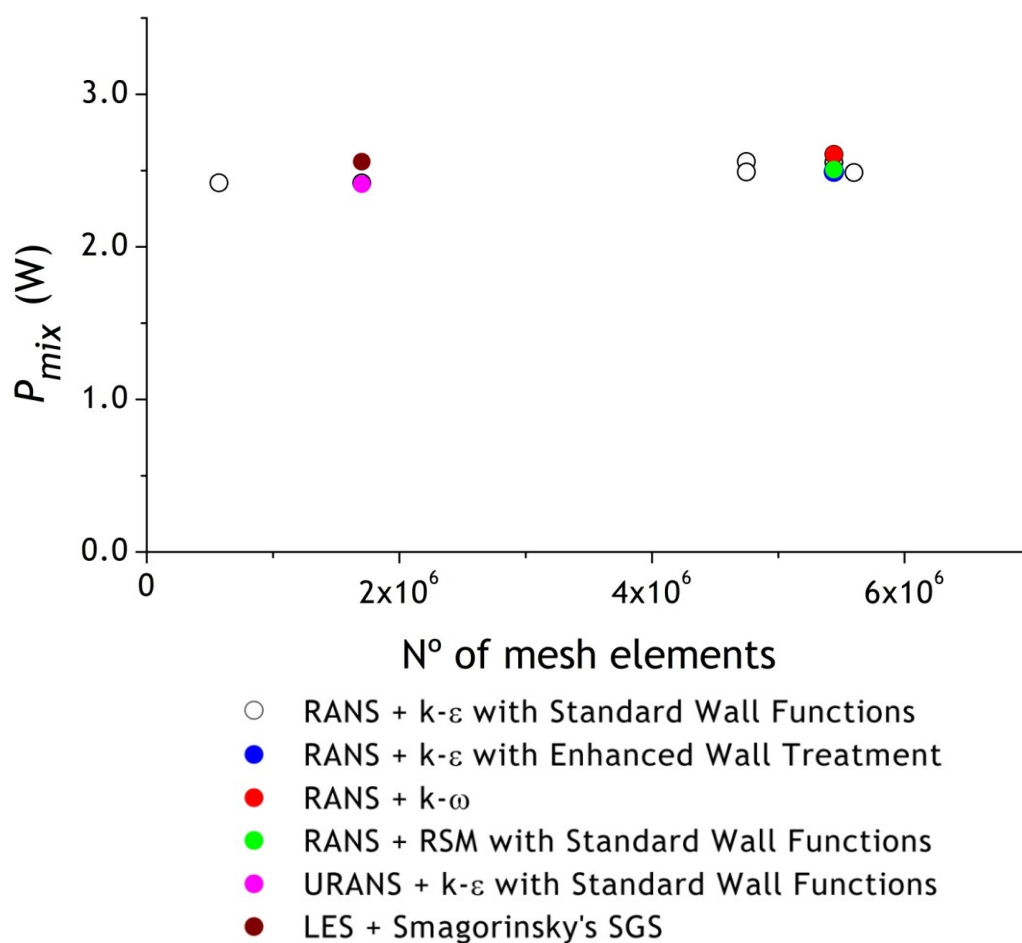


Figure 4.25 Power demand for mixing obtained from RANS, URANS and LES simulations with different turbulence models and for different mesh configurations.

4.6.5 Macromixing

In this work, CFD is used as a tool for assessment of the macromixing within the oxidation ditch. Particle tracking was used to determine the distribution of residence times in the oxidation ditch for the different turbulence models: RANS and URANS with standard $k - \varepsilon$ turbulence model and LES with Smagorinsky's SGS model. The simulations consider the hydrojets located in the mid-depth of the ditch. Due to large efforts in terms of RAM and CPU usage, Mesh 1 with 600 thousand cells was used in the simulations, due to its suitability to represent with reliable accuracy log-law and fully developed turbulent flow regions. The RTD was computed from the simulation of a pulse injection of 10 000 particles introduced into the ditch system through the inlet in a very short period, 10^{-3} s. The flux of the particles exiting the oxidation ditch through the outlet was recorded as function of flow time.

The computation of macromixing, and thus RTD of the fluid particles is strongly dependent on the turbulence model involved in the flow simulation. This can be seen from the RTD computed using the three models and shown in Figure 4.26. The average residence time of fluid in the tank, τ is 4 h, i.e. 14400 s. The $E(t)$ function, presented here as the RTD curves, refer only to the first 4 hours, due to the high computational times involved, during which the most dynamic changes in the ditch outlet were registered. The mean travel time of the flow across the entire ditch is approximately 200 s, thus the average number of turns of fluid particles within the ditch before exiting is around 70. For RANS and URANS the peaks of the RTD at the early time instants are associated with a considerable amount of particles exiting in the first two turns. The results with RANS and URANS suggest that the hydrojets caused an intense vertical segregation of the flow, with strong channelling from inlet to outlet. The particles not being transported to lower regions of the ditch in the first turns render usage of a small percentage of the ditch volume. The particles that are transported to the lower part of the ditch will be trapped there for long time, yielding a long tail in the RTD. However, the RTD plot obtained from LES does not show the peaks related with huge amounts of particles exiting in the first turns. This is due to the convective patterns in LES that promote transport to the lower regions of the ditch, and thus a greater fraction of the actual ditch volume is used.

The comparison of results from the different turbulence models is clear when the percentage of total injected particles exiting during the first 800 s is considered: 30% for RANS, 20% for URANS and 5% for LES. For a flow time equal to the mean hydraulic retention time, these values are 32% for RANS, 31% for URANS and 24% for LES, respectively. As seen from these figures, the turbulence model applied in the CFD simulations has a strong impact on the advection patterns taken by the particles in the oxidation ditch.

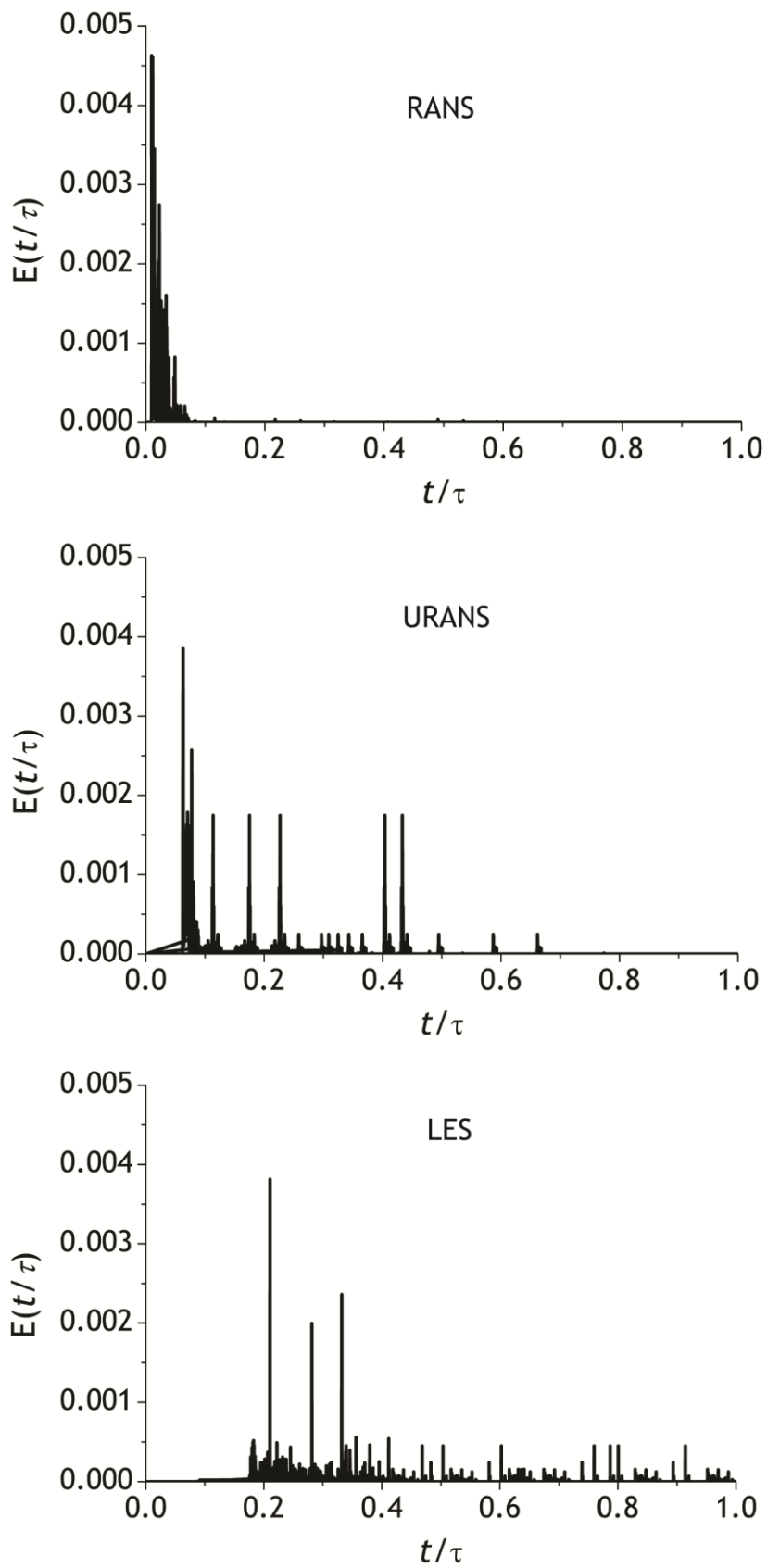


Figure 4.26 RTD curves obtained from oxidation ditch simulations with RANS, URANS and LES.

ASM1 has been widely employed to simulate and model wastewater treatment plants using ideal reactor models for its implementation. The ideal reactor models involved in ASM, one or a cascade of CSTRs assume a spatial invariance of the components concentration within the reactor, while in the PFR model, an axial dispersion term is rather sporadically enabled (Makinia and Wells, 2000a, b; Stamou, 1997). These simplified reactor models fail to represent the actual reactor flow dynamics, which is thus not considered on the results of the ASM1. The results obtained from ASM simulations may differ significantly from those from real scale units, particularly regarding the actual dissolved oxygen profiles along the ditch, which have a clear impact on the nutrient removal (Pereira et al., 2009). Even small changes in the horizontal velocity, ignored by ASM models, affect distinctly the oxygen profiles along the ditch and thus the nitrification process (Abusam et al., 2002; Gillot and Héduit, 2000). According to that, RTD curves and the hydrodynamics characteristics obtained from the CFD simulations of the oxidation ditch can be used to generate a suitable reactor model, i.e. in terms of number of CSTRs in series, recirculation rate and the flow pattern between each of the reactors, where the ASM can be implemented (Le Moullec et al., 2010b).

4.7 Conclusions

The hydrodynamics studies of the oxidation ditch concerned simulation of the fluid flow with different turbulence models. Regardless of the hydrojets placement, the same overall distribution of the flow patterns was obtained from RANS and URANS, where the hydrojets create an average flow with great stratification inside the volume of the ditch, characterized by poor vertical transport. In LES, the presence of eddies change the hydrojet plume into a sinuous path evolving dynamically throughout the ditch, promoting convective transport between the fluid layers.

Considering geometry, hydrojets placed at the surface exhibit average velocity values up to 30% larger than the other configurations resulting in higher energy efficiency of the system up to 52%, however they lead to formation of the extended dead zones near the ditch bottom, which may be related to the occurrence of the DO deficit zones. On the other hand, the hydrojets placed near the bottom demand for less than 5% energy for mixing than mid-depth and near-surface configurations, but also yield lower average velocities, what affects overall mixing in the ditch and decrease energy efficiency to 22%. Thus, geometry scenario with the hydrojets fixed in the mid-depth of the ditch was selected as the most adequate in terms of energy efficient mixing. The difference in the energy efficiency and power demand for mixing obtained from all simulations with RANS, URANS and LES, is less than 8 % for the same hydrojet configurations, thus for geometry

and power demand studies, the model which requires less computational resources, RANS, should be used.

In the hydrodynamic studies of the near-wall region, the grids refined at the boundaries, revealed to be the most accurate to represent the flow in both, viscous affected region and inertia dominated flow core. It was shown, that $k - \varepsilon$ with Enhanced Wall Treatment and $k - \omega$ turbulence models enable with almost identical accuracy to solve boundary layer with the appropriate refined mesh. Nonetheless, the $k - \varepsilon$ and RSM turbulence models coupled with the Standard Wall Functions are unsuitable to represent the flow in the wall adjacent cells, through the application of the bridging algorithms, adapting parameters solved at the viscous wall regions to the log-law region. As far as the flow in the viscosity-affected layer can be neglected, standard $k - \varepsilon$ model is suitable to solve accurately both, log-law and fully developed turbulent flow regions with distinctly coarser meshes.

Considering energy expenditure in the oxidation ditch, increase of the grid density yields higher power demand for mixing, nonetheless the differences in values obtained for the finest and the coarsest grid is less than 5%. Furthermore, considering the impact of the model and near-wall treatment, power demand obtained for the hydrojets zone increases with the solution accuracy. Thus the highest value was obtained for $k - \omega$ turbulence model, which is only 2% higher than for LES, and 5% higher than the one computed with the $k - \varepsilon$ model with Enhanced Wall Treatment. According to that, for the same mesh and geometry conditions (hydrojet placement) the model which accounts for less energy and computational efforts, namely RANS with standard $k - \varepsilon$ turbulence model, is appropriate for energy computing. On the other hand, regardless of the mesh resolution and turbulence model used, the power in the fluid flow delivered to the oxidation ditch and thus energy efficiency of the system depend on the average velocity of the fluid. It was shown, that for the considered hydrojets' configuration, increase of the average velocity by 10% yields 6 to 8% increase of energy efficiency of the system.

Macromixing determination is a useful tool to describe the actual reactor performance. However, this work shows the limitations of some approaches to the computation of the RTD. The RTD simulations based on the average flow field, RANS and URANS, lead to overestimation of channeling effects. The flow dynamics underlies mixing at all scales, both macro- and micro-, and thus this should always be accounted for. Furthermore, it has been shown that CFD data for ASM must account with the dynamics components of the

flow, thus LES simulations, which demand for more computational resources should be used for some specific purposes.

5 New Designs and Energy Efficiency Evaluation

5.1 Introduction

This chapter is divided in two main sections: in the first section, a review on power demand by different aeration devices is given, while the second section refers to determination of overall energy expenditure for proposed activated sludge system.

The review aims to present power demand assessment for aeration systems in wastewater treatment technology. Typical values of theoretic and actual daily oxygen and air demand per capita are given. Furthermore, depending on the source of oxygen and the type of aeration system, i.e. surface aeration or diffused aeration units, daily power and energy consumption per habitant is determined. Additional energy requirements by these systems due to operation of blowers and oxygen generators are also assessed.

Second part of the chapter concerns detailed assessment of energy expenditure in the proposed oxidation ditch system, aerated with slot hydrojets and external aeration unit - Pressurized Aeration Chamber (PAC). Overall energy expenditure considers computations of power demand on aeration, mixed liquor recirculation and mixing of the ditch content. Firstly, actual oxygen and air requirements for proposed PAC unit are assessed. Power demand by blower is determined taking into account actual pressure losses in designed air piping system. Additional computations of energy expenditure by oxygen generation in Vacuum Pressure Swing Adsorption (VPSA) process are also made. As PAC performance is connected with mixed liquor pumping and recirculation, thus power demand by pump is also determined, considering two hydrojets types: multi-slot injector and slot injector.

Finally, power demand on mixing of the oxidation ditch volume, and thus power by hydrojets is given.

5.2 Oxygen Demand for Wastewater Aeration

Aeration in most of the suspended growth activated sludge systems, such as an oxidation ditch, are designed to achieve carbonaceous Biochemical Oxygen Demand (*CBOD*) removal and nitrification. Considering long solid retention times in the oxidation ditch system, where nitrification and biodegradation occur simultaneously, oxygen requirement for effective substrate conversion and endogenous respiration can be assessed on the basis of the mass balance using influent Biochemical Oxygen Demand (*BOD*) concentration and the amount of the biomass wasted from the system per day. Typically, the values of *BOD* in the municipal wastewater depend upon the wastewater strength, and thus on water consumption, which varies from country to country, from rural to urban areas and from city to city. Typical value of the 5-day Biochemical Oxygen Demand (*BOD*₅) daily mass loading per capita for medium strength and average quality domestic wastewater is 54.0 gO₂ (capita·d)⁻¹ (Tchobanoglous et al., 2003). The value of per capita total biochemical oxygen demand (*BOD*_{total}) loading per day is computed from the following formula:

$$BOD_{total} = \frac{BOD_5}{f} \quad (5.1)$$

where the conversion factor *f* from *BOD*₅ to *BOD*_{total} total is 0.68.

Thus the *BOD*_{total} mass loading is 79 gO₂ per capita and day.

Some amount of the *BOD* present in the influent to the aeration tank is incorporated into the activated sludge cells. Kinetic relationship between secondary biomass production and the solids retention time (SRT), defined also as the sludge age or the mean cell residence time (MCRT) can be written as follows:

$$Y_{obs} = \frac{Y}{1 + \tau_c k_d} \quad (5.2)$$

where *Y*_{obs} is observed biomass yield coefficient expressed in g *VSS* produced per g *BOD*₅ of substrate removed; *Y* is the synthesis yield coefficient, g *VSS* per g *BOD*₅; *τ*_{*c*} denotes mean cell residence time, d; and *k*_{*d*} is the endogenous decay coefficient, d⁻¹.

The value of Y usually ranges from 0.3 to 0.7 and k_d for BOD_5 is around 0.06 (Quasim, 1999; Tchobanoglous et al., 2003). Thus, the values Y and k_d equal 0.6 and 0.06, respectively were assumed for further computations, yielding:

$$Y_{obs} = \frac{0.6}{1 + 0.06 \tau_c}$$

If the cell residence time, τ_c , ranges from 5 to 15 d, thus Y_{obs} ranges from 0.46 to 0.32 g VSS per g BOD_5 .

Considering average values of per capita flow rate q_p of 0.15 to 0.25 m³ d⁻¹ (Tchobanoglous et al., 2003) the BOD inflow concentration varies from 216 to 360 g m³. For the oxidation ditch process, organic substrate removal efficiency is up to 99% (EPA, 2000), yielding total mass removed equal approximately to the daily loading per capita. Therefore, the cells production, P_X , is given by following formula:

$$P_X = Y_{obs} \cdot q_p (S_0 - S_e) \approx Y_{obs} \cdot BOD_5 \quad (5.3)$$

where P_X net waste activated sludge daily production, g VSS d⁻¹.

Therefore, the theoretical oxygen requirement, $R_{O_2,th}$, is lowered from the BOD_5 by a quantity incorporated into cells mass (Tchobanoglous et al., 2003), in accordance to the following assumption (Karia and Christian, 2006; Tchobanoglous et al., 2003):

Oxygen required (kg d⁻¹) = total mass of BOD removed (kg d⁻¹) - 1.42 · mass of biomass (COD) wasted (kg d⁻¹).

In accordance with the Equation (5.3), this interrelationship can be written as:

$$R_{O_2,th} = \frac{BOD_5}{f} - 1.42 P_X = BOD_5 \cdot \left(\frac{1}{f} - Y_{obs} \right) \quad (5.4)$$

where $R_{O_2,th}$ is theoretical oxygen demand expressed in g d⁻¹ and 1.42 is stoichiometric conversion factor to obtain quantity (kg) O₂ required for ultimate oxidation of 1 kg of the cells.

Thus we have:

$$R_{O_2,th} = 54 \cdot \left(\frac{1}{0.68} - Y_{obs} \right)$$

According to the above, the quantity of consumed oxygen ranges from: 55 to 62 gO₂ d⁻¹.

5.2.1 Actual Air and Oxygen Demand

Knowing the total oxygen requirement, the determination of the quantity of atmospheric air that must be delivered to the system must consider the percentage of oxygen in air that is 23.2%. Thus we have:

$$R_{Air} = \frac{R_{O_2,th}}{0.232} \quad (5.5)$$

where R_{Air} denotes air requirement expressed in $g\ d^{-1}$.

Thus, the oxygen demand corresponds to air mass from 237 to 267 g per day. To assess R_{Air} expressed as a volumetric flow rate, the air density at the sea level and the temperature of 20 °C must be considered in the Equation (5.5)

$$R_{Air} = \frac{R_{O_2,th}}{0.232 \cdot \rho_{Air,20}} \quad (5.6)$$

where $\rho_{Air,20}$ is $1.2\ kg\ m^{-3}$. Here, the air demand is of around $0.2\ m^3\ d^{-1}$.

Daily demand for the aeration systems supplied by oxygen depends on the actual purity of the oxygen gas generated in VPSA process, which in this work is assumed 93%. For pure oxygen system the Equations (5.5) and (5.6) can be written as:

$$R_{O_2} = \frac{R_{O_2,th}}{0.93} \quad (5.7)$$

and

$$R_{O_2} = \frac{R_{O_2,th}}{0.93 \cdot \rho_{O_2,20}} \quad (5.8)$$

where $\rho_{O_2,20}$ is $1.33\ kg\ m^{-3}$.

The oxygen demand is 59 to 67 $g\ d^{-1}$, equivalent to 44 to 50 $L\ d^{-1}$. The data set presenting daily air/oxygen demand for considered mean cell retention time is shown in Table 5.1.

Table 5.1 Daily air/oxygen demand determined for mean cell residence time from 5 to 15 days.

τ_c	$R_{O_2,th}$	R_{Air}		R_{O_2}	
d	(g d ⁻¹)	(g d ⁻¹)	(m ³ d ⁻¹)	(g d ⁻¹)	(m ³ d ⁻¹)
5	55	237	0.20	59	0.04
15	62	267	0.22	67	0.05

5.2.2 Actual Air/Oxygen Demand for Diffused Aeration

For diffused air devices supplied either by atmospheric air or pure oxygen, the actual demand need to account for *SOTE* (Karia and Christian, 2006), and thus the formulas described by Equations (5.5) - (5.8), will be:

$$R_{Air,act} = \frac{R_{Air}}{SOTE} \quad (5.9)$$

and

$$R_{O_2,act} = \frac{R_{O_2}}{SOTE} \quad (5.10)$$

Typical values of *SOTE* for various types of devices within the group of diffused aerators commonly used in wastewater treatment technology are described in detail in Chapter 2, Section 2.2.3.4. For the purpose of the actual air and oxygen demand assessment, the average values of *SOTE* for each group of devices will be used.

The data set obtained for porous and nonporous diffusers and jet aerators is presented in Table 5.2. When comparing the data obtained for different devices it is seen that the highest daily demand values are for the devices characterized by the lowest *SOTE*, and thus nonporous diffusers, accounting for 1.4 to 1.6 kg of air, equivalent to 0.3 to 0.4 kg of oxygen. Porous diffusers- devices having highest *SOTE* yield lowest oxygen demand which is 0.2 kg d⁻¹ or 0.8 to 0.9 kg d⁻¹ of air. Jet aerators are considered intermediate group with daily oxygen demand of 0.3 kg, equivalent to air demand of 1.1 to 1.2 kg d⁻¹.

Table 5.2 Actual air/oxygen demand for various aeration devices.

Device	<i>SOTE</i>	τ_c	$R_{Air,act}$		$R_{O_2,act}$	
	(%)	(d)	(g d ⁻¹)	(m ³ d ⁻¹)	(g d ⁻¹)	(m ³ d ⁻¹)
Porous diffusers	30	5	790	0.66	197	0.15
		15	890	0.74	223	0.17
Nonporous diffusers	17	5	1394	1.16	347	0.26
		15	1571	1.30	394	0.29
Jet aerators	22	5	1077	0.89	268	0.20
		15	1214	1.01	305	0.23

5.3 Energy Expenditure in Aeration Systems

5.3.1 Surface Aerators

Until recently, aeration of the oxidation ditch was linked only with mechanical devices, namely horizontal brush rotors or surface low speed aerators. Typically the power consumption for mechanical aerators, assessed for the standard conditions and in clean water, is expressed in units of the oxygen transfer rate (*OTR*), which ranges from 1.2 to 2.8 kgO₂ kW⁻¹ h⁻¹ equal to 29 to 72 gO₂ W⁻¹d⁻¹ (Tchobanoglous et al., 2003). Usually, for design purposes, standard performance data obtained for the tap water have to be adjusted to the field conditions, thus wastewater, by using Eckenfelder and Ford equation of the following form:

$$P_m = P_{ST} \cdot f_c \cdot 1.024^{T-20} \cdot \alpha \quad (5.11)$$

where: P_m is power demand of mechanical aeration unit in field conditions; P_{ST} is power demand by aerator in standard pressure and temperature conditions and in clean water; α is ratio of $K_L a$ of wastewater to $K_L a$ of clean water; f_c is correction factor for field conditions salinity; and T is operating temperature.

The correction factor, f_c is computed from the following formula:

$$f_c = \frac{\beta_s \cdot C_{w,alt} - C_L}{9.17} \quad (5.12)$$

where β_s is the salinity - surface tension factor usually equal to 1, $C_{w,alt}$ is the oxygen saturation at given temperature and altitude in clean tap water, C_L is operating oxygen concentration.

The average field conditions used in to determine P_m are: operating temperature T equals 15 °C; altitude - 150 m; α for the group of mechanical aerators is 0.85; β_s is 0.9; and the operating DO concentration is 2.0 mg L⁻¹.

Therefore, the power demand by mechanical aerators ranges from 0.5 to 1.5 kgO₂ kW⁻¹ h⁻¹ equal to 12 to 36 gO₂ W⁻¹d⁻¹ (Tchobanoglous et al., 2003).

Knowing the actual daily oxygen demand that ranges from 55 to 62 gO₂ per habitant per day, power consumption per capita and day is computed as follows:

$$P = \frac{R_{Air}}{P_m} \quad (5.13)$$

where P is power consumption in kW.

Thus, power consumption per habitant per day in activated sludge with surface aerators ranges from 1.5 to 5.2 W.

To express the power demand in energy units, the following conversion shall be made:

$$E_{kWh} = P \cdot 3600 \quad (5.14)$$

where E_{kWh} is hourly energy demand per habitant, in kWh, and P is power demand in kW.

Thus, the daily energy demand per habitant will be:

$$E_{kWhd} = P \cdot 86400 \quad (5.15)$$

where E_{kWhd} is daily energy demand per capita in kWh d and P is power demand in kW.

Therefore, for mechanical aerators, the energy consumption is 5.5 to 18.6 kWh that gives 132 to 446 kWhd.

5.3.2 Diffused Aeration Systems

5.3.2.1 Air Piping

Air piping system in wastewater treatment technology consists of mains, valves, meters, and other fittings such as elbows and tees which convey compressed air from blowers to the diffused air device (Tchobanoglous et al., 2003). In engineering practice it is assumed, that the air pipeline should be sized so that the total loss in headers and manifolds is small when compared with the losses in the diffusers (i.e. DWP). Furthermore, when the pipes are oversized, the aeration system is difficult to control, while in case of pipes of too small diameter, potential headloss forces application of higher capacity blowers. From this reason determination of the headloss and thus, the pressure drop in air piping system is used to assess blower power requirement. Nonetheless, this section focus on the evaluation of the energy expenditure by various aeration systems typically used in the oxidation ditches without deeper insight into air piping system, and thus few “typical” design data to determine blower power requirements will be also arbitrarily assumed.

5.3.2.2 Power Demand by Blower - Air System

For diffused aeration systems, delivered power of blowers is computed from the adiabatic compression equation, expressed as:

$$P = \frac{wRT}{29.7 \cdot n \cdot e_B \cdot e_M} \left[\left(\frac{p_2}{p_1} \right)^{0.283} - 1 \right] \quad (5.16)$$

where P is the power requirement for each blower in kW, w is required air mass flow rate in kg s^{-1} , R is universal gas constant for air and $R= 8.314 \text{ kJ kmol}^{-1}\text{K}^{-1}$, and T is the inlet temperature in K, n is the constant and equals 0.283 for air, p_1 and p_2 are absolute pressures upstream and downstream (inlet, outlet) of compressor in atm, e_B is blower efficiency, usually in the range 70-90%, and e_M is motor efficiency, usually in the range of 90-94%.

For specific real scale aeration tank, computing power demand for blower requires proper blower sizing by prediction of the discharge pressure to give accurate values. Design discharge pressure of the blower, p_2 , is usually calculated for the worst operation scenario in the elevated temperatures typical for the hot summer day (Tchobanoglous et al., 2003) and the highest air flow requirements. Therefore it is assumed that the discharge pressure have to compensate: head losses for air piping from the blower location to the submerged aerators considering high pipe roughness, partially throttled valves and fittings; head losses due to DWP of diffusers increased by additional losses due to device ageing

(progressive fouling and scaling); safety factor and overpressure preventing blower surging. For such operating conditions, the assumed pressure head is 10.0 m H₂O equivalent to the compressor discharge pressure of 2.0 atm, representing typical value for the wastewater treatment installations (EPA, 2010; Quasim, 1999). Here, the inlet design temperature considered equals typical summer air temperature of 27°C (300 K), and the blower inlet pressure equals to the atmospheric pressure, thus 1.0 atm. Furthermore, blower efficiency of 70% and motor efficiency of 92% were used in power demand computation. Thus we have:

$$P = \frac{w \cdot 8.314 \cdot 300}{29.7 \cdot 0.283 \cdot 0.70 \cdot 0.92} \left[\left(\frac{2.0}{1.0} \right)^{0.283} - 1 \right]$$

Finally we obtained:

$$P = 100 \cdot w \tag{5.17}$$

where w denotes the air flow ranges equivalent to actual air demand in kg s⁻¹, presented in Table 5.2.

The power requirements per habitant will lie on the following intervals: 0.9 - 1.0 W for porous diffusers; 1.6 - 1.8 W for nonporous diffusers; and 1.3 - 1.4 W for jet aerators. To express the power demand in energy units per capita, i.e. in kWh, the Equation (5.14) was used. The data set presenting power and energy demand by blower considering different diffused air devices is shown in Table 5.3.

Table 5.3 Power and energy demand by blowers for different diffused aeration systems.

Device	τ_c (d)	w (kg s ⁻¹)	P (W)	E_{kWh} (kWh)
Porous Diffusers	5	$9.1 \cdot 10^{-6}$	0.91	3.29
	15	$1.0 \cdot 10^{-5}$	1.03	3.71
Nonporous Diffusers	5	$1.6 \cdot 10^{-5}$	1.61	5.81
	15	$1.8 \cdot 10^{-5}$	1.82	6.54
Jet Aerators	5	$1.2 \cdot 10^{-5}$	1.25	4.49
	15	$1.4 \cdot 10^{-5}$	1.40	5.06

5.3.2.3 Power Demand by Blower - Pure Oxygen System

Typical outflow pressures of oxygen produced in the Vacuum Pressure Swing Adsorption (VPSA), which are summarized in Chapter 2, Table 2.9 are low, therefore in aeration systems requiring higher operating pressures, energy efficient oxygen compressor built-in the unit is considered. In such cases it can be assumed, that if pure oxygen instead of atmospheric air is used, the power demand by blower needed for aeration reduces to 20%. Therefore energy consumption by compressor per capita drops to: 0.2 W for porous diffusers; 0.3-0.4 W for nonporous diffusers; and 0.3 W for jet aerators. The data set with computed values of power demand and energy expenditure per habitant is presented in Table 5.4.

Table 5.4 Power and energy demand by blowers for different diffused aeration systems supplied by pure oxygen.

Device	τ_c (d)	w (kg s ⁻¹)	P (W)	E_{kWh} (kWh)
Porous diffusers	5	$2.3 \cdot 10^{-6}$	0.18	0.66
	15	$2.6 \cdot 10^{-6}$	0.21	0.74
Nonporous diffusers	5	$4.0 \cdot 10^{-6}$	0.32	1.16
	15	$4.6 \cdot 10^{-6}$	0.36	1.31
Jet aerators	5	$3.1 \cdot 10^{-6}$	0.25	0.90
	15	$3.5 \cdot 10^{-6}$	0.28	1.01

5.3.2.4 Power Demand for Oxygen Generation

For AS systems aerated with high purity oxygen additional power demand for the oxygen generation in VPSA process must be considered. The typical values of power expenditure by commercial VPSA units were widely presented in Chapter 2, Section 2.4.5 (Determination of the Process Parameters) of the following dissertation. Assuming, that the energy requirements for oxygen production in VPSA unit is 0.350 kWh per Nm³, the power demand P_{O_2} was computed from the following formula:

$$P_{O_2} = 350 \cdot V_{O_2,N} \quad (5.18)$$

where $V_{O_2,N}$ is oxygen volume in standard pressure and temperature conditions, determined from the Combined Gas Law:

$$V_{O_2,N} = \frac{p_{O_2} \cdot V_{O_2} \cdot T_{O_2,N}}{p_{O_2,N} \cdot T_{O_2}} \quad (5.19)$$

where $V_{O_2,N}$ is the normalized volume of 1 m³ of oxygen at the reference gas temperature $T_{O_2,N}$ of 273.16 K and the normalized pressure $p_{O_2,N}$ of 101325 Pa, V_{O_2} denotes the actual volume of oxygen in m³ assessed from the volumetric flow rate, T_{O_2} is the actual oxygen temperature, assumed identical as for the blower, thus of 300 K, and p_{O_2} is the actual oxygen pressure equal to blower discharge pressure, and thus 2 atm.

Power and energy demand for oxygen separation in VPSA for different aeration devices are shown in Table 5.5. When comparing obtained data it is seen, that the device characterized by the highest and intermediate oxygen demand, namely nonporous diffusers and jet aerators, will account for the power demand of 0.002 W. Slight improvement is seen for the most efficient systems of porous diffusers which yield power requirements by VPSA process of 0.001 W.

Table 5.5 Power and energy demand by oxygen generation in VPSA process for different diffused aeration systems.

Device	τ_c (d)	$R_{O_2,act}$ ($m^3 h^{-1}$)	$V_{O_2,N}$ (Nm^3)	P_{O_2} (W)	E_{kWh} (kWh)
Porous diffusers	5	$6.1 \cdot 10^{-3}$	0.011	$1.1 \cdot 10^{-3}$	$3.9 \cdot 10^{-3}$
	15	$6.9 \cdot 10^{-3}$	0.013	$1.2 \cdot 10^{-3}$	$4.4 \cdot 10^{-3}$
Nonporous diffusers	5	$10.8 \cdot 10^{-3}$	0.020	$1.9 \cdot 10^{-3}$	$6.9 \cdot 10^{-3}$
	15	$12.3 \cdot 10^{-3}$	0.022	$2.2 \cdot 10^{-3}$	$7.8 \cdot 10^{-3}$
Jet aerators	5	$8.3 \cdot 10^{-3}$	0.015	$1.5 \cdot 10^{-3}$	$5.3 \cdot 10^{-3}$
	15	$9.5 \cdot 10^{-3}$	0.017	$1.7 \cdot 10^{-3}$	$6.0 \cdot 10^{-3}$

5.3.3 Evaluation of Energy Expenditure of Aeration Systems

When comparing all types of aeration devices used in activated sludge systems, which are supplied by atmospheric air, it is clear, that the most costly is mechanical surface aeration, yielding energy demand up to 19 kWh per capita. Considering values of daily energy demand determined for air compressor, porous diffusers are the most energy efficient, with energy requirements up to 4 kWh, which is about 5 times less than for mechanical aerators. The most energy intensive system within the diffused air technologies are nonporous diffusers, accounting for up to 6.5 kWh per habitat, yielding 76% increase of energy demand in comparison with the porous devices. Increase of energy demand of 38% is observed for jet aeration systems, considered as the intermediate option in terms of power requirements.

Undoubtedly, pure oxygen systems, besides higher aeration efficiency and better biological treatment effects, allow saving distinct percentage energy, when comparing with aeration systems supplied by air. In high purity oxygen systems, besides reduction of power demand by blower to 20% in cases when operating oxygen pressures are higher than the respective discharge pressure from VPSA unit, the additional efforts due to oxygen generation by VPSA process account for only 0.001 kWh for porous diffusers up to 0.008 kWh for coarse pore devices.

Therefore, from all aeration systems considered in the energy expenditure assessment, the most energy minded solution may be obtained by application of porous diffusers supplied by pure oxygen.

5.4 Aeration of the Oxidation Ditch with Hydrojets - Energy Analysis

The following sections consider assessment of overall energy expenditure for proposed oxidation ditch system, which accounts for power demand on aeration, mixed liquor recirculation and mixing of the ditch content.

5.4.1 Oxidation Ditch System

Hydraulic design of the proposed activated sludge system, which full-scale layout is shown in Figure 5.1, consists of: an oxidation ditch; a jet aeration device; Pressurized Aeration Chamber (PAC); mixed liquor recirculation pump; feed and discharge tubing; air manifold; and a pipeline connecting all equipments.

The full-scale oxidation ditch and PAC dimensions in this case-study are five times larger than the CFD models described in Chapters 2 and 4. The approximate capacity of the ditch having dimensions of $64.0 \times 15.0 \times 4.0$ m is 3900 m^3 . The dimensions of PAC are $0.8 \times 0.8 \times 3.5$ m. The mixed liquor, discharged from the ditch through the pipe fixed in the bottom is recirculated to PAC. Aeration chamber is placed 20.0 m below the tank and supplied with atmospheric air/oxygen. Such hydraulic arrangement provides favourable conditions for effective saturation of mixed liquor with oxygen up to 18 mg L^{-1} under pressure of 2 bars. The DO enriched stream from PAC is recirculated by pump through long vertical pipeline, splitting into two manifolds, supplying the hydrojets. Hydrojets reinject aerated mixed liquor into the ditch with the energy accelerating fluid flow throughout the tank with the velocities keeping the activated sludge flocs suspended, and ensuring efficient mixing of the ditch content. The advantage of such system configuration over conventional aeration is achieved by increase of *SOTE* and *AE* obtained through introduction of an external aeration unit, PAC, cooperating with the mixing and propulsion devices- slot jet modules (hydrojets). The studies on hydrodynamics,

performance and energy analysis of both, PAC unit alone and the oxidation ditch aerated with hydrojets, were previously explored in Chapter 2 and 4.

The main purpose of this section is to determine overall energy expenditure of the full-scale oxidation ditch system, which will account for power demand for aeration (PAC), mixing (hydrojets) and supporting equipment operation (air/oxygen and mixed liquor pipeline and the recirculation pump). Moreover, depending on the oxygen source (atmospheric air or pure oxygen) power demand by blowers or oxygen generation in VPSA will be also assessed.

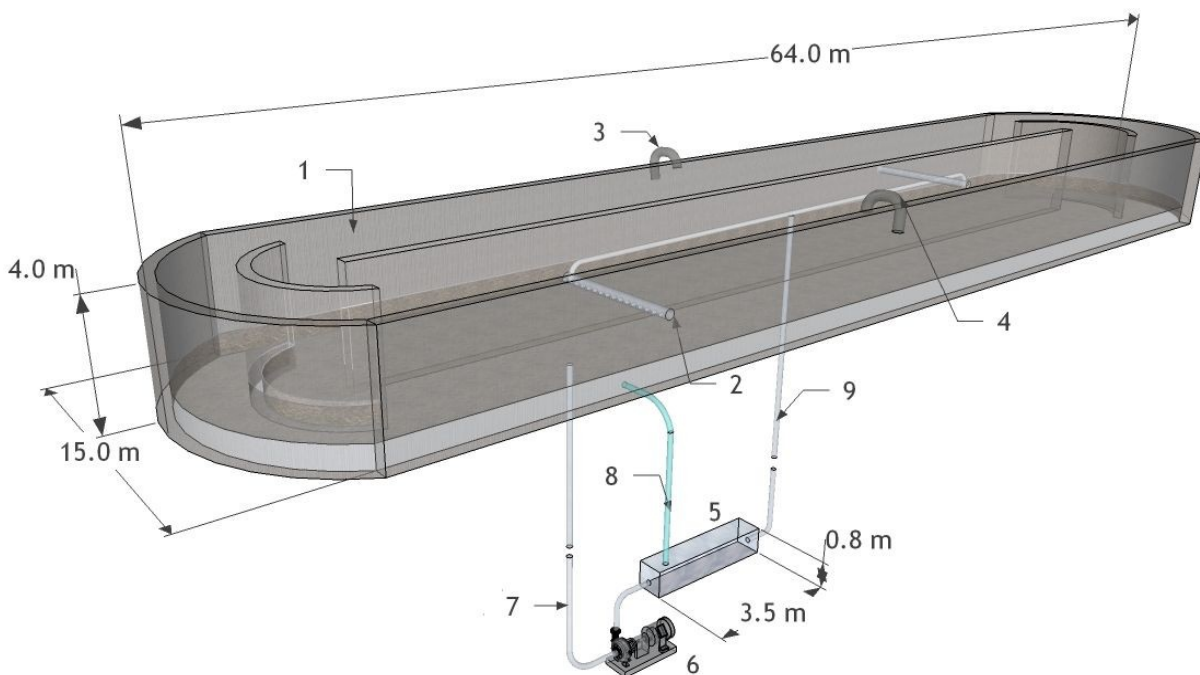


Figure 5.1 Oxidation ditch system layout: 1- oxidation ditch; 2- hydrojets; 3- inlet; 4- outlet; 5- PAC; 6- recirculation pump; 7- recirculated mixed liquor from the ditch; 8- air/oxygen manifold; 9- oxygen rich mixed liquor.

5.4.2 Power Demand on Aeration

The actual power demand on aeration depend on assumed aeration scenario, whether PAC will be supplied by atmospheric air or pure oxygen. According to that, energy expenditure due to blower performance and oxygen generation by VPSA unit will be determined.

5.4.2.1 Air Piping

Blower sizing, and thus accuracy of the headloss prediction requires an exact analysis of the air distribution system, which varies depending on the number of factors, such as: capacity of the wastewater treatment facility, and thus number and size of aeration tanks; the distance from the blower building to the tanks, and therefore the length of the air

header; type of aeration system, number of units and configuration within the activated sludge tank, and thus the distribution, number and length of the manifold sections; pipe material, inner diameter and operating flow rates; number and type of fittings, valves and other devices included in the pipeline; and blower silencer.

Nonetheless, to serve a general case-study purpose, several design simplifications of the hypothetical piping has been assumed to determine total headloss in the air distribution system of the featured oxidation ditch layout (Figure 5.1). It was assumed, that: the system consists of pipes of the uniform diameter of 200 mm and the total length of the pipeline is 20.0 m. Velocity of the air flow through the pipes is of 12.0 m s⁻¹. Stainless steel was selected as a pipe material considering its resistance against elevated temperature of air discharged by blower.

The total headloss in the air piping system is a sum of the major losses due to the friction during air flow in the straight mains, and minor losses which are due to change of velocity occurring during air flow through the valves, bends, and other pipe fittings.

The major (friction) headloss in the air pipeline are computed from Darcy-Weisbach formula of the following form:

$$h_f = f \frac{L}{D} \cdot h_{vel} \quad (5.20)$$

where h_f is friction loss in m of water, f is dimensionless Darcy friction factor, L and D are the pipe length and diameter in m, and h_{vel} is velocity head of air, in m.

For stainless steel air pipes, the friction factor f is determined from the following formula:

$$f = \frac{0.029 \cdot (D)^{0.027}}{Q^{0.148}} \quad (5.21)$$

where Q denotes air flow rate under prevailing temperature and pressure conditions, expressed in m³ min⁻¹.

Substituting term f (5.21) in Equation (5.20) we have:

$$h_f = 9.81 \cdot 10^{-8} \cdot \left(\frac{fLTQ^2}{pD} \right) \quad (5.22)$$

where T is air temperature in pipe, in K and p is air supply pressure equal to blower discharge pressure, in atm.

The air temperature in the pipeline is computed from the following formula (Tchobanoglous et al., 2003):

$$T = T_0 \left(\frac{p}{p_0} \right)^{0.283} \quad (5.23)$$

where T_0 is the ambient air temperature equal to the maximum summer temperature, K and p_0 is the ambient atmospheric pressure, atm.

It was assumed that T_0 equals 27°C (300 K), and p is typical discharge blower pressure of 2 atm and assumed p_0 is 1 atm. Therefore, the temperature T of the compressed air in the pipe is 365 K.

Considering air velocity of 12.0 m s⁻¹ and the tube diameter of 0.2 m, the airflow is 22.6 m³ min⁻¹ yielding f value of 0.018. The friction headloss computed for these data and the pipeline length of 20.0 m is 0.016 m of water.

Minor losses are computed using equivalent length method L_e/D , based on the assumption, that the local loss through a fitting can be expressed in terms of the equivalent length of straight pipe (L_e), that would yield the same head loss as the fitting. According to that, the Equation (5.20) will be:

$$h_f = f \frac{(L + L_e)}{D} \cdot h_{vel} \quad (5.24)$$

where L_e is the equivalent length of a pipe, m.

L_e can be obtained from the following formula:

$$L_e = 55.4 \cdot CD^{1.2} \quad (5.25)$$

where C is the resistance factor, characteristic for the particular fitting.

It was assumed, that considered in the show-case air piping system includes the following components: blower silencer, two control valves and four elbows. The value of C for blow-off butterfly valve is 0.47 and 0.33 for flanged 90° long radius elbow (AWWA, 2001; Tchobanoglous et al., 2003), yielding additional L_e of 14.4 m to be accounted in the formula (5.24). Thus, the sum of the losses in the air piping, accounting for major losses in the straight mains and minor losses in the components is 0.028 m of water per 20 m of piping, however additional local loss of 0.15 m by blower silencer have to be considered (Tchobanoglous et al., 2003), yielding total headloss of 0.18 m of water.

Considering a rule of thumb, that a properly designed piping should have a pressure loss lesser than 10 percent of the compressor’s discharge pressure measured to the point-of-use, computed head for the oxidation ditch air distribution system accounts for only 1% of the assessed blower operating pressure of 2 atm. From this reason, further computation of power demand by blower does not require increase of the discharge pressure.

5.4.2.2 Power Demand by Blower - Air System

Energy demand for air compression would be 3 times less than in case of porous diffusers, because the 30% *SOTE* factor from bubbles is dropped for the PAC case. Therefore we can assume that the power demand will be from 0.31 to 0.34 W.

The data set with computed values of power demand and hourly energy expenditure per habitant is presented in Table 5.6.

Table 5.6 Power and energy demand by blowers for PAC supplied by air.

Device	τ_c (d)	P (W)	E_{kWh} (kWh)
PAC	5	0.31	1.10
	15	0.34	1.24

5.4.2.3 Power Demand by Blower - Oxygen System

Similarly to the diffused aeration units, if pure oxygen is used there is a reduction to 20% of the power needed for injection, thus the power consumption by blower drops to a range of values 0.06 to 0.07 W. The data set with computed values of power demand and hourly energy expenditure per habitant is presented in Table 5.7.

Table 5.7 Power and energy demand by blowers for PAC supplied by oxygen.

Device	τ_c (d)	P (W)	E_{kWh} (kWh)
PAC	5	0.06	0.22
	15	0.07	0.25

5.4.2.4 Power Demand for Oxygen Generation

For PAC aerated with high purity oxygen additional power demand for oxygen generation in VPSA process must be considered. Considering 93% oxygen purity and $\rho_{O_2,20}$ is 1.33 kg m^{-3} , daily oxygen demand computed from the Equations (5.7) and (5.8) is 59 to 67 g d^{-1} , equivalent to 44 to 50 L d^{-1} .

Procedure for determination of power demand by VPSA system was widely described in Section 5.3.2.4 of this chapter. Therefore for PAC operating with pure oxygen, power demand for oxygen separation in VPSA is shown in Table 5.8. The overall power consumption by VPSA for PAC supplied by pure oxygen is up to 0.0004 W.

Table 5.8 Power and energy demand by oxygen generation in VPSA process for different diffused aeration systems.

Device	τ_c (d)	$R_{O_2,act}$ ($\text{m}^3 \text{ h}^{-1}$)	$V_{O_2,N}$ (Nm^3)	P_{O_2} (W)	E_{kWh} (kWh)
PAC	5	$1.8 \cdot 10^{-3}$	0.003	$3.2 \cdot 10^{-4}$	$1.2 \cdot 10^{-3}$
	15	$2.1 \cdot 10^{-3}$	0.004	$3.7 \cdot 10^{-4}$	$1.3 \cdot 10^{-3}$

5.4.3 Power Demand on Mixed Liquor Recirculation and Reinjection

Power demand on mixed liquor recirculation and reinjection depends upon: pump head necessary to recirculate mixed liquor through the PAC flow loop, which will need to balance headloss in the recirculation pipeline and the hydrojets; and a number of mixed liquor passages through PAC to achieve assessed level of oxygen saturation.

5.4.3.1 Head Loss in Piping System

The quantity of power required for recirculation and reinjecting of mixed liquor saturated with air/oxygen depends on the head loss in the pipeline and equipment in the oxidation ditch system. Therefore proposed design of the wastewater pipeline (Figure 5.2) of the minimum number of components and linear dimensions aims the decrease of the headloss. Detailed description of the ditch geometry and dimensions can be found in Paragraph 5.4.1 of the following section. The distance from the free surface of the wastewater to the pump centerline is 25.0 m, thus considering oxidation ditch depth of 4.0 m the pump is located 21.0 m below the bottom. PAC is positioned just 1.0 m above the pump centerline, thus at the distance of 20.0 m below the ditch bottom. Recirculation pipe lifts oxygen enriched mixed liquor at the level of mid-depth of the ditch, where the flow splits into two separate manifolds supplying the hydrojets, each having length of 10.0 m. The rationale behind the use of a long, vertical pipeline directing recirculated mixed liquor from the ditch to the external aeration unit is to induce optimal pressurized conditions for efficient saturation of wastewater with oxygen.

For proposed hydraulic design of the oxidation ditch aerated by PAC, the system head is computed as follows:

$$H_S = h_d - h_s \quad (5.26)$$

where H_S is system head, m, h_d is total discharge head, m, and h_s is total suction head, m.

The total discharge head consists of three components:

$$h_d = h_{sd} + h_{pd} + h_{fd} \quad (5.27)$$

where h_{sd} is discharge static head, h_{pd} is discharge surface pressure head and h_{fd} is discharge friction head.

The total suction head also consists of three separate heads, as follows:

$$h_s = h_{ss} + h_{ps} + h_{fs} \quad (5.28)$$

where h_{ss} is suction static head, h_{ps} is suction surface pressure head and h_{fs} is suction friction head.

Considering the fact, that oxidation ditch is a tank open to the atmosphere, discharge surface pressure head, h_{pd} and the suction surface pressure head h_{ps} are equal to atmospheric pressure plus the free surface quota. Moreover as the level of fluid in ditch is constant and thus relatively to the pump centerline static suction head h_{ss} and static discharge head h_{sd} are equal and of 25.0 m. According to that, the pump head will be equal to the sum of the discharge and suction friction heads.

For considered oxidation ditch pipeline layout, the friction heads, h_{fs} and h_{fd} will be determined as the total headloss, i.e. a sum of the major losses due to the friction during wastewater flow in the straight pipe sections and minor losses which are due to eddies occurring during water flow through the inlets, outlets, bends, and other pipe fittings.

Considering oxidation ditch layout (Figure 5.2) and from Bernoulli energy conservation equation we obtain:

$$\frac{p_1}{\rho g} + \frac{v_1^2}{2g} + z_1 = \frac{p_2}{\rho g} + \frac{v_2^2}{2g} + z_2 + h_{fd} + h_{fs} \quad (5.29)$$

where $p_1/\rho g$ and $p_2/\rho g$ term denote pressure heads on the suction and discharge side of the pump, respectively, $v_1^2/2g$ and $v_2^2/2g$ are the velocity heads, and z_1, z_2 are elevation heads.

Thus the system head, defined by Equation (5.26) will be equal to the sum of the frictional and local losses in the pipeline, as follows:

$$H_S = \sum (h_{f,d} + h_{l,d}) + \sum (h_{f,s} + h_{l,s}) \quad (5.30)$$

where $h_{f,d}, h_{f,s}$ are discharge and suction friction losses and $h_{l,d}, h_{l,s}$ are discharge and suction local losses, respectively.

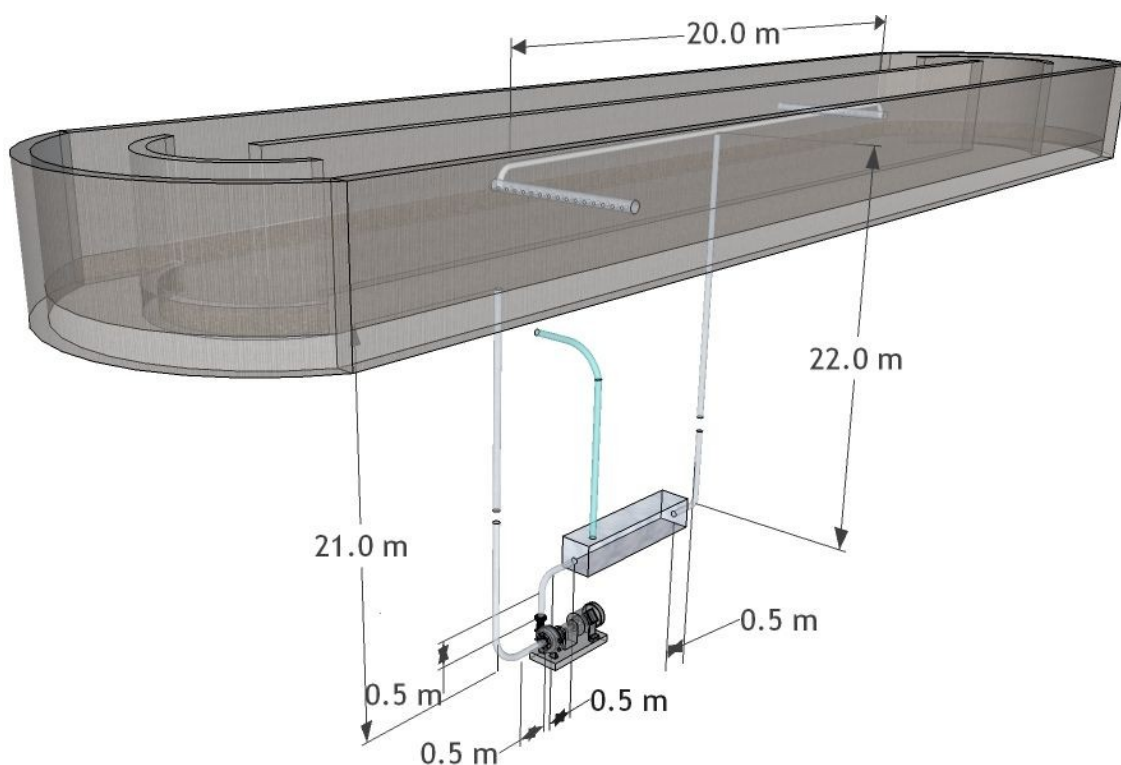


Figure 5.2 Schematic layout of the wastewater piping system in the oxidation ditch.

One of the methods to assess head loss in wastewater piping system is based on the computation of the head loss caused by water flow and multiplying the result by a constant factor, which is a function of the suspended sludge concentration in the mixed liquor. For oxidation ditches, having MLSS concentration in the range of $3000\text{--}5000\text{ mg L}^{-1}$, assumed multiplication factor is 2.

Due to the corrosive character of the mixed liquor, pipes are assumed to be made of galvanized iron having a roughness factor of 0.15 mm. Following the design guidelines for the wastewater tubing, an internal pipe diameter of 300 mm was assumed in the calculations. Mixed liquor flow in long conduits carries the risk of harmful deposits. Therefore, following general guidelines for wastewater pumping (Grundfos, 2002), velocity in vertical pipes should be maintained between $1.0\text{--}3.0\text{ m s}^{-1}$. In this work, velocity of 1.5 m s^{-1} was assumed in the piping system computations.

Friction losses

Following oxidation ditch hydraulic layout (Figure 5.2) the pipeline system considered in the suction friction headloss assessment consists of the following sections of the straight conduits: 21.0 m (ditch bottom - elbow distance); and 0.5 m (elbow - pump). Friction losses included in discharge head computing will be assessed for the pipes of the following

length: 0.5 m (pump-elbow); 0.5 m (elbow-PAC); 0.5 m (PAC-elbow); 22.0 m (elbow-ditch); 10.0 m (split-flow into two parallel branches supplying the hydrojets).

The major headloss is computed from Darcy-Weisbach formula for pressure loss expressed as:

$$\Delta p = f \frac{L}{D} \cdot \frac{\rho v^2}{2g} \quad (5.31)$$

where Δp is pressure loss, v denotes water velocity in the pipe and ρ is the density.

To express Darcy-Weisbach equation as headloss Equation (5.20) can be rewritten as:

$$h_f = f \frac{L}{D} \cdot \frac{v^2}{2g} \quad (5.32)$$

The Darcy's friction factor f is obtained from the Moody diagram. For the laminar flow conditions, such that $Re \leq 2300$, f depends only on Reynolds number and can be obtained from the following formula:

$$f = \frac{64}{Re} \quad (5.33)$$

For the turbulent flow, and thus for $Re > 4000$ the value of f depends on both, Reynolds number and the pipe roughness. For such conditions, the friction factor is computed from the Colebrook equation of the following form:

$$\frac{1}{\sqrt{f}} = -2.0 \log \left(\frac{e}{3.7D} + \frac{2.51}{Re\sqrt{f}} \right) \quad (5.34)$$

where e is the absolute roughness of the pipe, m.

After rearrangement we obtain:

$$f = \frac{1.325}{\left[\ln \left(\frac{e}{3.7D} + \frac{5.74}{Re^{0.9}} \right) \right]^2} \quad (5.35)$$

Reynolds number is calculated from the following formula:

$$Re = \frac{vD}{\nu} = \frac{vD\rho}{\mu} \quad (5.36)$$

where ν and μ are kinematic and dynamic viscosity of water and ρ is its density.

Considering: water density of 998.2 kg m^{-3} , dynamic viscosity of $1.0 \cdot 10^{-3} \text{ Pa s}$, velocity of the water flow of 1.5 m s^{-1} and pipe diameter of 0.3 m , Reynolds number is turbulent and equals approximately $5.0 \cdot 10^5$. Friction factor f assessed from the Equation (5.16) for the pipe roughness if $0.15 \cdot 10^{-3} \text{ m}$ is 0.018 .

For the pipeline system from ditch to recirculation pump having total length of 21.5 m , assessed total major loss on the suction side of the pump, $h_{f,s}$ is 0.15 m .

Major loss of discharge pipeline is a sum of frictional head loss in straight pipeline from pump to the tee junction, i.e. point of branching, having length of 23.5 m and in 10.0 m branch pipes connecting recirculation pipe with hydrojets.

In first case, i.e. considering the distance from the pump outlet to the pipe branching, the same flow conditions as in suction pipeline were assumed, for which computed frictional loss is 0.16 m .

Considering wastewater flow rate Q in the recirculation pipe which splits into a flow of Q_1 in the pipe connecting one hydrojet and Q_2 in pipe connecting second hydrojet, we assumed that:

$$Q_1 = Q_2 = \frac{Q}{2} \quad (5.37)$$

Considering branch pipe diameter of 0.25 m , velocity is 1.1 m s^{-1} . For these data, Reynolds number is turbulent and equals approximately $3.0 \cdot 10^5$, therefore friction factor f is 0.019 , yielding friction loss of 0.05 m .

The sum of major discharge losses from the pump to the hydrojets manifold is 0.21 m .

Local losses

Minor headloss in the pipeline caused by presence of the fittings and other flow obstruction devices is computed from the Darcy's formula of the following form:

$$h_l = k_l \frac{v^2}{2g} \quad (5.38)$$

where h_l is a local loss in m , and k_l is a local loss coefficient.

The k_l value is empirically determined and characteristic for the particular fitting. The values of local head loss coefficients of the devices and fittings in-series can be summed to determine the total k_l for the considered piping system. Therefore we have:

$$h_l = \frac{v^2}{2g} \cdot \sum k_l \quad (5.39)$$

Following the oxidation ditch hydraulic layout (Figure 5.2) the pipeline system considered in the suction local headloss determination contains flush entrance from the ditch to the pipe and elbow. The assumed values of k_l for entrance to a pipe and flanged 90° elbow are 0.5 and 0.3, respectively.

Therefore, the total local loss coefficient on the suction side of the pump is 0.8 yielding the total local suction loss $h_{l,s}$ of 0.09 m.

Local losses included in discharge head computation for the pipeline from pump to hydrojets will be assessed for gate valve, two elbows, tee, entrance and exit from PAC and entrance to the hydrojets' manifold. The value of k_l for gate valve and flanged 90° elbow is 0.3; for flanged tee splitting the flow k_l is 0.2. Considering geometry of the fitting connecting the pipe with hydrojets manifold, local loss coefficient was assumed equal to long radius 90° elbow, and thus 0.2.

Entrance to PAC is characterized by sudden enlargement of the cross-section area, for which empirical value of k_l is determined also from momentum, continuity and Bernoulli's equations, yielding the following:

$$k_l = \left(1 - \frac{A_1}{A_2}\right)^2 \quad (5.40)$$

where A_1 and A_2 are pipe and expansion cross-section areas.

Considering pipe of diameter 0.3 m and PAC having cross-section area of 0.64 m², k_l is 0.8. The value of k_l for the cases of sudden contraction, i.e. discharge from PAC to a pipe has to be derived. Here we are considering flow discharge from the larger flow area to the pipe, which is characterized by formation of contracted jet just inside the pipe (vena contracta), followed by headloss due to sudden expansion of the minimized flow area downstream contraction section until filling the whole pipe area. Applying continuity and Bernoulli's equation with headloss for the following case, the minor headloss will be:

$$h_l = \left(\frac{A_1}{A} - 1\right)^2 \frac{v_1^2}{2g} \quad (5.41)$$

where A is the contraction cross-section area and v_1 correspond to the velocity of flow in the discharge tube of the area A_1 .

Comparing this equation with (5.39) yields

$$k_l = \left(\frac{A_1}{A} - 1 \right)^2 \quad (5.42)$$

To determine k_l caused by vena contracta, it can be assumed, that the contraction is about 40% of the flow area in the pipe (Chadwick and Morfett, 1998). Therefore considering the region where head loss occurs, i.e. section with contraction-expansion having the areas of $0.6A_1$ and A_1 respectively, k_l obtained from Equation is 0.44. Therefore, headloss on PAC is 0.14 m.

Each entrance to the hydrojet manifold is characterized with ca. 20% expansion of the flow cross-section area, and thus k_l determined from Equation (5.40) is 0.03.

The values of k_l for assessed for particular fittings in considered oxidation ditch system are summarized in Table 5.9. The sum of the local losses, h_l in the pipeline system from pump to hydrojet manifold is 0.30 m.

Table 5.9 Local loss coefficients for the selected fittings.

Fitting / place in the oxidation ditch system	k_l
Exit ditch	0.50
Gate valve	0.30
Entrance PAC	0.79
Exit Pac	0.44
Elbow	0.30
Long radius elbow	0.20
Tee junction	0.20
Entrance - hydrojet manifold	0.03

5.4.3.2 Head Loss in Hydrojets

Power demand by recirculation pump, assessed for the operation of external aeration unit must be increased by a quantity necessary for hydrojets operation, i.e. reinjection of the oxygen enriched wastewater with the velocity sufficient to force circulation of the fluid throughout the ditch. Hydrojets operation is accompanied by headloss during flow discharge through the single or many slot nozzles, which must be included in assessment of

the total discharge head by recirculation pump. Computation of local losses on hydrojet aerator was made for two different hydrojets configurations: multi-slot injector (KLa Systems, 2007) and proposed single slot injector.

Multi-slot Injector

Each hydrojet aerator consists of the manifold extended across the ditch channel having slot nozzles distributed throughout the pipe length (KLa Systems, 2007). Schematic design of the hydrojet device is shown in Figure 5.3. The cross-section area of the manifold A_2 is 20% larger than of the recirculation tubing, thus equals 0.058 m^2 . The diameter of jet manifold is 0.27 m . Considering width of the middle wall of 0.6 m , separating ditch volume into two channels, the length of the hydrojet manifold is 7.2 m .

Velocity of the flow through the hydrojet manifold is assessed from the continuity equation, as follows:

$$Q_1 = Q_2 \Leftrightarrow A_1 \cdot v_1 = A_2 \cdot v_2 \tag{5.43}$$

where Q_1 is the mixed liquor flow rate in the recirculation branch pipe, Q_2 is the flow rate in the hydrojet manifold, A_1 is the cross-section area of the mixed liquor recirculation pipe supplying the hydrojets and A_1 is 0.05 m^2 , v_1 is the assessed in the pump head computation velocity of the flow in branch pipeline equal 1.1 m s^{-1} , and v_2 is velocity of the flow in the hydrojet manifold.

Considering all data, v_2 in hydrojet manifold is 0.92 m s^{-1} and the flow rate Q_1 and Q_2 is $0.05 \text{ m}^3 \text{ s}^{-1}$.

The friction loss for hydrojet manifold must be considered in determination of the total discharge friction loss. For the Reynolds number of $2.5 \cdot 10^5$, friction factor f assessed from Equation (5.35) is 0.019 . Therefore considering v_2 of 0.92 m s^{-1} , L of 7.2 m and D of 0.27 m , h_f computed from Equation (5.32) is 0.02 m .

To ensure uniform flow distribution from the slot injector orifices, it was assumed, that:

$$A_3 = \frac{A_2}{2} \tag{5.44}$$

where A_3 is total area of the flux from the slot jets.

Therefore, for the assumed data, computed A_3 is 0.029 m^2 .

If we assume, that the hydrojet aerator consists of 10 injectors, therefore the area of each nozzle A_n will be 0.003 m^2 and the approximate dimensions of each slot are $0.03 \times 0.10 \text{ m}$. As the flow in the manifold splits into 10 jet streams, therefore the flow rate from each nozzle is equivalent to $Q_2/10$, and thus $0.005 \text{ m}^3 \text{ s}^{-1}$. Velocity of the reinjected fluid into the ditch is computed from the continuity equation yielding:

$$v_3 = \frac{A_2 \cdot v_2}{A_n} \quad (5.45)$$

For all assumed data, computed velocity of the flow re-injected through the slot nozzles into the ditch is 1.8 m s^{-1} . Considering results obtained from the CFD simulations (Chapter 4 Section 4.6.1.), velocity of the fluid reinjected by slot jets of 1.8 m s^{-1} is sufficient to maintain mixed liquor circulation throughout the ditch.

Wastewater flow through the multi-slot injector is accompanied by pressure drop in the orifices. For convenience, discharge through long radius nozzle was assumed in the local loss computations. Here, the flow rate is computed from the following form:

$$Q_3 = A_3 v_3 = C \cdot A_n \sqrt{2gh_n} \quad (5.46)$$

where C is flow coefficient and h_n is local loss on the nozzle.

After rearrangement we obtain:

$$h_n = \frac{1}{2g} \left(\frac{Q_3}{CA_n} \right)^2 \quad (5.47)$$

Value of flow coefficient C is computed as follows:

$$C = \frac{C_d}{\sqrt{1 - \left(\frac{d_{vc}}{d_n} \right)^4}} \quad (5.48)$$

where C_d is discharge coefficient, d_{vc} is a diameter of contracted jet (vena contracta), and d_n is nozzle diameter.

Designed slot injector's outlet has approximately a rectangular shape, therefore hydraulic diameter d_n of nozzle, defined as ratio of cross-section area of nozzle to its wetted perimeter was computed:

$$d_n = \frac{4bh}{2b + 2h} \quad (5.49)$$

where b and h denote width and height of the rectangular nozzle cross-section.

For b equal 0.03 m and h of 0.10 m, hydraulic diameter of each nozzle d_n is 0.045 m. Considering 40% contraction of the jet area discharged through nozzle, the diameter of vena contracta, d_{vc} is 0.035 m.

Coefficient of discharge can be calculated using standards like ISO 5167-1:2003 “Measurement of fluid flow by means of pressure differential devices, Part 1: Orifice plates, nozzles, and Venturi tubes inserted in circular cross-section conduits running full” or other appropriate ASME (American Society of Mechanical Engineers) standards.

For long radius nozzles, C_d is calculated using the following:

$$C_d = 0.9965 - 0.00653 \sqrt{\frac{10^6 \left(\frac{d_{vc}}{d_n}\right)}{Re_D}} \quad (5.50)$$

where Re_D is Reynolds number computed for bigger diameter, i.e. d_n .

Considering d_n of 0.045 m, v_3 of 1.8 m s⁻¹, ρ and μ of water, Re_D is 0.8×10^5 . Therefore C_d assessed from Equation (5.50) is 0.976, for which C , computed from Equation (5.48) is 1.221. The local loss computed for multi-slot injector due to flow discharge through nozzle, defined by Equation (5.47) is 0.11 m.

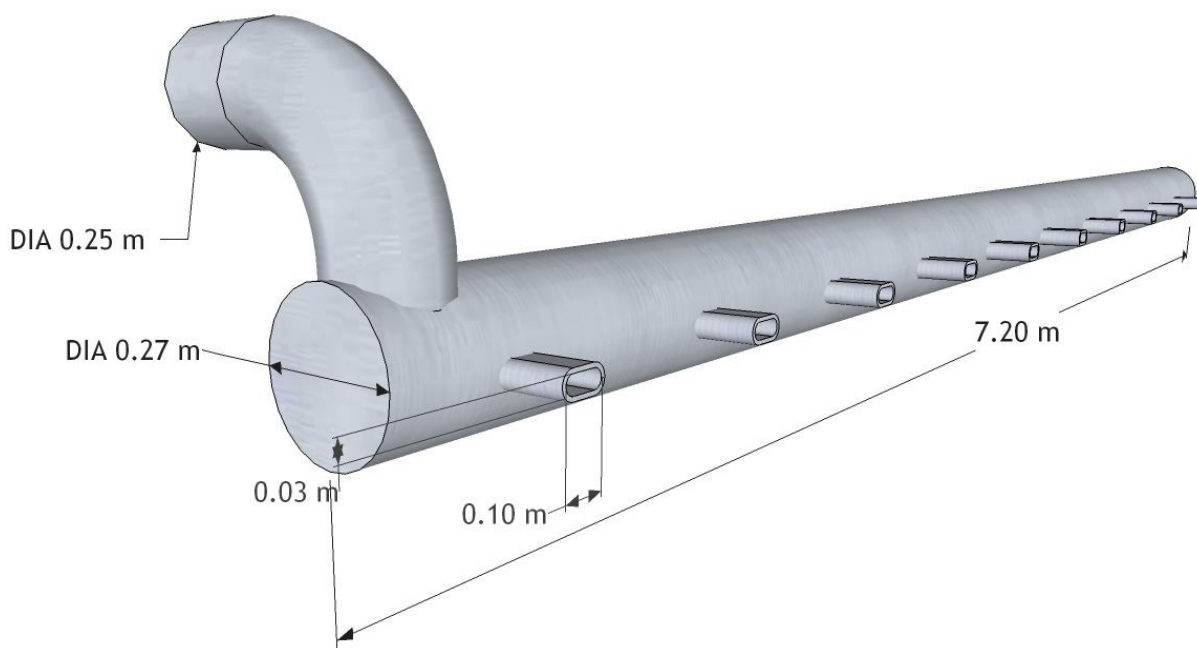


Figure 5.3 Schematic design of the hydrojet device with multiple slot injectors.

Slot Injector

Proposed hydrojet aerator consists of the manifold extended across the ditch channel having a single slot nozzle extended throughout the pipe length. Schematic design of the hydrojet device is shown in Figure 5.4. As in the previous multi-jet design, the cross-section area of the manifold, A_2 , is 20% larger than of the recirculation tubing and equals 0.058 m^2 . The diameter of jet manifold is 0.27 m and the length of the hydrojet manifold is 7.2 m . Considering velocity of 0.92 m s^{-1} and the Reynolds number of $2.5 \cdot 10^5$, friction factor f assessed from the Equation (5.35) is 0.019 . Therefore friction loss for hydrojet manifold, h_f computed from Equation (5.32) is 0.02 m .

The dimensions of the slot aperture of $0.01 \times 7.00 \text{ m}$ guarantee uniform flow distribution throughout the jet. The area of the surface flux from the slot jet aperture A_3 is 0.07 m^2 . For the parameters of the flow through the hydrojet manifold, velocity of the wastewater reinjected by slot jet, v_3 , assessed from the Equation (5.45) is 0.76 m s^{-1} . Considering results obtained from the CFD simulations (Chapter 4 Section 4.6.1.), velocity of the fluid reinjected by a single slot injector is sufficient to maintain mixed liquor circulation throughout the ditch.

Wastewater flow through slot injector is accompanied by local loss due to contraction in the nozzle discharging of the jet into the ditch volume.

The same procedure as in case of multi-slot injector will be used to determine hydraulic diameters of: nozzle, d_n and vena contracta, d_{vc} . Taking into account h of 0.01 m, l of 7.0 m, and $A_3 = A_n = 0.07 \text{ m}^2$, computed hydraulic diameter d_h is 0.020 m and d_{vc} is 0.015 m. Considering d_n of 0.020 m, v_3 of 0.75 m s^{-1} , ρ and μ of water, Re_D is 1.5×10^5 . Therefore C_d assessed from Equation (5.50) is 0.950, for which flow coefficient C , computed from (5.48) is 1.187. The local loss computed for multi-slot injector due to flow discharge through nozzle and defined by Equation (5.47) is 0.02 m.

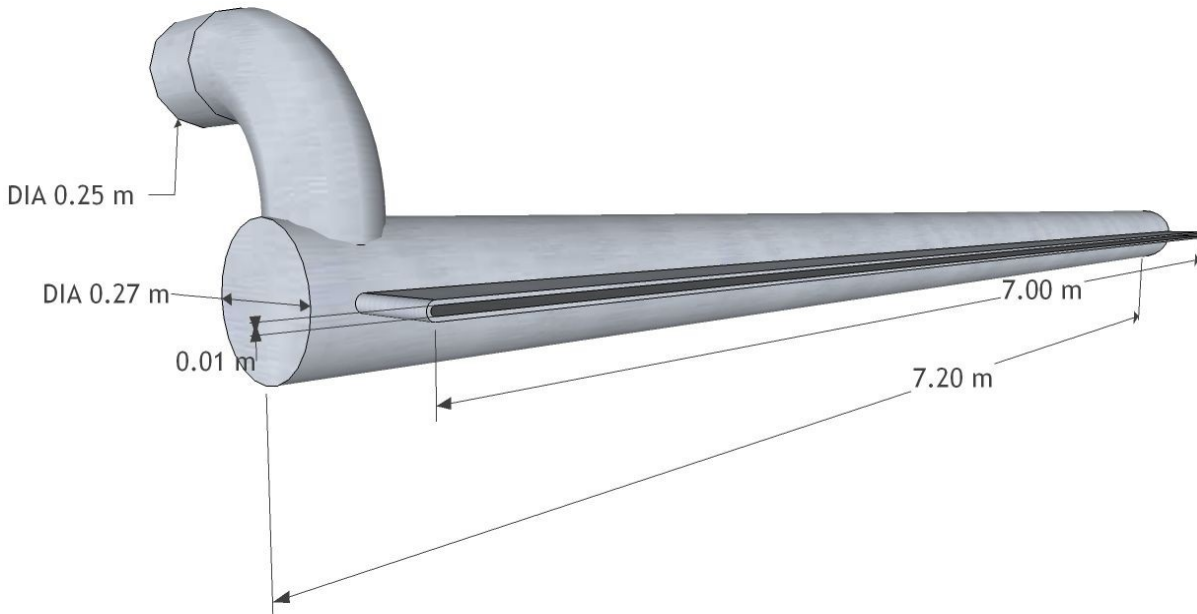


Figure 5.4 Schematic design of the hydrojet device with single slot injector.

5.4.3.3 Pump Head

Friction and local losses in the oxidation ditch piping system and the system head determined for two configurations of the hydrojet device, i.e. multi- and single- slot injector are presented in Table 5.10. The system head, H_S , computed from Equation (5.30) is a sum of frictional and local losses on both, suction and discharge sides of recirculation pump. Computation of H_S was based on determination of frictional and local losses due to water flow through the piping system. Therefore to assess pump head necessary for wastewater recirculation, differences in density and viscosity must be accounted, and conversion of data obtained for clean water is recommended. The conversion is based on multiplication of the headloss computed for water by a constant factor, which depends on the concentration of MLSS in wastewater being pumped. For oxidation ditch systems, having MLSS content of $3.0\text{-}5.0 \text{ g L}^{-1}$, assumed multiplication factor is 2. And thus, the

pump heads obtained for both hydrojets device configurations account for 1.70 and 1.52 m, respectively.

When comparing the values of local head loss on hydrojets it is clear, that configuration with multi-slot injector requires higher pump head by 0.2 m than the single slot, resulting in higher power demand for wastewater recirculation. This work aims to select the most energy efficient solutions and from this reason further computations of power and energy demand will focus on proposed energy-minded configuration- single slot hydrojet.

Table 5.10 Head loss and pump head in proposed mixed liquor recirculation and reinjection system.

		Multi-slot Injector	Slot Injector
Suction friction loss, $h_{f,s}$ (m)		0.15	
Suction local loss, $h_{l,s}$ (m)		0.09	
Suction friction h_{fS} (m)		0.24	
Discharge friction loss, $h_{f,d}$ (m)		0.23	
Discharge local loss, $h_{l,d}$ (m)		0.38	0.29
Discharge friction head, h_{fd} (m)		0.61	0.52
Total system head (m)	water	0.85	0.76
$H_S = h_{fS} + h_{fd}$	wastewater	1.70	1.52

5.4.3.4 Power Demand for Wastewater Pumping through PAC

Design considerations and performance of PAC was widely described in Chapter 2. CFD simulations of PAC complemented by reaeration tests considered aeration process based on water saturation with high purity oxygen, what resulted in distinctly higher oxygen transfer rates and aeration efficiencies than the respective standard process parameters of current best available technologies. Several preliminary trial experiments were also conducted on PAC aerated by air. It was found that process of reoxygenation by air is inhibited by increase of partial pressure of nitrogen present in compressed air. As the result, the process of saturation with oxygen took place only during first few passages of water through the PAC and stopped, as the chamber was being flushed out of oxygen. At this point, the studies on aeration were interrupted and air was substituted with pure oxygen.

Although the results revealed that the device is not suitable for air systems, for comparison purposes, such scenario was considered in following assessment of power demand for wastewater pumping.

Considering aeration system supplied by atmospheric air, solubility of oxygen in water in 20 °C and at the pressure of 2 bars is around 18 mg L⁻¹. Considering daily BOD_5 load of 54 g, the BOD_5 concentration depends on the wastewater flow rate per capita, q_p , as follows:

$$[BOD_5] = \frac{BOD_5}{q_p} \quad (5.51)$$

where $[BOD_5]$ is daily BOD_5 concentration in g m⁻³, and q_p is daily flow rate per capita, in m³ d⁻¹.

Typically, the values of q_p are in the range from 0.15 to 0.25 m³ d⁻¹ and thus $[BOD_5]$ ranges from 216 to 360 g m⁻³.

Similarly, the concentration of oxygen consumption, $[R_{O_2}]$, can be written as:

$$[R_{O_2}] = \frac{R_{O_2}}{q_p} \quad (5.52)$$

where $[R_{O_2}]$ is the concentration of daily oxygen consumption, g m⁻³, and daily R_{O_2} ranges from 55 to 62 gO₂ per capita.

According with the above, for assumed ranges of R_{O_2} and q_p the concentration $[R_{O_2}]$ ranges from 220 to 413 gO₂ m⁻³.

The number of times the wastewater is pumped through the PAC, designated as np , is given by the following formula:

$$np = \frac{[R_{O_2}]}{18} = \frac{R_{O_2}}{18 \cdot q_p} \quad (5.53)$$

Considering the percentage of oxygen in air that is 23.2%, the air requirement R_{Air} corresponding to oxygen demand computed from Equation (5.5) is from 237 to 267 g per day. According to that, wastewater has to pass through the PAC 53 to 99 times.

For the assumed flow rate q_p of 0.25 m³ d⁻¹, np is in the range of 53 to 59.

Therefore, for computed in Paragraph 5.4.3.3 elevation head given by the pump, the power necessary to pump wastewater with the flow rate of $2.9 \cdot 10^{-6} \text{ m}^3 \text{ s}^{-1}$, is computed from the following:

$$P = \frac{\rho g H_s q_p}{\eta} \quad (5.54)$$

where η is pump efficiency equal 0.8 and ρ is wastewater density assumed 1000 kg m^{-3} and H_s is 1.52 m.

Accordingly with the above, the power demand by pump is 0.05 W. Considering 53 to 59 passages, the power demand will be in the range from 2.84 to 3.19 W.

For the daily flow rate per capita of $0.15 \text{ m}^3 \text{ d}^{-1}$, and thus $1.7 \cdot 10^{-6} \text{ m}^3 \text{ s}^{-1}$, the power demand by pump wastewater drops to 0.03 W, however n_p in the range of 88 to 89 yields identical power expenditure of 2.85 to 3.17 W.

Considering PAC system supplied by pure oxygen (93% of purity), its solubility in water at $20 \text{ }^\circ\text{C}$ and at the pressure of 2 bars is around 18.0 mg L^{-1} . In such conditions and for daily R_{O_2} from 59 to 67 gO_2 per capita, n_p ranges from $3.2/q_p$ to $3.7/q_p$. For q_p of $0.15 \text{ m}^3 \text{ d}^{-1}$, wastewater have to pass through the PAC 22 to 25 times to achieve assumed level of oxygen saturation, while for q_p of $0.25 \text{ m}^3 \text{ d}^{-1}$ - only 12 to 15 times.

Power demand by pump assessed from (5.54) is the same as in case of air feed system, thus depending on the flow rate per capita, accounts for 0.03 W for $0.15 \text{ m}^3 \text{ d}^{-1}$ and 0.05 W for $0.25 \text{ m}^3 \text{ d}^{-1}$, respectively. Considering number of passages through PAC, power by pump for $0.15 \text{ m}^3 \text{ d}^{-1}$ is 0.71 to 0.81 W and for $0.25 \text{ m}^3 \text{ d}^{-1}$ - 0.70 to 0.81 W.

Computed values of power in W and energy demand in kWh by pump depending on number of passages and daily flow rates per capita are shown in Table 5.11. When comparing these values it is clear, that use of pure oxygen in PAC benefits in reduction of energy demand by recirculation pump unit by up to 75%.

Table 5.11 Power and energy demand by recirculation pump for PAC supplied by air and pure oxygen.

Oxygen source	q_p ($\text{m}^3 \text{d}^{-1}$)	np	P (W)	E_{kWh} (kWh)
Air	0.25/0.15	53/88	2.85/2.84	10.3/10.2
		59/99	3.17/3.19	11.4/11.5
Pure oxygen	0.25/0.15	13/22	0.70/0.71	2.52/2.56
		15/25	0.81	2.90

5.4.4 Energy Analysis

The overall energy requirement by aeration systems commonly used in oxidation ditches, namely diffused air system (membrane diffusers) and surface aerators, as well as by proposed PAC system supplied by pure oxygen was summarized in Table 5.12. For comparison, the data obtained for membrane diffusers supplied by pure oxygen were also included in the table.

When comparing the data obtained for different aeration systems it is clear, that even in situation requiring use of blower in VPSA process, aeration with PAC allows for 96-99% energy savings in comparison with surface aerators and 93% in case of diffused air systems. At the same time, energy demand for aeration with PAC constitutes 30-33% of the quantity required by membrane diffusers supplied by pure oxygen.

Table 5.12 Energy expenditure in oxidation ditch system aerated with PAC.

Process	Equipment	Oxygen source	Energy expenditure	Energy savings (PAC)
			(kWh)	(%)
Surface aeration	Brush rotor/low speed aerator	Air	5.50 - 18.60	96 - 99
	Blower	Air	3.29 - 3.71	93
Diffused aeration	Blower	Oxygen	0.66 - 0.74	67
	VPSA	Oxygen	3.9×10^{-3} - 4.4×10^{-3}	
Aeration in PAC	Blower	Oxygen	0.22 - 0.25	-
	VPSA	Oxygen	1.2×10^{-3} - 1.3×10^{-3}	

5.5 Conclusions

In the following chapter, energy demand by aeration systems commonly used in oxidation ditches was assessed. It was concluded, that the most energy efficient aeration scenario includes porous diffusers supplied by pure oxygen. Nonetheless, to assess overall energy expenditure in such systems additional computations of power expenditure for air piping and for mixing by e.g. vertical shaft impellers must be accounted for.

The overall energy expenditure for aeration and mixing in proposed oxidation ditch system aerated with hydrojets was assessed. Introduction of the external aeration unit, Pressurized Aeration Chamber revealed to be a promising solution providing distinct energy savings through reduction of power demand by blower in both, atmospheric air and pure oxygen aeration scenario, and oxygen generation in VPSA process, when comparing with porous diffusers. It was found, that aeration with PAC accounts for up to 4% of the total energy required by surface aeration, up to 7% by current BAT devices- membrane diffusers supplied by air and up to 33%- by membrane diffusers supplied by pure oxygen. Furthermore, for featured activated sludge system, energy demand on mixed liquor pumping and reinjection was determined, considering two different hydrojets' geometries. On the base of the required height of the elevation head, multi-slot injector configuration

was rejected due to generation of the higher local headloss in the system. PAC unit supplied by air and cooperating with the single slot injectors requires 1.5 m of the pump head, yielding energy expenditure of 10.2 to 11.5 kWh per capita for mixed liquor recirculation, saturation with oxygen and reinjection. Substitution of the air by pure oxygen allows reduction of the operation cost by pumping unit for 75%, yielding energy demand of 2.5 to 2.9 kWh per capita.

From the above it can be concluded, that proposed aeration system consisting of PAC and slot injector seems to be promising solution allowing for distinct power demand cut and thus energy savings, even when comparing with most efficient state-of-the-art membrane diffusers.

6 Final Remarks

6.1 Introduction

The aim of this work was to develop efficient and targeted energy saving wastewater aeration scenario, applicable in oxidation ditch process. This challenge has been undertaken by implementation of hydrodynamics modelling with CFD codes into activated sludge systems design process. Proposed hydraulic configuration of the oxidation ditch aerated with external pressurized device, PAC, and agitated by slot injectors, allows accomplishing the objectives of integrated water pollution prevention control and standards set in Urban Waste Water Treatment Directive, with sustainable strategy for centralized wastewater treatment.

The following chapter is divided into two sections: the first one, section 6.2, summarizes conclusions of the present dissertation, while section 6.3 provides the suggestions for the future work.

6.2 General Conclusions

In Chapter 2, the significance and principles of the aeration process in wastewater treatment were given, followed by historical review on development of aeration techniques, current technical status, and the ongoing research paths in the aeration sector. Typical design features, applications and operation of commonly used diffused air systems (several types of nonporous and porous diffusers, jet- and U-tube aerators),

mechanical devices (horizontal rotors, low- and high-speed surface aerators) and hybrid systems (sparge turbine and aspirating aerators) were comprehensively described. For selected types of the devices within presented aeration systems, typical ranges of the process parameters characterizing oxygen transfer and aeration efficiencies, assessed in clean water test method, were also summarized. It was concluded, that present BAT-perforated membrane panel diffusers, have the maximal *SOTE* up to 43%, but are also characterized by high O&M costs. Therefore, the main goal of the Chapter 2 has been focused on the development of the technology overcoming efficiency limitations of the porous diffusers.

In the following Chapter 2, the computational and experimental studies concerning development of an external pressurized aeration unit - PAC, had been described. Aeration in several configurations of PAC was simulated with ANSYS Fluent CFD code, aiming representation of the main trends in oxygen concentration distribution within all PAC layouts and pointing out the most robust geometry in terms of oxygen transfer, which ensures higher level of effluent saturation with oxygen. The most successful design of PAC, a rectangular tank equipped with system of baffles fixed to the bottom, having single gas (oxygen/air) and water inlets and one outlet, was constructed in lab-scale for reaeration experiments, to determine oxygen transfer rate parameters in accordance with ASCE standard clean water testing protocols. From the results of steady state clean water test run in PAC it was found, that with increase of the operating pressure from 0.5 to 1.5 bar, achieved *SOTE* ranged from 120 to 200%, yielding three to five times higher values than the current BAT, i.e. membrane diffusers. Moreover, considering power expenditure on oxygen generation, the values of *SAE* up to $8.0 \text{ kg O}_2 \text{ kW}^{-1} \text{ h}^{-1}$ were higher than commonly used porous diffusers, including membrane panels.

Steady state experiments, described in Chapter 2 aimed also validation of the results obtained from the 3D CFD simulations of PAC. It was concluded that simulated operating conditions complied with process conditions of the clean water test, run at oxygen pressure of 0.5 bar. The average value of *AE* obtained from the multiple reaeration experiments was $4.5 \text{ kgO}_2 \text{ kW}^{-1} \text{ h}^{-1}$, which is in good agreement with values obtained from the CFD simulations.

In Chapter 2, studies concerning applicability of a lab-scale 2D bubble column reactor (BCR), as the aeration device had been given. The features of the experimental system, packed bed column characteristics, its performance and common applications in water-wastewater technology had been widely described. The same experimental procedure of

ASCE steady state reaeration test used for PAC evaluation was applied to determine the impact of the operating conditions on hydrodynamics and aeration efficiency of the BCR. It was found, that gas hold-up has strong impact on aeration process performance, and can be used as a design parameter to set optimal operating conditions, i.e. air and water velocity ranges for the maximal oxygenation efficiency. The highest ranges of gas hold-up of 80% were observed for transition from churn to annular flow regime and overlapped with the maxima of the transfer rate parameters, while in conditions of dispersed flow with air content of 13%, oxygen mass transfer was negligible. The average values of *SOTE* obtained from the experiments were up to 93%, more than twice higher than the BAT devices, and may reach up to 150%. For BCR, the values of *SAE*, depend in greater extent from the power demand by blower and thus operating air flow rates. The maximal *SAE* obtained for the peak hold-up was $25 \text{ kgO}_2 \text{ kW}^{-1} \text{ h}^{-1}$ and thus three times higher than the corresponding values obtained for PAC. For the average operating conditions and gas hold-up of 50%, obtained *SAE* values were in the range of $5\text{-}9 \text{ kgO}_2 \text{ kW}^{-1} \text{ h}^{-1}$ corresponding to PAC and the upper range of BAT devices. Nonetheless, adaptation of the BCR system to wastewater aeration in oxidation ditch imposes sharp limits, especially on the bubble regime involved. As the efficient aeration depends on the long contact times and the extended contact area between activated sludge flocs and air bubbles, thus the oxygenated stream should contain fine bubbles. Therefore instead of operating in the air-water velocity ranges characteristic for annular flow, yielding the highest *SOTE* and *SAE*, heterogeneous churn flow with the efficiencies corresponding to wide range of porous diffusers seems to be reasonable solution. In addition to that, aerated effluent discharged from BCR should have a momentum sufficient for at least local mixing and mass transfer between the fluid layers in the aeration tank. While PAC operation combines efficient aeration with mixing due to energy of the discharged fluid plume, low pressure conditions in BCR may require implementation of additional momentum sources, such as pumps and flow boosters, which increase power expenditure of the whole system. Furthermore, application of BCR in activated sludge systems is limited by clogging of the column packing increasing pressure drop in the systems and requiring frequent maintenance and cleaning.

Although the oxidation ditch process is commonly used worldwide, its flow regime is still scarcely studied. A literature review on the process history, operating principles and the performance was presented in Chapter 3. Several works on experimental methods used in these systems to assess flow behaviour were also comprehensively reviewed. One of the main goals of this dissertation was to prove the impact of the hydrodynamics on the treatment performance in the oxidation ditch process. Chapter 3 covers the experimental approach to achieve this goal through determination of velocity, oxygen, nutrients and

solids concentration profiles along the channels of a pilot-scale tubular piston flow reactor with recirculation (PFRR) and a full-scale oxidation ditch at Areosa WWTP (Viana do Castelo).

It was concluded, that regardless of the horizontal velocity within the studied PFRR ditch, linearity of DO , nutrient and solids profiles and the constant concentrations within the reactor and at the outflow were as for the complete mix system, characteristic for the flow conditions in the CSTR. PFRR ditch behaviour was additionally evaluated in Residence Time Distribution experiments using pulse and step tracer techniques. The shapes of tracer concentration curves resembled the output profiles characteristic for the ideal CSTR vessel. Certain features of the RTD curves, namely presence of the early peaks and long tail were also detected, suggesting possibility of flow channeling, internal recirculation and stagnant fluid regions occurrence, having adverse effects on the reactor performance. Nonetheless, exact description of the reactor behaviour from the concentration curves could not be made due to the long sensor response time intervals of 20 s and the placement of the measurement probe within the reactor. Furthermore, 14-day long PFRR start-up time revealed to be insufficient to achieve pseudo-steady state in terms of activated sludge biokinetic stability, and thus wastewater treatment performance was not conclusively evaluated.

In case of the full scale oxidation ditch aerated with horizontal rotors, distribution of the DO concentration along the straight channel section was almost constant. When observing vertical profiles in these sections it was clear, that wastewater temperature has a large influence on the oxygen mass transfer. At elevated temperatures above 27 °C only surface wastewater layers were aerated, and steep oxygen stratification leading to formation of the extended oxygen deficit zone occurred. Decrease of the temperature to 20 °C, yielded almost constant DO content measured at different depths of the ditch. At the same time in ditch bend, dynamic changes in oxygen patterns were caused by dynamic mixing of fluid layers allowing oxygen transfer towards the ditch bottom independently on the wastewater temperature.

The concentration profiles of COD , $NH_4 - N$, $NO_3 - N$, $PO_4 - P$ and TSS along both, straight and curved channel sections were constant. As far as the oxygen mass transfer in the oxidation ditch depends on the local hydrodynamics, linearity of nutrients profiles should be associated with much slower biochemical reactions occurring in the activated sludge.

Wastewaters treatment efficiency in full scale oxidation ditch was also assessed in Chapter 3. When comparing *DO* profiles against the nutrients it was observed, that in high temperatures effluent did not comply with the quality standards due to biokinetics slowdown, yielding high ammonia and phosphates levels. Therefore it can be concluded, that efficiency of biological reactor performance, namely intensity of biodegradation, nitrification, denitrification and *P* uptake and bioaccumulation depends on the *DO* levels within the ditch, and thus indirectly relies on the system hydrodynamics.

In Chapter 4 current trends in engineering design of the activated sludge systems and potential advantages of the use of CFD modelling in wastewater sector were extensively discussed. This chapter covers computational approach to assess the hydrodynamics of the oxidation ditches through CFD simulations, used as a powerful design and diagnostic tool. The showcase considered in the CFD studies was an oxidation ditch aerated with external PAC unit, supplying oxygenated wastewater to the slot jet aerators - hydrojets, comprising functions of aerator and mixer. One of the objectives of the CFD studies was to evaluate performance of several configurations of slot jets simulated with different turbulence models and to assess their impact on the ditch hydrodynamics and energy expenditure for mixing. It was proven, that regardless of the hydrojets placement, the same overall distribution of the flow patterns was obtained with RANS and URANS, where the hydrojets created an average flow with great stratification inside the volume of the ditch, characterized by poor vertical transport. In LES, the presence of eddies changed the hydrojet plume into a sinuous path evolving dynamically throughout the ditch, promoting convective transport between the fluid layers. Furthermore it was found, that hydrojets placed at the surface yielded up to 30% higher average velocities, than the other configurations improving energy efficiency, however they led to formation of the dead zones extended near the ditch bottom. On the other hand, the hydrojets placed near the bottom demand for less 5% energy than mid-depth and near-surface configurations, but also yield lower average velocities, what affects overall mixing in the ditch and reduce energy efficiency to only 24%. Thus, the geometry with the hydrojets fixed in the mid-depth of the ditch was selected as the most economic and hydraulically efficient configuration, allowing use of up to 38% of supplied power in the fluid. For the same hydrojets' configurations, the difference in the energy expenditure obtained from all simulations with different models was less than 8%, thus it was concluded, that for design studies and power demand estimation, use of model requiring less computational resources, RANS, is recommended.

The hydrodynamics studies on the impact of mesh resolution and the models involved in boundary layer modelling on the energy expenditure were also presented in Chapter 4. It

was found, that the differences in values of power for mixing obtained for the finest grid of 5.7 million elements and the coarsest grid of 600 thousand elements is less than 5%. Furthermore, considering the impact of the model and near-wall treatment on the energy expenditure, it was found, that power demand increased with the solution accuracy. However, the highest value obtained for $k - \omega$ turbulence model, was only 2% higher than for LES, and 5% higher than for $k - \varepsilon$ model with Enhanced Wall Treatment. Furthermore, regardless of the turbulence model and mesh density, only the average velocity of the fluid has the impact on quantity of power supplied and thus on energy efficiency of the oxidation ditch system. Considering results of grid independence test and simulations with different turbulence models, the average velocity of the fluid in the oxidation ditch is 0.11 m s^{-1} , which for assessed power for mixing yields energy efficiency of 31%. Therefore one can conclude that the turbulence model accounting for less computational resources, RANS with $k - \varepsilon$ and Standard Wall Functions is appropriate for power expenditure and energy efficiency studies.

The analysis of the effect of turbulence models on the macromixing data obtained from the RTD simulations using particle tracking method was also made in Chapter 4. This work showed the limitations of some approaches in the computation of the RTD. It was found, that the RTD simulations based on the average flow field, RANS and URANS, allow achievement of the solution in the shorter physical time and with lesser computational efforts, but lead to overestimation of the channeling effects. The flow dynamics in oxidation ditch underlies mixing at all scales, both macro- and micro-, what should always be accounted for. As efficiency of wastewater treatment in activated sludge process depends on the bioreactor hydrodynamics, therefore CFD data for ASM must account with the all dynamic components of the flow. For such purpose, use of more complex approaches with higher computational costs, namely LES, is highly recommended.

Chapter 5 concerned determination of the energy expenditure on aeration in the oxidation ditch process. Computations were made to assess daily power consumption per capita by different groups of aeration devices commonly used in oxidation ditches and operated on the base of atmospheric air and high purity oxygen. It was concluded, that the most energy efficient aeration scenario are porous diffusers supplied by pure oxygen, accounting for ca. 0.7 kWh per capita, while the most energy-intensive is mechanical surface aeration with 19 kWh per capita. Nonetheless, to estimate overall energy expenditure in the oxidation ditch system equipped with porous diffusers, additional case-specific computations, such as determination of power consumption for air piping, mixed liquor recirculation and mixing by e.g. vertical shaft impellers or flow boosters, must be accounted for.

Detailed analysis of the energy budget in the proposed oxidation ditch system, aerated by PAC cooperating with hydrojets was made in Chapter 5. Computations of power demand on aeration considered actual oxygen requirements by PAC unit, and thus power demand by blower, and by oxygen generation. It was found, that introduction of the external aeration unit, PAC, is a promising solution providing distinct energy savings through 30% reduction of power demand by compressor in both, atmospheric air and pure oxygen aeration schemes, and thus oxygen generation in VPSA process, when comparing with BAT devices. Energy demand on mixed liquor pumping and reinjection was determined, considering two different hydrojets' designs. However, when comparing required elevation head, multi-slot injector configuration was rejected, as the one generating higher headloss, suggesting implementation of the second pumping unit in the system.

Scenario considering PAC unit supplied by air and cooperating with the single slot injectors required head of 1.5 m, yielding energy expenditure of up to 11.5 kWh per capita for mixed liquor recirculation and reinjection and up to 1.24 kWh for saturation with oxygen. Substitution of the air by pure oxygen allows reduction of the operation costs by blower by 80% and pumping unit by 75% yielding total energy demand for aeration of up to 0.3 kWh and up to 2.9 kWh per capita for recirculation and reinjection, respectively. From the above it can be concluded, that proposed aeration system consisting of PAC and slot injector seems to be promising solution allowing for distinct reduction of power demand and thus leading to energy savings, even when comparing with most efficient BAT systems - perforated membrane diffusers.

As final remark, the main achievements of this dissertation are:

- A new, highly efficient aeration technique based on the introduction of external aeration unit, PAC, into internal recirculation loop, was developed.
- Aeration performance in PAC is characterized by higher *SOTE* and *SAE* than current state of the art technologies.
- Considering pure oxygen systems, implementation of PAC allows reduction of energy expenditure on aeration by up to 67% in comparison with BAT devices. In comparison with aeration systems commonly used in oxidation ditches, energy demand by PAC constitutes 1-4% of the quantity required by surface aeration devices, horizontal rotors or slow-speed aerators and 7%- by membrane air diffusers.
- Extensive CFD studies on the hydrodynamics of the oxidation agitated with hydrojets ditch led to preparation of the guideline on the applicability of turbulence models serving different purposes. For design and energy efficiency

studies, RANS with $k - \varepsilon$ model accounting for less computational resources is recommended. For the hydrodynamics studies based on the RTD simulation for macromixing assessment, more complex modelling approaches of higher computational cost, such as LES, are more suitable.

- Proposed hydraulic configuration of the oxidation ditch aerated with PAC and agitated by slot injectors, allows to compromise objectives of integrated water pollution prevention control measures and standards set in Urban Waste Water Treatment Directive, combined with sustainable strategy for centralized wastewater treatment.

6.3 Future Work

Present work brought the insight into the ongoing research challenges in wastewater treatment sector. The suggestions for future work are as follows:

- Design and overall energy budget assessment of net-zero-energy wastewater treatment plants based on the oxidation ditch process aerated intermittently by PAC - hydrojets system and considering energy recovery from sludge digesters.
- Design studies on modification of height/length ratio in PAC aiming further enlargement of the oxygen/wastewater contact area, and thus diffusion layer surface.
- Computational and experimental approach to assess adaptation of PAC to wider range of devices, such as diffusers, and to aerate different wastewater treatment reactors, such as various multichannel oxidation ditch configurations, plug flow reactors and membrane bioreactors (MBR).
- Further CFD studies on oxidation ditch hydrodynamics involving solid - liquid modelling coupled to biokinetic reactions of wastewater treatment - aiming to overcome present modelling limitations concerning changes in growth and decay of biomass.
- Detailed studies on coupling of the RTD data obtained from CFD simulations of several most common oxidation ditch configurations (OrbalTM, CarrouselTM, ...) into ASM models, aiming development of more case-sensitive modelling guidelines.

7 References

- Abusam, A., Keesman, K.J., 1999. Effect of number of CSTR's on the modelling of oxidation ditches; steady state and dynamic analysis 13th Forum for Applied Biotechnology, Gent, Belgium, pp. 91-94.
- Abusam, A., Keesman, K.J., Meinema, K., Van Straten, G., 2001. Oxygen transfer rate estimation in oxidation ditches from clean water measurements. *Water Research* 35, 2058-2064.
- Abusam, A., Keesman, K.J., Spanjers, H., Van Straten, G., Meinema, K., 2002. Effect of oxidation ditch horizontal velocity on the nitrogen removal process. *European Water Management Online - European Water Association (EWA)*.
- Ahmed, T., Semmens, M.J., Voss, M.A., 2000. Energy loss characteristics of parallel flow bubbleless hollow fiber membrane aerators. *Journal of Membrane Science* 171, 87-96.
- Ahmed, T., Semmens, M.J., Voss, M.A., 2004. Oxygen transfer characteristics of hollow-fiber, composite membranes. *Advances in Environmental Research* 8, 637-646.
- Åmand, L., Carlsson, B., 2012. Optimal aeration control in a nitrifying activated sludge process. *Water Research* 46, 2101-2110.
- ANSYS, 2011. ANSYS FLUENT Theory Guide.
- Ardern, E., Lockett, W.T., 1914. Experiments on the Oxidation of the Sewage without the Aid of Filters. *Journal Society of Chemical Industries* 33, 523-539.
- ASCE, 1984. *Measurement of Oxygen Transfer in Clean Water*, New York, NY.

- ASCE, 1991. Measurement of Oxygen Transfer in Clean Water ANSI/ASCE 2-91, New York, NY.
- ASCE, 1997. Standard Guidelines for In-Process Oxygen Transfer Testing ASCE 18-96, New York, NY.
- ASCE, 2007. Measurement of Oxygen Transfer in Clean Water ASCE/EWRI 2-06, Reston, VA.
- AWWA, 2001. Manual of Water Supply Practices M 49: Butterfly Valves: Torque, Head Loss, and Cavitation Analysis. American Water Works Association, Denver, CO.
- Baghalian, S., Bonakdari, H., Nazari, F., Fazli, M., 2012. Closed-Form Solution for Flow Field in Curved Channels in Comparison with Experimental and Numerical Analyses and Artificial Neural Network. Engineering Applications of Computational Fluid Mechanics Vol. 6, 514-526.
- Baker, R., 1997. Environmental Law and Policy in the European Union and the United States. Greenwood Publishing Group, Westport, CT.
- Barnes, D., Foster, C.F., Johnstone, D.W.M., 1983. Oxidation ditches in wastewater treatment. Pitman Books, London.
- Benfield, L.D., Randall, C.W., 1980. Biological Process Design for Wastewater Treatment. Activated Sludge and its Process Modification Englewood Cliffs, NJ.
- Bhuyar, L.B., Thakre, S.B., Ingole, N.W., 2009. Design characteristics of Curved Blade aerator w.r.t. aeration efficiency and overall oxygen transfer coefficient and comparison with CFD modeling. International Journal of Engineering, Science and Technology 1, 1-15.
- Boden, S., Bieberle, M., Hampel, U., 2008. Quantitative measurement of gas hold-up distribution in a stirred chemical reactor using X-ray cone-beam computed tomography. Chemical Engineering Journal 139, 351-362.
- Bosma, A.J., Reitsma, B., 2007. Hydraulic Design of Activated sludge Tanks with CFD, COMSOL Users Conference Grenoble.
- Boyle, W.C., Stenstrom, M.K., Campbell, H.J., Brenner, R.C., 1989. Oxygen transfer in clean and process water for draft tube turbine aerators in total barrier oxidation ditch. Water Pollution Control Federation 61, 1449-1463.
- Brannock, M., Leslie, G., Wang, Y., Buetehorn, S., 2010a. Optimising mixing and nutrient removal in membrane bioreactors: CFD modelling and experimental validation. Desalination 250, 815-818.
- Brannock, M., Wang, Y., Leslie, G., 2010b. Mixing characterisation of full-scale membrane bioreactors: CFD modelling with experimental validation. Water Research 44, 3181-3191.
- Brischke, K., Woodrum, T., Hardison, J., Fisher, M., Olds, K., 2008. Sustainable Aeration Blower Design Saves Money Now. Proceedings of the Water Environment Federation 2008, 6416-6428.
- Brouckaert, C.J., Buckley, C.A., 1999. The Use of Computational Fluid Dynamics for Improving the Design and Operation of Water and Wastewater Treatment Plants Water Science & Technology 40, 81-89.

- Butler, B.J., Mayfield, C.I., 1996. *Cryptosporidium* spp. - A Review of the Organism, the Disease, and Implications for Managing Water Resources. Waterloo Centre for Groundwater Research Waterloo, Ontario, Canada.
- Cabral, J., Marques, C., 2006. Faecal Coliform Bacteria in Febros River (Northwest Portugal): Temporal Variation, Correlation with Water Parameters, and Species Identification. *Environmental Monitoring and Assessment* 118, 21-36.
- Canny, J., 1986. A computational approach to edge detection. *IEEE Transactions on Pattern Analysis and Machine Intelligence* 8, 679-698.
- Capela, S., Roustan, M., Héduit, A., 2001. Transfer number in fine bubble diffused aeration systems *Water Science & Technology* 43, 145-152.
- Chachuat, B., Roche, N., Latifi, M.A., 2001. Dynamic optimisation of small size wastewater treatment plants including nitrification and denitrification processes. *Computers & Chemical Engineering* 25, 585-593.
- Chachuat, B., Roche, N., Latifi, M.A., 2005. Long-term optimal aeration strategies for small-size alternating activated sludge treatment plants. *Chemical Engineering and Processing: Process Intensification* 44, 591-604.
- Chadwick, A., Morfett, J., 1998. *Hydraulics in Civil and Environmental Engineering*, Third Edition ed. E & FN Spon, London.
- Chen, Z., Guo, Y.C., Zhang, D.J., Xu, D.Y., 2006. Cross-correlation DPIV and application in oxidation ditch model. *Guangdian Gongcheng/Opto-Electronic Engineering* 33, 127-131.
- Chen, Z., Wu, H., 2010. Numerical simulation of hydraulic characteristic of oxidation ditch with eccentricity diversion wall, *Environmental Science and Information Application Technology (ESIAT)*, 2010 International Conference, pp. 500-503.
- Chiemchaisri, C., Yamamoto, K., 2005. Enhancement of oxygen transfer and nitrogen removal in a membrane separation bioreactor for domestic wastewater treatment. *Water Science & Technology* 51, 85-92.
- Chow, V.T., 1959. *Open-Channel Hydraulics*. McGraw-Hill Inc., New York.
- Cockx, A., Do-Quang, Z., Audic, J.M., Liné, A., Roustan, M., 2001. Global and local mass transfer coefficients in waste water treatment process by computational fluid dynamics. *Chemical Engineering and Processing* 40, 187-194.
- Coelho Pinheiro, M.N., Pinto, A.M.F.R., Campos, J.B.L.M., 2000. Gas Hold-up in Aerated Slugging Columns. *Chemical Engineering Research and Design* 78, 1139-1146.
- Cornel, P., Krause, S., 2006. Membrane bioreactors in industrial wastewater treatment - European experiences, examples and trends. *Water Science & Technology* 53, 37-44.
- Cornel, P., Wagner, M., Krause, S., 2003. Investigation of oxygen transfer rates in full scale membrane bioreactors. *Water Science & Technology* 47, 313-319.
- Cristea, S., de Prada, C., Sarabia, D., Gutiérrez, G., 2011. Aeration control of a wastewater treatment plant using hybrid NMPC. *Computers & Chemical Engineering* 35, 638-650.

- Czernuszenko, W., Rylov, A., 2002. Modeling of three-dimensional velocity field in open channel flows. *Modélisation des champs de vitesses tridimensionnelles en canal à surface libre* 40, 135-144.
- Dahikar, S.K., Gulawani, S.S., Joshi, J.B., Shah, M.S., Rama Prasad, C.S., Shukla, D.S., 2007. Effect of nozzle diameter and its orientation on the flow pattern and plume dimensions in gas-liquid jet reactors. *Chemical Engineering Science* 62, 7471-7483.
- Dani, A., Guiraud, P., Cockx, A., 2007. Local measurement of oxygen transfer around a single bubble by planar laser-induced fluorescence. *Chemical Engineering Science* 62, 7245-7252.
- De Araújo, A.C.B., Gallani, S., Mulas, M., Olsson, G., 2011. Systematic approach to the design of operation and control policies in activated sludge systems. *Industrial and Engineering Chemistry Research* 50, 8542-8557.
- DeMoyer, C.D., Schierholz, E.L., Gulliver, J.S., Wilhelms, S.C., 2003. Impact of bubble and free surface oxygen transfer on diffused aeration systems. *Water Research* 37, 1890-1904.
- Demuren, A.O., 1993. A numerical model for flow in meandering channels with natural bed topography. *Water Resources Research* 29, 1269-1277.
- Demuren, A.O., Rodi, W., 1986. Calculation of flow and pollutant dispersion in meandering channels. *Journal of Fluid Mechanics* 172, 63-92.
- Dhanasekharan, K.M., Sanyal, J., Jain, A., Haidari, A., 2005. A generalized approach to model oxygen transfer in bioreactors using population balances and computational fluid dynamics. *Chemical Engineering Science* 60, 213-218.
- Dhotre, M.T., Joshi, J.B., 2007. Design of a gas distributor: Three-dimensional CFD simulation of a coupled system consisting of a gas chamber and a bubble column. *Chemical Engineering Journal* 125, 149-163.
- Diamantis, V., Papaspyrou, I., Melidis, P., Aivasidis, A., 2010. High aeration rate enhances flow stratification in full-scale oxidation ditch. *Bioprocess and Biosystems Engineering* 33, 293-298.
- Díaz, M.E., Iranzo, A., Cuadra, D., Barbero, R., Montes, F.J., Galán, M.A., 2008a. Numerical simulation of the gas-liquid flow in a laboratory scale bubble column. Influence of bubble size distribution and non-drag forces. *Chemical Engineering Journal* 139, 363-379.
- Díaz, M.E., Montes, F.J., Galán, M.A., 2008b. Experimental study of the transition between unsteady flow regimes in a partially aerated two-dimensional bubble column. *Chemical Engineering and Processing: Process Intensification* 47, 1867-1876.
- Do-Quang, Z., Cockx, A., Liné, A., Roustan, M., 1999. Computational fluid dynamics applied to water and wastewater treatment facility modeling. *Environmental Engineering and Policy* 1, 137-147.
- Duchène, P., Cotteux, E., Capela, S., 2001. Applying fine bubble aeration to small aeration tanks. *Water Science & Technology* 44, 203-210.

- Dworak, T., Kampa, E., de Roo, C., Alvarez, C., Bäck, S., Benito, P., 2007. Simplification of European Water Policies - Study for the European Parliament's Committee on Environment, Public Health and Food Safety IP/A/ENVI/FWC/2006-172/Lot 1/C1/SC5
- Ekman, M., Björleinius, B., Andersson, M., 2006. Control of the aeration volume in an activated sludge process using supervisory control strategies. *Water Research* 40, 1668-1676.
- EPA, 1972a. Clean Water Act (CWA) - Federal Water Pollution Control Act Amendments of 1972, United States Environmental Protection Agency - Office of Water, Washington, DC.
- EPA, 1972b. Clean Water Act (CWA) - National Pollutant Discharge Elimination System (NPDES) Permit Program, United States Environmental Protection Agency - Office of Water, Washington, DC.
- EPA, 1985. Summary Report: Fine Pore (Fine Bubble) Aeration Systems, United States Environmental Protection Agency, Water Engineering Research Laboratory of Water, Cincinnati, OH.
- EPA, 1989. Design Manual: Fine Pore Aeration Systems, United States Environmental Protection Agency, Research and Development - Risk Reduction Engineering Laboratory, Cincinnati, OH
- EPA, 1999. Wastewater Technology Fact Sheet. Fine Bubble Aeration, United States Environmental Protection Agency - Office of Water, Washington, DC.
- EPA, 2000. Wastewater Technology Fact Sheet. Oxidation Ditches, United States Environmental Protection Agency - Office of Water, Washington, DC.
- EPA, 2010. Evaluation of Energy Conservation Measures of Wastewater Treatment Facilities, United States Environmental Protection Agency, Office of Wastewater Management, Pennsylvania, Washington, DC.
- EPA, 2013. Energy Efficiency in Water and Wastewater Facilities - A Guide to Developing and Implementing Greenhouse Gas Reduction Programs United States Environmental Protection Agency, Washington, DC.
- ETWWA, 2010. Water Partnership Program - Improving Wastewater Use in Agriculture: An Emerging Priority - Energy Transport and Water Department Water Anchor. The World Bank.
- Fan, L., Mao, Z., Wang, Y., 2005. Numerical simulation of turbulent solid-liquid two-phase flow and orientation of slender particles in a stirred tank. *Chemical Engineering Science* 60, 7045-7056.
- Fan, L., Xu, N., Wang, Z., Shi, H., 2010. PDA experiments and CFD simulation of a lab-scale oxidation ditch with surface aerators. *Chemical Engineering Research and Design* 88, 23-33.
- Farizoglu, B., Keskinler, B., 2007. Influence of draft tube cross-sectional geometry on K_La and ϵ in jet loop bioreactors (JLB). *Chemical Engineering Journal* 133, 293-299.
- Farrell, B.F., Ioannou, P.J., 1998. Perturbation Structure and Spectra in Turbulent Channel Flow. *Theoretical and Computational Fluid Dynamics* 11, 237-250.

- Fayolle, Y., Cockx, A., Gillot, S., Roustan, M., Héduit, A., 2007. Oxygen transfer prediction in aeration tanks using CFD. *Chemical Engineering Science* 62, 7163-7171.
- Fayolle, Y., Gillot, S., Cockx, A., Bensimhon, L., Roustan, M., Heduit, A., 2010. In situ characterization of local hydrodynamic parameters in closed-loop aeration tanks. *Chemical Engineering Journal* 158, 207-212.
- Fayolle, Y., Gillot, S., Cockx, A., Roustan, M., Heduit, A., 2006. In situ local parameter measurements for CFD modelling to optimize aeration, 79th Annual Technical Exhibition and Conference WEFTEC'06, Dallas, TX, pp. 3314-3325.
- Fernández, F.J., Castro, M.C., Rodrigo, M.A., Cañizares, P., 2011. Reduction of aeration costs by tuning a multi-set point on/off controller: A case study. *Control Engineering Practice* 19, 1231-1237.
- Fikar, M., Chachuat, B., Latifi, M.A., 2005. Optimal operation of alternating activated sludge processes. *Control Engineering Practice* 13, 853-861.
- Fonade, C., Doubrovine, N., Maranges, C., Morchain, J., 2001. Influence of a transverse flowrate on the oxygen transfer performance in heterogeneous aeration: Case of hydro-ejectors. *Water Research* 35, 3429-3435.
- Francois, J., Dietrich, N., Guiraud, P., Cockx, A., 2011. Direct measurement of mass transfer around a single bubble by micro-PLIFI. *Chemical Engineering Science* 66, 3328-3338.
- Fujasová, M., Linek, V., Moucha, T., 2007. Mass transfer correlations for multiple-impeller gas-liquid contactors. Analysis of the effect of axial dispersion in gas and liquid phases on "local" kLa values measured by the dynamic pressure method in individual stages of the vessel. *Chemical Engineering Science* 62, 1650-1669.
- Gillot, S., Capela-Marsal, S., Roustan, M., Héduit, A., 2005. Predicting oxygen transfer of fine bubble diffused aeration systems - Model issued from dimensional analysis. *Water Research* 39, 1379-1387.
- Gillot, S., Héduit, A., 2000. Effect of air flow rate on oxygen transfer in an oxidation ditch equipped with fine bubble diffusers and slow speed mixers. *Water Research* 34, 1756-1762.
- Gillot, S., Vanrolleghem, P.A., 2003. Equilibrium temperature in aerated basins—comparison of two prediction models. *Water Research* 37, 3742-3748.
- Glover, G.C., Printemps, C., Essemiani, K., Meinhold, J., 2006. Modelling of wastewater treatment plants-how far shall we go with sophisticated modelling tools. *Water Science & Technology* 53, 79-89.
- Gresch, M., Armbruster, M., Braun, D., Gujer, W., 2011. Effects of aeration patterns on the flow field in wastewater aeration tanks. *Water Research* 45, 810-818.
- Grundfos, 2002. *Wastewater Pumps - Engineering Manual*.
- Henze, M., van Loosdrecht, M.C.M., Ekama, G.A., Brdjanovic, D., 2008. *Biological Wastewater Treatment: Principles, Modeling and Design*. IWA Publishing, London.

- Holenda, B., Domokos, E., Rédey, Á., Fazakas, J., 2007. Aeration optimization of a wastewater treatment plant using genetic algorithm. *Optimal Control Applications and Methods* 28, 191-208.
- Holenda, B., Domokos, E., Rédey, Á., Fazakas, J., 2008. Dissolved oxygen control of the activated sludge wastewater treatment process using model predictive control. *Computers & Chemical Engineering* 32, 1270-1278.
- Hussain, I., Raschid, L., Hanjra, M., A., Marikar, F., van der Hoek, W., 2002. Wastewater Use in Agriculture: Review of Impact and Methodological Issues in Valuing Impacts - Working Paper 37. International Water Management Institute.
- Janssen, P.M.J., Meinema-Linders, K., Niermans, R.P., 2002. Surface aeration and a small footprint can be combined. *Water Science & Technology* 46, 309-316.
- Janzen, J.G., Herlina, H., Jirka, G.H., Schulz, H.E., Gulliver, J.S., 2010. Estimation of mass transfer velocity based on measured turbulence parameters. *AIChE Journal* 56, 2005-2017.
- Jimenez, M., Dietrich, N., Cockx, A., Hebrard, G., 2013. Experimental study of O₂ diffusion coefficient measurement at a planar gas-liquid interface by PLIF with inhibition. *AIChE Journal* 59, 325-333.
- Jin, B., Lant, P., 2004. Flow regime, hydrodynamics, floc size distribution and sludge properties in activated sludge bubble column, air-lift and aerated stirred reactors. *Chemical Engineering Science* 59, 2379-2388.
- Jin, B., Yin, P., Lant, P., 2006. Hydrodynamics and mass transfer coefficient in three-phase air-lift reactors containing activated sludge. *Chemical Engineering and Processing: Process Intensification* 45, 608-617.
- Jing, J.Y., Feng, J., Li, W.Y., 2009. Carrier effects on oxygen mass transfer behavior in a moving-bed biofilm reactor. *Asia-Pacific Journal of Chemical Engineering* 4, 618-623.
- Joseph, C., Hamilton, G., O'Connor, M., Nicholas, S., Marshall, R., Stanwell-Smith, R., Ndawula, E., Casemore, D., Gallagher, P., Harnett, P., 1991. Cryptosporidiosis in the Isle of Thanet; an outbreak associated with local drinking water. *Epidemiology and Infection* 107, 509-519.
- Kaliman, A., Rosso, D., Leu, S.-Y., Stenstrom, M.K., 2008. Fine-pore aeration diffusers: Accelerated membrane ageing studies. *Water Research* 42, 467-475.
- Kantarci, N., Borak, F., Ulgen, K.O., 2005. Bubble column reactors. *Process Biochemistry* 40, 2263-2283.
- Karia, G.L., Christian, R.A., 2006. *Wastewater Treatment: Concepts And Design Approach*. Prentice-Hall India, New Delhi.
- Karpinska, A.M., Dias, M.M., Boaventura, R.A., Lopes, J.C.B., Santos, R.J., 2012a. On the modelling and design of Oxidation Ditches Aerated with Hydrojets using CFD codes., 3rd IWA/WEF Wastewater Treatment Modelling Seminar-WWTmod2012, Mont-Sainte-Anne, QC, Canada, pp. 151-160.

- Karpinska, A.M., Dias, M.M., Boaventura, R.A., Santos, R.J., 2012b. CFD Approach on the Energy Analysis of an Oxidation Ditch Aerated with Hydrojets, IWA World Congress on Water, Climate and Energy 2012, Dublin, Ireland.
- Karpinska, A.M., Pereira, J.P., Dias, M.M., Santos, R.J., 2008. CFD simulation of an oxidation ditch, in: Ferreira, E.C., Mota, M. (Eds.), ChemPor - 10th International Chemical and Biological Engineering Conference, Braga, Portugal, pp. 73-74.
- Khosronejad, A., Rennie, C.D., Salehi Neyshabouri, S.A.A., Townsend, R.D., 2007. 3D numerical modeling of flow and sediment transport in laboratory channel bends. *Journal of Hydraulic Engineering* 133, 1123-1134.
- Kim, J., Moin, P., Moser, R., 1987. Turbulence statistics in fully developed channel flow at low Reynolds number. *Journal of Fluid Mechanics* 177, 133-166.
- KLa Systems, 2007. KLa Slot Injector, KLa Systems Inc., Assonet, MA.
- Klusener, P.A.A., Jonkers, G., During, F., Hollander, E.D., Schellekens, C.J., Ploemen, I.H.J., Othman, A., Bos, A.N.R., 2007. Horizontal cross-flow bubble column reactors: CFD and validation by plant scale tracer experiments. *Chemical Engineering Science* 62, 5495-5502.
- Kochevsky, A.N., 2004. Possibilities of Simulation of Fluid Flows Using the Modern CFD Software Tools.
- Kossay, K., Al-Ahmady, K., 2006. Analysis of oxygen transfer performance on sub-surface aeration systems. *International Journal of Environmental Research and Public Health* 3, 301-308.
- Kulkarni, A.A., Ekambara, K., Joshi, J.B., 2007. On the development of flow pattern in a bubble column reactor: Experiments and CFD. *Chemical Engineering Science* 62, 1049-1072.
- Kusiak, A., Wei, X., 2013. Optimization of the activated sludge process. *Journal of Energy Engineering* 139, 12-17.
- Launder, B.E., Reece, G.J., Rodi, W., 1975. Progress in the development of a Reynolds-stress turbulent closure. *Journal of Fluid Mechanics* 68, 537-566.
- Launder, B.E., Spalding, D.B., 1974. The numerical computation of turbulent flows. *Computer Methods in Applied Mechanics and Engineering* 3, 269-289.
- Le-Clech, P., Alvarez-Vazquez, H., Jefferson, B., Judd, S., 2003. Fluid hydrodynamics in submerged and sidestream membrane bioreactors. *Water Science & Technology* 48, 113-119.
- Le Moullec, Y., Gentric, C., Potier, O., Leclerc, J.P., 2010a. CFD simulation of the hydrodynamics and reactions in an activated sludge channel reactor of wastewater treatment. *Chemical Engineering Science* 65, 492-498.
- Le Moullec, Y., Gentric, C., Potier, O., Leclerc, J.P., 2010b. Comparison of systemic, compartmental and CFD modelling approaches: Application to the simulation of a biological reactor of wastewater treatment. *Chemical Engineering Science* 65, 343-350.

- Le Moullec, Y., Potier, O., Gentric, C., Leclerc, J.-P., 2008a. A general correlation to predict axial dispersion coefficients in aerated channel reactors. *Water Research* 42, 1767-1777.
- Le Moullec, Y., Potier, O., Gentric, C., Pierre Leclerc, J., 2008b. Flow field and residence time distribution simulation of a cross-flow gas-liquid wastewater treatment reactor using CFD. *Chemical Engineering Science* 63, 2436-2449.
- Lee, T.-C., Kashyap, R.L., 1994. Building skeleton models via 3-D medial surface/axis thinning algorithms. *CVGIP: Graphical Models and Image Processing* 56, 462 - 478
- Lesage, N., Spérandio, M., Lafforgue, C., Cockx, A., 2003. Calibration and Application of a 1-D Model for Oxidation Ditches. *Chemical Engineering Research and Design* 81, 1259-1264.
- Leschziner, M.A., Rodi, W., 1979. Calculation of strongly curved open channel flow. *Journal of Hydraulic Engineering (ASCE)* 105, 1297-1314.
- Lessard, P., Tusseau-Vuillemin, M.H., Héduit, A., Lagarde, F., 2007. Assessing chemical oxygen demand and nitrogen conversions in a multi-stage activated sludge plant with alternating aeration. *Journal of Chemical Technology and Biotechnology* 82, 367-375.
- Leu, S.-Y., Libra, J.A., Stenstrom, M.K., 2010. Monitoring off-gas O₂/CO₂ to predict nitrification performance in activated sludge processes. *Water Research* 44, 3434-3444.
- Levenspiel, O., 1999. *Chemical Reaction Engineering*, Third Edition ed. Wiley & Sons, New York, NY.
- Lewis, W.K., Whitman, W.G., 1924. Principles of Gas Absorption. *Industrial and Engineering Chemistry* 16, 1215-1220.
- Li, J., Zhu, L.-P., Xu, Y.-Y., Zhu, B.-K., 2010. Oxygen transfer characteristics of hydrophilic treated polypropylene hollow fiber membranes for bubbleless aeration. *Journal of Membrane Science* 362, 47-57.
- Libby, P.A., 1996. *Introduction to Turbulence*. Taylor & Francis.
- Lippi, S., Rosso, D., Lubello, C., Canziani, R., Stenstrom, M.K., 2009. Temperature modelling and prediction for activated sludge systems. *Water Science & Technology* 59, 125-131.
- Liu, C., Shen, M.Y., 2010. A three dimensional k- ϵ -Ap model for water-sediment movement. *International Journal of Sediment Research* 25, 17-27.
- Luo, H.P., Al-Dahhan, M.H., 2008. Local characteristics of hydrodynamics in draft tube airlift bioreactor. *Chemical Engineering Science* 63, 3057-3068.
- Machado, V.C., Gabriel, D., Lafuente, J., Baeza, J.A., 2009. Cost and effluent quality controllers design based on the relative gain array for a nutrient removal WWTP. *Water Research* 43, 5129-5141.
- Makinia, J., Wells, S.A., 2000a. A general model of the activated sludge reactor with dispersive flow - I. Model development and parameter estimation. *Water Research* 34, 3987-3996.

- Makinia, J., Wells, S.A., 2000b. A general model of the activated sludge reactor with dispersive flow - II. model verification and application. *Water Research* 34, 3997-4006.
- Mandt, M.G., Bell, B.A., 1984. *Oxidation ditches in wastewater treatment*. Ann Arbor Science Publishers.
- Marcelino, M., Guisasola, A., Baeza, J.A., 2009. Dynamic peroxide method for $kLaO_2$ estimation. *Journal of Chemical Technology & Biotechnology* 84, 1104-1110.
- Mineta, R., Salehi, Z., Yoshikawa, H., Kawase, Y., 2011. Oxygen transfer during aerobic biodegradation of pollutants in a dense activated sludge slurry bubble column: Actual volumetric oxygen transfer coefficient and oxygen uptake rate in p-nitrophenol degradation by acclimated waste activated sludge. *Biochemical Engineering Journal* 53, 266-274.
- Moraveji, M.K., Sajjadi, B., Davarnejad, R., 2012. CFD Simulation of hold-up and liquid circulation velocity in a membrane airlift reactor. *Theoretical Foundations of Chemical Engineering* 46, 266-273.
- Morchain, J., Maranges, C., Fonade, C., 2000. CFD modelling of a two-phase jet aerator under influence of a crossflow. *Water Research* 34, 3460-3472.
- Moser, R.D., Kim, J., Mansour, N.N., 1999. Direct numerical simulation of turbulent channel flow up to $Re(\tau) = 590$. *Physics of Fluids* 11, 943-945.
- Mueller, J.A., Boyle, W.C., Pöpel, H.J., 2002. *Aeration: principles and practice*. CRC Press.
- Nakamachi, K., Fujiwara, T., Chen, X., Hashimoto, T., Kawaguchi, Y., Tsuno, H., 2012. Energy Efficiency of Full-scale Oxidation Ditch with Dual Dissolved Oxygen Control Technology in Clean Water and Domestic Wastewater. *Journal of Water and Environment Technology* Vol. 10, 229-240.
- Nauman, E.B., 2007. *Residence Time Distributions, Chemical Reactor Design, Optimization, and Scaleup*. John Wiley & Sons, Inc., New Jersey, NJ, pp. 535-574.
- Nezu, I., Rodi, W., 1986. Open-channel Flow Measurements with a Laser Doppler Anemometer. *Journal of Hydraulic Engineering* 112, 335-355.
- Nicolella, A., van Loosdrecht, M., van der Lans, R., Heijnen, J., 1998. Hydrodynamic characteristics and gas-liquid mass transfer in a biofilm airlift suspension reactor. *Biotechnology and Bioengineering* 60, 627-633.
- Nogueira, S., Riethmuller, M.L., Campos, J.B.L.M., Pinto, A.M.F.R., 2006. Flow patterns in the wake of a Taylor bubble rising through vertical columns of stagnant and flowing Newtonian liquids: An experimental study. *Chemical Engineering Science* 61, 7199-7212.
- O'Brien, M., Mack, J., Lennox, B., Lovett, D., Wall, A., 2011. Model predictive control of an activated sludge process: A case study. *Control Engineering Practice* 19, 54-61.
- OECD/OCDE, 2001. *Guidelines for the Testing of Chemicals: Simulation Test - Aerobic Sewage Treatment: 303A Activated Sludge Units*.
- Olsson, C.K., 1993. *Image processing methods in materials science*. PhD Thesis. Technical University of Denmark, Lyngby, Denmark.

- Olsson, G., 2011. Water and Wastewater, Instrumentation, Monitoring, Control and Automation, in: Meyers, R.A. (Ed.), *Encyclopaedia of Sustainability Science and Technology*. Springer Verlagan, Germany.
- Pasveer, A., 1962. *Verfahren und Anlage zum Reinigen von Abwasser (Process and Device for the Purification of Sewage)*. Federal Institute of Intellectual Property (Switzerland). Passavant Werke, Netherlands.
- Paulson, L.D., 2012. *Planned Study to Create Roadmap for Net-Zero-Energy Wastewater Treatment*. Water in America, Water Research & Reports.
- Pereira, J.P., Karpinska, A., Gomes, P.J., Martins, A.A., Dias, M.M., Lopes, J.C.B., Santos, R.J., 2012. *Activated Sludge Models Coupled to CFD Simulations*, in: Dias, R., Lima, R., Martins, A.A., Mata, T.M. (Eds.), *Single and Two-Phase Flows in Chemical and Biomedical Engineering*. Bentham e-Books.
- Pereira, J.P., Karpinska, A.M., Dias, M.M., Santos, R.J., 2009. The dissolved oxygen profile in Oxidation Ditches: a numerical study on its effect on nutrient removal, 2nd IWA Specialized Conference on Nutrient Management in Wastewater Treatment Processes, Krakow, Poland, pp. 97-104.
- Pescod, M.B., 1992. *Wastewater treatment and use in agriculture - FAO irrigation and drainage paper 47*. Food and Agriculture Organization of the United Nations- Natural Resources Management and Environment Department
- Pinelli, D., Liu, Z., Magelli, F., 2010. Analysis of KLa Measurement Methods in Stirred Vessels: The Role of Experimental Techniques and Fluid Dynamic Models. *International Journal of Chemical Reactor Engineering* 8, 1542-6580.
- Pope, S.B., 2000. *Turbulent Flows*, 5th ed, New York, NY.
- Pöpel, H.J., 1979. *Aeration and gas transfer*, Second Edition ed. Delft University of Technology, Delft, The Netherlands.
- Potier, O., Leclerc, J.P., Pons, M.N., 2005. Influence of geometrical and operational parameters on the axial dispersion in an aerated channel reactor. *Water Research* 39, 4454-4462.
- Prandtl, L., 1904. Über Flüssigkeitsbewegung bei sehr kleiner Reibung., *Verh. III. Intern. Math. Kongr.*, Heidelberg.
- Prandtl, L., 1925. Bericht über Untersuchungen zur ausgebildeten Turbulenz. *Zeitschrift für Angewandte Mathematik und Mechanik (Applied Mathematics and Mechanics)* 5, 136-139.
- Quasim, S.R., 1999. *Wastewater Treatment Plants: Planning, Design and Operation Second Edition* ed. CRC Press LLC, Boca Raton, FL.
- Rao, A.R., Kumar, B., 2007. The use of circular surface aerators in wastewater treatment tanks. *Journal of Chemical Technology and Biotechnology* 82, 101-107.
- Rao, A.R., Patel, A.K., Kumar, B., 2009. Oxygen transfer in circular surface aeration tanks. *Environmental Technology* 30, 747-753.

7 References

- Ratanayaka, D.D., Brandt, M.J., Johnson, M., 2009. *Water Supply*, 6th ed. B-H Elsevier, Oxford.
- Reardon, D.J., 1995. Turning down the power. *Civil Engineering* 65, 54-56.
- Rigopoulos, S., Jones, A., 2003. A hybrid CFD-reaction engineering framework for multiphase reactor modelling: Basic concept and application to bubble column reactors. *Chemical Engineering Science* 58, 3077-3089.
- Roe, F.C., 1945. Porous Tube Air Diffusers. *Sewage Works Journal* 17, 878-888.
- Rosso, D., Huo, D.L., Stenstrom, M.K., 2006. Effects of interfacial surfactant contamination on bubble gas transfer. *Chemical Engineering Science* 61, 5500-5514.
- Rosso, D., Iranpour, R., Stenstrom, M.K., 2005. Fifteen Years of Off-Gas Transfer Efficiency Measurements on Fine Pore Aerators: Key Role of Sludge Age and Normalized Air Flux. *Water Environment Research* 77, 266-273.
- Rosso, D., Libra, J.A., Wiehe, W., Stenstrom, M.K., 2008a. Membrane properties change in fine-pore aeration diffusers: Full-scale variations of transfer efficiency and headloss. *Water Research* 42, 2640-2648.
- Rosso, D., Lothman, S.E., Jeung, M.K., Pitt, P., Gellner, W.J., Stone, A.L., Howard, D., 2011. Oxygen transfer and uptake, nutrient removal, and energy footprint of parallel full-scale IFAS and activated sludge processes. *Water Research* 45, 5987-5996.
- Rosso, D., Stenstrom, M.K., 2005. Comparative economic analysis of the impacts of mean cell retention time and denitrification on aeration systems. *Water Research* 39, 3773-3780.
- Rosso, D., Stenstrom, M.K., 2006. Surfactant effects on α -factors in aeration systems. *Water Research* 40, 1397-1404.
- Rosso, D., Stenstrom, M.K., Larson, L.E., 2008b. Aeration of large-scale municipal wastewater treatment plants: state of the art. *Water Science & Technology* 57, 973-978.
- Russ, J.C., 2011. *The image processing handbook*, Sixth Edition ed. CRC Press Taylor & Francis Group, Boca Raton, FL.
- Salim, S.M., Cheach, S.C., 2009. Wall y^+ Strategy for Dealing with Wall-bounded Turbulent Flows, International MultiConference of Engineers and Computer Scientists IMECS, Hong Kong.
- Schmid, A., 2009. A New Aeration Technology Using "Supercavitation". *Recent Patents on Chemical Engineering* 2, 176-180.
- Schmidt-Holthausen, H.J., Zievers, E.C., 1980. 50 Years of Experience in Europe with Fine Bubble Aeration, 53rd Annual Conference WPCF Las Vegas, NV.
- Semblex, 1987. *Static Tube Aerator Test*, Semblex, Springfield, MO.
- Shaikh, A., Al-Dahhan, M.H., 2007. A Review on Flow Regime Transition in Bubble Columns. *International Journal of Chemical Reactor Engineering* 5, 1-68.

- Shammas, N.K., Wang, L.K., 2009. Pure Oxygen Activated Sludge Process, in: Wang, L.K., Pereira, N.C., Hung, Y.-T., Shammas, N.K. (Eds.), *Handbook of Environmental Engineering: Biological Treatment Processes*. The Humana Press, Totowa, NJ.
- Shukry, A., 1950. Flow around Bends in an Open Flume. *Transactions, ASCE* 115, 751-779.
- Šimčík, M., Mota, A., Ruzicka, M.C., Vicente, A., Teixeira, J., 2011. CFD simulation and experimental measurement of gas holdup and liquid interstitial velocity in internal loop airlift reactor. *Chemical Engineering Science* 66, 3268-3279.
- Spicka, P., 2001. Hydrodynamics of 2D Gas-Liquid Reactors. Experimental Study and CFD Simulation. PhD Thesis. University of Porto, FEUP, Porto.
- Spicka, P., Dias, M.M., Lopes, J.C.B., 2001. Gas-liquid flow in a 2D column: Comparison between experimental data and CFD modelling. *Chemical Engineering Science* 56, 6367-6383.
- Spicka, P., Martins, A.A., Dias, M.M., Lopes, J.C.B., 1999. Hydrodynamics of gas-liquid flow in 2D packed/unpacked rectangular reactor. *Chemical Engineering Science* 54, 5127-5137.
- Stamou, A.I., 1997. Modelling of oxidation ditches using an open channel flow 1-D advection-dispersion equation and ASM1 process description. *Water Science & Technology* 36, 269-276.
- Stamou, A.I., 2008. Improving the hydraulic efficiency of water process tanks using CFD models. *Chemical Engineering and Processing: Process Intensification* 47, 1179-1189.
- Stenstrom, M.K., Gilbert, R.G., 1981. Effect of Alpha, Beta and Theta on Specification, Design and Operation of Aeration Systems. *Water Research* 15, 643-654.
- Stenstrom, M.K., Leu, S.-Y., Jiang, P., 2006. Theory to Practice: Oxygen Transfer and the New ASCE Standard, Water Environment Federation® Technical Exhibition and Conference WEFTEC® 2006. Water Environment Federation, pp. 4838-4852.
- Stenstrom, M.K., Rosso, D., 2008. Aeration and Mixing, in: Henze, M., van Loosdrecht, M.C.M., Ekama, G.A., Brdjanovic, D. (Eds.), *Biological Wastewater Treatment: Principles, Modeling and Design*. IWA Publishing, London, UK
- Suresh, S., Srivastava, V.C., Mishra, I.M., 2009. Techniques for oxygen transfer measurement in bioreactors: a review. *Journal of Chemical Technology & Biotechnology* 84, 1091-1103.
- Syron, E., Casey, E., 2008. Membrane-aerated biofilms for high rate biotreatment: Performance appraisal, engineering principles, scale-up, and development requirements. *Environmental Science and Technology* 42, 1833-1844.
- Tabib, M.V., Roy, S.A., Joshi, J.B., 2008. CFD simulation of bubble column-An analysis of interphase forces and turbulence models. *Chemical Engineering Journal* 139, 589-614.
- Takács, G., 2005. *Gas Lift: Manual*. PennWell Books, Tulsa, OK.
- Talvy, S., Cockx, A., Line, A., 2007. Modeling of oxygen mass transfer in a gas-liquid airlift, reactor. *AIChE Journal* 53, 316-326.

- Tang, C., Heindel, T.J., 2004. Time-dependent gas holdup variation in an air-water bubble column. *Chemical Engineering Science* 59, 623-632.
- Taricska, J.R., Chen, P., Hung, Y.-T., Wang, L.K., Zou, S.-W., 2009a. Surface and Spray Aeration, in: Wang, L.K., Pereira, N.C., Hung, Y.-T., Shammass, N.K. (Eds.), *Biological Treatment Processes*. The Humana Press, Totowa, NJ.
- Taricska, J.R., Huang, J.Y.C., Chen, P., Hung, Y.-T., Zou, S.-W., 2009b. Submerged Aeration, in: Wang, L.K., Pereira, N.C., Hung, Y.-T., Shammass, N.K. (Eds.), *Biological Treatment Processes*. The Humana Press, Totowa, NJ.
- Tchobanoglous, G., Burton, F.L., Stensel, H.D., Eddy, M., 2003. *Wastewater engineering: Treatment and reuse*, McGraw-Hill Series in Civil and Environmental Engineering, Fourth ed. McGraw-Hill New York, NY.
- Terasaka, K., Hirabayashi, A., Nishino, T., Fujioka, S., Kobayashi, D., 2011. Development of microbubble aerator for waste water treatment using aerobic activated sludge. *Chemical Engineering Science* 66, 3172-3179.
- Thakre, S.B., Bhuyar, L.B., Deshmukh, S.J., 2008. Effect of Different Configurations of Mechanical Aerators on Oxygen Transfer and Aeration Efficiency with respect to Power Consumption. *International Journal of Aerospace and Mechanical Engineering* 2, 100-108.
- UWWTD-REP, 2007. *Terms and Definitions of the Urban Waste Water Treatment Directive 91/271/EEC* Brussels.
- Vermande, S., Simpson, K., Essemiani, K., Fonade, C., Meinhold, J., 2007. Impact of agitation and aeration on hydraulics and oxygen transfer in an aeration ditch: Local and global measurements. *Chemical Engineering Science* 62, 2545-2555.
- Versteeg, H.K., Malalasekera, W., 1995. *An Introduction to Computational Fluid Dynamics. The Finite Volume Method.*, Second ed. Pearsons Prentice Hall, Harlow, Essex.
- Vieira, J., Fonseca, A., Vilar, V.P., Boaventura, R.R., Botelho, C.S., 2013. Water quality modelling of Lis River, Portugal. *Environmental Science and Pollution Research* 20, 508-524.
- von Kármán, T., 1930. Mechanische Ähnlichkeit und Turbulenz, *Nachrichten von der Gesellschaft der Wissenschaften zu Göttingen, Fachgruppe 1 (Mathematik)*, no. 5, pp. 58-76.
- von Sperling, M., 2007. *Basic Principles of Wastewater Treatment*. IWA Publishing, London.
- Wang, S.-J., Zhong, J.-J., 2007. Bioreactor Engineering, in: Yang, S.-T. (Ed.), *Bioprocessing for Value-Added Products from Renewable Resources: New Technologies and Applications* Elsevier Science, Oxford.
- WEF, 2009. *Energy Conservation in Water and Wastewater Treatment Facilities*, Water Environment Federation Manual of Practice No. 32; McGraw-Hill, Inc., New York, NY.
- WHO, 2000a. *Global Water Supply and Sanitation Assessment*. World Health Organization. Geneva, Switzerland.
- WHO, 2000b. *The World Health Report 2000 - World Health Organization (WHO)*. Geneva, Switzerland.

- WHO, 2006. Guidelines for the safe use of wastewater, excreta and greywater. Volume 2: Wastewater use in agriculture. WHO Press - World Health Organization, France.
- Wilcox, D.C., Traci, R.M., 1976. A complete model of turbulence, AIAA Paper 76-351, San Griego, CA.
- Wilson, C.A.M.E., Guymer, I., Boxall, J.B., Olsen, N.R.B., 2007. Three-dimensional numerical simulation of solute transport in a meandering self-formed river channel. *Journal of Hydraulic Research* 45, 610-616.
- Wolf, D., Resnick, W., 1963. Residence Time Distribution in Real Systems. *Industrial & Engineering Chemistry Fundamentals* 2, 287-293.
- Wu, B., Chen, Z., 2011. An integrated physical and biological model for anaerobic lagoons. *Bioresource Technology* 102, 5032-5038.
- Wu, S.Y., Zhou, D.Q., Zheng, Y., 2012. Energy configuration optimization of submerged propeller in oxidation ditch based on CFD. *IOP Conference Series: Earth and Environmental Science* 15.
- Xia, S.B., Liu, J.X., 2004. An innovative integrated oxidation ditch with vertical circle (IODVC) for wastewater treatment. *Journal of Environmental Sciences* 16, 367-370.
- Xu, N., Fan, L., Pang, H., Shi, H., 2010. Feasibility study and CFD-aided design for a new type oxidation ditch based on airlift circulation. *The Canadian Journal of Chemical Engineering* 88, 728-741.
- Xu, Z., Yu, J., 2008. Hydrodynamics and mass transfer in a novel multi-airlifting membrane bioreactor. *Chemical Engineering Science* 63, 1941-1949.
- Yang, Y., Yang, J., Zuo, J., Li, Y., He, S., Yang, X., Zhang, K., 2011. Study on two operating conditions of a full-scale oxidation ditch for optimization of energy consumption and effluent quality by using CFD model. *Water Research* 45, 3439-3452.
- Yunt, F.W., Hancuff, T.O., 1988. Aeration Equipment Evaluation- Phase I- Clean Water Test Results, United States Environmental Protection Agency, Research and Development - Water Engineering Research Laboratory, Cincinnati, OH
- Zerari, K., Seyssieq, I., Akretche, D.E., Roche, N., 2013. Enhancement of oxygen mass transfer coefficients in a hybrid membrane bioreactor. *Journal of Chemical Technology and Biotechnology* 88, 1007-1013.
- Zhang, D., Deen, N.G., Kuipers, J.A.M., 2006. Numerical simulation of the dynamic flow behavior in a bubble column: A study of closures for turbulence and interface forces. *Chemical Engineering Science* 61, 7593-7608.
- Zhang, D., Guo, L., Xu, D., Chen, Y., 2010. Simulation of component distributions in a full-scale carrousel oxidation ditch: a model coupling sludge-wastewater two-phase turbulent hydrodynamics with bioreaction kinetics. *Environmental Engineering Science* 27, 159-168.
- Zima, P., Makinia, J., Swiniarski, M., Czerwionka, K., 2009. Combining computational fluid dynamics with a biokinetic model for predicting ammonia and phosphate behavior in aeration tanks. *Water Environment Research* 81, 2353-2362.